



Technische Universität München
TUM School of Engineering and Design

Impedance Based Design and Assessment of Interoperability within Wireless Power Charging Systems for Electric Vehicles

Denis Kraus

Vollständiger Abdruck der von der TUM School of Engineering and Design
der Technischen Universität München zur Erlangung eines

Doktors der Ingenieurwissenschaften (Dr.-Ing.)

genehmigten Dissertation.

Vorsitz: Prof. Malte Jaensch, Ph.D.

Prüfer*innen der Dissertation: 1. Prof. Dr.-Ing. Hans-Georg Herzog

2. Prof. Grant Covic, Ph.D.

Die Dissertation wurde am 25.04.2023 bei der Technischen Universität München eingereicht
und durch die TUM School of Engineering and Design am 27.09.2023 angenommen.

Abstract

Inductive power transfer (IPT) technology enables electrical power transmission without a physical connection, making it suitable for wirelessly charging electric vehicles (EVs). IPT offers a range of benefits, including safe, reliable and convenient battery charging, as well as the potential for dynamic and autonomous charging. These advantages can help drive the widespread adoption of EVs and promote a more sustainable transportation future.

However, the lack of a physical connection means that there is no defined interface between the charging infrastructure side and the vehicle, as is the case with conductive charging. In inductive power transfer systems (IPTs), energy is transferred across the air-gap from the ground transmitter coil (primary) to the vehicle receiver coil (secondary) via magnetic field coupling. This introduces additional degrees of freedom because of inherent tolerances due to varying air-gaps and parking offsets that can negatively affect the quality of the coupling.

Ensuring interoperability between the primary and secondary sides of IPTs is critical to their success, especially in public charging situations, and requires careful consideration during the design phase. Given the number of components involved and the potential differences in performance targets between primary and secondary designers, it can be challenging to evaluate, describe, and ensure interoperability without impeding the technology. This thesis explores how interoperability can be incorporated into the design of IPTs for EV battery charging applications. A novel approach based on impedance planes (IPPs) is presented that facilitates interoperability considerations during the design stage. An impedance plane method (IPM), a highly flexible design and assessment methodology, is derived in this thesis to achieve this goal.

The IPM is an extension of an existing standardization-oriented approach, developed here to provide a comprehensive understanding of the performance of IPTS components under various operating conditions. This was achieved by simplifying the IPTS topology and formulating the necessary assumptions that are used to derive the IPM. Four impedance interfaces were introduced together with operational constraints and system/component requirements at each interface, to establish capability planes that can be applied to define and assess design spaces at any other interface. The IPM was successfully applied to an EV charging use-case, demonstrating its effectiveness in redesigning and assessing systems with a focus on interoperability. The method provides real operational boundaries and can analyze multiple operating points (such as battery voltage ranges) simultaneously.

The IPM was further improved by conducting separate studies of the individual components of the IPTS, with a focus on their respective interoperability issues. The study of the magnetics led to a novel approach for estimating leakage flux at various distances from the secondary coil within the IPPs, enabling IPTS human exposure safety regulations for EV charging to be considered within the IPM. The study also examined the effects of the coupling factor and coil current limitations on the impedance zone that an IPTS can provide. The combination of all considerations allowed the derivation of an interoperability zone linked to output power and minimum coupling factor that ensures safe operation under all requirements.

In addition, the electronics aspects of power conversion within the IPTS, in particular the rectifier stage and the power supply inverter, have been studied. The results of this

investigation led to an extension of the IPM that enabled losses to be taken into account, thereby improving its significance. Consequently, six power interfaces were established and, based on certain assumptions, loss estimations were derived for each component, neglecting details of switching and core losses given that the model focuses on the fundamental component and assumes linearization. Despite these simplifications, the incorporation of losses allows the IPM to calculate heatmaps of efficiencies and other parameters, thus enabling a comprehensive study of the distribution within the IPPs. This was demonstrated in a comprehensive public charging use-case where a primary was evaluated for different secondaries under various operating conditions, further highlighting the extensive performance analysis capabilities of the IPM. This analysis identified limiting factors and suggested adjustments to improve interoperability. The presented public charging use-case demonstrated how the primary electronics can be re-evaluated to operate under all conditions, and how losses reduce the size of the IPPs due to the increased power requirements that components must cover at each interface.

Moreover, a sensitivity analysis was carried out on the tuning components of the IPTS to gain deeper insight into their impacts on the system operation and their interdependencies. The tuning parameters were varied to facilitate the design of the tuning process for interoperability, as opposed to conventional approaches that often target a single operating condition. These results were then applied to a 50 kW IPTS, demonstrating the ability of the IPM to account for leakage, coupling, and current constraints while coping with battery voltage and coupling variations.

Finally, to provide critical insight into vehicle assemblies designed for operation with surface-mount systems but made to operate with a flush-mount ground assembly system and vice versa, the full IPM, including its extension, was used to compare two 50 kW IPTSs. The ability of the IPM to address interoperability issues by identifying the limiting factors and suggesting improved design decisions was demonstrated. The results highlighted the challenge of achieving full interoperability using only passive elements due to system complexity, variation and tolerances. The study showed that the use of active elements or control can reduce the stress on the entire IPTS, thereby improving interoperability.

Overall, the IPM provides a comprehensive approach to address interoperability in IPTSs, particularly in EV charging applications. It has the potential to be widely applicable in other areas due to its ability to be tailored to specific use-cases, allowing for the consideration of numerous interoperability aspects. However, several assumptions and simplifications were necessary to develop and present the IPM, and future work should consider incorporating additional system boundaries, develop an improved method that incorporates other key losses and important harmonics in order to further enhance the performance and applicability of the IPM.

Kurzfassung

Die Technologie der induktiven Energieübertragung (IET) ermöglicht die Übertragung elektrischer Energie ohne physische Verbindung und eignet sich daher für das kabellose Laden von Elektrofahrzeugen. IET bietet eine Reihe von Vorteilen wie sicheres, zuverlässiges und bequemes Aufladen der Fahrzeugbatterie sowie das Potenzial für dynamisches und autonomes Laden. Diese Vorteile könnten dazu beitragen, die breite Akzeptanz von Elektrofahrzeugen voranzutreiben und eine nachhaltigere Zukunft des Verkehrs zu fördern.

Aufgrund der fehlenden physikalischen Verbindung gibt es im Gegensatz zum konduktiven Laden keine definierte Schnittstelle zwischen Ladeinfrastruktur und Fahrzeug. Bei induktiven Energieübertragungssystemen (IETSs) wird die Energie durch Magnetfeldkopplung über den Luftspalt von der Senderspule am Boden (Primärseite) auf die Empfängerspule im Fahrzeug (Sekundärseite) übertragen. Dieser zusätzliche Freiheitsgrad führt jedoch zu Toleranzen aufgrund unterschiedlicher Luftspalte und Parkversätze, die sich negativ auf die Qualität der Kopplung auswirken können.

Die Interoperabilität zwischen der Primär- und Sekundärseite von IETSs ist entscheidend für deren Erfolg, insbesondere im öffentlichen Ladebereich, und muss in der Entwurfsphase sorgfältig berücksichtigt werden. Aufgrund der Anzahl der beteiligten Komponenten und der potenziell unterschiedlichen Designziele der Entwickler auf der Primär- und Sekundärseite kann es eine Herausforderung sein, die Interoperabilität zu bewerten, zu beschreiben und sicherzustellen, ohne die Technologie zu beeinträchtigen. Diese Dissertation untersucht wie Interoperabilität im Entwurf von IETSs für Elektrofahrzeug-Batterieladeanwendungen integriert werden kann. Es wird ein neuartiger, auf Impedanzräumen basierender Ansatz vorgestellt, der die Berücksichtigung der Interoperabilität während der Entwurfsphase ermöglicht. Um dieses Ziel zu erreichen, wird in dieser Dissertation die Impedanzraum-Methode (IPM), eine sehr flexible Entwurfs- und Bewertungsmethode, hergeleitet.

Die IPM ist eine Erweiterung eines bestehenden Ansatzes, um ein umfassendes Verständnis der IETS-Komponenten unter verschiedenen Betriebsbedingungen zu ermöglichen. Dazu wurde die IETS-Topologie vereinfacht und notwendige Annahmen formuliert, die dann zur Herleitung der IPM verwendet wurden. Es wurden vier Impedanzschnittstellen eingeführt, wobei Komponenten- und Systemgrenzen sowie Anforderungen an jeder Schnittstelle berücksichtigt wurden, um durch das IETS bedienbare Zonen abzuleiten. Diese können dann auf jede andere Schnittstelle übertragen und flexibel zur Bewertung des Systems verwendet werden. Die Fähigkeiten der IPM zur Bewertung und zum Design von IETSs im Hinblick auf Interoperabilität wurden anhand eines Beispiels für das Laden von Elektrofahrzeugen demonstriert. Die Methode erlaubt es, mehrere Betriebspunkte gleichzeitig zu untersuchen und dabei individuelle Systemgrenzen an verschiedenen Schnittstellen zu berücksichtigen.

Die IPM wurde durch die detaillierte Betrachtung einzelner Komponenten des IETS erweitert. Der Schwerpunkt lag dabei auf den jeweiligen Interoperabilitätsproblemen. Die Untersuchung der Magnetspulen lieferte einen neuen Ansatz zur Abschätzung der Streuflussdichten in verschiedenen Abständen von der Sekundärspule innerhalb der Impedanzräume. Damit können sicherheitskritische Aspekte beim Laden von Elektrofahrzeugen mit der IPM berücksichtigt werden. Darüber hinaus wurden die Auswirkungen des Kopplungsfaktors und

der Stromgrenzen der Spulen auf die Impedanzräume, die ein IETS zur Verfügung stellen kann, untersucht. Die Kombination aller Untersuchungen ermöglichte die Ableitung einer leistungs- und kopplungsabhängigen Interoperabilitätszone, in der ein sicherer Betrieb unter allen Anforderungen gewährleistet ist.

Des Weiteren wurden die elektronischen Komponenten innerhalb des IETSs, insbesondere die Gleichrichterstufe und der Wechselrichter, untersucht. Die Ergebnisse dieser Untersuchung führten zu einer Erweiterung der IPM, die die Berücksichtigung von Verlusten und damit detailliertere Ergebnisse ermöglicht. Dazu wurden sechs Leistungsschnittstellen definiert und Verlustabschätzungen für alle Komponenten abgeleitet, wobei Aspekte der Schalt- und Kernverluste aufgrund der Vereinfachung der Oberschwingungen und Linearisierung vernachlässigt wurden. Trotz dieser Vereinfachungen erlaubt die Einbeziehung der Verluste der IPM die Berechnung von Wirkungsgraden und Kennfeldern anderer Parameter, wodurch eine umfassende Untersuchung der Verteilung innerhalb der Impedanzräume ermöglicht wird. Dies wurde in einem umfassenden Anwendungsfall für öffentliche Ladestationen demonstriert, in dem eine Primärseite für verschiedene Sekundärseiten unter verschiedenen Betriebsbedingungen untersucht wurde. Diese Analyse ermöglichte es, limitierende Faktoren zu identifizieren und Anpassungen zur Verbesserung der Interoperabilität vorzuschlagen. Im vorgestellten Anwendungsfall wurde gezeigt, wie die primäre Leistungselektronik neu entworfen werden kann, um unter allen Bedingungen interoperabel zu sein. Weiterhin wurde aufgezeigt, wie Verluste die Größe der Impedanzräume aufgrund des erhöhten Leistungsbedarfs der Komponenten an jeder Schnittstelle verringern.

Zusätzlich wurde eine Sensitivitätsanalyse für die Kompensationskomponenten des IETSs durchgeführt, um einen detaillierten Einblick in deren Auswirkungen auf den Systembetrieb zu erhalten. Die Kompensationsparameter wurden zunächst einzeln variiert, um anschließend die Erkenntnisse auf die Auslegung der Kompensationsnetzwerke zu übertragen, mit dem Ziel der maximalen Interoperabilität. Diese Erkenntnisse wurden dann auf ein 50 kW IETS angewendet, um zu zeigen, dass die IPM die Analyse von Streufluss-, Kopplungs- und Strombegrenzungen bei gleichzeitiger Berücksichtigung von Spannungs- und Kopplungsschwankungen ermöglicht.

Schließlich wurde die gesamte IPM einschließlich der Erweiterung verwendet, um zwei 50 kW IETSs zu vergleichen. Dies ermöglichte einen detaillierten Einblick in den Betrieb von oberflächenmontierten Systemen mit bündig montierten Systemen und umgekehrt. Dadurch wurde die Fähigkeit der IPM demonstriert, Interoperabilitätsprobleme zu lösen, indem einschränkende Faktoren identifiziert und verbesserte Designentscheidungen vorgeschlagen wurden. Außerdem zeigten die Ergebnisse, dass es aufgrund der Systemkomplexität, der Abweichungen und Toleranzen schwierig ist, eine vollständige Interoperabilität mit nur passiven Elementen zu erreichen. Die Ergebnisse deuten darauf hin, dass die Verwendung aktiver Elemente oder einer kontrollierten Steuerung die Belastung des gesamten IETSs verringern und somit die Interoperabilität verbessern kann.

Insgesamt bietet die IPM einen umfassenden Ansatz zur Untersuchung der Interoperabilität in IETSs, insbesondere in Elektrofahrzeug-Ladeanwendungen, und hat das Potenzial, auch in anderen Bereichen anwendbar zu sein, da es auf spezifische Anwendungsfälle zugeschnitten werden kann und die Berücksichtigung zahlreicher Interoperabilitätsaspekte ermöglicht. Für die Entwicklung und Darstellung der IPM wurden jedoch einige Annahmen und Vereinfachungen getroffen. Zukünftige Arbeiten, wie z.B. die Entwicklung einer verbesserten Methode zur Berücksichtigung aller Verluste und Oberschwingungen, könnten die Leistungsfähigkeit und Anwendbarkeit der Methode weiter verbessern.

Acknowledgments

I would like to express my gratitude to all the people who have supported and guided me throughout my journey towards this thesis.

First, I would like to express my deepest appreciation to Professor Hans-Georg Herzog for being an incredible mentor. Your insightful guidance and shared knowledge have been invaluable to me throughout my academic journey. Your unwavering encouragement and high scientific standards have inspired me greatly. I am grateful for the relentless discussions we had. Your invested efforts in proofreading my papers and providing feedback have significantly improved the quality of my work. I will always cherish the wonderful time I spent at the Institute under your guidance and all the valuable lessons I learned from you.

I would also like to express my sincere appreciation to Professor Grant Covic for his exceptional supervision and support during my dissertation. You treated me as one of your own Ph.D. students, and I am very grateful for that. Thank you for the numerous discussions, proofreading, and inviting me to New Zealand twice and to all the post-grad meetings. Your guidance on my impedance planes and innovative ideas were instrumental in shaping my thesis and I cannot thank you enough. I also appreciate your dedication and efforts to keep me motivated throughout my research, especially with the time difference.

My sincere thanks also go to my colleagues who have accompanied me on this journey. I am grateful for the exchange of knowledge, discussions, events, trips and after-work drinks that we shared. I would like to thank Sebastian, Jörg, David, Stephan, Sonja, Markus, Julian, Laurenz, Konstantin, Michael W., Andreas, Taha, Michael M., Michael E., Leo, and Christoph. To Stefanie, Abdurahim, Norbert and Rainer, thank you for the good times we shared. A special mention goes to my office mate, Carina, for her valuable input, feedback, and proofreading of my thesis and publications, always under time pressure. It was a great time working together in our office.

I would also like to thank the Auckland research group for welcoming me to their meetings and looking after me during my visit. To Jackman, I am grateful for your guidance and input. Thank you for your help with the measurements, and for letting me stay at your place. To Patrick, I sincerely thank you for your patience and the great effort you put into the lab measurements. I am also thankful to Brian, Cody, Matthew, and Kai for the many lunches and company they provided during my visit. To Seho, thank you for the insightful discussions and for putting things into perspective.

Also, I am grateful to Daniel Kürschner for mentoring me and putting me in touch with Grant, and to Marius Hassler for providing a starting point for my thesis with the impedance planes. I would also like to thank Thorsten Kurpat for the valuable discussions and catch-ups we had.

Ich möchte auch meiner Familie, insbesondere meinen Eltern Albert und Maria, einen großen Dank aussprechen. Ich bin euch dankbar, dass ihr immer an mich geglaubt und mich in jeder Hinsicht unterstützt habt. Ihr habt mir jederzeit das Fundament gegeben, das es mir ermöglicht hat, meinen Weg und meine Ziele so gut wie möglich zu verfolgen. Das weiß ich sehr zu schätzen.

In addition, I want to thank Rainer and Beate for their support and constant motivation. Thank you for always giving me positive thoughts and encouragement.

Finally, and most importantly, I would like to say a very special thank you to Anna. Your unwavering support in so many ways over the years, and especially at the end, has been invaluable. I could not have completed this thesis without your emotional support and the countless conversations in which you encouraged, motivated, grounded, and pushed me to do my best. Your tireless efforts and patience to support me in the best way possible are deeply appreciated and I am forever grateful for everything you have done for me and for having you in my life at this time.

Munich, April 2023

Denis Kraus

Contents

List of Figures	V
List of Tables	XIII
Nomenclature	XV
1 Introduction	1
1.1 A Brief History of IPT	3
1.2 EV Charging: Interoperability and Challenges	5
1.3 Motivation and Goals	7
1.4 Thesis Outline	9
2 Fundamentals of IPT	11
2.1 IPT for EV Charging	11
2.2 Components of an IPT System	12
2.2.1 Battery Load	13
2.2.2 Secondary Rectifier and Control	13
2.2.3 Secondary Compensation	19
2.2.4 Primary Power Supply	22
2.2.5 Primary Compensation	25
2.2.6 Magnetic Coils	28
2.3 Practical Considerations and System Simplifications	31
2.3.1 First Harmonic Approximation	31
2.3.2 Full Circuit Analysis	32
2.4 Simulation Tools	36
2.5 Interoperability Aspects	37
2.5.1 Standardization	38
2.5.2 Impedance Planes	41
2.6 Summary	42
3 Design and Assessment Method for Interoperable IPT Systems Based on Impedance Planes	45
3.1 Assumptions and Goals	45
3.2 Procedure of the Impedance Planes Method	47
3.2.1 Inverter Capability Planes	49
3.2.2 Integration of System Boundaries into Impedance Planes	51
3.3 Applications of the Impedance Plane Method	55
3.4 IPM Example 1: Inverter Assessment with Operational Boundaries	56
3.5 Summary and Results	66

4	Interoperability Aspects of Magnetics	69
4.1	Magnetic Coil Properties	69
4.1.1	Magnetic Coupling and Coil Topologies	69
4.1.2	Leakage Flux Density and Regulatory Issues	71
4.1.3	Shielding	73
4.2	Integration of Magnetic Aspects into the IPM	74
4.2.1	Coil Capability Planes	74
4.2.2	Boundaries and Limitations of CCPs	76
4.2.3	Magnetic Leakage Flux Density in the IPM	77
4.3	IPM Example 2: Inverter Design Space for an Interoperable Primary System	85
4.4	Summary	90
5	Impact of Power Conversion Aspects and Losses on Interoperability of IPT Systems	91
5.1	Modeling of Losses in IPT System Components	92
5.1.1	Primary Side Inverter Losses	92
5.1.2	Rectifier Losses	94
5.1.3	Magnetic Losses	95
5.1.4	Other System Losses	96
5.1.5	Efficiency	96
5.2	Loss Extension of the IPM	96
5.3	IPM Example 3: Public Charging	103
5.3.1	System, Use-Case and Boundaries	103
5.3.2	Process Flowchart of the Use-Case	105
5.3.3	Experimental Verification	107
5.3.4	Full System Simulation	108
5.3.5	Results and Discussion	113
5.4	Summary	119
6	Tuning Sensitivity Analysis within IPT Systems	121
6.1	Impact of Tuning Changes on IPT Systems	122
6.1.1	Variations in L_s , C_s and C_p	123
6.1.2	Active Tuning	126
6.1.3	Impact on Efficiency and Heatmaps	129
6.2	Application of the IPM: Compensation Design for a 50 kW IPT System . . .	131
6.2.1	Coils and Boundaries	131
6.2.2	Design Considerations: Series-Series and LCC–LCC Compensation . .	133
6.2.3	Evaluation and Results	140
6.3	Summary	142
7	Assessment of Two High-Power 50 kW IPT Systems	145
7.1	50 kW Coil Systems	145
7.1.1	TUM Coils	145
7.1.2	UoA Coils	146
7.2	System Boundaries and Use-Case	148
7.3	Validation of the UoA System	151
7.3.1	Measurement Setup	152
7.3.2	Comparison with Simulation Models	153

7.4	Interoperability Assessment	157
7.4.1	Combination of Systems	158
7.4.2	Results and Evaluation	163
7.5	Summary	166
8	Summary and Future Work	167
8.1	Conclusions and Contributions	167
8.2	Publications	168
8.3	Contributions to Research Projects	168
8.4	Suggestions for Future Work	169
A	Appendix	i
A.1	Extension of the IPM Example 3: Loss Analysis under Misalignment	i
A.2	Extension of the 50 kW Interoperability Assessment: Results at k_{\min} and k_{\max}	ii
	List of Publications	vii
	List of Supervised Students Work	ix
	Bibliography	xi

List of Figures

1.1	Categories of electromagnetic coupling methods [3].	1
1.2	Overview of WPT technologies [1].	2
1.3	Principle of a ideal transformer, left: strongly coupled, right: loosely coupled.	2
1.4	Examples of the Tesla coil, which is a type of resonant transformer (25 kHz–2 MHz), invented in 1891 [9].	3
1.5	Roadway-powered electric bus and cross section of roadway and onboard power inductors [20].	4
1.6	State of the art for wireless EV charging [30].	5
1.7	Overview of an IPTS for EV battery charging. Magnetics are highlighted in red and electronics in blue.	6
1.8	Example of a charging station for conductive charging with bad interoperability from the infrastructure side [51].	8
2.1	Simplified topology of an IPTS.	11
2.2	Typical battery charging profile.	13
2.3	Secondary side AC/DC converter.	14
2.4	Passive full bridge rectifier (current source), (a) topology and (b) waveforms.	14
2.5	Topologies of passive rectification stages, (a) current doubler and (b) voltage doubler.	15
2.6	Passive impedance compression network rectifier.	16
2.7	Active rectifier with (decoupled) boost controller.	17
2.8	Active rectifier with buck controller.	18
2.9	Secondary rectifier with FHA simplification.	18
2.10	Series or parallel resonance tuning principle for current-controlled primaries.	19
2.11	Ideal secondary series tuned circuit.	20
2.12	Ideal secondary parallel tuned circuit.	21
2.13	Ideal secondary LCL tuned circuit.	21
2.14	Ideal secondary LCC tuned circuit.	22
2.15	Ideal secondary partial-series tuned circuit.	23
2.16	Schematic of the full bridge inverter topology.	23
2.17	H-bridge inverter waveforms with (a) $\alpha = 180^\circ$ and (b) $\alpha = 120^\circ$	25
2.18	Primary compensation networks, (a) series tuning, (b) LCL tuning and (c) LCC tuning.	27
2.19	Fundamental flux coupling principle.	29
2.20	Equivalent circuit of coupled coils based on the T-transformer representation.	29
2.21	3D perspective and cross-sectional view of the (a) CP and (b) DDP topologies.	30
2.22	Simplified IPTS circuit topology for an LCC–LCC tuned system.	32
2.23	Simplified IPTS circuit topology for a series-series tuned system.	33
2.24	Example of a transfer function for different loads (battery voltages) in the frequency domain, (a) magnitude and (b) phase.	35
2.25	SAE J2954 definitions of (a) ground clearance and (b) GA mounting types [50].	39

2.26	Definition of the GA and VA impedance interfaces, taken from [107].	42
2.27	SAE J2954 IPPs, (a) creation of an IPP, (b) GA reference planes [50].	42
3.1	Topology of an IPTS with impedance interfaces and FHA simplifications. . .	46
3.2	A general two-port network with its equivalent impedances.	47
3.3	Coils Transformer Equivalent Circuit Diagram with Transfer Matrix Simplifications.	48
3.4	ICP (green) restricted by voltage and current boundaries (black and shaded black) as well as phase angle limitations (red and shaded red).	52
3.5	IPPs (white) for different apparent, active and reactive power restrictions caused by component voltage (blue) and current (red) limitations.	54
3.6	ICP (green) for delivering $P \geq P_{out,min}$ (blue) with a maximum apparent power limitation (red) and inverter boundaries (black).	55
3.7	Flowchart of the IPM for an assessment of inverter capabilities for a given system with load variation within real operational boundaries.	57
3.8	FEM simulation models of the SAE coils used for the IPM Example 1, (a) primary coil, (b) secondary coil and (c) both coils.	58
3.9	IPM Example 1: Simplified circuit with LCC–LCC compensation and active tuning and the IPP interfaces highlighted in red.	59
3.10	IPM Example 1: ICP with inverter boundaries shown at the inverter interface.	60
3.11	IPM Example 1: ICP with inverter and (a) $S_{in,max}$ and (b) $P_{out,min}$ boundaries at the inverter interface.	60
3.12	IPM Example 1: Resulting ICP (ICP _{in} , green) with all inverter boundaries and power requirements. Result of Step 2.	61
3.13	IPM Example 1: ICP transfer from inverter to GA interface with primary LCC tuning.	61
3.14	IPM Example 1: ICPs and CCPs at GA interface, (left) GA CCPs, (right) ICPs and $I_{1,max}$ limitation.	62
3.15	IPM Example 1: ICP transfer from GA to VA interface at $(x,y,z) = (75,100,210)$ mm.	62
3.16	IPM Example 1: ICP transfer from VA to output interface with secondary LCC tuning.	63
3.17	IPM Example 1: All ICPs and OPs at the output interface with all ICP explanations.	64
3.18	IPM Example 1: Final ICPs with all boundaries and OPs at all interfaces. . .	65
3.19	Example ICP: Final ICPs with an added boost converter on the secondary side and partially reduced output power.	66
4.1	Coupling factor xy-maps of two sets of CP with different geometries, P1 and P2, at $z = 140$ mm, (a) P1-P1 (primary side-secondary-side), (b) P2-P2, (c) P1-P2, (d) P2-P1. [P.3]	70
4.2	Coupling factor over different air-gaps.	71
4.3	Safety regulations defined by SAE J2954 based on ICNIRP reference levels (taken from [50]), (a) front view, (b) side view.	72
4.4	Secondary side aluminum shield in a FEM simulation.	73
4.5	Different CCPs at the GA and VA interface.	75
4.6	VA CCPs at the GA Interface (zoomed in on Fig. 4.5).	75

4.7	GA CCP (blue) for $P_{\text{out}} = 10$ kW with VA CCPs (red, green and magenta) transferred to the GA interface at different coupling conditions, (a) Detailed view of the VA CCPs for different couplings and (b) the resulting interoperability zone for k_{min}	76
4.8	GA (red) and VA CCPs at the GA interface for $P_{\text{out,min}} = 10$ kW for a fixed coupling of $k = 0.1224$ and different secondary coil limitations: $I_{2,\text{max}} = 60$ A (turquoise), $I_{2,\text{max}} = 75$ A (blue) and $I_{2,\text{max}} = 90$ A (purple).	77
4.9	FEM simulation with planes for obtaining the leakage flux values.	78
4.10	Leakage flux plane analysis of the IPM Example 1. (a)-(c) x-, y-, and z-components and (g) B_{max} of BY-plane at $I_1 = 75$ A and $I_2 = 0$ A at $(x,y,z) = (0,75,210)$ mm, (d)-(f) x-, y-, and z-components of BX-plane for the same operating conditions, (h) B_{max} of BY-plane at same position with $I_1 = 75$ A, $I_2 = 70$ A and $\varphi_{i2} = 90^\circ$, (i) similar to (h) but with phase adjusted to $\varphi_{i2} = 60^\circ$	80
4.11	Leakage flux plane analysis of IPM Example 1 (10 kW OP) at different distances (BY-plane), (a) 800 mm, (b) 900 mm and (c) 1000 mm distance of the secondary coil center.	81
4.12	Integration of leakage flux effects into the CCP, (a) $B_{\text{max},800\text{mm}}$ as a function of i_1 and i_2 , (b) maximum allowed primary coil current for $B < 15$ μT (red) and required I_1 for $P_{\text{out}} = 10$ kW (blue) and (c) effects of leakage flux consideration on the CCP with a new interoperability zone and new k_{min}	82
4.13	ICP (green) for delivering $P \geq P_{\text{out,min}}$ (blue) with a maximum apparent power limitation (red), inverter boundaries (black) and leakage flux considerations (purple).	83
4.14	Leakage flux effects for a matched coil system. B_{max} as a function of I_1 and I_2 for (a) nominal coupling and (c) three coupling conditions (both at 800 mm distance); (b) maximum allowed primary coil current for $B < 15$ μT for different values of I_2 and (d) the maximum allowed coil current combinations to stay below 15 μT for the coupling conditions from (c).	84
4.15	CCP heatmaps of the matched 10 kW system at k_{min} , GA CCP with (a) I_1 , (c) I_2 and (d) B_{max} heatmaps; (b) VA CCP with I_2 heatmap.	85
4.16	Flowcharts of the methodology for evaluation of the coil couplings and guideline for deriving a design space for interoperable GA electronics.	86
4.17	Different WPT3 CCPs, (a) GA CCP at the GA interface. In (b)-(f) the red zone describes the impedance area which lies within the primary coil boundaries but outside the secondary coil boundaries. In (c)-(f) the blue and golden zones represent the impedance areas which lie within both coil boundaries, where the golden zone describes the interoperability zone. The gradient of the blue color represents the amount of operable points from almost all positions in light blue to only one in dark blue.	88
4.18	IPM Example 2: CCPs with leakage flux heatmaps under (a) k_{max} and (b) k_{min} coupling conditions.	89
5.1	IPTS topology with simplifications, impedance interfaces, transfer matrices and power definitions.	92
5.2	Waveforms of the MOSFET switch gate voltages and currents and the resulting inverter output current (LCC-LCC system).	94
5.3	Flowchart for loss implementation with constant P_{in} into the IPM.	98
5.4	Flowchart for loss implementation with constant P_{out} into the IPM.	99

5.5	ICPs of IPM Example 1 with the respective interface current as heatmap. . .	100
5.6	Rectifier losses in the ICP at the rectifier and inverter interface. The ICP without losses is shown in green for comparison.	100
5.7	ICP with P_{rect} heatmap at the inverter interface.	101
5.8	Loss analysis of the IPM Example 1 at k_{min} with (a)-(b) magnetic loss and (c)-(d) inverter loss heatmaps.	102
5.9	(a) Loss and (b) efficiency analysis of the IPM Example 1 at k_{min} with isolines for different power levels.	102
5.10	$B_{\text{max},800\text{mm}}$ leakage flux heatmap of the IPM Example 1 at k_{min}	103
5.11	Overview of the use-case scenario. The electronics of Case A or Case B are connected to the primary coil and four different cars are parking over this charging station and should be charged under different parking and battery voltage conditions with $P_{\text{out}} = 10$ kW.	104
5.12	IPM Example 3: Flowchart of the public charging use-case.	106
5.13	Circuit topology of the measured system.	107
5.14	Lab leakage flux measurement setup.	108
5.15	Scopes of the circuit measurements for the nominal position, (a) waveforms of coil currents and inverter bridge and (b) captured output values.	110
5.16	Schematics of the PLECS simulation.	111
5.17	Waveforms of the PLECS simulation.	112
5.18	Waveforms of the inverter switches in the PLECS simulation.	113
5.19	Results of the process flowchart from Fig. 5.12 for (a)-(d) each secondary case.	114
5.20	Results of the process flowchart from Fig. 5.12 for all cases at k_{min}	114
5.21	Results of the loss considerations (black hull curve with efficiency heatmap) for Case A on the primary and (a)-(d) each secondary case at the GA interface and k_{nom} . The blue hull curve represents the lossless ICP.	116
5.22	Results of the loss considerations (black hull curve with efficiency heatmap) for Case B on the primary and (a)-(d) each secondary case at the GA interface and k_{nom} . The blue hull curve represents the lossless ICP.	117
5.23	Results of the redesigns of the Case A (light-blue) and Case B (purple) electronics in (a), with (b)-(c) efficiency heatmaps and (d)-(e) leakage flux heatmaps, respectively.	118
6.1	10 kW ICP_{in} with different colored edges at all four impedance interfaces for ideal resonance LCC–LCC tuning ($X_{\text{GA}} = 7.2 \Omega$, $X_{\text{VA}} = 8.5 \Omega$). The OPs for $V_{\text{bat}} = 280 - 450$ V are shown in yellow with the nominal voltage $V_{\text{bat}} = 400$ V highlighted in magenta.	122
6.2	Deconstructed IPP transfer from inverter to GA interface for an ideal LCC tuned primary side ($X_{\text{GA}} = 7.2 \Omega$).	124
6.3	Sensitivity analysis of the IPP transfer from inverter to GA interface for various conditions; (a)-(c) LCC transfer for (a) $X_{\text{GA}} = 5 \Omega$, (b) $X_{\text{GA}} = 10 \Omega$ and (c) $X_{\text{GA}} = 3.6 - 10.8 \Omega$; (d) $\underline{Z}_{\text{Ls1}} = \underline{Z}_{\text{Cs1}} = 0$ and $\underline{Z}_{\text{Cp1}} = 2.16 - 21.6 \Omega$; (e) $\underline{Z}_{\text{Cp1}} = 7.2 \Omega$ (const.) and $\underline{Z}_{\text{Ls1}} = 0.5 - 20 \Omega$ (f) $\underline{Z}_{\text{Ls1}} = 7.2 \Omega$ (const.) and $\underline{Z}_{\text{Cp1}} = 0.5 - 20 \Omega$	125
6.4	IPP transfer from inverter to GA interface for variations in each LCC parameter and their combinations.	126
6.5	IPTS circuit with LCC–LCC compensation and active tuning.	126

6.6	OPs of Z2 (red) and Z3 (blue) VAs with passive rectification for different coupling conditions (each at their k_{\min} and k_{\max}) over the full battery voltage and active tuning X_{VA} ranges.	127
6.7	Impact of active tuning on the ICP and the system interoperability; (a) variations of X_{GA} and the resulting ICP (green), (b) new OPs (same conditions but with impedance compression network) and final ICP (orange) after GA current boundary is imposed, (c) selections of X_{VA} values and (d) adjusted X_{VA} values and minimum X_{GA} range (16–20 Ω , new ICP in blue) for achieving full interoperability.	128
6.8	ICP Heatmaps with variations in active tuning; (a) full ICP with I_{in} heatmap, (b)-(f) ICP ($X_{GA} = 8 \Omega$) with (b) I_1 , (c) I_2 at k_{\max} , (d) I_2 at k_{\min} heatmaps, (e) and (f) respective $B_{\max,800\text{mm}}$ heatmaps.	130
6.9	Leakage flux heatmaps of ICP over full active tuning range for (a) k_{\max} and (b) k_{\min} coupling conditions with the OPs from Fig. 6.7d.	131
6.10	FEM simulation models of the matched primary and secondary coils, (a) 3D view and (b) top view. The car mimic aluminum shield is not depicted. The aluminum is shown in grey, ferrite in black and the litz-wire winding in brown.	132
6.11	Leakage flux study for changing currents and couplings; (a) $B_{\max,800\text{mm}}$ and (b) $B_{\max,900\text{mm}}$ as a function of (I_1 , I_2) for three coupling conditions. The maximum allowed coil current combinations to stay below 15 μT for the same coupling conditions at (c) 800 mm and (d) 900 mm distance.	133
6.12	IPTS topology, impedance interfaces (red dashed), impedance transfers and coupling conditions for the compensation design procedure.	134
6.13	VA interface analysis of the secondary compensation design. The CCPs are shown for maximum (red), nominal (blue) and minimum (green) coupling. Each topology was tuned for resonance at each coupling condition and the OPs are represented in purple with an asterisk (k_{\max}), circle (k_{nom}) or plus (k_{\min}) marker.	136
6.14	GA interface analysis of the secondary compensation design. The differently tuned OPs (asterisk (k_{\max}), circle (k_{nom}) and '+' (k_{\min}) marker) are presented at the GA interface for the three coupling conditions in red, blue and green; simplified leakage flux boundaries for k_{\max} (red), k_{nom} (blue) and k_{\min} (green) are shown as shaded areas in (a)–(b) 800 mm and (c)–(d) 900 mm distance.	137
6.15	CCP assessment at k_{\max} coupling condition with (a) I_1 , (b) I_2 , (c) $B_{\max,800\text{mm}}$ and (d) $B_{\max,900\text{mm}}$ heatmaps.	138
6.16	Inverter interface analysis of the primary compensation design. The differently tuned OPs ('*' (k_{\max}), 'o' (k_{nom}) and '+' (k_{\min}) marker) are presented at the inverter interface for the three coupling conditions in red, blue and green. The ICP is shown in black.	139
6.17	Balanced configuration of the primary LCC tuning at the inverter interface with $X_{GA} = 8 \Omega$	140
6.18	Full system tuning, OP and leakage flux assessment at k_{\min} coupling condition. The OPs are shown in black, green (S–S tuning) and orange (LCC–LCC tuning); I_{in} heatmaps for the (a) S–S and (b) LCC–LCC systems, (c) $B_{\max,800\text{mm}}$ and (d) $B_{\max,900\text{mm}}$ leakage flux heatmaps (tuning independent).	142
7.1	Lab prototype of the TUM coils. Photo Credits: Reiner Nowitzki.	146

7.2	FEM simulation models of the UoA coils, (a) primary coil and (b) secondary coil with aluminum shield ($1000 \times 1000 \times 1$ mm).	148
7.3	ICPs of the (a) UoA–UoA and (b) TUM–TUM systems for all coupling conditions and system constraints.	149
7.4	ICP efficiency analysis of both 50 kW systems under different coupling conditions. The OPs (V_{bat} see Tab. 7.1) are shown in black with $V_{\text{bat,max}}$ highlighted in turquoise and the blue isoline represents the $B_{\text{max},900\text{mm}} = 15$ μT constraint.	150
7.5	ICP leakage flux heatmaps and output power variation analysis of the two 50 kW systems at minimum coupling. The black, purple, and gold isolines mark the IPPs at which the system can transfer 45 kW, 48 kW, and 50 kW, respectively ($P_{\text{out,min}}$). The corresponding OPs are shown in the same color.	151
7.6	Experimental setup for full circuit and leakage flux measurements, (a) front view and (b) side view.	152
7.7	Leakage flux planes and probes in FEM simulation.	153
7.8	Leakage flux study of the UoA–UoA ICP for $P_{\text{out,min}} = 50$ kW; (a) maximum allowed currents for $B \leq 15$ μT under all coupling conditions and two leakage flux plane distances, (b) ICP with leakage flux $B_{\text{max},950\text{mm}}$ -heatmap and $B_{\text{max}} = 15$ μT isolines.	154
7.9	Screenshots of the waveforms and scopes, (a) primary measurements, (b) PLECS primary waveforms, (c) secondary measurements and (d) PLECS secondary waveforms.	156
7.10	Final ICP with experimentally measured values, leakage flux isolines and OPs for different coupling conditions, (a) k_{max} , (b) k_{nom} and (c) k_{min}	157
7.11	ICPs of the (a) UoA–TUM and (b) TUM–UoA systems for all coupling conditions and system constraints.	158
7.12	Interoperability Assessment of the UoA and TUM GAs at three different coupling conditions and three power levels.	159
7.13	Efficiency analysis of all four systems at k_{nom}	160
7.14	Magnetic loss analysis of all four systems at k_{nom} ; (a)-(d) total coil losses $P_{\text{l,mag}}$ and (e)-(h) only VA coil losses $P_{\text{l,mag,VA}}$	161
7.15	Inverter conduction loss analysis ($P_{\text{l,inv}} = P_{\text{l,diode}} + P_{\text{l,mos}}$) of all four systems at k_{nom}	162
7.16	Switching loss analysis of the series-series tuned TUM–TUM system at three coupling conditions with (a)-(c) showing the total inverter losses ($P_{\text{l,inv}} + P_{\text{l,sw}}$) and (d)-(f) showing only the switching losses $P_{\text{l,sw}}$	163
7.17	Adjustments for increased interoperability (shown at k_{max}), (a) boost converter and (b) change of battery voltage range to $V_{\text{bat}} = 600 - 800$ V.	164
A.1	Results of the loss considerations (black hull curve with efficiency heatmap) for Case A (a)–(d) and Case B (e)–(h) on the primary and each secondary case at the GA interface and k_{min} . The blue hull curve represents the lossless ICP.	i
A.2	Efficiency analysis of all four systems at k_{min}	ii
A.3	Efficiency analysis of all four systems at k_{max}	ii
A.4	Magnetic loss analysis (coil losses $P_{\text{l,mag}}$) of all four systems at k_{min}	iii
A.5	Magnetic loss analysis (coil losses $P_{\text{l,mag}}$) of all four systems at k_{max}	iii
A.6	VA magnetic loss analysis (only VA coil losses $P_{\text{l,mag,VA}}$) of all four systems at k_{min}	iv

A.7	VA magnetic loss analysis (only VA coil losses $P_{l,mag,VA}$) of all four systems at k_{max} .	iv
A.8	Inverter conduction loss analysis ($P_{l,inv} = P_{l,diode} + P_{l,mos}$) of all four systems at k_{min} .	v
A.9	Inverter conduction loss analysis ($P_{l,inv} = P_{l,diode} + P_{l,mos}$) of all four systems at k_{max} .	v

List of Tables

1.1	A Sample of Important Milestones, Products and Projects related to IPT . . .	6
2.1	Calculation of the AC-Values (FHA) for Different Rectifier Topologies	18
2.2	Summary of all Tuning Topologies, their Resonance Conditions and Load Quality Factor	24
2.3	Expressions for Z_{VA} and Z_{in} for Different Secondary and Primary Tunings .	34
2.4	Expressions of the Current Ratios for Different Secondary and Primary Tunings	35
2.5	SAE J2954 WPT Power Classifications	39
2.6	SAE J2954 WPT VA Z-Classes	39
2.7	Range of input kVA by Interoperability Class	40
2.8	SAE J2954 Operating Range Requirements	40
2.9	SAE J2954 Class I Minimum System Efficiency Requirements	40
2.10	SAE J2954 Class II Minimum System Efficiency Requirements	41
2.11	SAE J2954 Reference Coil Overview	41
3.1	Overview of Transfer Matrices for all Compensation Networks	50
3.2	Overview of all Impedance Transfer Matrices	51
3.3	FEM Simulation Model Inductance Results	56
3.4	Compensation Network Values	58
3.5	System Boundaries for the IPM Example 1	59
5.1	IPM Example 3: System Boundaries for the Use-Case Scenario	105
5.2	Overview of Tuning Equations for the IPM Example 3	105
5.3	Overview of Tuning Values for the IPM Example 3	106
5.4	Tuning Values of the Experimental Setup	108
5.5	Comparison between Measurements and Circuit Simulations	109
5.6	Comparison between Magnetics Measurements and FEM Simulations	109
5.7	New Inverter Boundaries	116
6.1	Inductances and Coupling of the 50 kW Coils for all Positions	132
6.2	System Boundaries for the Compensation Design	134
6.3	Overview of Tuning Design Values for 50 kW Coils	135
7.1	System Constraints and Component Limitations of both 50 kW IPTSs	147
7.2	Tuning Values of the 50 kW IPTSs	147
7.3	Comparison of both 50 kW Coil Parameters	148
7.4	Simulated Inductances of the 50 kW IPTSs and their Combinations	149
7.5	Leakage Flux Comparison between Measurements and FEM Simulations . . .	153
7.6	Comparison between Measurements, Analytical Calculation (FHA) and Circuit Simulation (PLECS)	154
7.7	Offset in Power and Losses between Measurements and Simulations	156

7.8 Offset in Switching Loss Calculations for all Positions 157

Nomenclature

List of Abbreviations

CCM	Continous Conduction Mode
CCP	Coil Capability Plane
CIED	Cardiac Implantable Electronic Device
CP	Circular Pad
CPT	Capacitive Power Transfer
DCM	Discontinous Conduction Mode
DDP	Double-D Pad
EMC	Electromagnetic Compatibility
EMF	Electromagnetic Field
EMI	Electromagnetic Interference
ESR	Equivalent-Series-Resistance
EV	Electric Vehicle
FEM	Finite-Element-Method
FFT	Fast-Fourier-Transformation
FHA	First Harmonic Approximation
FOD	Foreign Object Detection
GA	Ground Assembly
HD	Heavy-Duty
ICNIRP	International Comission on Non-Ionizing Radiation Protection
ICP	Inverter Capability Plane
IPM	Impedance Plane Method
IPP	Impedance Plane
IPT	Inductive Power Transfer
IPTS	Inductive Power Transfer System
LD	Light-Duty
LOP	Live Object Protection
OP	Operating Point
THD	Total Harmonic Distortion
TUM	Technical University of Munich

UoA	University of Auckland
VA	Vehicle Assembly
WPT	Wireless Power Transfer
ZVS	Zero Voltage Switching

Attributes of Symbols

x	AC Value
\hat{x}, \hat{X}	Amplitude of x, X
$\arg\{\underline{x}\}, \angle \underline{x}$	Argument of \underline{x} (in degree)
$\underline{x}, \underline{X}$	Complex quantity
$\underline{x}^*, \underline{X}^*$	Complex conjugate of $\underline{x}, \underline{X}$
X, X_{rms}	DC value, RMS value or magnitude of complex quantity
$x_{(N)}$	N-th harmonic of x
$\text{Im}(\underline{x})$	Imaginary part of \underline{x}
$ X $	Magnitude of X
\underline{X} \sim	Matrix X
$\text{Re}(\underline{x})$	Real part of \underline{x}
\vec{x}, \vec{X}	Vector notation of x, X

List of Symbols

α	Conduction angle
B	Magnetic flux density
B_{max}	Maximum leakage flux density
$B_{\text{max},\text{nm}}$	Maximum leakage flux density at a distance of n (e.g. 800 mm) of the center of the secondary coil
$B_{x,\text{max}}$	Maximum leakage flux density in x-direction offset
$B_{y,\text{max}}$	Maximum leakage flux density in y-direction offset
C_f	Filter capacitance
C_{p1}	Primary parallel compensation capacitance
C_{p2}	Secondary parallel compensation capacitance
C_{s1}	Primary series compensation capacitance

C_{s2}	Secondary series compensation capacitance
D	Duty cycle
η	Efficiency
f_s	Switching frequency
H	Magnetic field strength
I_1, I_{GA}	Primary coil current
I_2, I_{VA}	Secondary coil current
I_{bat}	Battery current
I_{cp1}	Primary parallel tuning capacitor current
I_{cp2}	Secondary parallel tuning capacitor current
I_{in}	Inverter output current
I_m	Magnetization current
I_{out}	Rectifier input current
I_s	Source current
I_{sc}	Short-circuit current
k	Coupling coefficient
k_{max}	Maximum coupling coefficient
k_{min}	Minimum coupling coefficient
k_{nom}	Nominal coupling coefficient
L_1	Primary coil inductance
L_2	Secondary coil inductance
L_f	Filter inductance
L_{s1}	Primary series compensation inductance
L_{s2}	Secondary series compensation inductance
M	Mutual inductance
μ_0	Vacuum magnetic permeability
μ_r	Magnetic permeability
ω	Angular frequency
P	Active power
φ_i	Phase angle of current
φ_v	Phase angle of voltage
P_{out}	Output power
P_{GA}	Output power at GA interface
P_{in}	Input power
$P_{in,max}$	Maximum input power
P_{inv}	Output power at inverter interface
$P_{1,comp1}$	Primary compensation losses
$P_{1,comp2}$	Secondary compensation losses

$P_{1,\text{inv}}$	Inverter losses
$P_{1,\text{mag}}$	Magnetic coil losses
P_{loss}	Total losses
$P_{1,\text{rect}}$	Rectifier losses
P_{out}	Output power
$P_{\text{out,min}}$	Minimum output power
P_{rect}	Output power at rectifier interface
P_{su}	Uncompensated power
P_{VA}	Output power at VA interface
Q	Reactive power
Q_2	Load quality factor
Q_i	Current boost quality factor
Q_v	Voltage boost quality factor
R	Resistance or real part of impedance
R_1, R_{ga}	Primary coil resistance
R_2, R_{va}	Secondary coil resistance
R_{ac}	Equivalent AC resistance
R_{bat}	Battery (load) resistance
S	Apparent power
$S_{\text{in,max}}$	Maximum input apparent power
V_1, V_{GA}	Primary coil voltage
V_2, V_{VA}	Secondary coil voltage
V_{bat}	Battery voltage
V_{in}	Inverter output voltage
V_{out}	Rectifier input voltage
V_{s}	Source voltage
V_{oc}	Open-circuit voltage
X	Reactance or imaginary part of impedance
X_{GA}, X_1	Reactance of primary series tuning element
X_{VA}, X_2	Reactance of secondary series tuning element
Y_1	Current ratio $\frac{i_{\text{in}}}{i_1}$
Y_2	Current ratio $\frac{i_1}{i_2}$
Y_3	Current ratio $\frac{i_2}{i_{\text{out}}}$
Z_{Cp1}	Impedance of primary parallel compensation capacitance
Z_{Cp2}	Impedance of secondary parallel compensation capacitance
Z_{Cs1}	Impedance of primary series compensation capacitance
Z_{Cs2}	Impedance of secondary series compensation capacitance
Z_{GA}	GA impedance
Z_{L1}	Impedance of primary coil

Z_{Ls1}	Impedance of primary series compensation inductance
Z_{Ls2}	Impedance of secondary series compensation inductance
Z_{L2}	Impedance of secondary coil
Z_M	Impedance of the mutual inductance
Z_{out}	Output impedance (Load)
Z_{refl}	Reflected impedance
Z_{VA}	VA impedance

The nomenclature does not contain all symbols and abbreviations: Only occasionally used symbols and abbreviations are not listed in the directory and are introduced in the respective context.

1 Introduction

Inductive Power Transfer (IPT) is a practical Wireless Power Transfer (WPT) method that enables the transfer of electrical energy between a source and a load via magnetic field coupling without the need for a physical connection. IPT is classified as a subcategory of electromagnetic coupling WPT, which also includes Capacitive Power Transfer (CPT), which uses electric fields, and other methods such as Acoustic WPT and Optical WPT, which transfer energy via acoustic and light waves, respectively [1, 2].

Electromagnetically coupled WPT can be further categorized into short and long range distance WPT as well as the method of coupling. However, coupling via magnetic or electric fields can only be separated at short range distances. At far field distances the Poynting vector, which describes the electromagnetic energy flow, can no longer be neglected. Thus, the electric and magnetic fields are not decoupled, which usually happens at very high frequencies (≥ 2 GHz, [3]). An overview of the different electromagnetic coupled WPT methods and WPT technologies can be found in Fig. 1.1 and Fig. 1.2, respectively. This represents the state of the art at the beginning of this thesis, while more recent research has led to increasing power levels for up to 15 kW for CPT [4] and 500 kW–1 MW for IPT [5, 6].

WPT has a wide variety of applications due to its different operating principles. One particular application that has generated a lot of interest in research and industry in recent years is the idea of wirelessly charging the battery of an Electric Vehicle (EV). In addition to being more convenient and safer, wireless charging of EVs has great potential to enable dynamic charging of EVs as well as the push towards autonomous driving, as the charging process can be fully automated [7]. In addition to wireless charging of an EV, the general technology of WPT can be useful (and is already being used) in many different fields, some of which are listed in Fig. 1.1.

TABLE 1–OVERVIEW OF CET TECHNOLOGIES.						
TECHNOLOGY (MEDIUM)	CONVERTER SWITCHING FREQUENCY (KHZ)	OUTPUT POWER (W)	DISTANCE LENGTH (MM)	EFFICIENCY (%)	PROPERTIES	TYPICAL APPLICATIONS
Acoustic (sound)	20–100	0.01–1000	0.2–1 1–300	1–80	Strong directional High distance/size When EM waves are not allowed	Through–metal–wall Sensor nuclear technology Biomedical Ultrasonic CET
Light (optical EM)	(10^{15}) 700–1,400 nm	1–100	Long (m to km)	20–30	Laser beaming Long distance Thermal derating	Space Terrestrial technology Biomedical
Capacitive (electric field)	100 kHz to several MHz	1–50	Low 0.1–0.5	50–80	Metal penetration Reduced EMI Low standing Power losses	LED supply Mobile phones Playing robots Sensors
Inductive (magnetic field)	20 kHz to several MHz	1 W–200 kW	0.2–2,000	≥ 80 –90	High efficiency High EMI Low distance/size No metal penetration abilities	EV and battery chargers Robots and manipulators Cranes and AG–EV Mobile devices Sensors and actuators

Figure 1.1 – Categories of electromagnetic coupling methods [3].

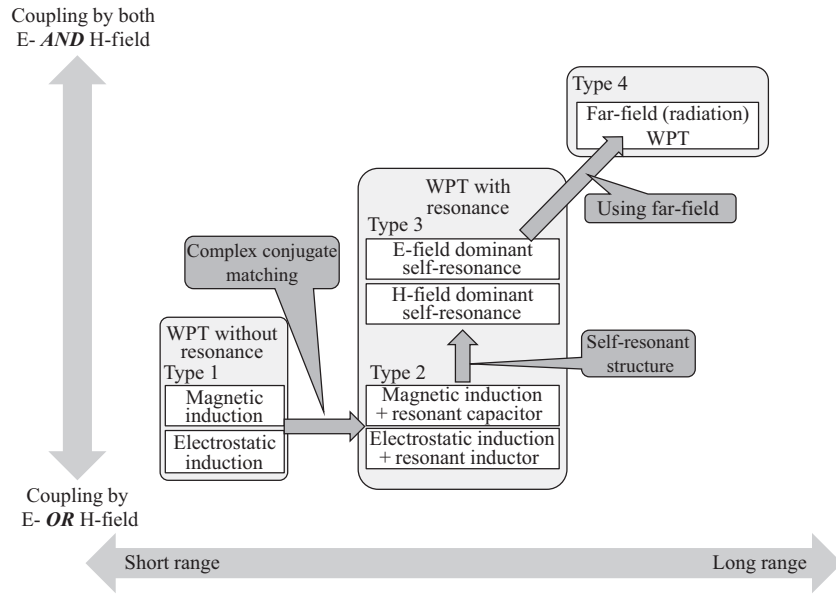


Figure 1.2 – Overview of WPT technologies [1].

When it comes to the proper WPT technology, Fig. 1.2 shows that not every method is suitable for EV charging. To compete with conductive charging, EV charging needs to transfer several kW with high efficiency over a reasonably high ground clearance provided by the vehicle. Due to the increasing demand for high power transfer capabilities, minimal radio frequency interference potential and efficiency, acoustic, light and capacitive WPT are not suitable for this application. This leaves IPT as the preferred solution.

The concept of IPT is based on the principle of transformers and magnetic induction discovered, experimentally verified and theorized by scientists such as Faraday, Henry, Ampère, Oersted, Maxwell and Hertz [8]. IPT can be thought of as a loosely coupled transformer, as shown in Fig. 1.3, since the presence of an air-gap reduces the coupling of the magnetic fields, but the principle remains the same.

This usually results in low efficiency, but can be solved by using magnetic resonance. This helps to increase the range of the IPT, as seen in Fig. 1.2. For a better understanding of

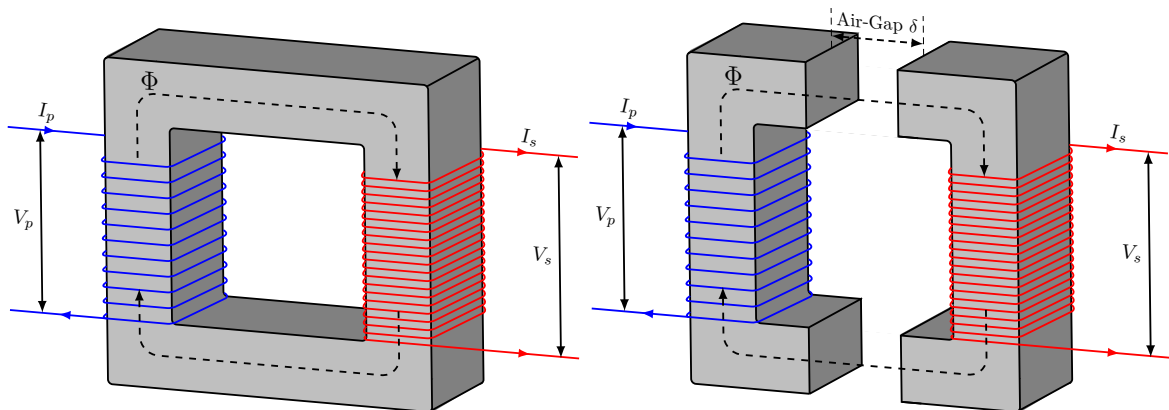


Figure 1.3 – Principle of a ideal transformer, left: strongly coupled, right: loosely coupled.

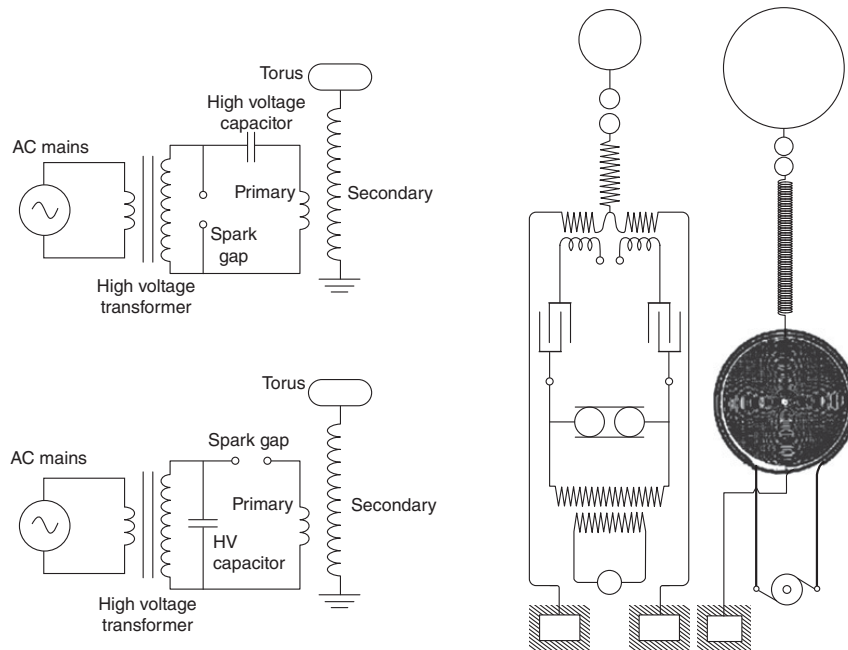


Figure 1.4 – Examples of the Tesla coil, which is a type of resonant transformer (25 kHz–2 MHz), invented in 1891 [9].

resonant IPT, a brief history of the technology is provided in the following section. More on the general history of WPT can be found in [1–3, 8, 9].

1.1 A Brief History of IPT

The first Inductive Power Transfer Systems (IPTs) were proposed in 1890 by Hutin and Leblanc (for an electric tram) [10, 11] and around 1900 by Nikola Tesla ([12–15]). Tesla is also well known for his work on resonant circuits in transformers and invented the famous Tesla coil (1891, [16]) which is a resonant transformer, see Fig. 1.4. He is also known for his idea of free wireless power transmission around the world which he tried to realize with his research project at the Wardencliff Tower [15].

Due to the lack of suitable power electronics (switches), these ideas could not be properly applied and viable solutions came much later in history.

The first IPTS for EV charging was implemented about 40 years later by Babat in 1943 [17] and almost 30 years later, in 1972, Otto proposed and patented an inductively powered vehicle [18], but the work was eventually abandoned [19].

In the 1980s, a project of the Partners for Advanced Transportation Technology (PATH) was founded in California (UC Berkeley), where a roadway powered IPT vehicle with a variable air-gap was developed [20], see Fig. 1.5. Due to the use of an iron core and the lack of good control methods, only 60 % efficiency was achieved [21].

A wave of more recent work and academic interest began with the development of an IPTS for materials handling by Boys and Green in 1991 at the University of Auckland (UoA) [22, 23], which also marks the first real success of the IPT technology as it was licensed and funded by Daifuku Co. Ltd [19]. It is a track-based system using an elongated coil on the primary driven by a resonant power supply.

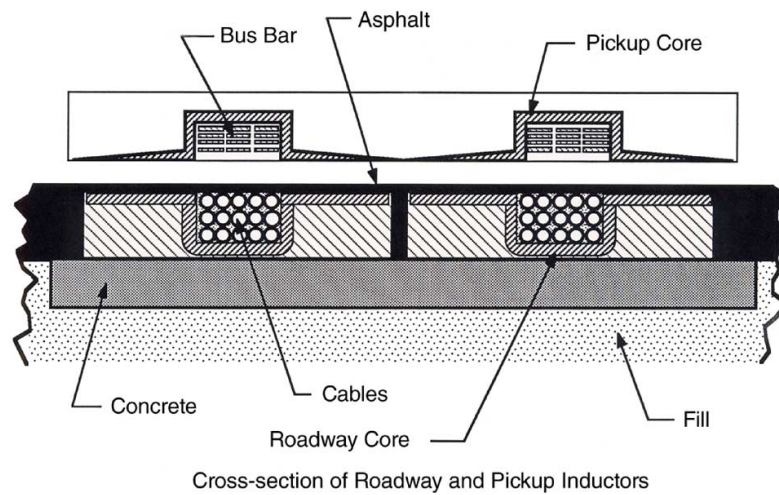


Figure 1.5 – Roadway-powered electric bus and cross section of roadway and onboard power inductors [20].

This marked the beginning of a widespread interest in resonant IPTSs, an overview of which is given in Tab. 1.1 and Fig. 1.6. Other comprehensive reviews of the state of the art or development can be found in [24–29].

Regarding EV charging, prominent magnetic resonance work has been published by Kurs et al. [31], which seemingly “successfully mathematically formulated the resonant coupled power transfer between two resonant coils, demonstrating the transfer of 60 W at a distance of 1.8 m using 10 MHz AC electricity.” but ultimately uses the resonance principle already demonstrated by Tesla [32]. A critical review of this controversy as well as an overview of the history of magnetic resonance for WPT can be found in [32] and [33].

One reason for the slow development of WPT technology for EV charging was the lack of a standard and the long development time. However, the first standards are in place since 2020 (more in Section 2.5.1), and recent development is focused on Heavy-Duty (HD) charging and increasing power transfer [28, 49].

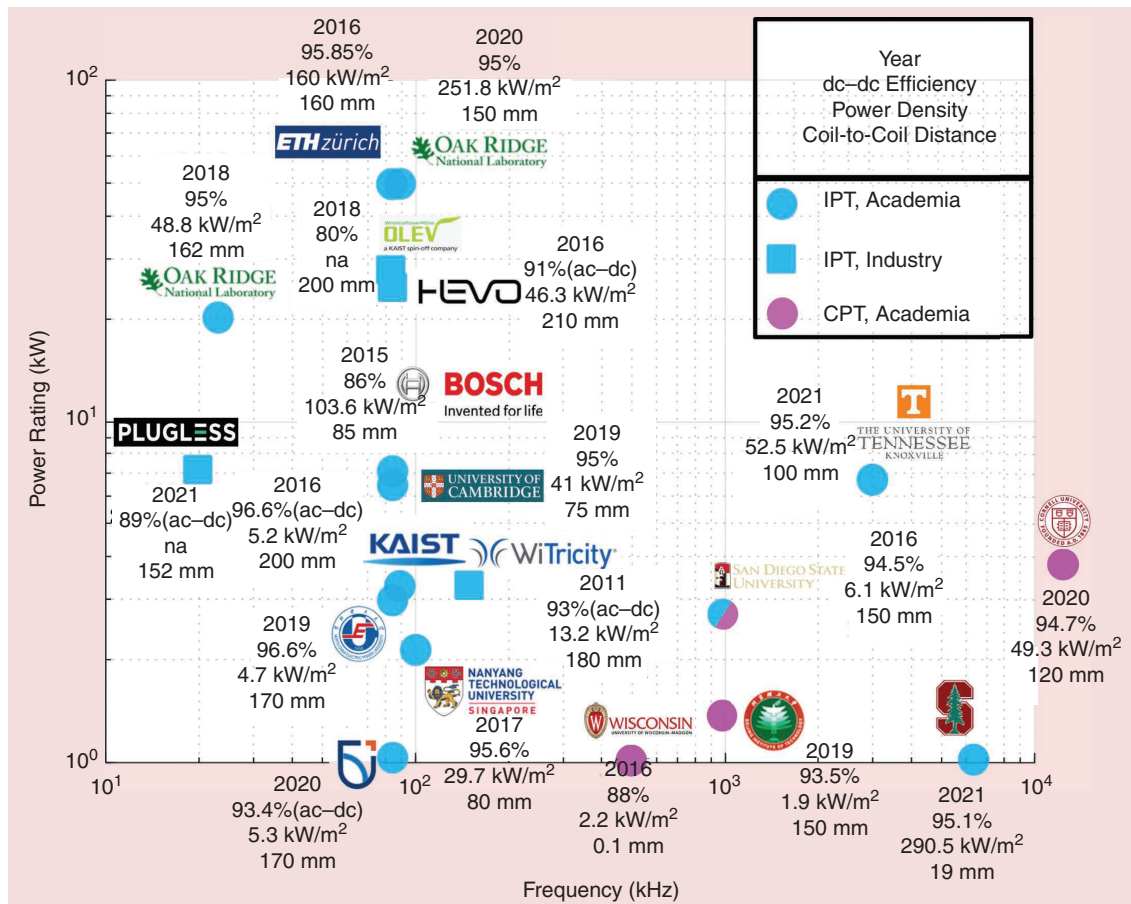


Figure 1.6 – State of the art for wireless EV charging [30].

1.2 EV Charging: Interoperability and Challenges

Interoperability describes the ability of a system to work or communicate with another system. In the context of EV charging, interoperability is a system characteristic that specifies the ability of a charging station to address many different receiver sides or vice versa. Unlike conductive charging, wireless EV charging does not provide a connector or plug that clearly defines the interfaces and thus the interoperability between charger and receiver.

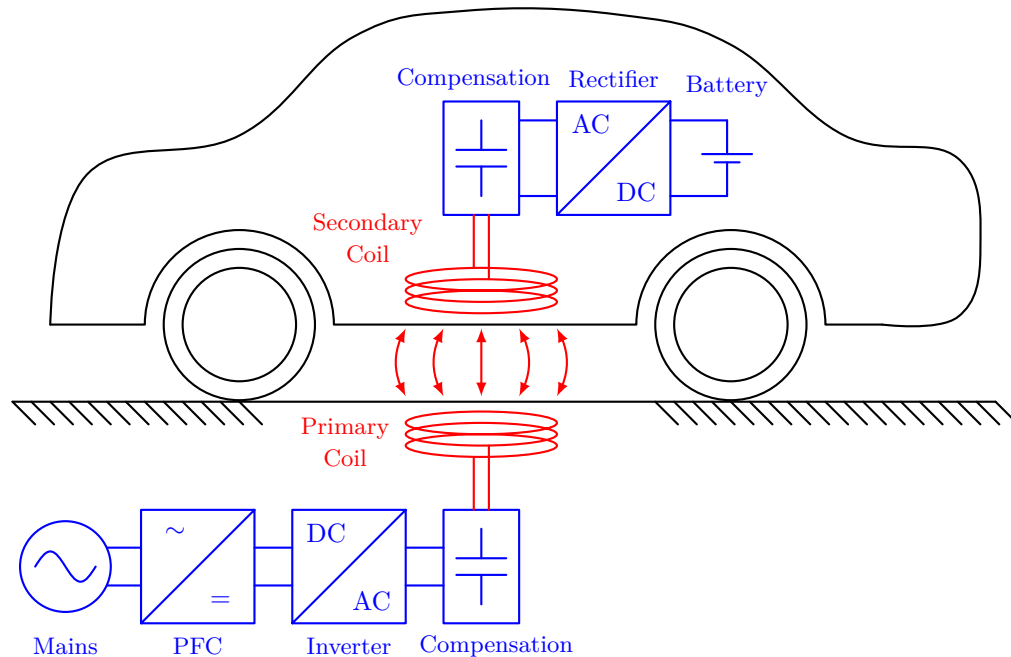
As a result, interoperability requires special consideration during the design process of a wireless charging system. The structure of an IPTS is shown in Fig. 1.7. The application of EV charging introduces interoperability challenges that can be categorized into magnetic and electrical interoperability, highlighted in red and blue, respectively.

Due to the high air-gap, related to the ground clearance of an EV, the magnetic coupling between the charging coil on the ground surface and the receiving coil on the bottom of the EV is very low and also depends on the ground clearance of the EV. In addition, parking over the charging coil will always involve some misalignment. There may also be differences between coil sizes and coil topologies, which can lead to different fundamental magnetic field distributions that may not be compatible with each other. Ultimately, this leads to tolerances and variations in the magnetic coupling that must be handled by the IPTS.

In addition to magnetic interoperability, there may be fundamental differences in the circuit topologies used by different EVs or charging stations. This may result in different

Table 1.1 – A Sample of Important Milestones, Products and Projects related to IPT

Manufacturer/Project	Applications	Power/Frequency	Air-Gap
IPT Technology/ENRX [34]	Bus (static/dynamic)	180 kW	–
WAVE [6, 35]	Bus (static)	50 – 1 MW/20 kHz	15 – 25 cm
Momentum Dynamics/InductEV [36, 37]	Bus (static)	300 kW	–
WiTricity [38]	Car (static/dynamic)	11 kW/85 kHz	25 cm
KAIST (OLEV) [39]	Bus (dynamic)	200 kW/20 kHz	10 – 20 cm
EVATRAN (Gen 2) [40]	Car (static)	7.2 kW/N/A	17.8 cm
ORNL [41, 42]	Car (static)	200 kW/85 kHz	10 cm
FABRIC [43]	Car (dynamic)	22 kW/85 kHz	25 cm
UNPLUGGED [44]	Bus (static)	50 kW/25 kHz	25 cm
STILLE [45]	Car (static)	11–22 kW/85 kHz	25 cm
BiPolPlus [46]	Car (static)	22 kW/85 kHz	12.5 cm
InterOp [47]	Car (static)	3 kW/140 kHz	–
INTIS [48]	Car (static)	22 kW/ 85 kHz	–

**Figure 1.7** – Overview of an IPTS for EV battery charging. Magnetics are highlighted in red and electronics in blue.

system behavior and requirements (e.g., rated currents) that cannot be provided by the other side. Also, the rated power or frequency of the primary or secondary side may be different, which can result in inefficient charging or incompatible transmitters and receivers. The magnetic coupling variation also affects the electrical components and influences the choice of topologies, such as tuning networks. Typically, the two domains cannot be designed separately.

In the context of electrical interoperability, communication between the primary and secondary sides is also very important, as it is necessary to clarify which protocol is to be used and what type of information needs to be transmitted. This also applies to the control of an IPTS, which is often related to cost issues.

At last, as mentioned above, there are standards to which an IPTS must comply. These standards, most important for EV charging is SAE J2954 [50], define expected interoperability requirements and set performance expectations such as frequency, efficiency, power levels, air-gaps, alignment tolerance and communication. SAE J2954 also provides a framework to describe system-level interoperability. It introduces two interfaces on the primary and secondary sides and defines impedance zones that must be matched by the primary and secondary electronics to be interoperable. Details of this approach are discussed in Section 2.5.

On the one hand, these standards are very helpful because they provide a design framework that facilitates independent design of the primary and secondary sides. On the other hand, each IPTS must be compliant with those standards, which may limit the design space. Thus, conformity with all required standards must be considered during the design phase and may be difficult to achieve in some cases.

For IPTSs for EV charging to be successful, interoperability between the primary and secondary sides is crucial. Especially for use-cases like public charging, the prospect of having an IPTS in an EV and only being able to charge at certain proprietary charging stations does not look promising. On the other hand, installing a charging station in a public place that is only capable of addressing a few EVs is not economically feasible and would most likely not be well accepted. An example of what charging stations can look like when interoperability is not properly considered is shown in Fig. 1.8. It shows a conductive charging station and emphasizes the importance of interoperability, as this is a situation that should be avoided.

Even if a proprietary IPT EV charging system is the design goal (e.g., as Tesla (Inc.) does with its own conductive chargers [52], or for other corporate design reasons), there will still be tolerances in the coupling (parking offset, height tolerances due to luggage, etc.) that cannot be avoided and will affect the overall system performance.

1.3 Motivation and Goals

With the presented IPT background and the challenges associated with achieving interoperability in EV charging, the following questions which this thesis aims to address arise, are:

- How can interoperability be defined and evaluated in the context of IPTSs for EV battery charging?
- How can a system design be achieved that balances both high interoperability and good performance, given that the two are not always aligned?
- Is it possible to design an efficient system for interoperability when only one side or part of the system is known or can be influenced?
- How can interoperability be incorporated into the complete design stage of IPT EV charging systems?
- How can a high degree of freedom for designers be maintained when considering interoperability and regulations (and not slowing or stopping innovation for the technology)?



Figure 1.8 – Example of a charging station for conductive charging with bad interoperability from the infrastructure side [51].

To address these issues, this thesis aims to develop a design and evaluation methodology for IPTSs with a focus on interoperability. To achieve this, the aforementioned impedance-based approach from [50] is used. This thesis expands on that approach and uses it to develop a design methodology. Furthermore, all components of an IPTS are examined for their magnetic and electrical interoperability issues in order to better understand the impact of tolerances and changes to the system, as well as interoperability aspects within the system behavior and different interfaces. Therefore, an analytical model is established and four interfaces are introduced. The most common topologies between these interfaces are discussed. Most importantly, variations of important (to be identified) metrics such as coupling, tuning and leakage and their consideration in the design methodology will be discussed.

Another goal of this thesis is to keep the design method as adaptable as possible, so that it can be applied to as many use-cases as possible, while considering different interoperability aspects at different design stages. The ultimate goal is to provide a customizable design

method where the designer can set the interoperability requirements (which may be completely different from system to system), apply the method, and get a reasonably good design. It should not matter whether a system has to be built from scratch for public charging or an inverter has to be redesigned for a specific proprietary system.

Finally, this thesis aims to present some examples where the method is applied to design or evaluate different scenarios.

1.4 Thesis Outline

The thesis is structured as follows:

Chapter 2 provides an overview of the fundamental principles of an IPTS. This chapter presents the different topologies of each part of the system, along with important equations and the effects on system behavior. This section establishes the fundamentals necessary to develop the methodology and presents the previous work done on it.

Chapter 3 introduces the Impedance Plane Method (IPM) and establishes the basic interfaces necessary for its implementation. Different system boundaries are implemented and the transfer of impedances between interfaces is introduced for different topologies. An example with step-by-step explanations of the analytical method is included to provide a clear understanding of the IPM.

After presenting the method, Chapter 4 elaborates on the magnetic parts of the system and discusses the effects of changes in coupling factor, leakage flux, and coil design on the Impedance Planes (IPPs). The effects of these investigations are then shown in another example.

Similarly, Chapter 5 examines the electrical parts of the IPTS, such as different rectification topologies. The method is extended by introducing losses in various parts of the system, which are then incorporated into the IPP analysis. An extensive public charging use-case and the impact of the loss extension of the IPM are presented.

In Chapter 6 the aspects of different compensation topologies as well as active tuning effects are discussed. These aspects are studied in a sensitivity analysis and it is shown how the method can be used for active tuning design.

After extending the methodology and studying the magnetics and electronics in detail, the complete IPM is then applied to higher power, 50 kW systems in Chapter 7. The interoperability of two independently designed 50 kW systems is assessed.

Chapter 8 summarizes the thesis, reflects on the contributions and results, and then gives an outlook on open issues and suggests future work that could not be covered within this thesis.

2 Fundamentals of IPT

A comprehensive examination of the impact of interoperability aspects on IPTSs requires a thorough understanding of their behavior. This chapter aims to provide such an understanding by detailing the fundamentals of an IPTS and the specific functionalities of each of its components.

The chapter begins with a discussion of the general requirements of an IPTS for EV charging, followed by a detailed overview of the different topologies for each component. Important metrics, notations, practical considerations, and common simplifications frequently used throughout this thesis are derived. In addition, the chosen approaches for circuit analysis and simulation methods are presented.

Furthermore, the interoperability aspects in the context of EV charging, which were previously addressed in the last chapter, are further examined from a technical perspective. Special emphasis is placed on their impact on the operation of the IPTS, which allows for a more comprehensive understanding of the impact of interoperability aspects on the IPTS.

2.1 IPT for EV Charging

The structure of the IPTS shown in Fig. 1.7 can be simplified as shown in Fig. 2.1. The magnetic coils in the central block transfer power across the air-gap. Due to the high air-gap required by the application, IPTSs for EV charging have low couplings, so reactive power compensation is required at each coil, along with operating at or near resonance. The inverter provides high frequency electrical energy from the grid (or power factor correction (PFC)) to the primary coil. The AC energy received on the secondary is rectified to provide DC power to the battery (load).

The first assumption made throughout this thesis is that the grid and PFC are considered ideal and can be replaced by an ideal DC voltage source. This is a feasible assumption since

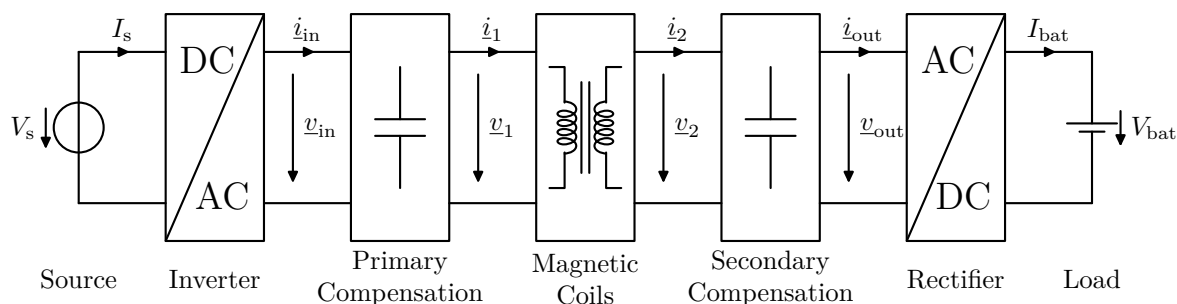


Figure 2.1 – Simplified topology of an IPTS.

the power factors of modern PFCs are very high. This thesis will consider the apparent input power provided from the grid, known as

$$\underline{S} = \underline{v} \cdot \underline{i}^* = VI \cdot e^{j(\varphi_v - \varphi_i)} = S \cdot e^{j\varphi} \quad (2.1)$$

$$P = \text{Re}(\underline{S}) = S \cdot \cos(\varphi) \quad (2.2)$$

$$Q = \text{Im}(\underline{S}) = S \cdot \sin(\varphi) \quad (2.3)$$

as ideal, which means that there is no reactive power provided by the grid, so $\varphi = 0^\circ$ and the DC input power is purely active:

$$S_{\text{in}} = P_{\text{in}} = V_s \cdot I_s. \quad (2.4)$$

The general equations for active power P and reactive power Q are given in Eq. (2.2) and Eq. (2.3), respectively.

As can be seen in the previous equations, this thesis uses capital letters to indicate DC and constant values and lower letters to indicate AC and time-dependent values, except for commonly used metrics and Greek letters. Phasors and complex values are underlined, while matrices are underlined with a curly bracket. The analysis performed in this thesis assumes steady state conditions, which implies that only the phasor \underline{x} of a time-varying sinusoidal function $\underline{x}(t)$, usually described by $\underline{x}(t) = \underline{x} \cdot e^{j\omega t} = X \cdot e^{j(\omega t + \varphi_x)}$, is considered. Voltage and current are also time-dependent and can be simplified using phasors.

The primary objective of an IPTS for EV charging is to ensure efficient charging of the battery. To achieve this goal, each component of the IPTS in Fig. 2.1 should be designed to operate as ideally as possible. However, it is important to recognize that perfection in IPTS design is difficult to achieve in practical applications, and it is necessary to account for various sources of tolerance that can affect system performance.

One such source of tolerance in IPTSs is the misalignment of the primary and secondary coils in the x-, y-, and z-directions, which can lead to changes in the magnetic coupling between the coils. The misalignment tolerance has a significant impact on the overall system behavior and its effects must be considered in the design and operation of an IPTS.

In addition to the technical aspects, the regulatory and safety issues discussed in the previous chapter must also be considered. The magnetic field generated by the coils can pose a danger to pedestrians or animals, so appropriate safety measures must be taken. In this thesis, only the leakage flux field distribution is discussed, while topics such as Foreign Object Detection (FOD) and Live Object Protection (LOP) are beyond the scope of this research (see [9, 53, 54]). Furthermore, the focus of this thesis is on unidirectional power transfer from the grid to the battery, so bidirectional power transfer (e.g. [55, 56]), as well as dynamic charging (e.g. [57–60]) and three-phase systems (e.g., [61–66]), are also not considered.

The regulatory framework has chosen a frequency of 85 kHz, which makes it possible to ignore far-field radio frequency effects. In order to limit the variations, HD charging is also excluded. The regulatory framework for this use-case is not far advanced, and the applications and power levels are very different from static EV Light-Duty (LD) charging, which is the use-case in this thesis.

2.2 Components of an IPT System

This section discusses all the components shown in the simplified circuit in Fig. 2.1, their most common topologies, and the (steady-state) simplifications that can be made.

2.2.1 Battery Load

Fig. 2.2 shows a typical charging profile as observed for lithium-ion batteries [67]. For EV charging, a constant current output is desired [68]. For the purposes of this thesis, ideal DC values are assumed and DC ripple is neglected. Consequently, the output power is simplified as active power only and can be calculated using the expression:

$$P_{\text{out}} = V_{\text{bat}} \cdot I_{\text{bat}}, \quad (2.5)$$

where V_{bat} is the constant voltage modeled for the battery, and I_{bat} is the current output. By modeling the battery with a constant voltage, it can be simplified and represented as a resistive load, as shown by the following equation:

$$V_{\text{bat}} = R_{\text{bat}} \cdot I_{\text{bat}}. \quad (2.6)$$

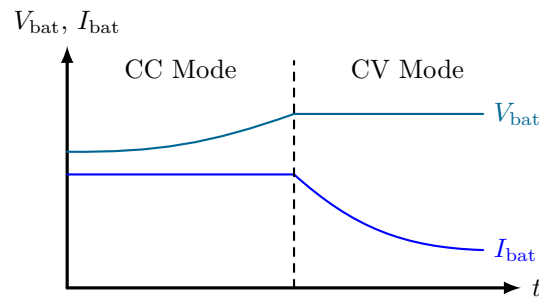


Figure 2.2 – Typical battery charging profile.

2.2.2 Secondary Rectifier and Control

Efficient charging of an EV battery requires a mechanism to control the AC power received from the secondary coil and convert it to DC power. To accomplish this, AC/DC converters are used, as shown in Fig. 2.3.

Several rectification topologies are available, each with a different impact on the system performance. Secondary power flow control is typically included in this stage. Although active rectification can reduce losses, it also increases the cost of the system. The following sections describe the most commonly used passive and active rectifier topologies. System behavior is generally dependent on the primary topology and operation, and for simplicity this section assumes a current-controlled primary.

Passive Rectification Topologies

Full Bridge Rectifier A full-bridge rectifier consists of four diodes arranged in a bridge configuration. The secondary coil is connected to the input of the rectifier and the load (i.e., the battery and filter components) is connected to the output of the rectifier, as shown in Fig. 2.4a.

During the positive half cycle of the AC voltage, diodes D1 and D4 are conducting and current flows through the load in the forward direction. During the negative half cycle of

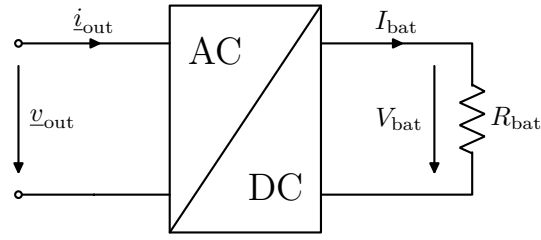


Figure 2.3 – Secondary side AC/DC converter.

the AC voltage, diodes D2 and D3 are conducting and current flows through the load in the reverse direction, see Fig. 2.4b.

In this case, the output of the compensation network represents the rectifier source, which differs depending on the tuning topology chosen, and also affects the load filter (capacitive or inductive filter). However, if the input is a sinusoidal current source, Fig. 2.4 shows the rectifier topology and the resulting waveforms (with the fundamental output voltage $v_{\text{out}(1)}$).

In many cases, only the fundamental wave is of interest, and in this case the entire rectifier can be replaced by an equivalent AC resistor [69]. The relationship between DC and AC resistances or values can be calculated as follows for a current source (series) converter:

$$I_{\text{out}} = \frac{\pi}{2\sqrt{2}} I_{\text{bat}} \quad (2.7)$$

$$V_{\text{out}} = \frac{2\sqrt{2}}{\pi} V_{\text{bat}} \quad (2.8)$$

$$R_{\text{ac}} = \frac{V_{\text{out}}}{I_{\text{out}}} = \frac{8}{\pi^2} R_{\text{bat}} = \frac{8}{\pi^2} \frac{V_{\text{bat}}^2}{P_{\text{out}}} \quad (2.9)$$

where I_{out} and V_{out} are the RMS values of i_{out} and v_{out} , respectively.

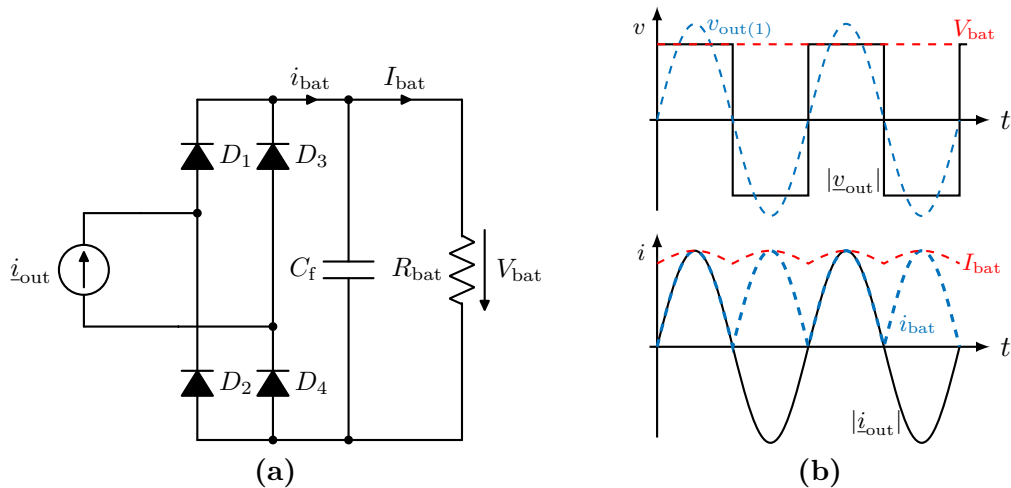


Figure 2.4 – Passive full bridge rectifier (current source), (a) topology and (b) waveforms.

In the case of a voltage source (parallel) converter (topology and waveforms can be found in [69]) the equivalent AC-values can be derived with:

$$V_{\text{out}} = \frac{\pi}{2\sqrt{2}} V_{\text{bat}} \quad (2.10)$$

$$I_{\text{out}} = \frac{2\sqrt{2}}{\pi} I_{\text{bat}} \quad (2.11)$$

$$R_{\text{ac}} = \frac{V_{\text{out}}}{I_{\text{out}}} = \frac{\pi^2}{8} R_{\text{bat}} = \frac{\pi^2}{8} \frac{V_{\text{bat}}^2}{P_{\text{out}}}. \quad (2.12)$$

Current Doubler Another well known passive topology is the current doubler, which is very useful for high current, low voltage systems [70]. The topology is shown in Fig. 2.5a and the ideal relationships between equivalent AC and DC values are as follows:

$$I_{\text{out}} = \frac{1}{2} \cdot \frac{2\sqrt{2}}{\pi} I_{\text{bat}} \quad (2.13)$$

$$V_{\text{out}} = 2 \cdot \frac{\pi}{2\sqrt{2}} V_{\text{bat}} \quad (2.14)$$

$$R_{\text{ac}} = 4 \cdot \frac{\pi^2}{8} R_{\text{bat}} = \frac{\pi^2}{2} \frac{V_{\text{bat}}^2}{P_{\text{out}}}. \quad (2.15)$$

It can be seen that this topology allows twice the DC current to be obtained for the same AC current compared to the conventional full bridge rectifier. However, it also changes the load presented to the coils. This topology has been used by Double-D Pad (DDP) systems (informative appendix) in [50].

Voltage Doubler Contrary to the current doubler, the voltage doubler can be used. Here, the DC voltage is doubled compared to the regular full bridge rectifier (current source converter) for the same AC voltage. This rectifier topology has been used to reduce losses in [71], as well

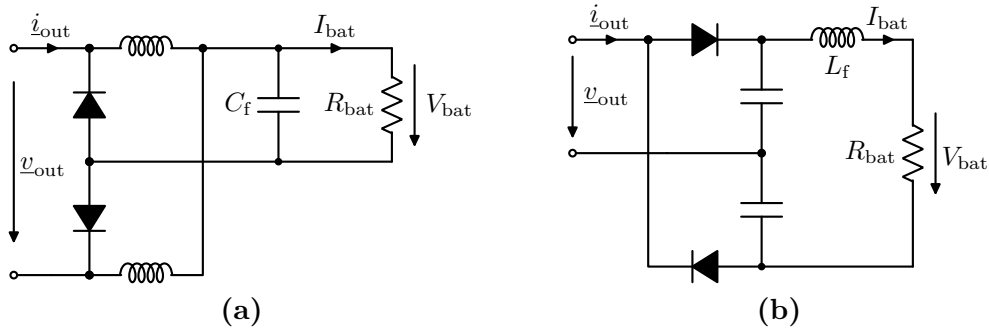


Figure 2.5 – Topologies of passive rectification stages, (a) current doubler and (b) voltage doubler.

as in a bidirectional system discussed in [72]. The topology of the voltage doubler rectifier is shown in Fig. 2.5b, and the ideal equations for AC-DC conversion are given below:

$$I_{\text{out}} = 2 \cdot \frac{\pi}{2\sqrt{2}} I_{\text{bat}} \quad (2.16)$$

$$V_{\text{out}} = \frac{1}{2} \cdot \frac{2\sqrt{2}}{\pi} V_{\text{bat}} \quad (2.17)$$

$$R_{\text{ac}} = \frac{1}{4} \cdot \frac{8}{\pi^2} R_{\text{bat}} = \frac{2}{\pi^2} \frac{V_{\text{bat}}^2}{P_{\text{out}}}. \quad (2.18)$$

Impedance Compression Network Another passive topology, commonly referred to as the “Impedance Compression Network”, is utilized by the reference secondary coils (SAE Vehicle Assembly (VA) WPT3 Z1-Z3, see Section 2.5.1) in [50], as shown in Fig. 2.6. The objective of this topology is to reduce the stress on the AC side caused by battery voltage variations (by compressing the range of the resulting impedances). An analysis of this topology can be found in [73]. The total impedance of the rectifier can be expressed as

$$\underline{Z}_{\text{rect}} = \frac{\underline{X}^2 + R_{\text{ac}}^2}{R_{\text{ac}}}, \quad (2.19)$$

where R_{ac} is calculated using Eq. (2.9).

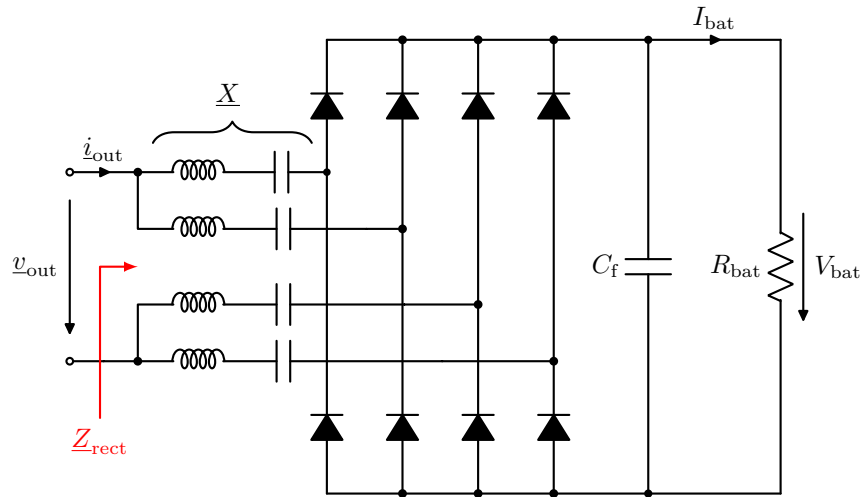


Figure 2.6 – Passive impedance compression network rectifier.

Active Rectification Topologies

Active rectification can be a useful technique to control power flow and to compensate or reduce losses on the secondary side of an IPTS. There are several solutions for active rectification, including phase shift control [74, 75], switched controlled capacitors [76], and active impedance control [77]. For bidirectional power transfer, an active rectification stage is inevitable to enable the direction of power flow to be changed [78].

However, a detailed discussion of active rectification is beyond the scope of this thesis. Instead, this thesis focuses on simpler control methods, such as a rectifier followed by either a buck or boost converter, depending on the tuning, which will be discussed in the following section.

Boost Converter The boost converter is a widely used DC-DC converter that uses a decoupled controller to regulate the output voltage. It operates by changing the duty cycle of the switch to alter the load presented to the resonant converter. The amount of voltage boost is proportional to the duty cycle. Therefore, the output voltage can be controlled by adjusting the duty cycle.

The boost converter is often used to regulate the output voltage in parallel tuned systems due to its current source nature (when using a current controlled primary).

One of the main advantages of the boost converter is its simplicity and few components, making it a cost-effective solution for many applications. However, it should be noted that the boost converter can affect the equivalent AC resistance of the system, which should be considered during the design phase.

Applications of the boost converter can be found in various papers such as [23, 79, 80], and its topology is shown in Fig. 2.7.

The AC to DC conversion of the load can be determined using a similar approach as that used in the previous sections, but with the inclusion of the duty cycle D as an additional degree of freedom that is restricted to the range of 0 – 1:

$$V_{\text{out}} = \frac{\pi}{2\sqrt{2}}(1 - D)V_{\text{bat}} \quad (2.20)$$

$$I_{\text{out}} = \frac{2\sqrt{2}}{(1 - D)\pi}I_{\text{bat}} \quad (2.21)$$

$$R_{\text{ac}} = \frac{V_{\text{out}}}{I_{\text{out}}} = \frac{\pi^2}{8}(1 - D)^2 R_{\text{bat}} = \frac{\pi^2}{8}(1 - D)^2 \frac{V_{\text{bat}}^2}{P_{\text{out}}}. \quad (2.22)$$

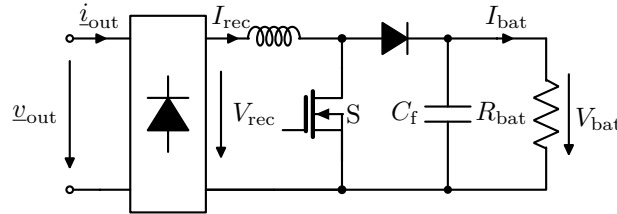


Figure 2.7 – Active rectifier with (decoupled) boost controller.

Buck Converter The buck converter is commonly used in series tuned systems for power control due to its voltage source nature (when the primary side supplies a constant current). The topology of the buck converter is shown in Fig. 2.8. More detailed discussions on the application of buck converters can be found in studies such as [81–83].

The load can be controlled in a similar manner as in the boost converter by adjusting the duty cycles, and the corresponding AC equivalent values can be determined using the equation (as presented in [81]):

$$R_{\text{ac}} = \frac{\pi^2}{8} \frac{D^2}{R_{\text{bat}}}. \quad (2.23)$$

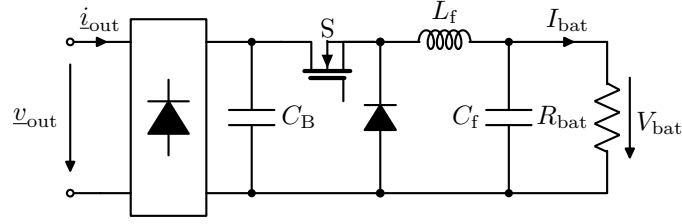


Figure 2.8 – Active rectifier with buck controller.

Summary and Simplifications

To simplify the analysis, the effect of harmonics is usually neglected (see Section 2.3) and continuous conduction is assumed. In many cases, only the fundamental wave is of interest (First Harmonic Approximation (FHA) can be applied, see Section 2.3.1). In such scenarios, the presented AC resistance R_{ac} can be determined and replace the rectification stage in the circuit, as shown in Fig. 2.9.

This approach eliminates the need to account for the non-linear switching behavior, and the calculation can be simplified with fundamental harmonic analysis using RMS values. An overview of all the presented rectifiers and their conversion from DC to equivalent (fundamental) AC-values is given in Tab. 2.1.

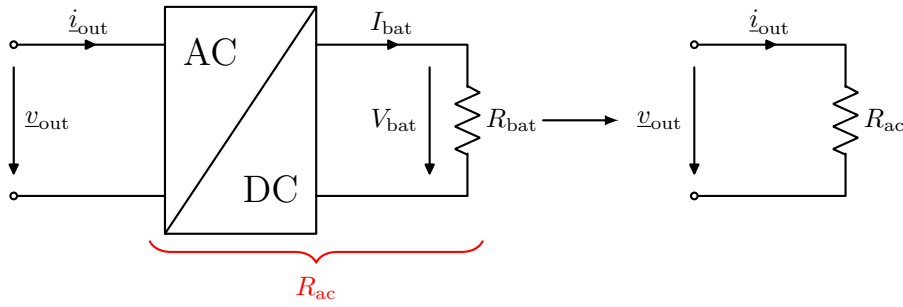


Figure 2.9 – Secondary rectifier with FHA simplification.

Table 2.1 – Calculation of the AC-Values (FHA) for Different Rectifier Topologies

Rectifier	V_{out}	I_{out}	R_{ac}
Full Bridge Rectifier (current source)	$\frac{2\sqrt{2}}{\pi} V_{bat}$	$\frac{\pi}{2\sqrt{2}} I_{bat}$	$\frac{8}{\pi^2} R_{bat}$
Full Bridge Rectifier (voltage source)	$\frac{\pi}{2\sqrt{2}} V_{bat}$	$\frac{2\sqrt{2}}{\pi} I_{bat}$	$\frac{\pi^2}{8} R_{bat}$
Current Doubler	$2 \cdot \frac{\pi}{2\sqrt{2}} V_{bat}$	$\frac{1}{2} \cdot \frac{2\sqrt{2}}{\pi} I_{bat}$	$4 \cdot \frac{\pi^2}{8} R_{bat}$
Voltage Doubler	$\frac{1}{2} \cdot \frac{2\sqrt{2}}{\pi} V_{bat}$	$2 \cdot \frac{\pi}{2\sqrt{2}} I_{bat}$	$\frac{1}{4} \cdot \frac{8}{\pi^2} R_{bat}$
Impedance Compression Network	$\frac{2\sqrt{2}}{\pi} V_{bat}(X=0)$	$\frac{\pi}{2\sqrt{2}} I_{bat}(X=0)$	$\frac{R_{ac}^2 + X^2}{R_{ac}}$
Boost Converter	$\frac{\pi}{2\sqrt{2}} V_{bat}(1-D)$	$\frac{2\sqrt{2}}{\pi(1-D)} I_{bat}$	$\frac{\pi^2}{8} R_{bat}(1-D)^2$
Buck Converter	$\frac{2\sqrt{2}}{\pi \cdot D} V_{bat}$	$\frac{\pi}{2\sqrt{2}} I_{bat} \cdot D$	$\frac{8}{\pi^2} \frac{D^2}{R_{bat}}$

2.2.3 Secondary Compensation

As discussed in more detail in the Section 2.2.6, the primary coil induces a voltage in the secondary coil. If the secondary coil is open-circuited, the induced voltage can be calculated using the equation (2.24).

$$V_{oc} = j\omega MI_1. \quad (2.24)$$

On the other hand, if the secondary is short-circuited, the current flowing through the coil can be determined using

$$I_{sc} = \frac{V_{oc}}{j\omega L_2} = \frac{M}{L_2} I_1, \quad (2.25)$$

with L_2 , M and I_1 being the secondary self-inductance, mutual inductance and primary coil current, respectively.

V_{oc} and I_{sc} are fundamental characteristics of the secondary coil as they define the uncompensated power P_{su} which can be transferred through the coil as

$$P_{su} = V_{oc} \cdot I_{sc}. \quad (2.26)$$

When a load is connected to the coil terminals, the maximum transferable output power is (see [84])

$$P_{out,max} = \frac{1}{2} P_{su}. \quad (2.27)$$

However, in practical applications such as IPTSs for EV charging, the maximum transferable output power is often insufficient at low coupling [85]. To compensate for this, a capacitor is tuned to the resonant frequency f_s and compensates for the inductive impedance.

The effects of tuning are illustrated in Fig. 2.10. There are basically two methods of resonant tuning: series compensation and parallel compensation, and when used, they allow the secondary to draw more power from the system. Series tuning holds V_{oc} constant while increasing the output current by $Q_2 I_{sc}$, and parallel tuning holds I_{sc} constant while increasing the output voltage by $Q_2 V_{oc}$. The load quality factor Q_2 describes the ratio of reactive power to active power.

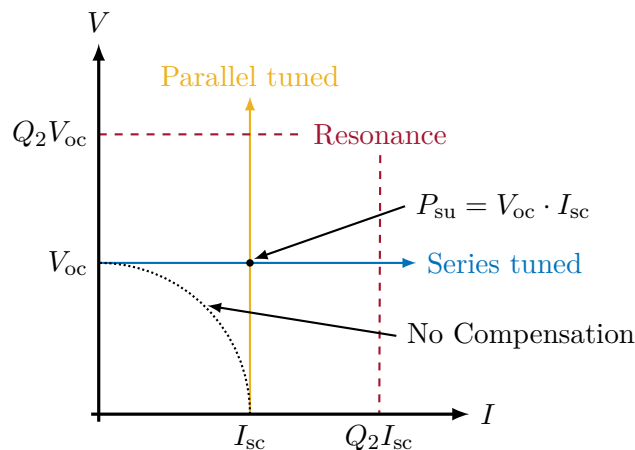


Figure 2.10 – Series or parallel resonance tuning principle for current-controlled primaries.

The load quality factor is an important metric and primarily describes how much the power transfer can be increased [85]. Using Eq. (2.24) and (2.25) the output power in a compensated system can be calculated as

$$P_{\text{out}} = \omega \frac{M^2}{L_2} I_1^2 Q_2. \quad (2.28)$$

There are several ways to tune a system, and any topology can be used for interoperability, so the most common topologies are described below. The naming convention for tuning is always in the direction towards the coil terminals. The following analysis is done in steady-state, considering only the RMS values and reactances (with the corresponding impedance being $\underline{Z} = jX$).

Series Tuning

A secondary series tuned and loaded circuit is shown in Fig. 2.11 on the left side. If the impedance of the inductor and the capacitor are in resonance ($\omega L_2 = X_{L2} = X_{Cs2} = \frac{1}{\omega C_{s2}}$), they cancel each other out and the circuit simplifies as shown on the right side.

As previously mentioned, V_{oc} is connected to the load and the current I_2 is boosted and can be calculated as

$$I_2 = I_{\text{sc}} \cdot Q_2 \quad (2.29)$$

with Q_2 being the loaded quality factor, which is

$$Q_2 = \frac{\omega L_2}{R_{\text{ac}}} = \frac{1}{\omega C_{s2} R_{\text{ac}}} \quad (2.30)$$

in a series tuned circuit. Further information can be found in [84–86].

Parallel Tuning

A parallel tuned circuit is shown in Fig. 2.12 and can be simplified to a current source circuit (in resonance) using the Norton equivalent [85]. The resonance condition is similar to the series tuning, in this case $X_{L2} = X_{Cp2} = \frac{1}{\omega C_{p2}}$. Here the load current is similar to I_{sc} while the output voltage is boosted by $Q_2 V_{\text{oc}}$ with

$$Q_2 = \frac{R_{\text{ac}}}{\omega L_2} = \omega C_{p2} R_{\text{ac}}. \quad (2.31)$$

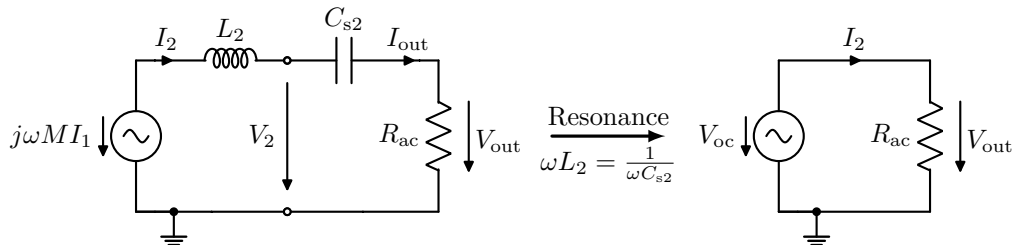


Figure 2.11 – Ideal secondary series tuned circuit.

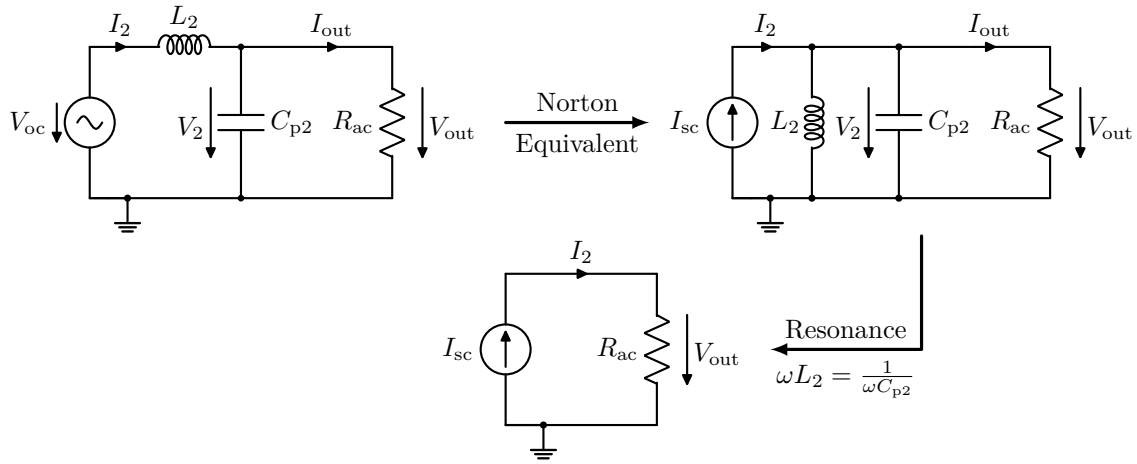


Figure 2.12 – Ideal secondary parallel tuned circuit.

LCL Tuning

The circuit and simplification of an LCL tuned secondary is shown in Fig. 2.13. The LCL circuit combines the previous two topologies as it acts like a parallel tuned system because it provides a current source to the load.

However, it acts like a series tuned system when coupled to another coil [86]. The load quality factor is similar to Eq. (2.31) and the resonance condition is $X_2 = \omega L_2 = \frac{1}{\omega C_{p2}} = \omega L_{s2}$.

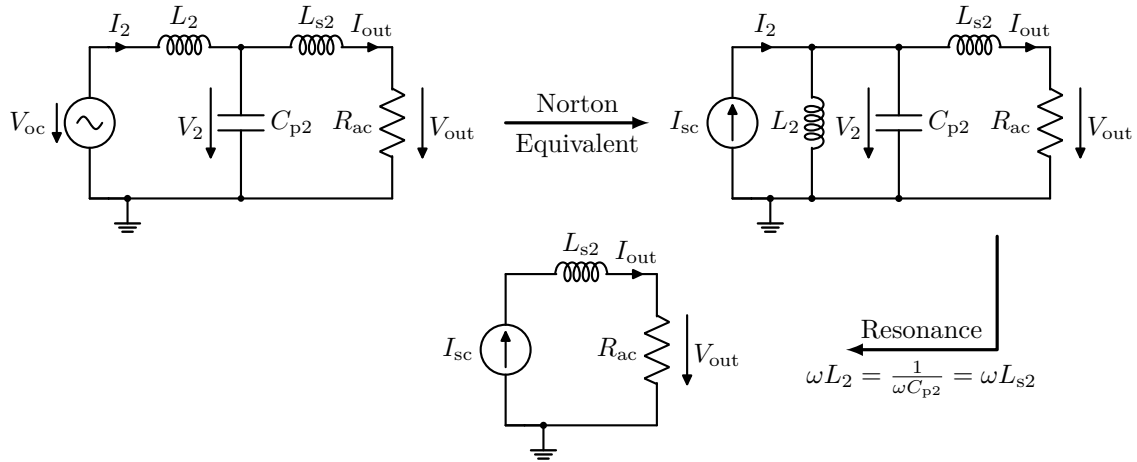


Figure 2.13 – Ideal secondary LCL tuned circuit.

LCC Tuning

The topologies shown above boost either current or voltage. More complex topologies, such as LCC tuning, can be used when both need to be boosted. For this purpose, the load quality factor can be divided into a current boost factor Q_i and a voltage boost factor Q_v (see [85]):

$$Q_2 = Q_i \cdot Q_v = \left(\left| \frac{I_{out}}{I_{sc}} \right| \right) \cdot \left(\left| \frac{V_{out}}{V_{oc}} \right| \right). \quad (2.32)$$

In the case of an LCC tuned circuit, the current and voltage boost factor can be calculated as

$$Q_i = \frac{\omega L_2}{X_2} \quad (2.33)$$

$$Q_v = \frac{R_{ac}}{X_2} \quad (2.34)$$

with X_2 being the reactance of the partial compensated inductor $X_2 = \omega L_2 - \frac{1}{\omega C_{s2}}$. The resonance condition is $X_2 = \omega L_2 - \frac{1}{\omega C_{s2}} = \frac{1}{\omega C_{p2}} = \omega L_{s2}$ and the circuit is shown in Fig. 2.14.

Partial-Series Tuning

Similar to the LCC tuned circuit, the partial-series tuned system increases current and voltage, but does not have the additional inductance and actually acts like a parallel tuned system. The circuit is shown in Fig. 2.15 and the quality factors and resonance condition are similar to the LCC tuned circuit.

Summary

The resonance conditions, the ratio of coil current and voltage to load current and voltage, and the quality factors for all the tuning topologies presented are summarized in Tab. 2.2.

Extensive research has been conducted on compensation and its design, with varying scopes. Some comprehensive overviews and analyses can be found in the literature in [87–93].

2.2.4 Primary Power Supply

Inverters are required to energize the primary coil to provide the primary current (along with the primary tuning, which will be discussed in the next section) needed for the power transfer as described in the previous section.

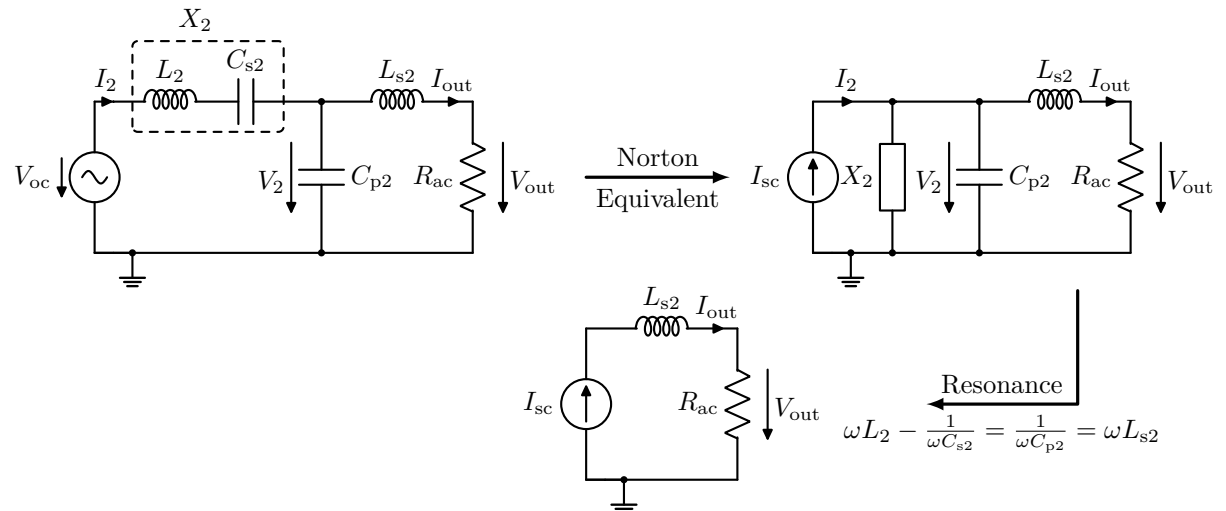


Figure 2.14 – Ideal secondary LCC tuned circuit.

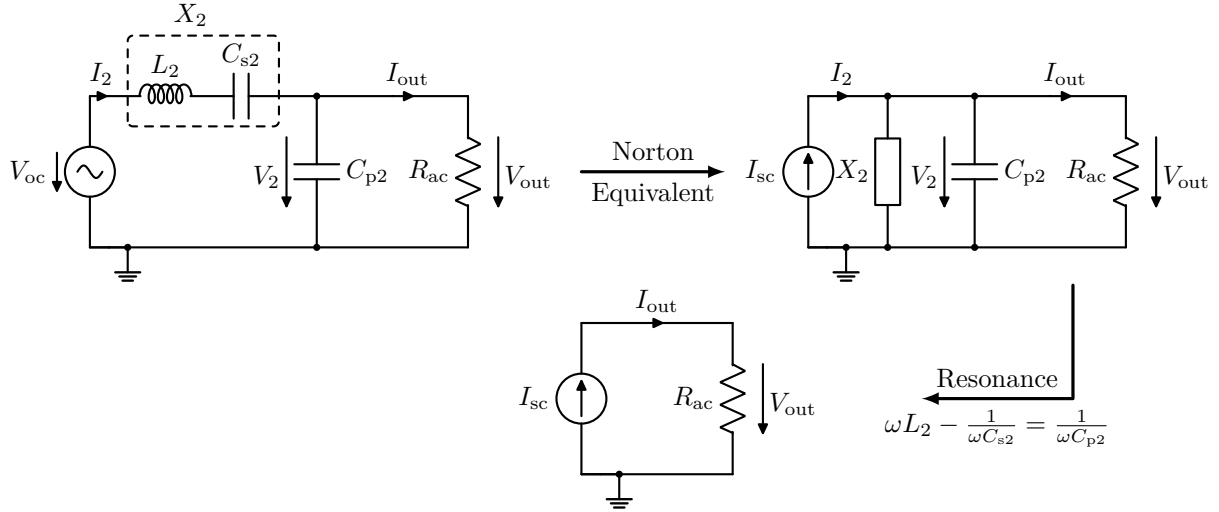


Figure 2.15 – Ideal secondary partial-series tuned circuit.

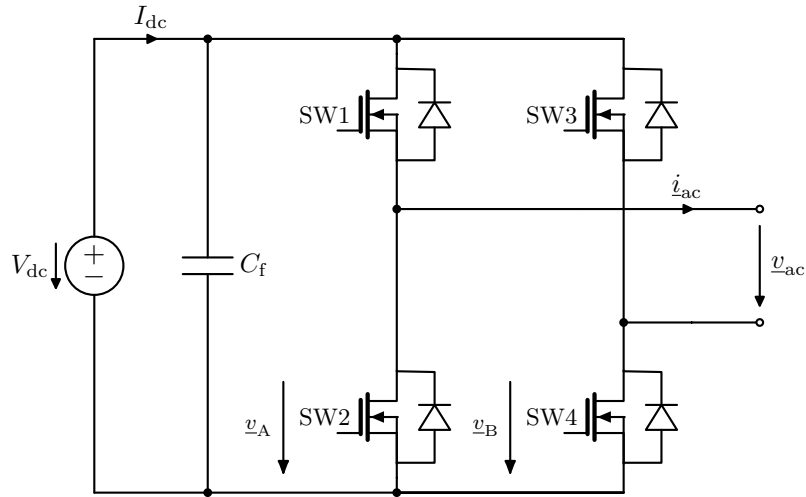


Figure 2.16 – Schematic of the full bridge inverter topology.

The most common voltage source inverter topology is the H-bridge shown in Fig. 2.16. Other topologies such as half-bridge, Class E or Class D inverter [94], Boost Active Bridge [95] or the current sourced push-pull inverter [96], can be found in the literature and are not discussed here.

The H-bridge has four switches (SW1-SW4) and is powered directly from the DC bus. It consists of two legs that are typically driven 180° out of phase (conduction angle α) with a duty cycle of 50 % and the typical waveforms are shown in Fig. 2.17a. This operating mode is chosen to easily achieve Zero Voltage Switching (ZVS). In practice, it is necessary to add some dead time to prevent current shoot through [97].

The load connected to a voltage source inverter cannot have a parallel capacitor across the output terminals and should be inductive in order to achieve ZVS. Mostly MOSFETs are used as switches, which have a higher turn-on energy and therefore higher turn-on losses, thus ZVS is an important condition to achieve.

Table 2.2 – Summary of all Tuning Topologies, their Resonance Conditions and Load Quality Factor

Tuning	S	P	PS	LC	LCC
Q_i	$\frac{\omega L_2}{R_{ac}}$	1	$\frac{\omega L_2}{X}$	1	$\frac{\omega L_2}{X}$
Q_v	1	$\frac{R_{ac}}{\omega L_2}$	$\frac{R_{ac}}{X}$	$\frac{R_{ac}}{\omega L_2}$	$\frac{R_{ac}}{X}$
V_{out}	V_{oc}	$V_{oc} \cdot Q_2$	$V_{oc} \cdot Q_v$	$V_{oc} \cdot Q_2$	$V_{oc} \cdot Q_v$
I_{out}	$I_{sc} \cdot Q_2$	I_{sc}	$I_{sc} \cdot Q_i$	I_{sc}	$I_{sc} \cdot Q_i$
V_2	$V_{oc} \sqrt{1 + Q_2^2}$	$V_{oc} \cdot Q_2$	$V_{oc} \sqrt{(1 - Q_i)^2 + Q_2^2}$	$V_{oc} \sqrt{1 + Q_2^2}$	$V_{oc} \sqrt{1 + Q_2^2}$
I_2	$I_{sc} \cdot Q_2$	$I_{sc} \sqrt{1 + Q_2^2}$	$I_{sc} \cdot Q_i \sqrt{1 + Q_v^2}$	$I_{sc} \cdot Q_2$	$I_{sc} \cdot Q_2$
Resonance Condition	$C_{s1} = \frac{1}{\omega^2 L_1}$	$C_{p1} = \frac{1}{\omega^2 L_1}$	$\omega L_2 = \frac{1}{\omega C_{s2}} + \frac{1}{\omega C_{p2}}$	$L_2 = L_{s2} = \frac{1}{\omega^2 C_{p2}}$	$L_{s2} = \frac{1}{\omega^2 C_{p2}}$ $= L_2 - \frac{1}{\omega^2 C_{s2}} = \frac{X}{\omega}$
X	–	–	$X = \omega L_2 - \frac{1}{\omega C_{s2}} = \frac{1}{\omega C_{p2}}$	$X = \omega L_2 = \frac{1}{\omega C_{p2}}$	$X = \omega L_2 - \frac{1}{\omega C_{s2}} = \frac{1}{\omega C_{p2}} = \omega L_{s2}$

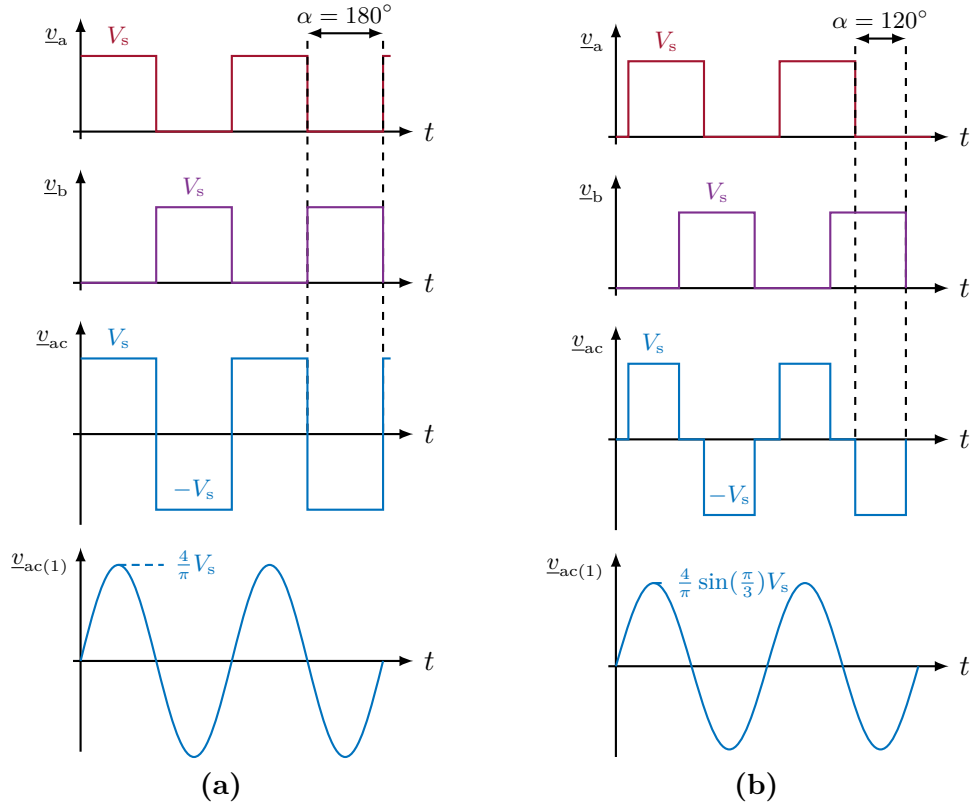


Figure 2.17 – H-bridge inverter waveforms with (a) $\alpha = 180^\circ$ and (b) $\alpha = 120^\circ$.

If only the fundamental wave is considered, the output voltage V_{in} can be calculated as a function of the conduction angle and input voltage:

$$V_{in} = \frac{2\sqrt{2}}{\pi} \sin\left(\frac{\alpha}{2}\right) V_{DC}. \quad (2.35)$$

In some cases, the phase shift control is used as a control method to vary the output voltage as seen in Eq. (2.35) under conditions where the DC bus cannot be lowered. When α is set to 120° , this condition results in the lowest Total Harmonic Distortion (THD) in the voltage and current waveforms [97] and the waveforms are shown in Fig. 2.17b. Under these conditions, it is more difficult to achieve ZVS.

Other ways to control the coil current (or output voltage) are to change the bus voltage V_{dc} or the duty cycle D or the conduction angle α , which is basically a control of the primary quality factor. However, these control methods are not necessarily the most efficient.

For most of the thesis, only the fundamental wave is needed, which allows the inverter to be modeled as an ideal sinusoidal voltage source where Eq. (2.35) is used to calculate the voltage \underline{v}_{in} . This approach neglects switching losses and this will be discussed in detail in Chapter 5.

2.2.5 Primary Compensation

As mentioned above, the goal of the inverter is to supply current to the primary coil, and the primary side compensation (or tuning) network is used to match the input impedance of the

resonant inverter to the resonant load (secondary side). This is necessary to ensure that the system operates at or near resonance, which reduces the reactive load seen by the inverter, which in turn reduces the ratings of the switches and therefore cost and space [68].

Without a compensation network, the input impedance of the resonant inverter may not match the resonant load impedance, resulting in poor power transfer efficiency, increased losses, and potential damage to circuit components. The compensation network is designed to provide the necessary reactive components to achieve impedance matching between the inverter and the load and to maintain resonance over a range of load conditions. In addition, it acts as a natural bandpass filter, making the square wave more sinusoidal, allowing for the approximation of considering only the fundamental, and also reducing Electromagnetic Interference (EMI) [68].

The design of the compensation network depends on several factors, including the resonance frequency of the coils, the load resistance, and the coupling coefficient between the primary and secondary coils. In general, the compensation network consists of a series or parallel resonant network tuned to match the resonance frequency of the coils and achieve maximum power transfer efficiency.

As mentioned above, it is not possible to use a parallel network directly when using a voltage source inverter. There are solutions that require current source topologies, transformers with DC blocking caps (large) or push-pull inverters, and many others, but these are beyond the scope of this thesis (see [68] for more background information). The three topologies considered for primary tuning in this paper are series, LCL and LCC, as shown in Fig. 2.18.

One of the most important considerations in primary tuning is the effect of the reflected impedance Z_{refl} . The reflected impedance is the impedance seen by the primary coil due to the presence of the receiver coil, and is a function of the coupling coefficient between the two coils as well as the secondary side tuning or load impedance.

Series tuning (Fig. 2.18a) is often used because it is simple and ZVS can be easily achieved. The primary coil current can be calculated as

$$\dot{i}_1 = \frac{v_{\text{in}}}{j\omega L_1 + \frac{1}{j\omega C_{s1}} + Z_{\text{refl}}} \quad (2.36)$$

and if resonance ($\omega L_1 = \frac{1}{\omega C_{s1}}$) is achieved then the current can be simplified to

$$\dot{i}_1 = \frac{v_{\text{in}}}{Z_{\text{refl}}}. \quad (2.37)$$

The primary current is controlled by the reflected impedance, and if Z_{refl} varies greatly, as it does when using different secondaries (Δk), it will affect the tuning points and may be difficult to control or achieve constant power transfer. When no load is present, the primary current is infinite, so this must be avoided or the components may be damaged. In addition, the harmonics introduced in a series-tuned coil can be very large (reflected from the secondary) [97].

This can be avoided with a different tuning topology. In an LCL tuned circuit, as shown in Fig. 2.18b, the primary current is independent of the load. Under resonance conditions ($\omega L_1 = \frac{1}{\omega C_{s1}} = \omega L_{s1}$), the bridge current only has to supply the real power (if the secondary is ideally tuned) and can be calculated as follows

$$\dot{i}_{\text{in}} = \frac{v_{\text{in}} Z_{\text{refl}}}{\omega^2 L_1^2}. \quad (2.38)$$

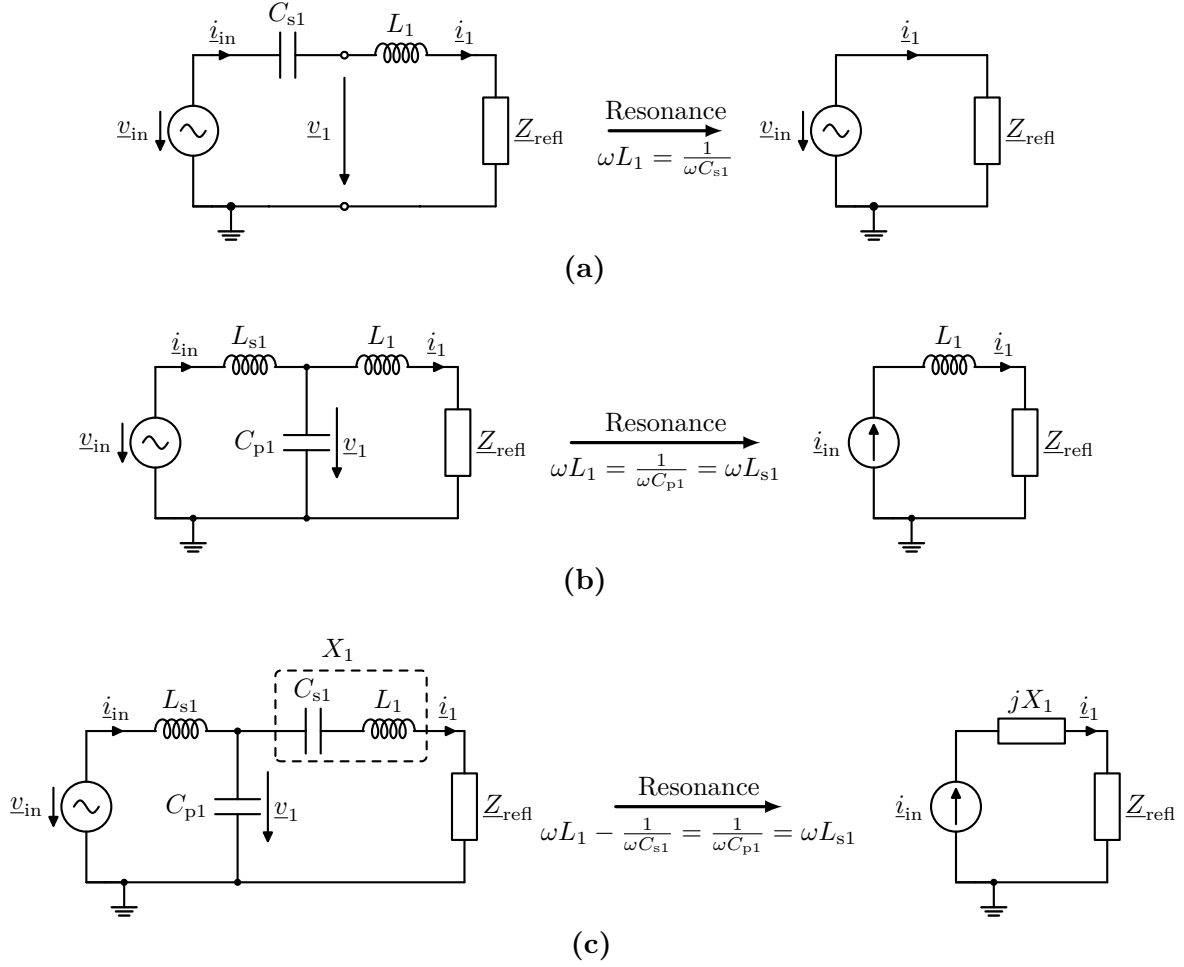


Figure 2.18 – Primary compensation networks, (a) series tuning, (b) LCL tuning and (c) LCC tuning.

The primary coil current can then be derived as

$$\dot{i}_1 = \frac{v_{in}}{j\omega L_1} \quad (2.39)$$

and it can be seen that the coil current is independent of the load. The topology allows the inverter to act as a current source to the primary coil. In addition, the LCL tuning results in the primary current having a low THD, regardless of the secondary side [97].

If the LCL topology is used and an additional current boost is required (due to V_{in} constraints), the LCC topology (Fig. 2.18c) can be used. This will either allow a larger primary current for the same inverter voltage as the resonance condition and the reactance seen by the parallel capacitor is now $\omega L_1 - \frac{1}{\omega C_{s1}} = \omega L_{s1} = \frac{1}{\omega C_{p1}}$ or allows to drive the same current with a lower inverter voltage compared to LCL tuning [97]. The current can then be calculated as

$$\dot{i}_1 = \frac{v_{in}}{j\omega L_1 - \frac{1}{j\omega C_{s1}}}. \quad (2.40)$$

To deal with variations in coupling or reflected impedance or self-inductance, active tuning can be used, which adjusts the tuning values to achieve resonance over a wide range. This is discussed in detail in the Chapter 6.

2.2.6 Magnetic Coils

As mentioned in Chapter 1, the coupling between the coils is based on the principle of electromagnetic induction. When an AC current is passed through a transmitter coil, in this case the primary side, a magnetic field develops around this coil. When a receiver (secondary coil) is placed in the vicinity of the magnetic field, the coil captures the magnetic flux and induces a voltage that drives a current. Thus, electrical energy is transferred from the primary to the secondary via magnetic field coupling, similar to a transformer.

Depending on the position and relatively high air-gap, the coils in an EV charger are usually loosely coupled, which means that only a fraction of the magnetic flux is captured. In general, a distinction is made between the main flux, which determines the energy transfer, and the leakage flux, which does not participate in the energy transfer and should be avoided, especially in the proximity of humans.

The magnetic flux in a coil depends on the magnetic field flux density \vec{B} and the coil area \vec{A} and can be calculated as

$$\Phi = \iint \vec{B} d\vec{A}, \quad (2.41)$$

while the magnetic flux density is related to the magnetic field \hat{H} generated by the AC current through the coil (Maxwell's equations). The magnetic flux density depends on the material and its properties (relative permeability μ_r) in which it is distributed:

$$\hat{B} = \mu_0 \mu_r \hat{H}. \quad (2.42)$$

Consequently, magnetic materials with high permeability, such as ferrite, are used to increase the flux density.

Using Faraday's law, the induced voltage in a coil can be calculated as

$$v = N \frac{d\Phi}{dt} \quad (2.43)$$

where N is the number of the winding turns.

The inductance of a coil is defined as

$$v = L \frac{di}{dt} \quad (2.44)$$

and with Eq. (2.43) it can be seen that the inductance is the ratio between magnetic flux linkage $\Psi = N\Phi$ and the current i :

$$L = \frac{N\Phi}{i}. \quad (2.45)$$

If the current and magnetic field come from the same coil, L is referred to as self-inductance. If the magnetic flux couples to another coil, the ratio of the current (from the other coil) to the flux from the source coil is called the mutual inductance M .

The magnetic flux through a coil can then be distinguished by the sources:

$$\Psi_1 = \Psi_{11} + \Psi_{12} = N_1\Phi_{11} + N_2\Phi_{12} = L_1 \cdot i_1 + M \cdot i_2 \quad (2.46)$$

$$\Psi_2 = \Psi_{22} + \Psi_{21} = N_2\Phi_{22} + N_1\Phi_{21} = L_2 \cdot i_2 + M \cdot i_1 \quad (2.47)$$

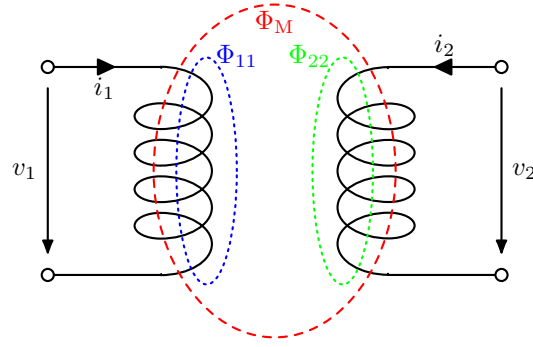


Figure 2.19 – Fundamental flux coupling principle.

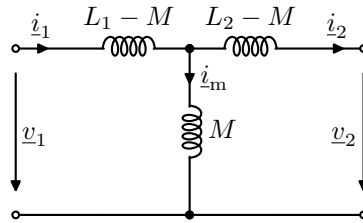


Figure 2.20 – Equivalent circuit of coupled coils based on the T-transformer representation.

with $\Psi_{12} = \Psi_{21} = \Psi_M$.

The differential voltage equations for coupled coils as shown in Fig. 2.19 can then be calculated as

$$v_1(t) = R_1 \cdot i_1(t) + \frac{Nd\Phi_1}{dt} = R_1 \cdot i_1(t) + L_1 \cdot \frac{di_1(t)}{dt} + M \cdot \frac{di_2(t)}{dt} \quad (2.48)$$

$$v_2(t) = R_2 \cdot i_2(t) + \frac{Nd\Phi_2}{dt} = R_2 \cdot i_2(t) + L_2 \cdot \frac{di_2(t)}{dt} + M \cdot \frac{di_1(t)}{dt} \quad (2.49)$$

which can then be represented as a T-transformer circuit, as shown in Fig. 2.20.

An important metric for quantifying coupling quality is the ratio of the leakage flux to the main flux, also known as the coupling factor k which can be calculated as

$$k = \frac{M}{\sqrt{L_1 L_2}}. \quad (2.50)$$

This metric is very important because it quantifies the amount of power being transferred across the air-gap by the coils.

The magnetic material and air-gap cannot be changed, so the coupling will be low, but the shape of the coils can be adjusted to alter the field and improve coupling and unwanted leakage flux. Factors such as size, area, material, and shape play a significant role in determining the level of coupling, and extensive research has been conducted on this topic. Among the single coil topologies, the Circular Pad (CP) and DDP are the most commonly used and are shown in Fig. 2.21a and Fig. 2.21b, respectively. While numerous other topologies exist, this thesis focuses on the CP and DDP, and a brief overview of multi-coils and other topologies will be provided in Chapter 4.

The common structure is to have an aluminum shield at the bottom for shielding purposes, shown in gray. The ferrite layer above the shield, shown in black, is for proper flux guidance

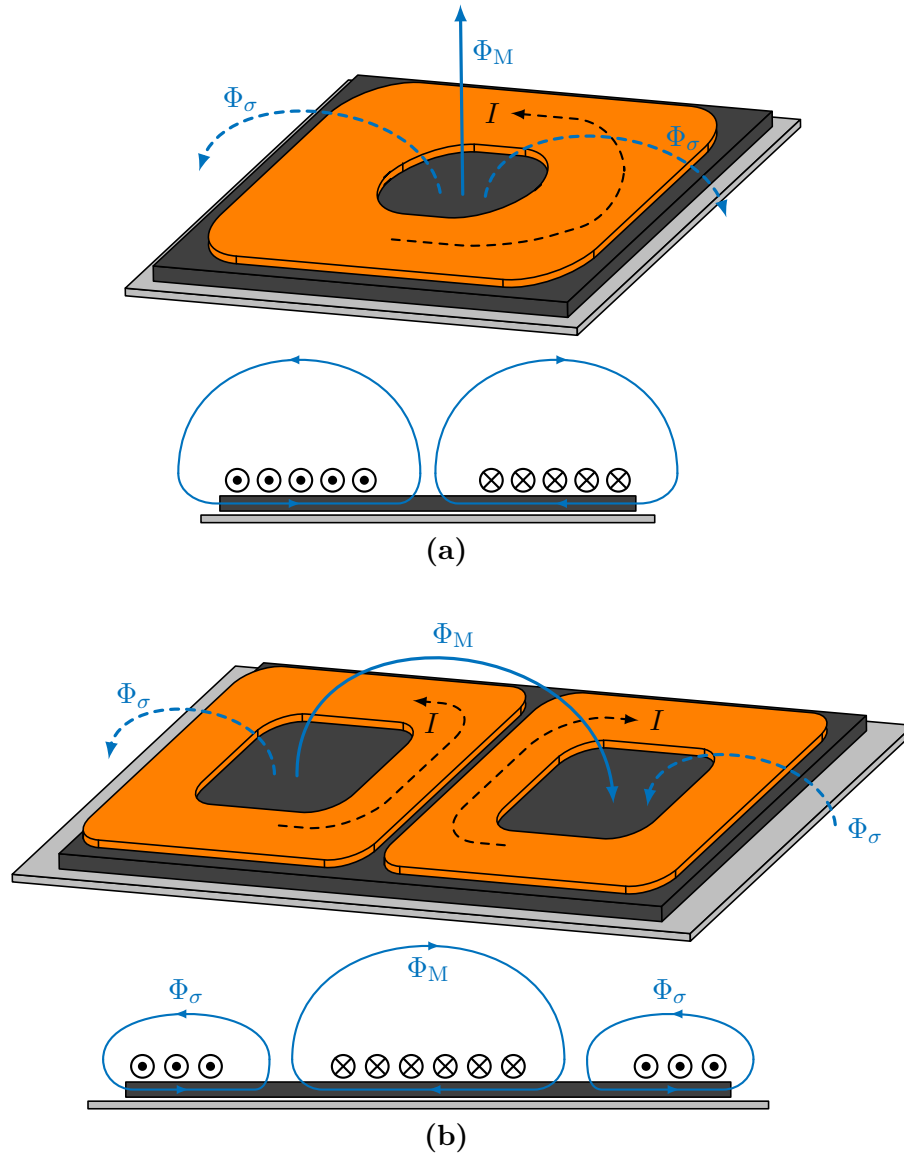


Figure 2.21 – 3D perspective and cross-sectional view of the (a) CP and (b) DDP topologies.

and coupling increase and is also a topic in the literature [98–101]. Other materials are possible (e.g. nanocrystalline [102], soft magnetic composite (SMC) [103, 104]) for reasons of cost, robustness or weight and research is ongoing in this area, but throughout the thesis ferrite is assumed since it is most common and has low loss. It has a high permeability and usually saturation can be neglected, which is done in this thesis. Therefore a high and constant μ_R is assumed.

The shape of the ferrite must match the flux distribution and there are two main field types, polarized (DDP) and non-polarized (CP), often referred to as unipolar and bipolar structures. They refer to the field distribution as shown by the blue arrows. The CP has one pole in the center, whereas the DDP has two poles with different polarization, so that the main flux goes from one pole to the other. These principles are fundamentally different and lead to interoperability problems, since two different coils will not couple to each other

when aligned at their centers, because they do not see their respective fields. More on coil interoperability will be discussed in Chapter 4.

The CP creates a single sided vertical flux due to the ferrite layer underneath, and the main flux is perpendicular to the main area of the coil. The main flux is in the center of the coil, as such a similar receiver should be placed to capture the flux, which decreases with increasing height (Biot-Savart equation, i.e. see [105]).

The DDP consists of a single figure eight, which can be thought of as two circular/rectangular coils connected in such a manner that each coil has a different current direction. As a result, the main flux is parallel to the main coil surface. Since the field has a direction (x, y) , it is a polarized field. The pole pitch is an important design metric because it determines the height of the flux and therefore the coupling capability [106].

The top layer consists of litz-wire and is the most important part since the $N \cdot I$ generation of the coil creates the field. Due to the high frequency, it is necessary to use litz-wire to reduce skin and proximity effect losses. The main parameters are the number of strands, the diameter of the winding, the number of turns and the area that is covered. Inductance L is determined by the coil winding and is a key metric in power transmission because it affects many other different system parameters. In addition, it affects several economic issues such as weight and cost etc., but this is not the main interest of this thesis.

A good magnetic design comprises a stable coupling factor and inductance, but there are so many different applications and requirements that a universal design or recommendation is not possible.

As can be seen, the coils produce leakage flux and this is an important aspect of the investigation in IPTS as there are safety rules, details on this are discussed in Chapter 4.

2.3 Practical Considerations and System Simplifications

This section presents a summary of the previously derived aspects of each component and simplifies the IPTS to enable circuit analysis. This simplification is necessary because the complexity of the system makes it difficult to study otherwise.

First, this section details the FHA and its assumptions. Next, the simplified circuit topology is derived and the nomenclature used in the analysis is introduced. In addition, this section provides the transfer function of the IPTS and the impedances and efficiency calculations in a generalized form suitable for interoperability studies.

2.3.1 First Harmonic Approximation

The FHA is a common simplification used in IPTS analysis. This approximation is based on the assumption that the current and voltage waveforms are near resonance and sufficiently filtered to be sinusoidal. As a result, the circuit is assumed to behave as if it were driven by a single frequency waveform, which is the fundamental switching frequency.

This approximation is justified for IPTSs because the harmonics have much higher frequencies and, as mentioned earlier, are generally filtered out by the circuit components, such as the inductors and capacitors in the tuning networks, which have low band-pass characteristics. As a result, the FHA can be used to simplify the analysis of the IPTS by ignoring the higher harmonic components and focusing on the fundamental frequency characteristics. This simplification is especially useful when designing or optimizing WPT systems, as it allows for faster and more calculations.

However, it is important to keep in mind that this approximation may not be accurate in all cases. Higher-order harmonics can affect the behavior of the circuit, especially in LCC tuned systems. Additionally, the following assumptions are made during the analysis:

- Steady-state conditions are assumed, and as such, transients and system dynamics are disregarded.
- The components of the WPT system are considered to be ideal, meaning that they have no losses and operate at their rated values.
- Continuous Conduction Mode (CCM) is assumed.
- Equivalent source resistance of the tuning components are neglected.
- The grid and PFC are considered ideal and behave like a DC voltage source.
- Saturation effects are neglected and components are assumed to be constant and linear.

As described earlier, this allows the rectifier stage to be simplified to an AC resistor R_{ac} and the inverter to be modeled as an ideal sinusoidal voltage source \underline{v}_{in} . In total, all assumptions allow the IPTS circuit shown in Fig. 2.1 to be simplified as shown in Fig. 2.22 for an LCC–LCC tuned system.

Although good results can be obtained with FHA, a detailed loss study that includes the switches is not possible, and the implications of this for system design are discussed in Chapter 5.

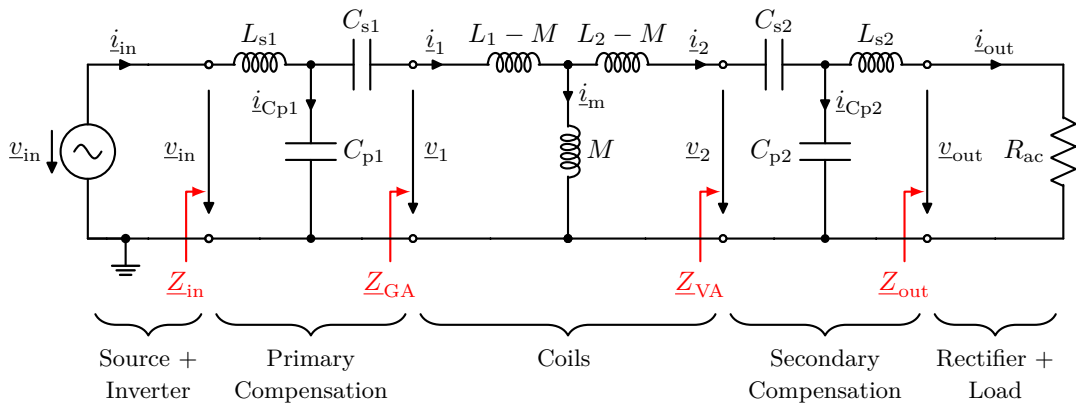


Figure 2.22 – Simplified IPTS circuit topology for an LCC–LCC tuned system.

2.3.2 Full Circuit Analysis

In order to analyze the system in Fig. 2.22, a discussion of nomenclature is necessary.

Since circuit analysis does not necessarily imply that the system is in resonance (especially when there are variations such as Δf , ΔL , or ΔC), changes in these variables and their implications are examined. Furthermore, it is not sufficient to use RMS values, as was done in the previous sections for reasons of simplification. A generalized description is required, so proper complex vectors are used. Thus, AC voltages and currents are defined as

$$\underline{v}_{ac} = \hat{V} \cdot e^{j(\omega t + \varphi_v)} = \sqrt{2} \cdot \underline{v} \cdot e^{j\omega t} \quad (2.51)$$

$$\underline{i}_{ac} = \hat{I} \cdot e^{j(\omega t + \varphi_i)} = \sqrt{2} \cdot \underline{i} \cdot e^{j\omega t} \quad (2.52)$$

where the AC voltage and current phasors (in steady state the $e^{j\omega t}$ parts of the phasors can be eliminated) are described by

$$\underline{v} = V \cdot e^{j\varphi_v} \quad (2.53)$$

$$\underline{i} = I \cdot e^{j\varphi_i} \quad (2.54)$$

with V and I representing the RMS values. φ_v and φ_i describe the phase angles of each phasor. The apparent power \underline{S} , the active power P and the reactive power Q are then given as stated in Eq. (2.1), (2.2) and (2.3) with $\varphi = \varphi_v - \varphi_i$.

In the case of the inverter input impedance \underline{Z}_{in} from Fig. 2.22, this impedance can be described as

$$\underline{Z}_{in} = \frac{\underline{v}_{in}}{\underline{i}_{in}} = \frac{V_{in} \cdot e^{j\varphi_v}}{I_{in} \cdot e^{j\varphi_i}} = \frac{V_{in}}{I_{in}} \cdot e^{j(\varphi_v - \varphi_i)} = Z_{in} \cdot e^{j\varphi_{in}} = R_{in} + jX_{in}. \quad (2.55)$$

where $R_{in} = \text{Re}(\underline{Z}_{in})$ and $X_{in} = \text{Im}(\underline{Z}_{in})$. φ_{in} describes the phase angle of the input impedance seen by the inverter, while in general the phase angle of any impedance is described by $\varphi_z = \varphi_v - \varphi_i$.

Transfer Function

The transfer function is used in the analysis of the IPTS because it provides a mathematical characterization of its behavior and relates the input to the output of the system. By using transfer functions, the response of the system to various inputs, such as changes in load, resonant frequency, or coupling coefficient, can be analyzed and optimized. In addition, such transfer functions can be used to determine the stability, bandwidth, and other important parameters of an IPTS that are critical to its design and operation.

Each transfer function varies depending on the system topology, and since interoperability is of interest, a generalized approach is derived and illustrated by a series-series (S-S) tuned example shown in Fig. 2.23.

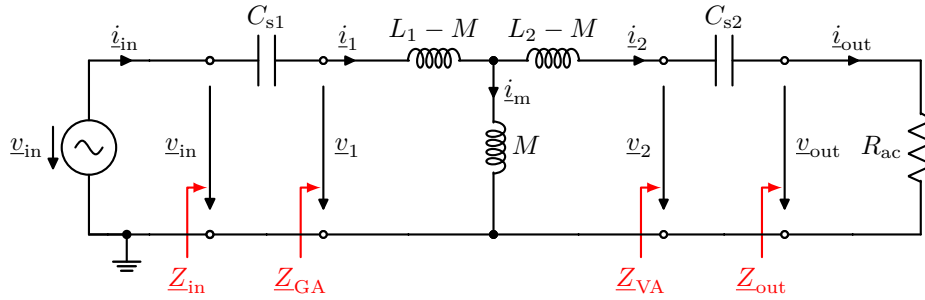


Figure 2.23 – Simplified IPTS circuit topology for a series-series tuned system.

In order to present the load defined by V_{bat} and P_{out} to the primary, while taking into account the variation in secondary tuning topologies, the \underline{Z}_{VA} impedance is introduced. This impedance summarizes all secondary electronics (VA) and was first defined in [107], as will be discussed in Section 2.5. In the case of a series tuned secondary, the impedance is defined as

$$\underline{Z}_{VA} = \underline{Z}_{Cs2} + R_{ac} \quad (2.56)$$

with $\underline{Z}_{Cs2} = \frac{1}{j\omega C_{s2}}$.

Table 2.3 – Expressions for \underline{Z}_{VA} and \underline{Z}_{in} for Different Secondary and Primary Tunings

Tuning Topology	\underline{Z}_{VA}	\underline{Z}_{in}
Series	$\underline{Z}_{Cs2} + R_{ac}$	$\underline{Z}_{Cs1} + \underline{Z}_{GA}$
Parallel	$\frac{\underline{Z}_{Cp2}R_{ac}}{\underline{Z}_{Cp2} + R_{ac}}$	–
LCL	$\frac{\underline{Z}_{Cp2}(\underline{Z}_{Ls2} + R_{ac})}{\underline{Z}_{Cp2} + \underline{Z}_{Ls2} + R_{ac}}$	$\underline{Z}_{Ls1} + \frac{\underline{Z}_{Cp1}\underline{Z}_{GA}}{\underline{Z}_{Cp1} + \underline{Z}_{GA}}$
LCC	$\underline{Z}_{Cs2} + \frac{\underline{Z}_{Cp2}(\underline{Z}_{Ls2} + R_{ac})}{\underline{Z}_{Cp2} + \underline{Z}_{Ls2} + R_{ac}}$	$\underline{Z}_{Ls1} + \frac{\underline{Z}_{Cp1}(\underline{Z}_{Cs1} + \underline{Z}_{GA})}{\underline{Z}_{Cp1} + \underline{Z}_{Cs1} + \underline{Z}_{GA}}$
Partial-Series	$\underline{Z}_{Cs2} + \frac{\underline{Z}_{Cp2}R_{ac}}{\underline{Z}_{Cp2} + R_{ac}}$	–

An overview of all \underline{Z}_{VA} impedances is given in Tab. 2.3 with all impedances being $\underline{Z}_{Ls1} = j\omega L_{s1}$, $\underline{Z}_{Cs1} = \frac{1}{j\omega C_{s1}}$, $\underline{Z}_{Cp1} = \frac{1}{j\omega C_{p1}}$, $\underline{Z}_{L1} = j\omega L_1$, $\underline{Z}_{L2} = j\omega L_2$, $\underline{Z}_M = j\omega M$, $\underline{Z}_{Ls2} = j\omega L_{s2}$ and $\underline{Z}_{Cp2} = \frac{1}{j\omega C_{p2}}$.

To study the effect of magnetics separately, the \underline{Z}_{GA} impedance can be used, which describes the total impedance seen by the primary compensation. This consists of the primary self-inductance and the reflected impedance as discussed in the previous section. The impedance can be calculated with one equation independent of the secondary tuning when \underline{Z}_{VA} is used:

$$\underline{Z}_{GA} = j\omega L_1 + \underline{Z}_{refl} = j\omega L_1 + \frac{\omega^2 M^2}{j\omega L_2 + \underline{Z}_{VA}}, \quad (2.57)$$

and in the case of an ideal series tuned system, the reflected impedance would be $\underline{Z}_{refl} = \frac{\omega^2 M^2}{R_{ac}}$.

It has to be noted that the AC-resistances of the coils are not shown in this study but can easily be added in series with the self inductances.

The total impedance \underline{Z}_{in} seen by the primary inverter can then be calculated and depends on the chosen tuning topology and the load presented to the primary electronics by the coils \underline{Z}_{GA} . The equations for all impedances are given in Tab. 2.3.

Continuing with the example from Fig. 2.23, the total impedance \underline{Z}_{in} in an ideal series-series tuned system would be $\underline{Z}_{in} = \underline{Z}_{refl} = \frac{\omega^2 M^2}{R_{ac}}$ since each inductance is canceled out. The impedances for all other tuning combinations can now be calculated in a similar way.

To derive the transfer function in a generalized way it is more helpful to derive the current ratios $Y_1 = \frac{i_{in}}{i_1}$, $Y_2 = \frac{i_1}{i_2}$ and $Y_3 = \frac{i_2}{i_{out}}$ and the results are listed in Tab. 2.4 for Y_1 and Y_3 for all tuning topologies. Y_2 can be calculated independently of the tuning as

$$Y_2 = \frac{i_1}{i_2} = \frac{j\omega L_2 + \underline{Z}_{VA}}{j\omega M} \quad (2.58)$$

The transfer function is defined here as the output to input voltage gain

$$G = \left| \frac{v_{out}}{v_{in}} \right| = \left| \frac{R_{ac} \cdot i_{out}}{\underline{Z}_{in} \cdot i_{in}} \right| \quad (2.59)$$

and with $i_{in} = Y_1 i_1 = Y_1 Y_2 i_2 = Y_1 Y_2 Y_3 i_{out}$ it can be derived to:

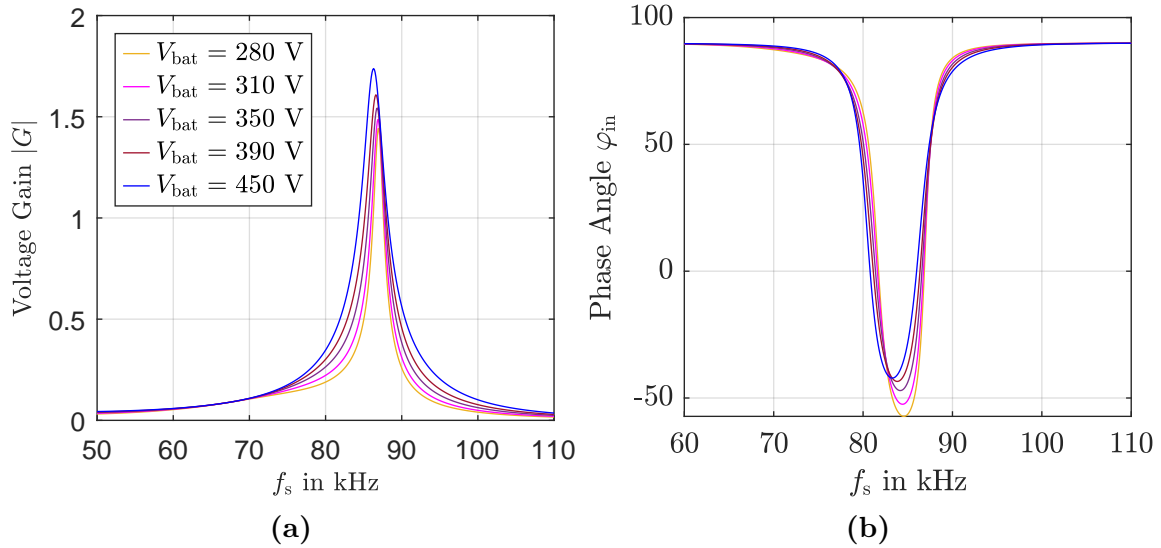
$$G = \left| \frac{R_{ac}}{\underline{Z}_{in}} \cdot \frac{1}{Y_1 Y_2 Y_3} \right|. \quad (2.60)$$

Table 2.4 – Expressions of the Current Ratios for Different Secondary and Primary Tunings

Tuning Topology	Y_1	Y_3
Series	1	1
Parallel	–	$\frac{R_{ac}}{Z_{VA}}$
LCL	$\frac{Z_{GA}}{Z_{in} - Z_{Ls1}}$	$\frac{Z_{Ls2} + R_{ac}}{Z_{VA}}$
LCC	$\frac{Z_{Cs1} + Z_{GA}}{Z_{in} - Z_{Ls1}}$	$\frac{Z_{Ls2} + R_{ac}}{Z_{VA} - Z_{Cs2}}$
Partial-Series	–	$\frac{R_{ac}}{Z_{VA} - Z_{Cs2}}$

With the relations from Tab. 2.1 and Eq. (2.35) the DC-DC ratio can be derived. This is effectively a function of the system parameters and the frequency and can now be used in many ways.

Typically, a Laplace transformation is performed and the system is studied in the frequency domain (ZVS range, required input voltage, frequency ranges, etc.), as was done in [75, 78, 108, 109], for example. As an illustration, the magnitude and phase for the system from the next chapter are shown in Fig. 2.24 for different EV battery voltages.


Figure 2.24 – Example of a transfer function for different loads (battery voltages) in the frequency domain, (a) magnitude and (b) phase.

Efficiency

With the results from the previous section, the input and out power of the circuit can be calculated as

$$P_{\text{in}} = \text{Re}(\underline{Z}_{\text{in}}) \cdot |\dot{i}_{\text{in}}|^2 \quad (2.61)$$

$$P_{\text{out}} = R_{\text{ac}} \cdot |\dot{i}_{\text{out}}|^2 \quad (2.62)$$

This allows the efficiency of the system to be derived to

$$\eta = \frac{P_{\text{out}}}{P_{\text{in}}} = \frac{R_{\text{ac}}}{\text{Re}(\underline{Z}_{\text{in}})} \cdot \frac{1}{(Y_1 Y_2 Y_3)^2} \quad (2.63)$$

It has to be noted that various assumptions have been made and many losses have been neglected. Consequently, this simplified analysis results in high efficiency values. However, it can still provide reasonable approximations and useful insights into the behavior of the IPTS in terms of how design changes such as power or voltage limits affect operation.

2.4 Simulation Tools

The many components comprising an IPTS can be complex, making analytical analysis difficult or impossible. Therefore, simulation tools are commonly used to aid in the design and analysis of such systems. This section provides a brief overview of the necessary simulation tools and methods used in this thesis.

Typically, an IPTS can be divided into a magnetic and an electrical domain. Finite-Element-Method (FEM) is used for the magnetic domain, while the circuit operation can be calculated analytically or evaluated using physical simulation tools such as PLECS, LTspice or Simscape.

FEM is a numerical technique that can be used to solve partial differential equations, such as those encountered in electromagnetics, and is useful for analyzing the magnetic fields in an IPTS. FEM simulations can provide insight into magnetic field distributions and losses, as well as assist in the design and optimization of magnetic components such as coils and magnetic cores. Additionally, FEM simulations are used to investigate the coupling coefficient and the mutual and self-inductance of the coils, which are important factors affecting the efficiency and power transfer capability of the IPTS. In general, FEM simulations are time consuming because 3D models are required to account for positional tolerances. In this thesis, ANSYS Maxwell, an electromagnetic field simulation software, is used to obtain the magnetic parameters such as inductances and leakage flux fields to feed the transformer in the circuit analysis.

FEM simulation can also be used to study EMI and Electromagnetic Compatibility (EMC) issues as well as core, coil and eddy current losses. However, obtaining reliable results of these is very difficult as they depend on many factors in reality, such as temperature, manufacturing, saturation and loss. Hence, these are out of scope of this thesis.

The simplified circuit analysis shown in the previous section can theoretically be done by hand. In this thesis, a script-based approach is used in the MATLAB software. Computer-aided circuit analysis provides the ability to test different design scenarios and evaluate their impact on the performance of an IPTS. This helps in optimizing the design of the system for maximum efficiency and performance.

Another advantage of computer-aided circuit analysis is the ability to perform sensitivity analyses to determine the effect of component variations and environmental factors on system

behavior. This is particularly important for IPTSs, where performance is highly dependent on the coupling between the primary and secondary coils, as well as the operating frequency.

As already mentioned, FHA provides reasonably good first results, but when the design process moves to the detailed design of a real system, it is inevitable to include the impact of the inverter and rectifier and their (non-linear) switches. Therefore, physical simulation tools such as LTspice, PLECS or Simscape can be used. In this thesis, PLECS, a toolbox within MATLAB Simulink, is used.

PLECS allows a more detailed analysis of a circuit compared to FHA. By taking into account the switches, a more accurate analysis is possible. In addition, changes in duty cycle, harmonic effects, transient response, voltage and current ripple and waveforms, and ZVS (generally losses) can be studied with this simulation method.

Compared to the FHA approach, this method is more time-consuming, but it is inevitable when losses are of interest, as will be shown in Chapter 5.

Finally, validation of all simulation models is necessary to ensure that the simulation results accurately represent the behavior of the real system. Simulation models are based on mathematical equations and assumptions that may not always reflect the actual behavior of the physical system. As such, it is important to validate the simulation models to ensure that they can be used to accurately predict the behavior of the real IPTS under different conditions.

Validation of simulation models can be done by comparing the simulation results with experimental measurements of the physical system. If the simulation results agree with the experimental measurements, then the simulation model is considered to be validated. This validation process helps build confidence in the simulation results and ensures that the simulation model can be used to make accurate predictions about the behavior of the physical system under different conditions. This is undertaken in the Chapters 5 and 7.

2.5 Interoperability Aspects

This chapter presented the various components of which an IPTS consist. In the design process, there are many variations caused by either unintentional tolerances or intentional choices. These decisions are based on multiple factors such as design space, physical aspects, regulatory issues, cost, weight, complexity, the chosen application, marketing, corporate branding, and many more. All of these aspects have some level of impact on system behavior.

If the infrastructure side and the vehicle side develop their systems independently, the risk of creating incompatible or non-interoperable systems is high. A common basis or set of rules for interoperability is essential to avoid the development of proprietary systems that exist in parallel. Otherwise, the issues that arose with conductive charging may be repeated, as shown in Fig. 1.8. Ideally, this should be avoided or it would make WPT for EV charging unattractive.

To avoid this, standardization in the broader sense (not just interoperability, but other rules as well) is needed, and the state of the art will be discussed in the next section.

Regulating every aspect would discourage innovation and creativity and thus impede the development of technology for this application. This makes standardization a balancing act. There are unavoidable tolerances and variations, such as different air-gaps for a sports car and an SUV, so interoperability must be addressed within the standards in a non-restrictive way that still allows freedom of design so that the best solution for the technology can evolve.

Standardization provides a ready framework for interoperability, but it is the goal of this thesis to shed some insight on these interoperability aspects and to provide a scientific method that addresses the mentioned aspects. Therefore, this section also reviews the state of the art on interoperability studies at the start of this thesis and shows the description of interoperability at the beginning, which provided the guidelines for the developed methods in the following chapters.

2.5.1 Standardization

There are different standards and standardization groups related to WPT, depending on region and scope. The two most important standards for this thesis are ISO 61980-3 [110] and SAE J2954 [50], both of which were in development at the begin of this thesis and are in place since October 2020. There is a lot of overlap in the content of the two standards, as people are either on both committees or work closely together, so the rest of the thesis will only focus on SAE J2954¹. A brief summary of the main provisions and definitions is given in the next subsection and can also be found in [111].

SAE J2954 (and other standards) have been developed, but have focused separately on LD and HD applications. Initially, the focus was on power levels (≤ 11.1 kVA) for LD vehicles covered by SAE J2954, while on the other hand, higher power levels (≥ 60 kW) are being targeted for HD vehicles covered by SAE J2954/2, a standard that is under development at the end of this thesis and a draft (Technical Information Report, TIR) was released in December 2022 [112]. Since only the LD version is currently active, the WPT for EV is only regulated up to 11.1 kVA and the scope of this thesis is on the development on LD vehicles, but the method will be applicable for higher power as will be shown in Chapter 6.

In addition, IPTS must comply with many other regulations and standards such as International Commission on Non-Ionizing Radiation Protection (ICNIRP) [113], CISPR 11 [114], Communications [115] and many more. The additional required regulations are all referenced within SAE J2954, so they will be included as well, with the exception of ICNIRP since the leakage flux will be of particular interest in later chapters.

SAE J2954

To enable IPTS for EV charging, a common understanding of the details is required. Many definitions are made within the SAE J2954 standard, and the nomenclature introduced here is taken from [50]. The normalized frequency has been set to 85 kHz with a frequency range of 79–90 kHz.

Other topics as communications, FOD, LOP, and positioning systems (basically all ancillary systems) are also defined in [50], but are beyond the scope of this thesis. Further literature regarding these topics can be found in [9, 53, 116].

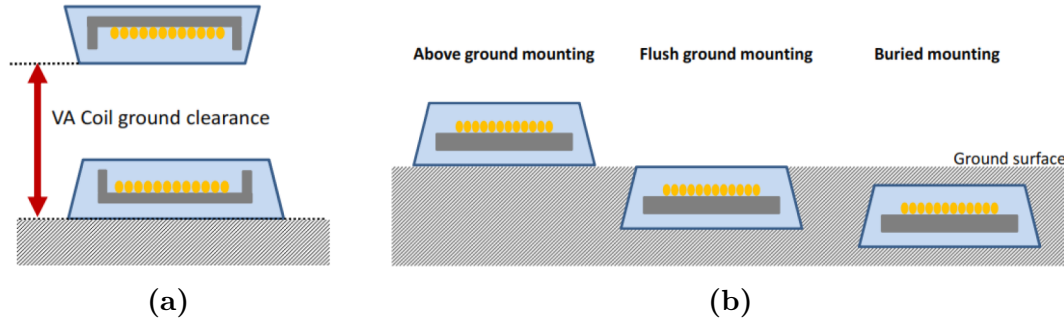
WPT Power Classes The power transfer level is defined by the maximum power drawn from the grid in volt-amps (VA), and Tab. 2.5 lists the defined power classes, noting that WPT4 and WPT5 are only listed as under consideration for future versions of this standard. As previously mentioned, WPT is only regulated up to 11.1 kVA or WPT3 at the end of this thesis². Therefore, anything above WPT3 will be referred to as “high power”.

¹This also includes other standards such as GB/T 38775, which is applicable in China.

²SAE J2954/2 defines power levels from 20 kW to 500 kW (HD-WPT9) but also changed the definition from input kVA to delivered output power in kW.

Table 2.5 – SAE J2954 WPT Power Classifications

	WPT1	WPT2	WPT3	WPT4	WPT5
Maximum Input VA	3.7 kVA	7.7 kVA	11.1 kVA	22 kVA	60 kVA

**Figure 2.25** – SAE J2954 definitions of (a) ground clearance and (b) GA mounting types [50].

WPT Z-Classes The distance from the primary pad to the secondary pad is an important parameter for power transmission and is defined as the ground clearance, which is the distance between the ground surface and the lower surface of the VA coil. To classify different vehicle types and their ground clearance range, three Z-classes are defined by [50] and listed in Tab. 2.6.

Table 2.6 – SAE J2954 WPT VA Z-Classes

Z-Class	VA Coil Ground Clearance Range in mm
Z1	100 – 150
Z2	140 – 210
Z3	170 – 250

The definition of ground clearance for the Z-Class is illustrated in Fig. 2.25a and the coil-to-coil distance, which is an important parameter as it defines the coupling, depends on the mounting type of the Ground Assembly (GA). Different types are shown in Fig. 2.25b. Mostly above ground mounting is covered in the active standard, which will be the default assumption throughout this thesis.

Interoperability Classes On the GA side, there exist two interoperability classes with different requirements. This allows designers to distinguish between GAs intended for public use (Class I), which have more requirements to satisfy (such as being able to operate over the full VA ground clearance ranges), and GAs developed as proprietary systems or systems for a specific use (Class II), where fewer interoperability requirements are needed. The most significant requirements are the power level and efficiency expectations over specific Z-ranges.

Tab. 2.7 lists the requirements for Interoperability Classes I & II. As noted, the requirements for efficiency and alignment ranges are different, so the following sections also distinguish between the two classes, in Tables 2.8–2.10.

The scope of interoperability studies in this thesis, unless otherwise noted, focuses on Interoperability Class I, which is intended for public use and is more complex to design for interoperability.

Table 2.7 – Range of input kVA by Interoperability Class

Interoperability Class	Minimum Input kVA Rating	Maximum Input kVA Rating
Class I	1 kVA	11.1 kVA
Class II	1 kVA	specified by manufacturer

Alignment Tolerance As mentioned previously, the coupling is affected by both the Z-Class and the type of mounting. In addition, the coupling is also impacted by the misalignment of the coils, which is why the operating ranges are also limited. The different limitations for VAs and the different types of GAs are listed in Tab. 2.8.

In addition, there are requirements for VAs to operate over a certain range of roll, pitch, and yaw (2 deg, 2 deg, and 3 deg). These effects are minimal and are neglected in this thesis. An even alignment of the VA is always assumed.

Table 2.8 – SAE J2954 Operating Range Requirements

Offset direction	VA Offset in mm	GA Interoperability Class I Offset in mm	GA Interoperability Class II Offset in mm
ΔX	± 75	± 75	± 75
ΔY	± 100	± 100	± 100
Z range	manufacturer specification	all Z-classes	manufacturer specification

WPT Efficiency System efficiency is measured from the AC grid connection to the HV battery, and GA Interoperability Class I & II have different requirements. Tab. 2.9 shows the requirements for Class I GA systems. These efficiencies must be met across all the variations and requirements introduced above. Since they must cover the full power range, no distinction is made between power classes as is done for Class II and shown in Tab. 2.10. More details on the test specifications and requirements can be found in [50].

Table 2.9 – SAE J2954 Class I Minimum System Efficiency Requirements

WPT Class of Test VA	At Centered Position	In Alignment Tolerance Area
WPT1	80%	75%
WPT2	82 %	77 %
WPT3	85 %	80%

Table 2.10 – SAE J2954 Class II Minimum System Efficiency Requirements

WPT Class Difference of VA	At Centered Position and Over Alignment Tolerance Area
Same Power Class	80%
One Power Class Difference	77 %
Two Power Class Difference	75 %

WPT Reference Coils The appendix to SAE J2954 [50] provides reference coils that have been used for normative interoperability (and requirements) testing. If a GA designer wants to ensure the interoperability of a product, he must perform tests with all specified VAs and vice versa.

These reference systems are equipped with compensation networks and rectifiers or inverters, but for the purposes of this thesis, only the coils are being considered. An overview of these systems and their corresponding nomenclature, as used throughout this thesis, is presented in Tab. 2.11. All of the coils are circular in shape, and additional information can be found in [50].

Table 2.11 – SAE J2954 Reference Coil Overview

Annex	Type	Power Level	Z-Class	Nomenclature
A.1	VA	WPT1	Z1	SAE VA WPT1 Z1
A.2	VA	WPT1	Z2	SAE VA WPT1 Z2
A.3	VA	WPT1	Z3	SAE VA WPT1 Z3
A.4	VA	WPT2	Z1	SAE VA WPT2 Z1
A.5	VA	WPT2	Z2	SAE VA WPT2 Z2
A.6	VA	WPT2	Z3	SAE VA WPT2 Z3
A.7	VA	WPT3	Z1	SAE VA WPT3 Z1
A.8	VA	WPT3	Z2	SAE VA WPT3 Z2
A.9	VA	WPT3	Z3	SAE VA WPT3 Z3
B.1	GA	WPT1-3	Z1-Z3	SAE UGA WPT3

2.5.2 Impedance Planes

In order to ensure, regulate, or assess interoperability, a method to describe it is required, which is why SAE J2954 also contains an annex (J) to describe system interoperability. This section is based on the work of Hassler et al. [73, 107, 117] and serves as a baseline for this thesis.

This approach simplifies the system parameters behind the impedances, which allows for independent design without overly restricting the designer (e.g., providing normative inductances). The capabilities of the GA or VA provide different impedances and the area of all Operating Points (OPs) form an impedance zone or plane that can be driven by the system.

In order to do this, two impedance interfaces were introduced, the GA and VA interfaces, as shown in Fig. 2.26. The idea behind this approach is on the one hand to distinguish between

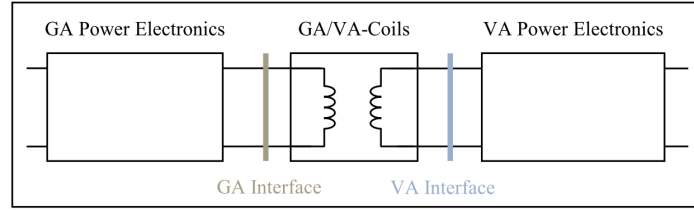


Figure 2.26 – Definition of the GA and VA impedance interfaces, taken from [107].

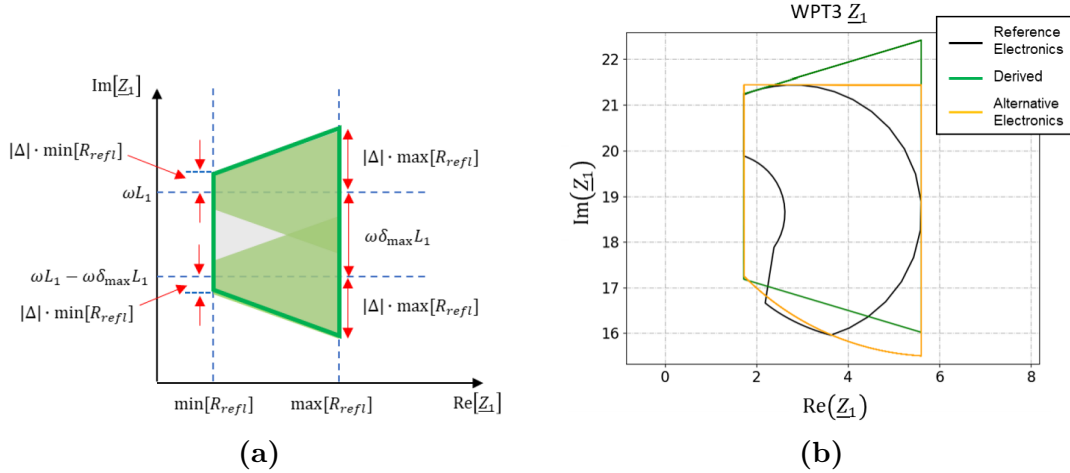


Figure 2.27 – SAE J2954 IPPs, (a) creation of an IPP, (b) GA reference planes [50].

magnetics and electronics, but also between GA and VA designers. Different VA electronics can be summarized in the VA impedance and, when tested with the reference electronics, mapped to the GA interface and vice versa. The normative GA and VA systems then provide impedance ranges that must be matched if interoperability is desired.

This approach allows design freedom and, as long as the reference impedance zone is matched at the GA and VA interface, interoperability is ensured. The Fig. 2.27 shows the creation of the impedance zone (Fig. 2.27a) and the GA reference IPP (Fig. 2.27b).

The focus of the previous work was to provide a regulatory framework to ensure interoperability testing procedures for standardization. As this work was the first attempt to quantify and assess interoperability, it left many gaps. Consequently, a methodical approach and investigation of the boundaries and consideration of many aspects (losses) still needed to be developed, which served as the main motivation for the work of this thesis.

2.6 Summary

This chapter has provided a comprehensive overview of the fundamental aspects of IPTSs for EV charging, with an emphasis on interoperability. In order to ensure the seamless operation of the IPTS with different EV models and charging infrastructures, the establishment of common standards and protocols is essential.

The chapter began with an explanation of the basics of IPTSs for EV charging, followed by a discussion of the various components of an IPTS. The impact of rectification, control and the different secondary tuning topologies were presented, along with their respective

advantages and limitations. The primary power supply and tuning networks were discussed in detail, including the functions and components used.

The basic principles of magnetic and resonant coupling, various coil topologies and their magnetic field distributions and sensitivities were also explained. Practical considerations to enable circuit analysis of the IPTS were introduced, and the transfer function and impedance calculations of the IPTS were provided in a generalized form for interoperability studies. The importance of simulation tools such as FEM and PLECS in the design and analysis of an IPTS was also highlighted.

Finally, interoperability issues that need to be considered in the design of an IPTS were described, with a focus on standardization and the existing IPP approach. This serves as a foundation for the next chapter, which develops this approach into a scientific design and evaluation methodology.

3 Design and Assessment Method for Interoperable IPT Systems Based on Impedance Planes

As presented in the previous chapter, interoperability introduces a certain complexity in IPTSs and their design. Interoperability is especially important in applications where proprietary systems are not feasible, such as wireless EV charging in public spaces. In addition, tolerances and parking offsets cannot be eliminated in wireless EV charging, and thus interoperability must be emphasized in the design of such systems.

The design of IPTSs is affected by many factors or design choices such as cost, third party requirements, regulations, available space in the EVs, corporate identity, preferred use-case and many more. These considerations lead to the fact that a primary side or charging station needs to address a variety of OPs, power classes and air-gaps instead of just one nominal case, which may also apply to the secondary side depending on the application. Unavoidable tolerances must also be taken into account. In summary, an IPTS has to deal with a lot of variations and tolerances and the question is how to account for these factors in the design.

Hassler et al. proposed a methodology for describing interoperability in IPTSs in their work [107]. The approach involved the use of impedances, which were found to be a useful tool for summarizing the variations and tolerances of each component in a IPTS. Given the potential of the impedance-based approach, the question is whether it can be effectively applied to the design of an IPTS and help address interoperability concerns during the design phase.

This chapter presents a design methodology for interoperable IPTSs that utilizes and extends the approach discussed in Section 2.5, and allows the constraints and limitations of different components to be incorporated at each interface. The goal is to enable a deeper understanding of the real capabilities and dependencies of different components, and also to derive a design space for the primary or secondary electronics. The design method can also be used to accurately evaluate an entire IPTS or just one component for many different OPs at once. Further work on interoperability can be found in [63, 118–126].

First, the impedance interfaces within the IPTS and the assumptions are introduced and the goals of the presented IPM are described. Second, the details of the IPM procedure are described. Finally, various boundaries and their integration into the design method are explained in detail. Before summarizing the chapter, the possibilities of the IPM are discussed and to demonstrate the method, it is applied to a WPT3 example with a detailed discussion of the procedure.

3.1 Assumptions and Goals

The goal of this method is to provide results during a design or assessment procedure which give extensive insights compared to a conventional design process. Usually, a nominal OP is chosen and the system is designed in such manner that it can address it properly. In IPTSs for EV charging a lot of tolerances and changes can occur as previously described. The structure

of an IPTS is shown in Fig. 3.1 and was already explained in Chapter 2. The topology of each block may vary, making a universal system-level design complex. For example, the compensation networks can consist of a simple passive series compensation or a more complex active LCC compensation on both sides (with tunable L_{s1} and L_{s2}). Furthermore, different rectifier topologies and loads as well as coupling conditions change the system behavior and the impedances seen by the inverter.

The goal of the IPM is to address these variations in detail and provide an understanding of the system limitations and their causes. Common limitations in such systems are the maximum or minimum currents that can be driven by the inverter and coils, the voltage range and phase angles that can be provided by the inverter, and the maximum coil terminal voltages. The goal of an IPTS for EV charging is to transfer a certain (active) power to the battery, which imposes further requirements on the load and the transferred power at each interface, with the additional limitation that the grid (or PFC) also provides only limited (apparent) power.

The results can then be used to create design spaces with strong significance which help guarantee the design of a system that can drive all OPs. IPPs have proved themselves (as discussed in Section 2.5) to be well suited for handling many OPs and positions at once and thus are chosen for the method.

Due to the number of variations and OPs, some additional assumptions must be made. Considering the nonlinear switching behavior of the inverter and rectifier with physical circuit simulations would be time consuming, so an analytical approach is used.

Other assumptions are:

- Switching behavior is considered ideal. The inverter can be modeled as an ideal voltage source.
- For fundamental analysis, the inverter voltage source has no harmonics, only the fundamental wave is modeled and the load and rectifier can be expressed by their fundamental AC equivalent resistance R_{ac} (see Section 2.3).
- Switching and conduction losses in the power electronics (inverter and rectifier) are neglected.

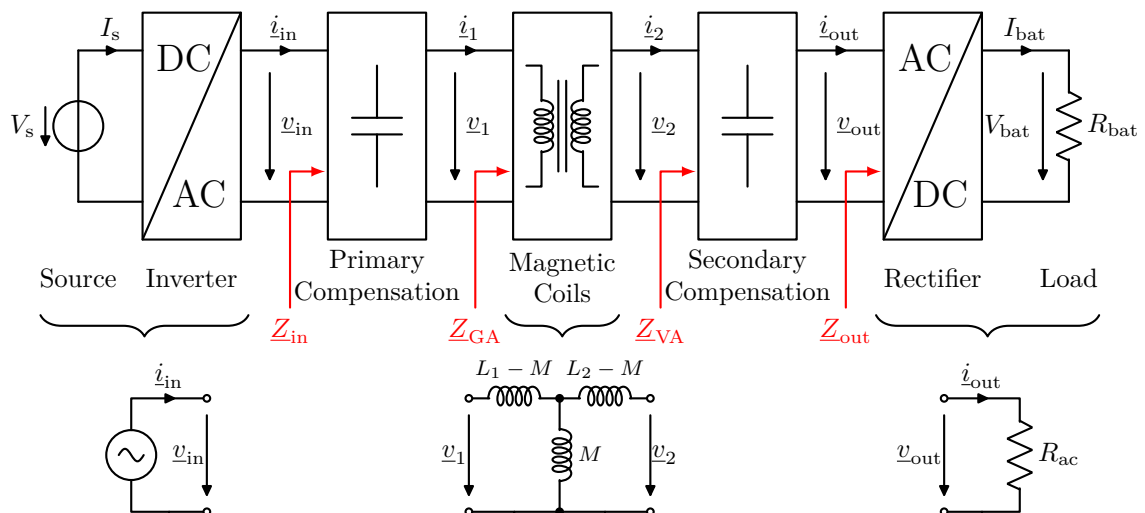


Figure 3.1 – Topology of an IPTS with impedance interfaces and FHA simplifications.

- Saturation and thermal effects in the magnetics are neglected (resistances and inductances are constant).
- The ESR of all capacitors are neglected.

The circuit simplifications for the IPM are also shown in Fig. 3.1. The four interfaces between the inverter and rectifier, highlighted in red, represent the impedance interfaces which are used for this design method. The indices “in”, “1”, “2” and “out” will be used to describe the inverter, primary coil, secondary coil and the rectifier impedance interfaces, respectively.

By making these assumptions, the method can also be used to gain insight of the various design elements at an early design stage. For a better understanding of the principle of the method, the first iteration (Chapter 3) introduces it in a simplified way and then a second iteration enhances the significance of the IPM by partially removing the assumptions and taking a closer look on some of the magnetics (Chapter 4), power electronics (Chapter 5) and system (Chapter 6) interoperability aspects and their impact on the IPPs.

3.2 Procedure of the Impedance Planes Method

The general idea of the presented method is to use the boundaries (if any) of each component, such as voltage ranges, current limits, and maximum phase angles, to derive a capability plane for a certain power level and describe it in terms of the real and imaginary parts of the resulting impedance at the interface to the next component.

With circuit analysis those capability planes can be transferred to any other interface. For better understanding a general two-port network is shown in Fig. 3.2. This approach was first used (in WPT research context) in [126]. With the typically used conventions, the relationship between voltage and current vectors for the ports on each side can be described as

$$\begin{bmatrix} v_1 \\ i_1 \end{bmatrix} = \tilde{A} \cdot \begin{bmatrix} v_2 \\ -i_2 \end{bmatrix}. \quad (3.1)$$

So with Eq. (3.1), any impedance \underline{Z}_1 defined by v_1 and i_1 can be expressed in terms of v_2 and i_2 and vice versa.

For IPTSs for EV charging it is useful to change the current direction of the secondary current in order to represent the power flow from the grid to the battery (bidirectional power transfer is out of scope as mentioned in Chapter 1) and keep the conventions made in the previous section.

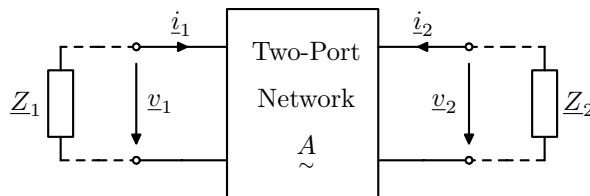


Figure 3.2 – A general two-port network with its equivalent impedances.

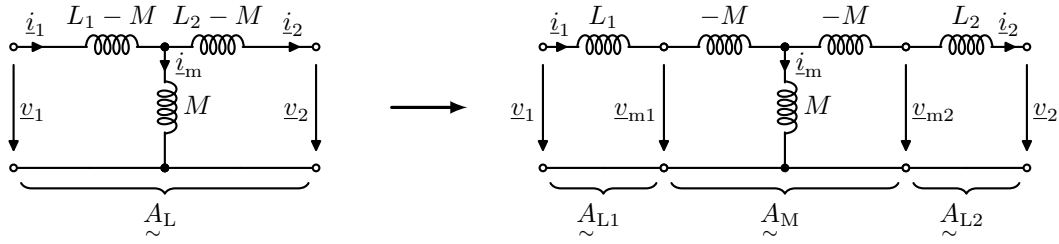


Figure 3.3 – Coils Transformer Equivalent Circuit Diagram with Transfer Matrix Simplifications.

By using a general description of the matrix, the impedances on both sides of the two port network can be directly related to each other. The renewed equation with the changed i_2 current direction is given as

$$\begin{bmatrix} v_1 \\ i_1 \end{bmatrix} = \underset{\sim}{A} \cdot \begin{bmatrix} v_2 \\ i_2 \end{bmatrix} = \begin{bmatrix} a_{11} & a_{12} \\ a_{21} & a_{22} \end{bmatrix} \cdot \begin{bmatrix} v_2 \\ i_2 \end{bmatrix}. \quad (3.2)$$

For a comprehensive analysis, it is necessary to transfer impedances in both directions. In this thesis, the direction of power flow from the source to the battery is defined as “forward” and the opposite direction is defined as “reverse”. The matrix for the reverse direction is defined as $\underset{\sim}{B}$ and the transfer equation can be derived as

$$\begin{bmatrix} v_2 \\ -i_2 \end{bmatrix} = \underset{\sim}{B} \cdot \begin{bmatrix} v_1 \\ -i_1 \end{bmatrix} = \begin{bmatrix} b_{11} & b_{12} \\ b_{21} & b_{22} \end{bmatrix} \cdot \begin{bmatrix} v_1 \\ -i_1 \end{bmatrix}. \quad (3.3)$$

From Eq. (3.2) and (3.3) the relations between the impedances on both sides can be calculated depending on the given matrix with:

$$\underline{Z}_1 = \frac{a_{11} \cdot \underline{Z}_2 + a_{12}}{a_{21} \cdot \underline{Z}_2 + a_{22}} = \frac{b_{22} \cdot \underline{Z}_2 + b_{12}}{b_{21} \cdot \underline{Z}_2 + b_{11}} \quad (3.4)$$

$$\underline{Z}_2 = \frac{-a_{22} \cdot \underline{Z}_1 + a_{12}}{a_{21} \cdot \underline{Z}_1 - a_{11}} = \frac{-b_{11} \cdot \underline{Z}_1 + b_{12}}{b_{21} \cdot \underline{Z}_1 - b_{22}} \quad (3.5)$$

and from both equations it can be seen that $\underset{\sim}{B}$ can be derived from $\underset{\sim}{A}$ with

$$b_{11} = a_{22} \quad (3.6)$$

$$b_{12} = a_{12} \quad (3.7)$$

$$b_{21} = a_{21} \quad (3.8)$$

$$b_{22} = a_{11} \quad (3.9)$$

which makes impedance transfer in both directions very simple. The transfer matrices for these impedance transfers can now be derived for each compensation topology, as well as the coils, in order to be able to transfer an impedance to any other interface.

For a series connection of two or more two-port networks, their matrices can simply be multiplied [127]. This can be used to derive the matrix for the T-transformer model representing the coils (see Section 2.2.6). As shown in Fig. 3.3, the network can be divided into three subnetworks. The transfer matrix $\underset{\sim}{A}_L$ of the coils can be split as follows:

$$\begin{aligned}
 \underline{\tilde{A}}_L &= \underline{\tilde{A}}_{L1} \cdot \underline{\tilde{A}}_M \cdot \underline{\tilde{A}}_{L2} = \begin{bmatrix} 1 & \underline{Z}_{L1} \\ 0 & 1 \end{bmatrix} \cdot \begin{bmatrix} 0 & -\underline{Z}_M \\ \frac{1}{\underline{Z}_M} & 0 \end{bmatrix} \cdot \begin{bmatrix} 1 & \underline{Z}_{L2} \\ 0 & 1 \end{bmatrix} \\
 &= \frac{1}{\underline{Z}_M} \begin{bmatrix} \underline{Z}_{L1} & \underline{Z}_{L1}\underline{Z}_{L2} - \underline{Z}_M^2 \\ 1 & \underline{Z}_{L2} \end{bmatrix}
 \end{aligned} \tag{3.10}$$

with the impedances being $\underline{Z}_{L1} = j\omega L_1$, $\underline{Z}_{L2} = j\omega L_2$ and $\underline{Z}_M = j\omega M^1$. For the reverse direction, the matrix $\underline{\tilde{B}}$ can be derived as (with Eq. (3.6)–(3.9))

$$\begin{aligned}
 \underline{\tilde{B}}_L &= \underline{\tilde{B}}_{L2} \cdot \underline{\tilde{B}}_M \cdot \underline{\tilde{B}}_{L1} = \underline{\tilde{A}}_{L2} \cdot \underline{\tilde{A}}_M \cdot \underline{\tilde{A}}_{L1} \\
 &= \frac{1}{\underline{Z}_M} \begin{bmatrix} \underline{Z}_{L2} & \underline{Z}_{L1}\underline{Z}_{L2} - \underline{Z}_M^2 \\ 1 & \underline{Z}_{L1} \end{bmatrix}.
 \end{aligned} \tag{3.11}$$

This approach essentially allows an impedance to be transferred through any combination of series or parallel branches by a simple matrix multiplication which is very powerful when many different topologies need to be analyzed.

This process has been repeated for the most common compensation topologies and the results are shown in Tab. 3.1 with the impedance notations from Section 2.3.

In summary, it can be stated that with Eq. (3.2), (3.4) and (3.5) any impedance \underline{Z}_i can be expressed in terms of \underline{Z}_j and vice versa, although in this thesis $\{i,j\} \in \{\text{“in”}, \text{“GA”}, \text{“VA”}, \text{“out”}\}$.

A generalized equation can be stated as

$$\underline{Z}_i = f(\underline{\tilde{A}}, \underline{Z}_j) \quad \{i,j\} \in \{\text{“in”}, \text{“GA”}, \text{“VA”}, \text{“out”}\} \tag{3.12}$$

and an overview of the required matrices (for this thesis) for all combinations is listed in Tab. 3.2, with $\underline{\tilde{A}}_{C1}$ and $\underline{\tilde{A}}_{C2}$ representing any primary or secondary compensation topology, respectively.

3.2.1 Inverter Capability Planes

Based on the limitations at an interface, an impedance area which can be driven or accessed by any component, a so called capability plane, can be derived. As shown, circuit analysis allows the transfer of impedances to any interface and thus the transfer of capability planes to any other interface, as first presented in [P.1] and extended in [P.2].

Using the impedance notation from Eq. (2.55), it can be seen that constraints on voltage and current magnitudes (of any component) result in a maximum and minimum magnitude of impedance, where

$$Z_{\min} = \frac{V_{\min}}{I_{\max}} \tag{3.13}$$

$$Z_{\max} = \frac{V_{\max}}{I_{\min}}. \tag{3.14}$$

In general, Eq. (2.55) can be rearranged and expressed in terms of its real and imaginary parts as

$$R^2 + X^2 = \left(\frac{V}{I}\right)^2 \tag{3.15}$$

¹The matrix $\underline{\tilde{A}}_M$ was created by further splitting up the matrix in each series or parallel branch which is not shown.

Table 3.1 – Overview of Transfer Matrices for all Compensation Networks

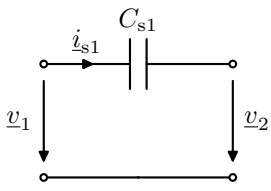
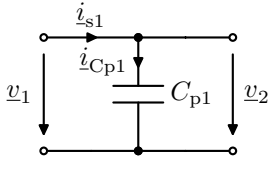
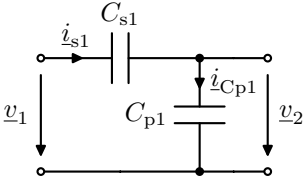
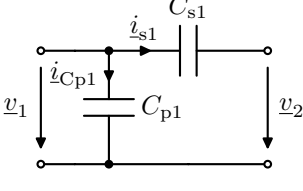
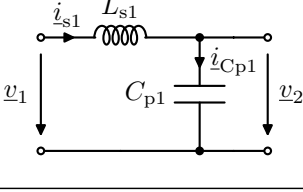
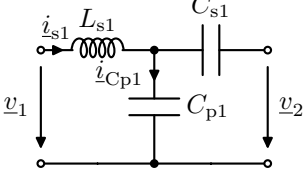
Circuit Topology	Two-Port Network Matrix	
	Series Tuning	
	$\tilde{A}_S = \begin{bmatrix} 1 & \underline{Z}_{Cs1} \\ 0 & 1 \end{bmatrix},$	$\tilde{B}_S = \begin{bmatrix} 1 & \underline{Z}_{Cs1} \\ 0 & 1 \end{bmatrix}$
	Parallel Tuning	
	$\tilde{A}_P = \begin{bmatrix} 1 & 0 \\ \frac{1}{\underline{Z}_{Cp1}} & 1 \end{bmatrix},$	$\tilde{B}_P = \begin{bmatrix} 1 & 0 \\ \frac{1}{\underline{Z}_{Cp1}} & 1 \end{bmatrix}$
	Series-Parallel Tuning	
	$\tilde{A}_{SP} = \begin{bmatrix} \frac{\underline{Z}_{Cs1} + 1}{\underline{Z}_{Cp1}} & \underline{Z}_{Cs1} \\ \frac{1}{\underline{Z}_{Cp1}} & 1 \end{bmatrix},$	$\tilde{B}_{SP} = \begin{bmatrix} 1 & \underline{Z}_{Cs1} \\ \frac{1}{\underline{Z}_{Cp1}} & \frac{\underline{Z}_{Cs1} + 1}{\underline{Z}_{Cp1}} \end{bmatrix}$
	Parallel-Series Tuning	
	$\tilde{A}_{PS} = \begin{bmatrix} 1 & \underline{Z}_{Cs1} \\ \frac{1}{\underline{Z}_{Cp1}} & \frac{\underline{Z}_{Cs1} + 1}{\underline{Z}_{Cp1}} \end{bmatrix},$	$\tilde{B}_{PS} = \begin{bmatrix} \frac{\underline{Z}_{Cs1} + 1}{\underline{Z}_{Cp1}} & \underline{Z}_{Cs1} \\ \frac{1}{\underline{Z}_{Cp1}} & 1 \end{bmatrix}$
	LCL Tuning	
	$\tilde{A}_{LCL} = \begin{bmatrix} \frac{\underline{Z}_{Ls1} + 1}{\underline{Z}_{Cp1}} & \underline{Z}_{Ls1} \\ \frac{1}{\underline{Z}_{Cp1}} & 1 \end{bmatrix},$	$\tilde{B}_{LCL} = \begin{bmatrix} 1 & \underline{Z}_{Ls1} \\ \frac{1}{\underline{Z}_{Cp1}} & \frac{\underline{Z}_{Ls1} + 1}{\underline{Z}_{Cp1}} \end{bmatrix}$
	LCC Tuning	
	$\tilde{A}_{LCC} = \begin{bmatrix} \frac{\underline{Z}_{Ls1} + 1}{\underline{Z}_{Cp1}} & \underline{Z}_{LCC} \\ \frac{1}{\underline{Z}_{Cp1}} & \frac{\underline{Z}_{Cs1} + 1}{\underline{Z}_{Cp1}} \end{bmatrix},$	$\tilde{B}_{LCC} = \begin{bmatrix} \frac{\underline{Z}_{Cs1} + 1}{\underline{Z}_{Cp1}} & \underline{Z}_{LCC} \\ \frac{1}{\underline{Z}_{Cp1}} & \frac{\underline{Z}_{Ls1} + 1}{\underline{Z}_{Cp1}} \end{bmatrix}$
	with $\underline{Z}_{LCC} = \underline{Z}_{Ls1} + \underline{Z}_{Cs1} + \frac{\underline{Z}_{Ls1}\underline{Z}_{Cs1}}{\underline{Z}_{Cp1}}$	

Table 3.2 – Overview of all Impedance Transfer Matrices

$= \setminus f(\cdot)$	\underline{Z}_{in}	\underline{Z}_{GA}	\underline{Z}_{VA}	\underline{Z}_{out}
\underline{Z}_{in}	1	\underline{A}_{C1}	$\underline{A}_{C1} \cdot \underline{A}_L$	$\underline{A}_{C1} \cdot \underline{A}_L \cdot \underline{A}_{C2}$
\underline{Z}_{GA}	\underline{B}_{C1}	1	\underline{A}_L	$\underline{A}_L \cdot \underline{A}_{C2}$
\underline{Z}_{VA}	$\underline{B}_L \cdot \underline{B}_{C1}$	\underline{B}_L	1	\underline{A}_{C2}
\underline{Z}_{out}	$\underline{B}_{C2} \cdot \underline{B}_L \cdot \underline{B}_{C1}$	$\underline{B}_{C2} \cdot \underline{B}_L$	\underline{B}_{C2}	1

which describes a circle in the complex plane with the magnitude of the impedance as the radius. Consequently, maximum and minimum limitations result in inner and outer circles as boundaries, where only the area in between defines an operating zone that does not exceed the limits given by the component.

An example for the inverter interface (with limitations given by the inverter electronics) is visualized in Fig. 3.4. Here the black shaded area lies outside of the inverter capability, restricted by its voltage and current limits from Eq. (2.55). Further restrictions are given by the phase angle limitations, shown in red, which narrow the resulting area down to a fraction of the remaining “doughnut”. All inverter limitations together result in an Inverter Capability Plane (ICP) as an usable impedance area, which is highlighted in green. The ICP serves as a starting point for further analysis.

If V_{min} or I_{min} is zero, then the inner or outer boundary disappears, because $Z_{min} = 0$ or $Z_{max} \rightarrow \infty$, respectively.

3.2.2 Integration of System Boundaries into Impedance Planes

In order to make the capability planes, or in this case the ICP, more significant, this section describes how common boundaries can be incorporated into these IPPs in general. Since this analysis can be applied to any interface, it is presented without indices.

Maximum Power

Power classes in [50] are defined by the maximum available apparent power (e.g. WPT3 = 11.1 kVA, see Section 2.5.1) and often also represent the limit which can be provided by the grid. The magnitude of the apparent power from Eq. (2.1) can be written as

$$S = |\underline{S}| = I^2 \cdot |\underline{Z}| = \frac{V^2}{|\underline{Z}|} \quad (3.16)$$

and the impedance magnitude $|\underline{Z}|$ (with $\underline{Z} = R + jX$) can also be expressed in circle equation form in the complex IPP as

$$R^2 + X^2 = \left(\frac{V^2}{S}\right)^2 \quad (3.17)$$

and

$$R^2 + X^2 = \left(\frac{S}{I^2}\right)^2. \quad (3.18)$$

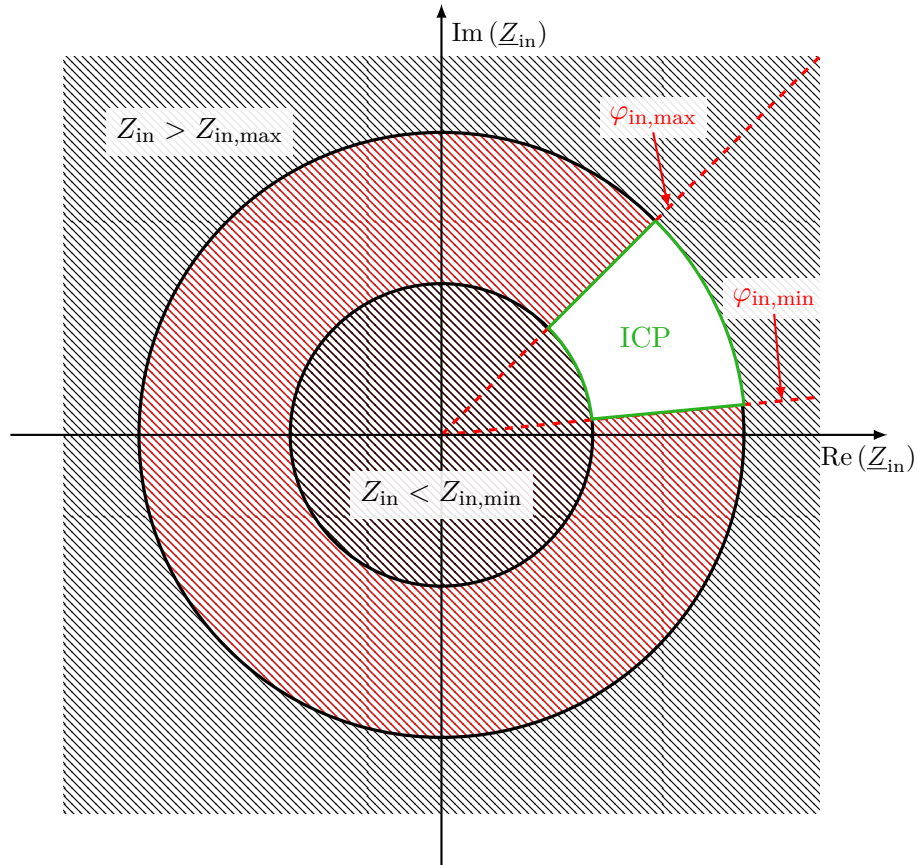


Figure 3.4 – ICP (green) restricted by voltage and current boundaries (black and shaded black) as well as phase angle limitations (red and shaded red).

Similar to the previous section, this results in two circles with the inner limitation set by

$$Z_{min} = V_{min}^2 / S_{max} \quad (3.19)$$

and the outer limitation by

$$Z_{max} = S_{max} / I_{min}^2. \quad (3.20)$$

This is visualized in Fig. 3.5a, where the red shaded area represents the restrictions introduced by the current and the blue area is the added restraint from the voltage limitation. It has to be emphasized, that these values may differ from the boundaries provided by the inverter boundaries.

If apparent power is limited to a maximum rated value, active and reactive power are also limited to the same value. To study the effects of a given P_{max} and Q_{max} , Eq. (2.1) can be split into real and imaginary parts:

$$\underline{S} = R \cdot \underline{i}^2 + j \cdot X \underline{i}^2 = P + jQ \quad (3.21)$$

$$\underline{S} = \frac{v^2 \cdot R}{R^2 + X^2} + j \cdot \frac{v^2 \cdot X}{R^2 + X^2} = P + jQ. \quad (3.22)$$

The following analysis focuses on the active power because the reactive power is usually not directly restricted or may be less important in real operation. Nevertheless, similar conclusions can be derived for reactive power limitations as is shown in Fig. 3.5e and Fig. 3.5f.

When looking at the active power, Eq. (3.21) yields

$$R = \frac{P}{I^2} \quad (3.23)$$

and this is maximized for

$$R_{\max,P} = \frac{P_{\max}}{I_{\min}^2}. \quad (3.24)$$

Eq. (3.24) defines the maximum real part of the impedance which cannot be exceeded and is shown as the red area in Fig. 3.5c.

In terms of maximum active power and voltage limitations, Eq. (3.22) results in

$$\left(R - \frac{1}{2} \frac{V^2}{P}\right)^2 + X^2 = \left(\frac{1}{2} \frac{V^2}{P}\right)^2 \quad (3.25)$$

which results in a circle with the smallest radius

$$r_{\min} = \frac{1}{2} \frac{V_{\min}^2}{P_{\max}} \quad (3.26)$$

and a real part offset with the same value. This is marked as the blue area in Fig. 3.5c. Again, these boundaries diminish if one of both V_{\min} or I_{\min} are zero.

If $S_{\max} = P_{\max}$, then the restrictions from Eq. (3.21) and Eq. (3.22) are already included in Eq. (3.17) and Eq. (3.18) or Fig. 3.5a, respectively. Nevertheless, the approach of this method is to provide the possibility of imposing boundaries that are as general as possible, since requirements may differ in each application.

Minimum Power

Usually, the purpose of a charging station is to transfer a certain amount of active power, which leads to another requirement for the IPPs. The same equations as in the previous section can be applied, with the results for the apparent power shown in Fig. 3.5b and for the active power in Fig. 3.5d.

In the case of providing minimum power, the maximum values of the component voltage and current limitations define the boundaries (instead of the lower limits as in the previous section), and the relations are reversed. I_{\max} now provides the inner circle (Fig. 3.5b) or left side boundary (Fig. 3.5d) and now the outside of the V_{\max} circle is the restricted area (blue), which represents a severe restriction especially for the $P \geq P_{\min}$ case.

Voltage, Current and Phase Angle Limitations

When the IPPs are directly related to a certain power level such as $P = P_{\text{out}}$ further boundaries may emerge from the voltage and current. With $P = V \cdot I$ the left and right boundaries for the real part of the IPP can be calculated as:

$$R_{\min,I} = \frac{P_{\text{out}}}{I_{\max}^2} \quad (3.27)$$

$$R_{\max,I} = \frac{P_{\text{out}}}{I_{\min}^2} \quad (3.28)$$

$$R_{\min,V} = \frac{V_{\min}^2}{P_{\text{out}}} \quad (3.29)$$

$$R_{\max,V} = \frac{V_{\max}^2}{P_{\text{out}}} \quad (3.30)$$

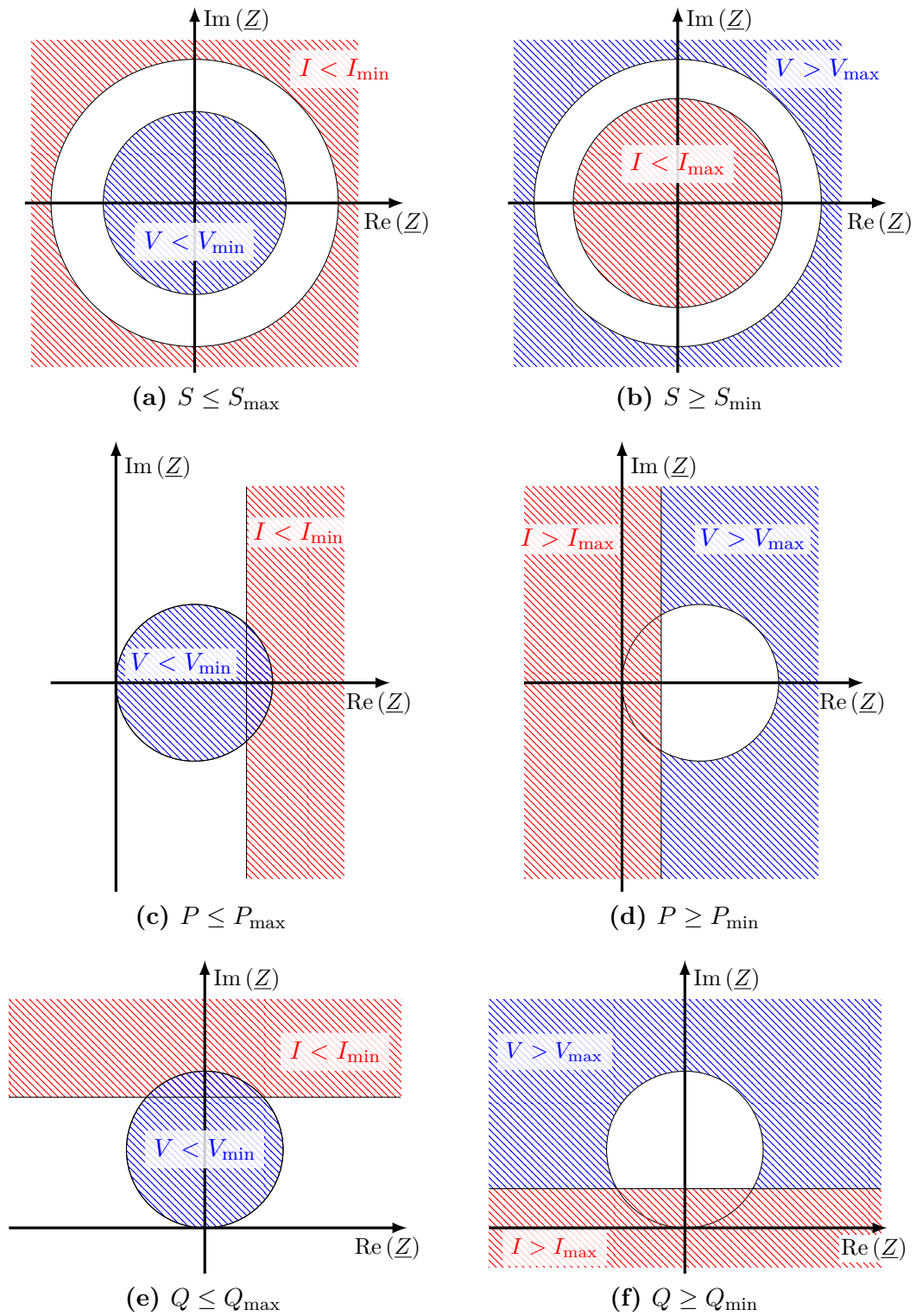


Figure 3.5 – IPPs (white) for different apparent, active and reactive power restrictions caused by component voltage (blue) and current (red) limitations.

where the larger of both lower limits and the smaller of both upper limits represent the ICP boundaries.

Phase angle constraints do not directly affect active power transfer, but they do affect the required apparent power with $S = P \cos(\varphi)$ and the impedance with $\underline{Z} = Z \cdot e^{j\varphi}$, and must be considered (at each interface) when constraints exist. Their effects on the ICPs are shown in Fig. 3.4.

All discussed limitations together result in an updated ICP (compared to Fig. 3.4), shown in green in Fig. 3.6. In this impedance area a minimum active power transfer of $P_{\text{out,min}}$ is now ensured whilst never exceeding voltage, current and phase angle limitations from the inverter ($V_{\text{in,min}} < V < V_{\text{in,max}}$, $I_{\text{in,min}} < I < I_{\text{in,max}}$, $\varphi_{\text{in,min}} < \varphi < \varphi_{\text{in,max}}$) and never requiring more apparent (grid) power than $S_{\text{in,max}}$.

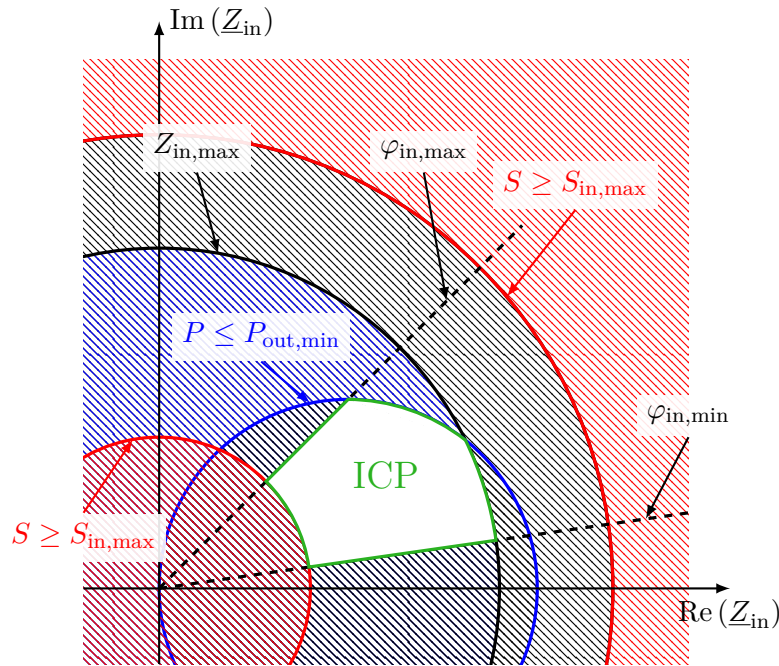


Figure 3.6 – ICP (green) for delivering $P \geq P_{\text{out,min}}$ (blue) with a maximum apparent power limitation (red) and inverter boundaries (black).

3.3 Applications of the Impedance Plane Method

Impedance transfer is a very powerful design tool when focusing on interoperability because of the many ways it can be used to assess the system. Some of these include the ability to:

- assess compensation topologies by exchanging the matrix \underline{A} and compare the resulting IPPs,
- derive capability planes for the inverter or the magnetic coils and visualize them,
- present the many OPs associated to the different secondary positions as seen by the primary electronics and derive a suitable design space for the electronics,

- visualize and include actual operational boundaries of any selected component in the design by including boundaries of other components,
- study the effects of various limitations,
- analyze in depth the effects of any chosen impedance matching network.

The impedance transfer approach is very general, making it applicable to a wide range of cases. However, its versatility makes it difficult to explain in a generalized (or application independent) flowchart. To better understand how the method works, the following section presents an example application of the IPM, complete with actual values.

3.4 IPM Example 1: Inverter Assessment with Operational Boundaries

The flowchart of the presented example is shown in Fig. 3.7. For a proper understanding of the procedure, each stage will be described step-by-step. Experimental verification of the investigated system will be presented later in Chapter 5.

Step 1

First, the topology has to be defined and every parameter between the inverter and rectifier interface of the system has to be characterized.

For the purpose of this example, reference systems from the SAE standard [50] were chosen. For the primary coil, the normative universal GA (SAE UGA WPT3, for more details see [50], Appendix B.2) was chosen which is designed for the power classes WPT1–WPT3. The dimensions of the bottom aluminum plate and the coil windings are 750×600 mm and 650×500 mm, respectively. The inherent FEM simulation model is shown in Fig. 3.8a. On the secondary side, the coil which was designed for power class WPT3 and air-gap class Z2 was chosen (SAE VA WPT3 Z2, see [50], Appendix A.8) with the aluminum shield and coil dimensions being 350×350 mm and 320×320 mm. The simulation model of the secondary coil as well as both coils together are shown in Fig. 3.8b and Fig. 3.8c, respectively. A “car-mimick” created using an aluminum shield (dimensions $800 \times 800 \times 2$ mm) on the top of the secondary was also used but is not shown.

To illustrate the effect of the coil limitations in the analysis, the coils were positioned at their lowest coupling within air-gap class Z2 with a ground clearance of 210 mm and a misalignment of $(x,y) = (75,100)$ mm. The FEM simulation results for this coupling condition as well as the nominal position (no misalignment) at the same ground clearance are listed in Tab. 3.3.

Table 3.3 – FEM Simulation Model Inductance Results

x (mm)	y (mm)	z (mm)	L_1 (μH)	L_2 (μH)	M (μH)	k
0	0	210	38.07	41.26	4.85	0.12
75	100	210	38.56	41.21	3.75	0.09

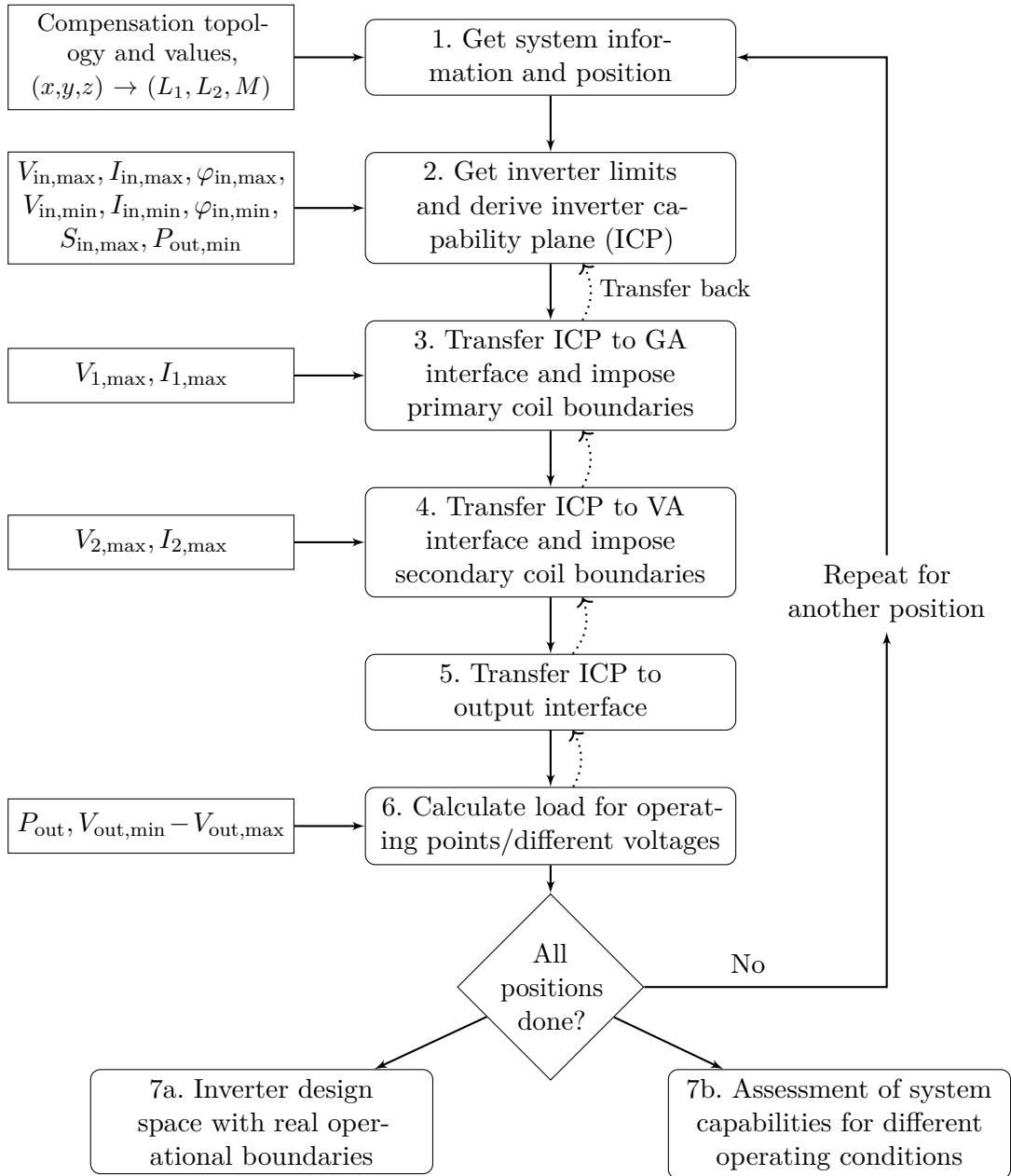


Figure 3.7 – Flowchart of the IPM for an assessment of inverter capabilities for a given system with load variation within real operational boundaries.

In [50], the secondary side uses an impedance compression network as shown in Section 2.2.2 for rectification, which is replaced here by a simplified passive rectifier (see Fig. 2.4) in this example, since this represents worst-case operation in a low-cost installation. A full bridge inverter is used on the primary side. In order to explain the IPM, FHA is used and therefore both the rectifier and the inverter are simplified as shown in Section 2.3.

In terms of reactive power compensation, the proposed system uses an active tuning solution with an LCC topology on both sides. For the purpose of this example, active tuning is not discussed, so the compensation values were fixed and are listed in Tab. 3.4. The capacitor

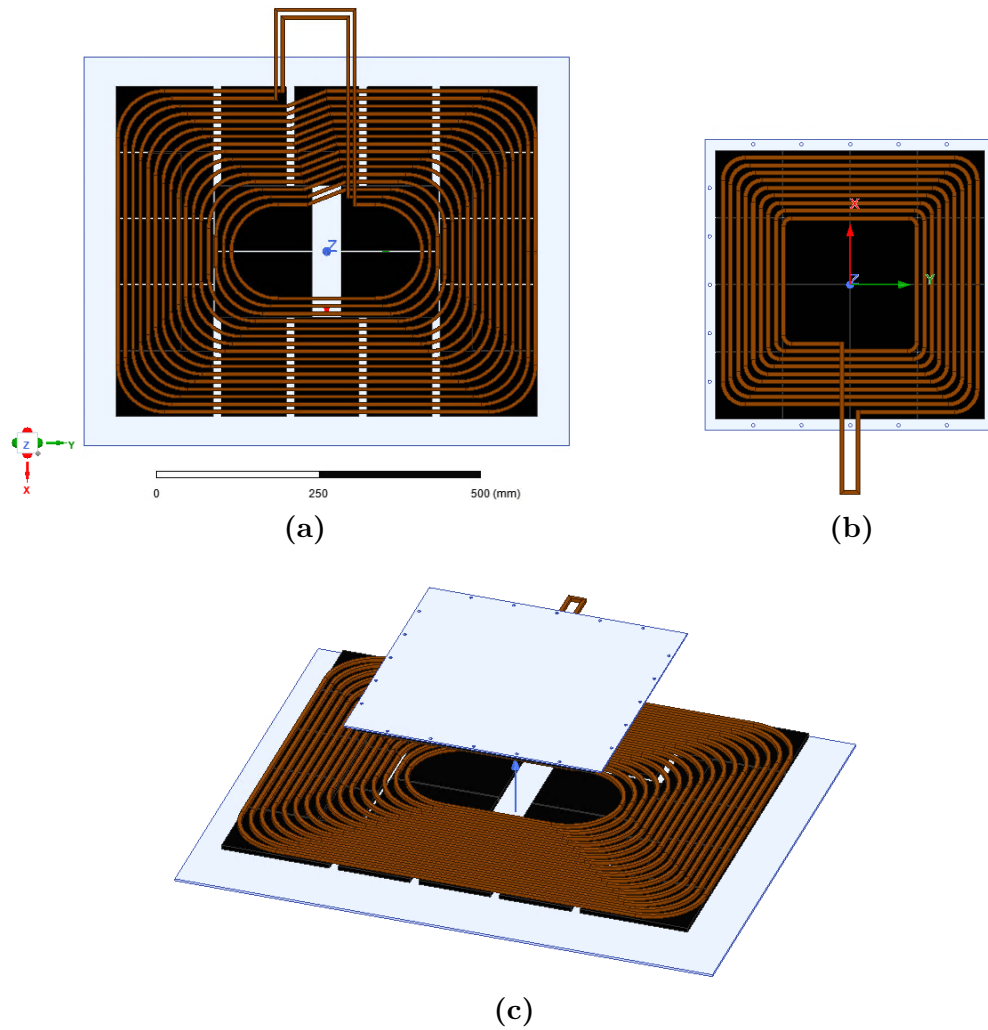


Figure 3.8 – FEM simulation models of the SAE coils used for the IPM Example 1, (a) primary coil, (b) secondary coil and (c) both coils.

Table 3.4 – Compensation Network Values

	$C_{s1,s2}$ (nF)	$C_{p1,p2}$ (nF)	$X_{GA,VA}$ (Ω)
Primary Side	160	270	24
Secondary Side	135	145	-18

values were chosen according to the reference systems in [50], and the values of X_{GA} and X_{VA} were set to give good results at low coupling for this example. Chapter 6 will examine the effects of active tuning and how to choose these values. The fully determined and simplified circuit is shown in Fig. 3.9.

Since the chosen system was designed for WPT3, a boundary of $P_{out} \geq 10$ kW and an assumption that the grid only provides 11.1 kVA was set. All boundaries, the battery voltage range, and the component limitations which are based on [50] are listed in Tab. 3.5, which

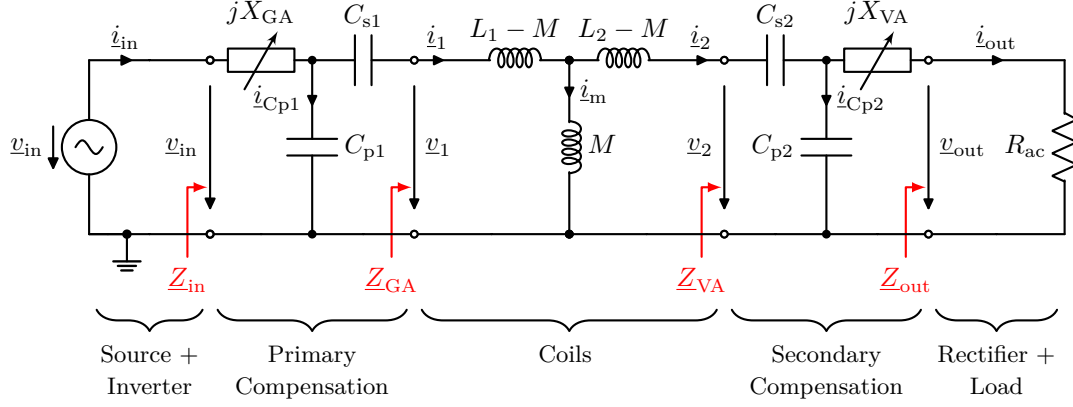


Figure 3.9 – IPM Example 1: Simplified circuit with LCC–LCC compensation and active tuning and the IPP interfaces highlighted in red.

Table 3.5 – System Boundaries for the IPM Example 1

Grid/Inverter	Coils	Rectifier/Load
$S_{in,max} = 11.1 \text{ kVA}$	$V_{1,max} = V_{2,max} = 2 \text{ kV}$	$V_{bat} = (280 - 450) \text{ V}$
$V_s = (380 - 500) \text{ V (DC)}$	$(I_{1,max}, I_{2,max}) = (75, 75) \text{ A}$	$P_{out,min} = 10 \text{ kW}$
$I_{in} = (20 - 40) \text{ A (AC)}$	$(x, y, z) = (75, 100, 210) \text{ mm}$	$R_{ac} = 8/\pi^2 \cdot V_{bat}^2/P_{out}$
$\varphi_{in} = (0 - 45) \text{ deg}$		

also concludes Step 1. Losses, ZVS and harmonics are neglected for this example but will be discussed further in Chapter 5.

Step 2

With the complete circuit determined and all boundaries given, the ICP can be constructed.

The initial ICP can be derived with the inverter voltage, current and phase angle limitations at the inverter interface (DC values transferred to AC according to Section 2.3) with Eq. (3.13) and (3.14):

$$Z_{in,min} = \frac{V_{s,min}}{I_{in,max}} = \frac{\frac{2\sqrt{2}}{\pi} \cdot 380\text{V}}{40\text{A}} = 8.553 \Omega$$

$$Z_{in,max} = \frac{V_{s,max}}{I_{in,min}} = \frac{\frac{2\sqrt{2}}{\pi} \cdot 500\text{V}}{20\text{A}} = 22.5 \Omega$$

$$\varphi_{in,min} = 0^\circ$$

$$\varphi_{in,max} = 45^\circ.$$

The resulting ICP is shown in Fig. 3.10. Following the explanations of Section 3.2.2 the upper and lower limitations of $S_{in,max}$ and $P_{out,min}$ can be implemented into the ICP and the results are shown in Fig. 3.11a and 3.11b, respectively.

When combined, all these boundaries lead to the green ICP, shown in Fig. 3.12. This area represents the impedance area which can be driven by the inverter within its boundaries

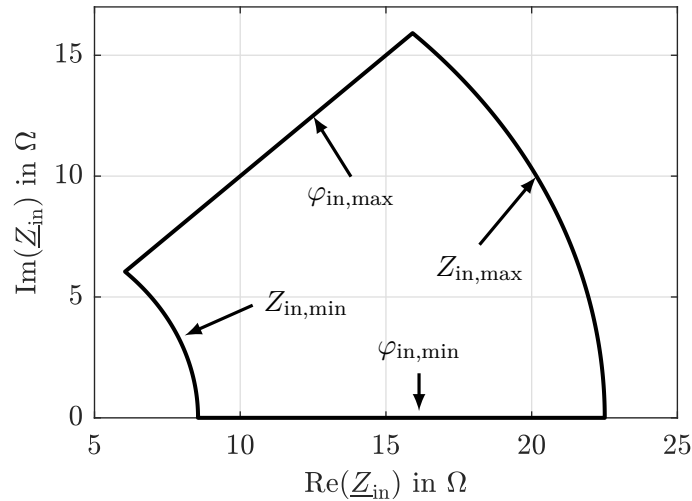


Figure 3.10 – IPM Example 1: ICP with inverter boundaries shown at the inverter interface.

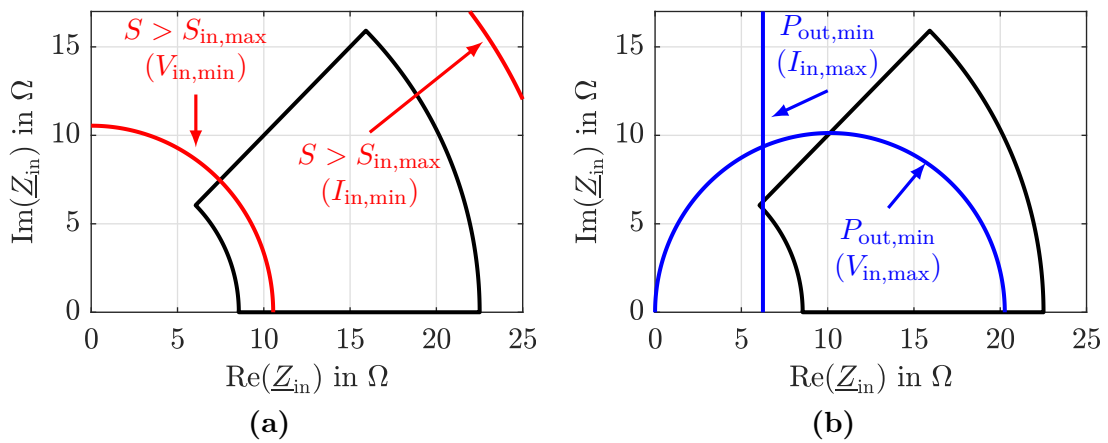


Figure 3.11 – IPM Example 1: ICP with inverter and (a) $S_{in,max}$ and (b) $P_{out,min}$ boundaries at the inverter interface.

and the imposed power requirements. With this approach, it is easy to distinguish which boundary affects and restricts this zone and that allows a detailed assessment or streamlined re-design. For this purpose, the analysis is continued with all four different ICPs (with the coloring and naming shown in the legend) from Fig. 3.12 instead of only the final green ICP.

Step 3

As described in Section 3.2, all impedances can then be transferred to the GA interface. Based on the primary LCC-topology of the circuit, the \tilde{A}_{LCC} matrix from Tab. 3.1 with the values from Tab. 3.4 is used for this step and the resulting ICPs of the transfer are shown Fig. 3.13.

To further improve the significance of the ICP, the primary coil boundaries from Tab. 3.5 can be implemented in the ICP. The primary coil itself has a capability range (GA Coil Capability Plane (CCP)) at the GA interface defined by its voltage and current limits. As

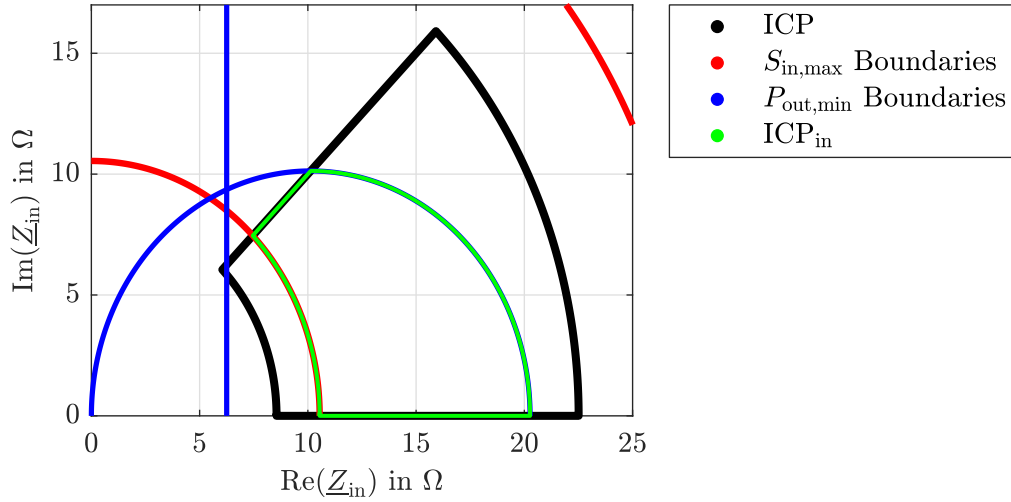


Figure 3.12 – IPM Example 1: Resulting ICP (ICP_{in} , green) with all inverter boundaries and power requirements. Result of Step 2.

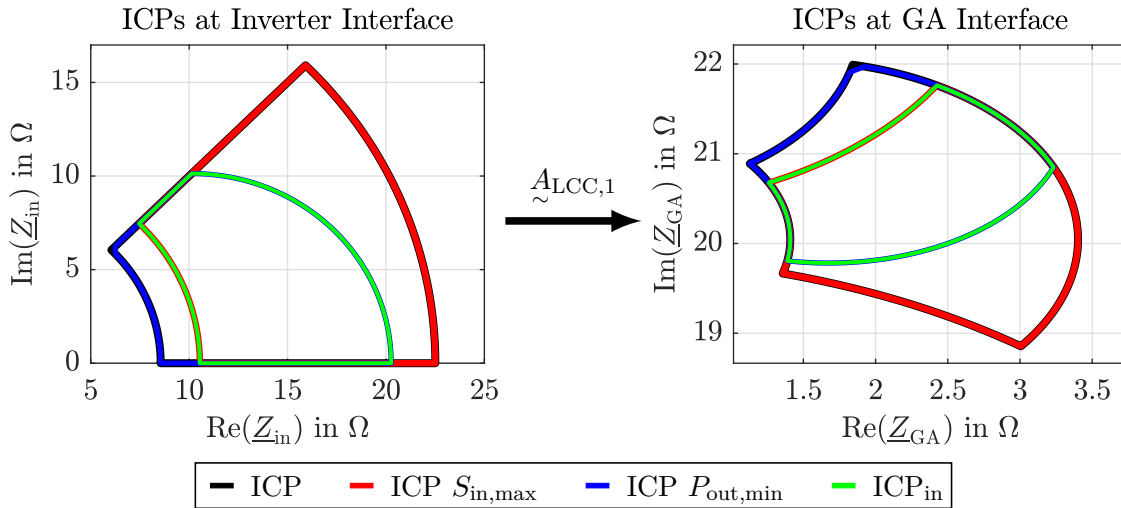


Figure 3.13 – IPM Example 1: ICP transfer from inverter to GA interface with primary LCC tuning.

a result, there may be impedances that can be driven by the inverter but are outside the capabilities of the GA CCP. The intersection of the GA CCP and the ICP then describes the real usable impedance range.

Since the coils have no component related lower limit for voltage and current, their CCPs are very large. However, the lower limits usually result from the requirement that $P_{out} \geq P_{out,min}$. Details of magnetics and their CCPs will be discussed in detail in Chapter 4.

To demonstrate the effect of the $P_{out,min}$ requirement on the CCP, the GA CCP of the example coil is shown in Fig. 3.14 (left), once with the lower voltage and current limits of 10 V and 1 A (GA CCP in purple) and again with the same limits and the additional requirement of $P_{out,min} \geq 10$ kW (GA CCP $P_{out,min}$ in magenta).

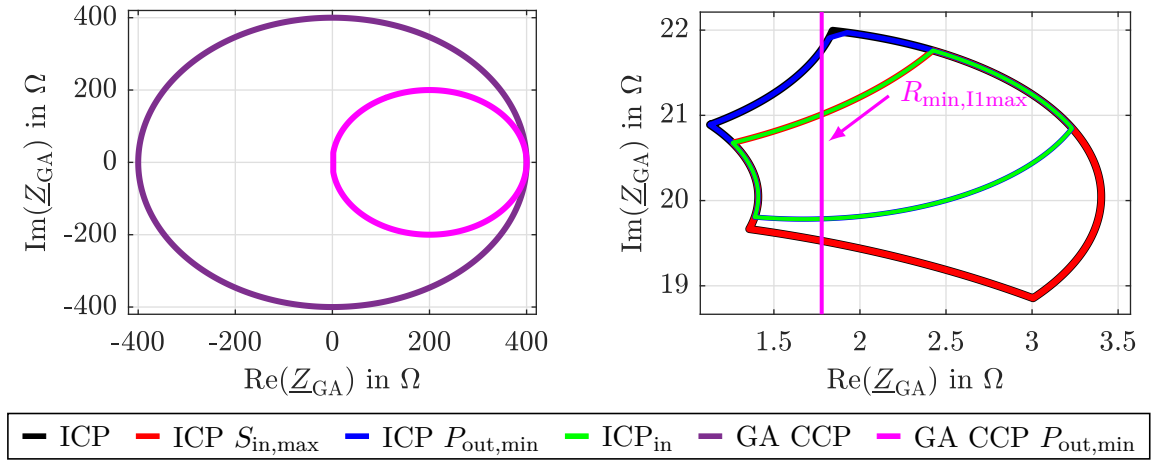


Figure 3.14 – IPM Example 1: ICPs and CCPs at GA interface, (left) GA CCPs, (right) ICPs and $I_{1,\max}$ limitation.

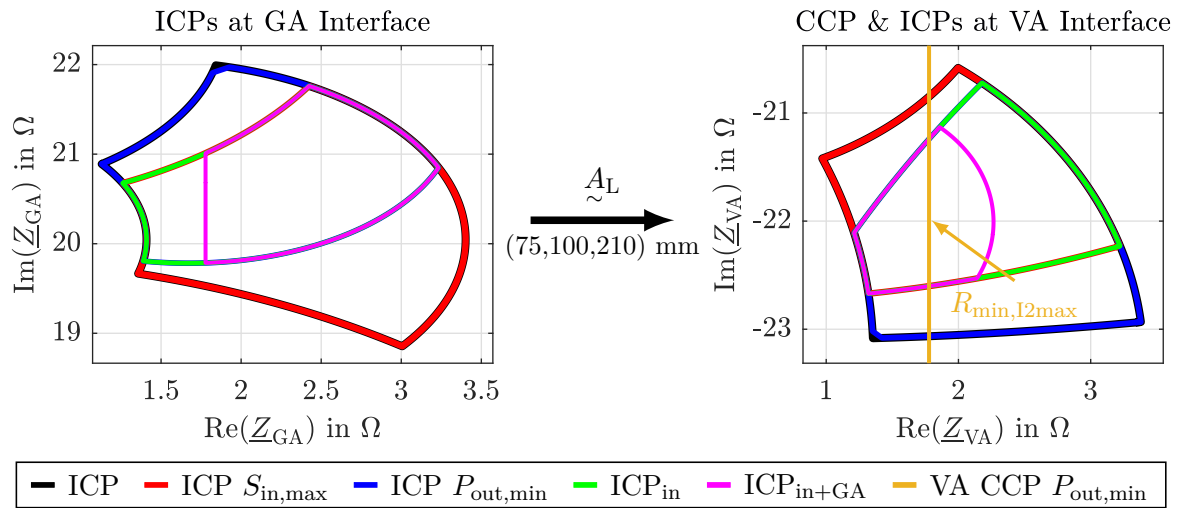


Figure 3.15 – IPM Example 1: ICP transfer from GA to VA interface at $(x,y,z) = (75,100,210)$ mm.

The impact of the GA CCP on the ICP from Fig. 3.13 is shown Fig. 3.14 on the right. Due to the primary coil current limitation of $I_{1,\max} = 75$ A, the GA CCP has a lower real part limitation $R_{\min,I1\max}$. Considering the complete system, the area left of $R_{\min,I1\max}$ cannot be addressed and the real ICP gets further narrowed down and is shown on the left in Fig. 3.15.

Step 4

Step 4 is a repetition of Step 3, where the ICPs are first transferred and then new boundaries are imposed. The GA ICPs are shown on the left side in Fig. 3.15 and are transferred to the VA side with the \tilde{A}_L matrix, where the relative coil position (with the values from Tab. 3.3) determines the impedance transfer.

The transfer results are shown on the right side and similar to the previous step, the VA CCP is very large and only the current limitation has a relevant impact. With $R_{\min, I1\max} = R_{\min, I2\max}$ the limitations are the same, but as can be seen in the resulting ICPs in Fig. 3.16 on the left, the real usable area decreases further. On the VA interface, the orange envelope now represents $ICP_{in+GA+VA}$, which is the area that can be driven within the limitations of the inverter, primary and secondary coils, and also ensures that the required output power can be delivered while never exceeding $S_{in, \max}$.

Step 5

This step is repeated, similar to Step 3, for the secondary side LCC-compensation topology with transfer matrix $\tilde{A}_{LCC,2}$ with the values from Tab. 3.4. This is shown in Fig. 3.16.

The intersection of all boundaries, requirements and limitations results in the area shown to be enclosed by the orange envelope within which the inverter can deliver the required output power and stay within all deployed limits.

It has to be emphasized that these envelopes can also be transferred back to the inverter plane (if needed) as shown by the dotted arrows in Fig. 3.7. This was not done in this example in order to point out the design process of the flowchart.

Step 6

The result of applying all the above steps is an ICP presented to the output interface, where the limitations of all system components are considered. This allows a direct check to determine whether the load of an OP can be driven by the system. As shown in step 6 and 7b, it is possible to assess the various system capabilities resulting from a change in operation at a given output power because of battery voltage variation. All ICPs and the OPs for transferring $P_{out} = 10$ kW at the battery voltage range provided in Tab. 3.5 are shown in Fig. 3.17.

If required, this process can be repeated for different positions of the coil that affect the transfer between the GA and VA interfaces and can decrease the resulting capability plane at

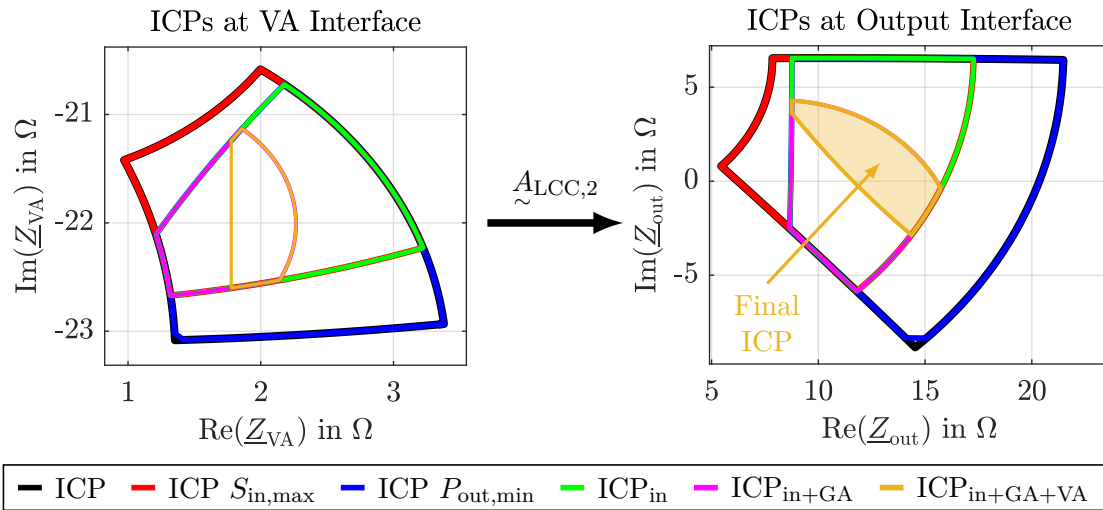


Figure 3.16 – IPM Example 1: ICP transfer from VA to output interface with secondary LCC tuning.

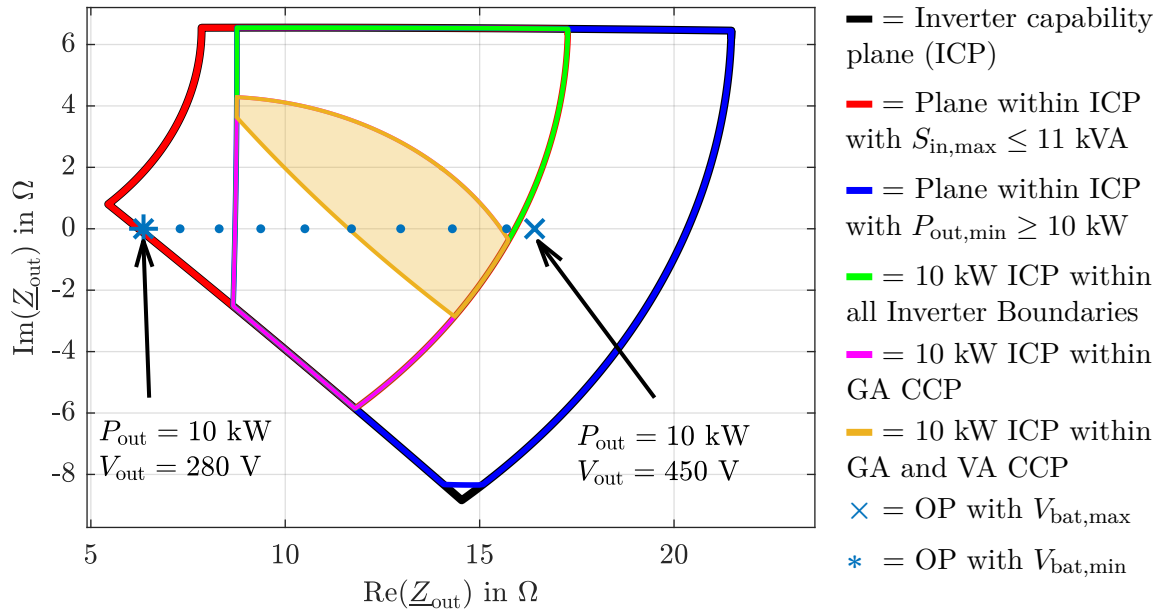


Figure 3.17 – IPM Example 1: All ICPs and OPs at the output interface with all ICP explanations.

the output. For this example only one position, $(x,y,z) = (75,100,210)$ mm, was considered which means that no repetition was required.

Step 7

Finally, the resulting capability planes and OPs from the output interface can be transferred back to any interface and this is shown in Fig. 3.18.

These results can now be used in a number of ways. The flowchart from Fig. 3.7 offers two possibilities. First, it can help define an inverter design space by narrowing down the real inverter requirements (Step 7a), or second, it can assess the system capabilities for the given operating conditions (Step 7b). Many other interpretations or conclusions are possible (e.g., adjustments of compensation values, topologies, and components), and because of the many possibilities and the purpose of this example is only to introduce the method, only a brief evaluation of the results is provided below.

If a designer considered only the initial ICP (black envelope), one might think that all OPs could be driven by the system. A closer look at the final ICP (orange envelope) shows that the OPs with the lower voltages ($V \leq 380$ V) as well as the maximum voltage are outside the secondary and primary coil limits (cutoffs at R_{\min} in Fig. 3.18c and 3.18b, respectively) and in reality cannot be driven by the system.

So this method directly shows the practical limitations within the system. These envelopes can now be used to tailor components or to re-define requirements in order to be able to drive all necessary OPs.

Another approach could be to adjust the OPs using impedance regulators so that the final ICP covers them all. There are many solutions to achieve this, including control strategies, exchanging topologies, active tuning, and more. The initial secondary system from [50] uses an impedance compression network as described in Section 2.2.2, which reduces the spread of

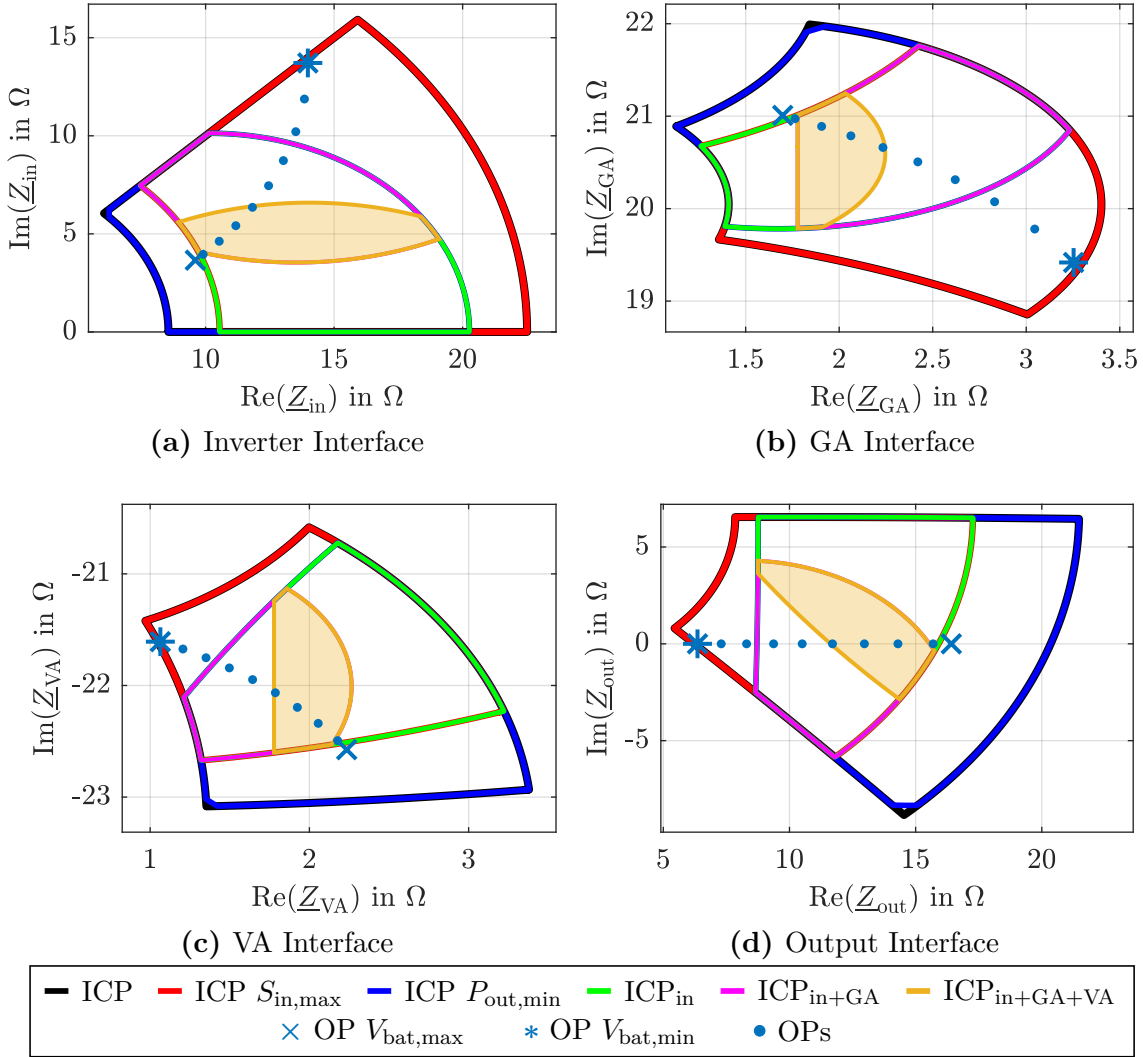


Figure 3.18 – IPM Example 1: Final ICPs with all boundaries and OPs at all interfaces.

the OPs (by effectively changing R_{ac}) as shown in [73]. Similar results can be achieved using a boost converter. To demonstrate the effect on the OPs, Fig. 3.19 shows the previous results (Fig. 3.18) with a boost converter added on the secondary side. The duty cycle of each OP has been slightly adjusted to stay within the final ICP.

The last measure discussed here is the change in output power. The evaluation showed that many OPs cannot be driven because of the high secondary current required. A simple solution is to reduce the transferred power, since it is not necessary to transfer the rated power over the entire misalignment range, see [50]. The dark red OPs in Fig. 3.19 represent operation with reduced power to bring them closer to the final ICP. Since it is not the goal to redesign the system to make it fully interoperable and improve performance, no further measures were taken within this example.

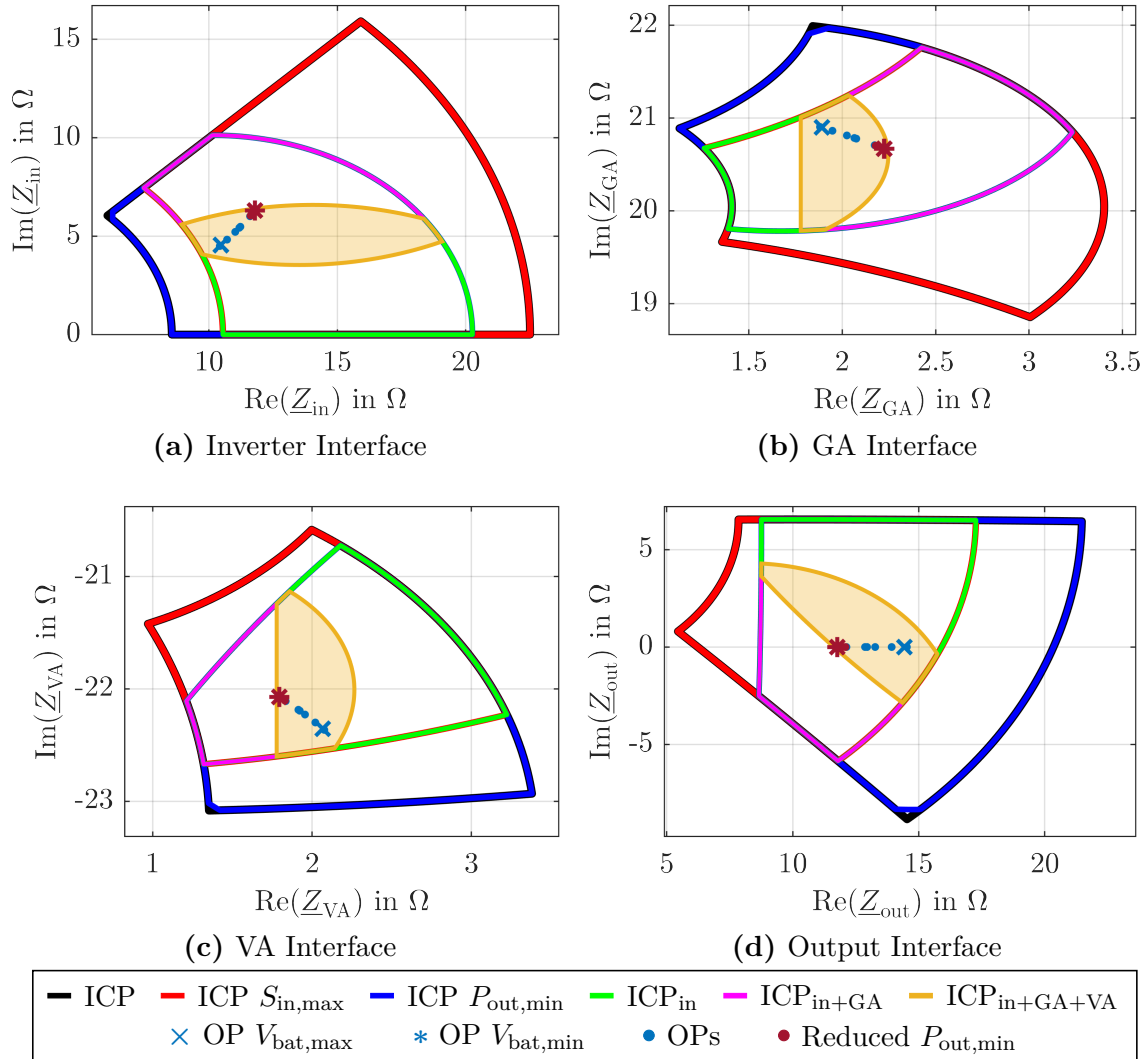


Figure 3.19 – Example ICP: Final ICPs with an added boost converter on the secondary side and partially reduced output power.

3.5 Summary and Results

A design and assessment methodology for IPTSs using IPPs has been presented. This method allows different interoperability considerations at different IPTSs design stages due to its general approach. Operational system boundaries from power electronics and magnetics are used to derive capability planes that can be shifted to any interface by impedance transfer and thus used to design or assess a system component. Furthermore, it was shown how different operational boundaries for EV charging, such as the transfer of a minimum active power, maximum available apparent power or component voltage, current and phase limitations, can be implemented in these IPPs.

The method has been applied to an example to demonstrate the process and the complexity introduced by interoperability in early stage design.

The main contribution of this chapter is an extension of the impedance-based approach for describing interoperability by using additional impedance interfaces as well as a methodical approach that incorporates different boundaries from each interface to gain a deeper understanding of the system capability. The interpretation of these IPPs provides a design space for system-level design where constraints and boundaries can be easily implemented and considered in the early stages of design with a focus on interoperability and real-world tolerances such as battery voltage variation and positional offset. In addition to being useful for system design, this method can also be used to evaluate existing systems at various boundaries and verify that they meet interoperability requirements while taking constraints into account. Evaluation of different compensation topologies is also easily possible.

This method can be used in many ways to contribute to a much deeper understanding of system design, which justifies further research. With respect to high power systems, the interoperability and compensation challenges will be more difficult to achieve without improved magnetic topologies with higher coupling, otherwise the IPPs will be smaller and harder to match.

In order to address these issues and enable their successful application and improvement, the significance of IPPs needs to be increased, which requires a more detailed discussion of all components and their interoperability issues. Therefore, a closer look at the magnetics is provided in Chapter 4, the electronics such as inverters and rectifiers are extensively discussed in Chapter 5, and compensation networks and active tuning are discussed in Chapter 6.

4 Interoperability Aspects of Magnetics

Chapter 2 discussed the basics of magnetic coils, their coupling principle, and the interpretation as a loosely coupled transformer. In the previous section, the coils were modeled using their equivalent T-shape circuit diagram without discussing the details of the resulting parameters.

However, as the central link between the charging station on the ground side and the receiver in the vehicle, the coils represent the most critical component where the most tolerance or variety is introduced into the system, either by unintentional misalignment or by intentional ranges that must be covered for interoperability or other reasons.

Therefore, a large part of the success of an IPTS can be addressed by good magnetic design here, and a closer look is required. In addition, the focus in these components is more on the magnetic and geometric properties, combined with the electronic and regulatory aspects, which is a very different focus compared to other components with a large impact on system behavior. The electronic and power conversion aspects of interoperability are discussed in detail in Chapter 5.

To understand the interoperability aspects introduced into the IPTS by the behavior of the magnetic coils, this section first discusses coils and their properties. Second, the integration of these aspects into the IPM from Chapter 3 is presented, followed by an example to highlight the impact of the coils on an IPTS.

4.1 Magnetic Coil Properties

As shown in Section 2.2.6, the coupling quality between primary and secondary coils relies on the amount of flux captured by the secondary coil, which is heavily influenced by the topology and relative position of the coils. The power transferred across the air-gap can be determined by

$$P_{\text{out}} = k\sqrt{VA_1 VA_2} \cdot \sin(\varphi_{12}) \quad (4.1)$$

where $VA_1 = \omega L_1 I_1^2$ and $VA_2 = \omega L_2 I_2^2$ and $\varphi_{12} = \angle I_1, I_2$ [128]. This equation illustrates that both the coupling factor and coil inductances significantly impact the power transfer, emphasizing the importance of proper coil design.

In addition, the leakage flux, which is a function of both coil currents, plays a critical role in the deployment of IPTSs as will be discussed in Section 4.1.2. This highlights the significance of the coil design and designated currents through them.

This section summarizes research on magnetics for the context of the application of IPT for EV charging.

4.1.1 Magnetic Coupling and Coil Topologies

The fundamentals chapter introduced important properties and the coupling principle. However, due to the nonlinear nature of materials such as ferrite, it is difficult to determine the coupling analytically. Hence, FEM simulations are commonly used. As discussed in the standardization Section 2.5.1, IPTSs must comply with regulations. Since the coupling is

mainly defined by the air-gap, it must be considered in the design process. Fig. 4.1 shows the coupling factors of two sets of circular coils (see [P.3]) at different horizontal offsets, while Fig. 4.2 shows the coupling factor of the same coils but for different air-gaps ranging from 140 – 250 mm, without any misalignment (solid) and misaligned (dashed).

It can be seen, that the coupling factor varies greatly with a change in the air-gap and also depends on the geometric design. The coupling factor map of P2 shows that the prototype was designed to have more tolerance in the y-direction. Moreover, the secondary determines the coupling quality, while the primary determines the shape of the coupling zones. As a result, a large range of k must be addressed in IPTSs, especially if interoperability class I is desired (public charging, see [50] and Section 2.5). In terms of Eq. (4.1), this means that a lot of variety is introduced into the system, making it difficult to transfer constant rated power over the whole coupling factor range.

The situation is even worse, when different topologies such as polarized (DDP) and non-polarized (CP) topologies are combined. These topologies have no coupling when placed on top of each other, requiring the introduction of a “natural offset” as defined in [50] to make

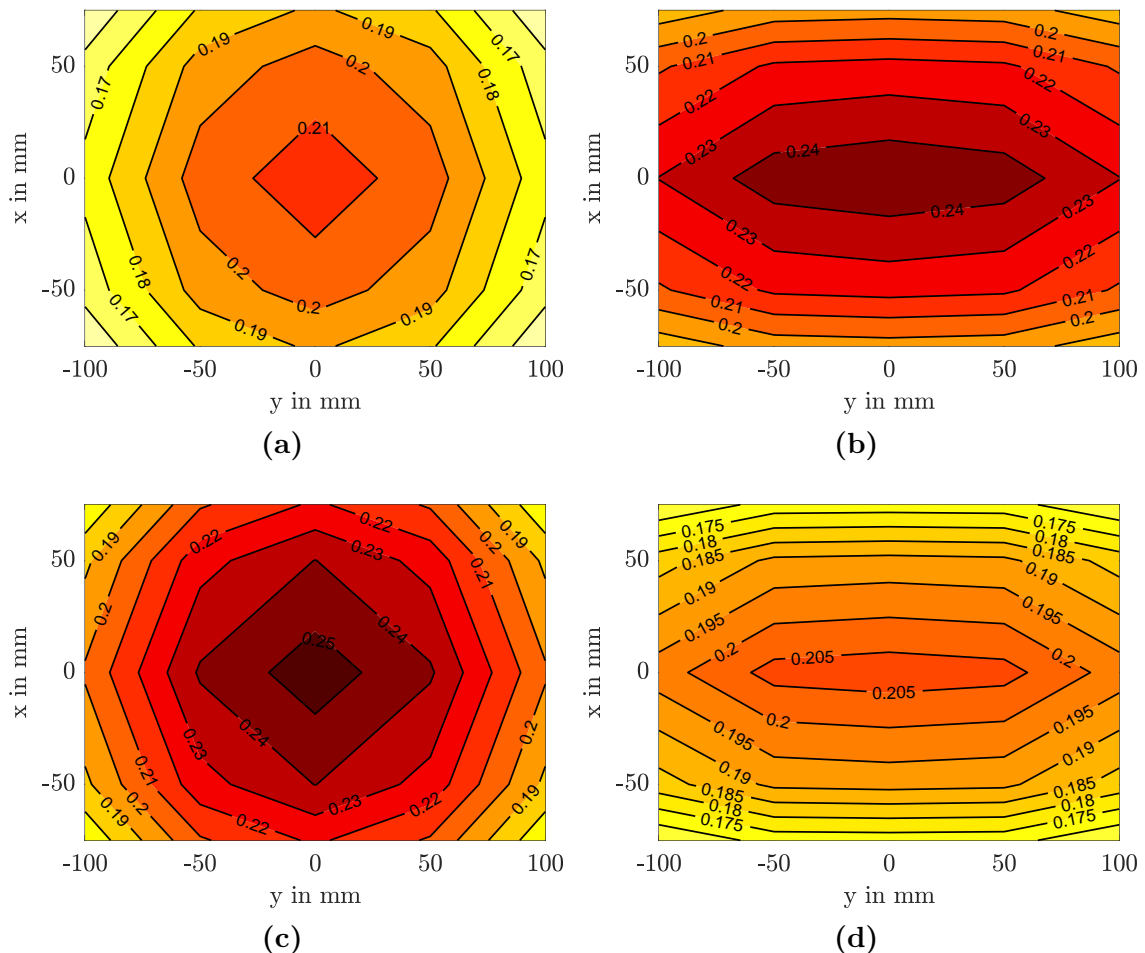


Figure 4.1 – Coupling factor xy-maps of two sets of CP with different geometries, P1 and P2, at $z = 140$ mm, (a) P1-P1 (primary side-secondary-side), (b) P2-P2, (c) P1-P2, (d) P2-P1. [P.3]

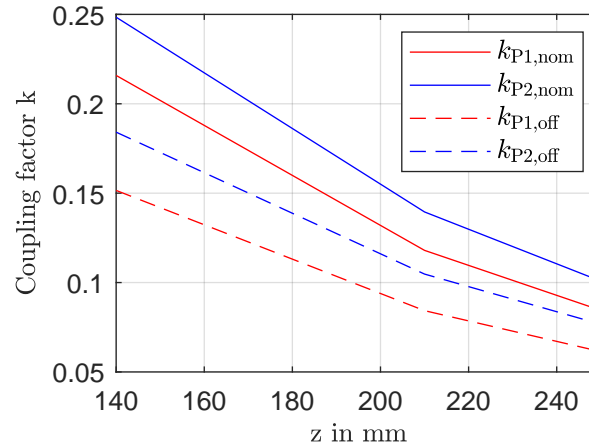


Figure 4.2 – Coupling factor over different air-gaps.

them compatible. This can lead to inherent positional sensitivity and increased leakage flux emissions [129, 130].

A lot of research was conducted to address the above mentioned issues, such as coils with increased coupling factor or less change in coupling factor [98–100, 106, 131–141], novel coil topologies [28, 59, 63, 142–147, P.4, 148–151], and designs with focus on emission reduction or novel (active) shielding [42, 64, 130, 152–162].

These designs are typically tailored to specific applications and power levels to optimize the coupling factor range, which is a critical consideration. However, developing a design for broad interoperability can be challenging because it requires both sides, and designing a primary coil for multiple secondaries (or vice versa) can be difficult because all possible coil combinations must be investigated. One possible solution to this problem is to establish a fixed coupling range that designers of both sides must comply with.

It should be noted that an IPTS with low coupling can still transmit rated or high power if the coil VA input is increased, as shown in Eq. (4.1). However, this is limited by other factors, such as litz-wire current limitations, thermal limits, and leakage flux emissions, and cannot be done indefinitely. This means that increasing power inherently leads to an increase in coil size, especially on the secondary side (see [P.5]), or power density [144, 163], which can lead to other issues such as thermal problems [164], cost, weight, volume, losses and emissions.

In general, the design of a coil is a multi-objective task that requires trade-offs in various aspects. As a result, this thesis does not consider the coil design itself, which includes factors such as winding turns, ferrite layout, shield size, and others, due to its complexity. Ultimately, the key aspects of the magnetics within the IPM are typically limited to maximum VAs, coupling, changes in coupling due to air-gap variations or interoperability requirements, and leakage flux emissions.

4.1.2 Leakage Flux Density and Regulatory Issues

As discussed earlier, leakage flux emissions are dependent on coil design and position and must be considered early in the design and evaluation. An important safety regulation is defined by the ICNIRP limitation as discussed in Section 2.5.1. Fig. 4.3 shows the zones that is critical and where the leakage flux emission limit of 15 μT applies to ensure safety for

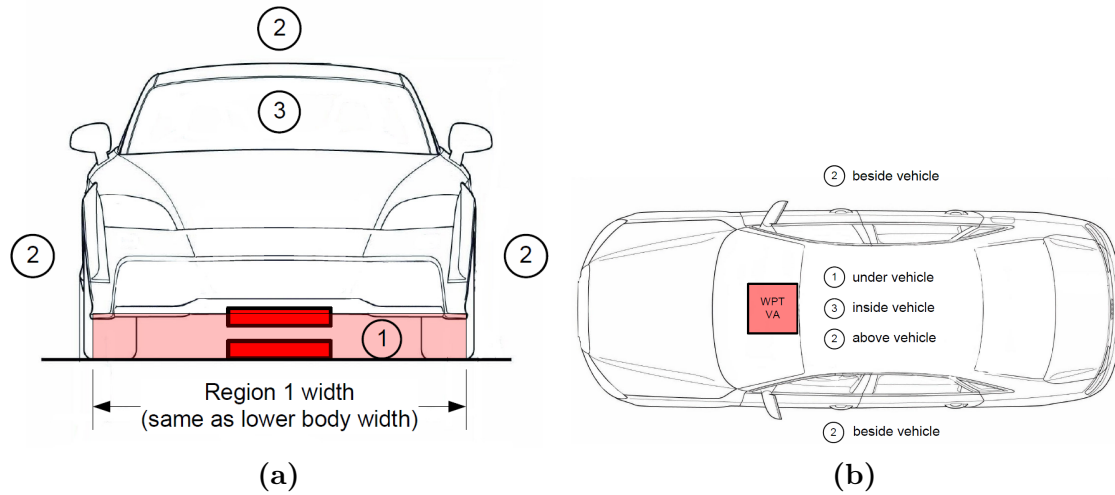


Figure 4.3 – Safety regulations defined by SAE J2954 based on ICNIRP reference levels (taken from [50]), (a) front view, (b) side view.

Cardiac Implantable Electronic Device (CIED)¹. In this work, the leakage flux at the edge of zone 1 is of interest.

It can be seen that the leakage flux at a certain distance is of interest, depending on the car width. To ensure that the emissions are below the reference value, FEM simulations are used. In order to capture this, leakage flux planes in XZ- or YZ-dimensions are placed in the simulation at a distance of (800–1100) mm, depending on the studied car width and the size of the measuring probe, from the center of the secondary coil (which is connected to the EV). To cover a range of car widths, the presented approach considers many planes at different distances. This also depends on the power level, as lower power IPTSs target smaller cars, while high power IPTSs typically target larger cars or HD vehicles.

The maximum leakage flux density in RMS is of interest and will be referred to as $B_{x,max}$ for the YZ-plane (in the x-direction) and $B_{y,max}$ for the XZ-plane (in the y-direction) in the following. The total maximum of both planes is called B_{max} . If the maximum at a certain distance is required, the distance is added to the index, e.g. a distance of 800 mm in x-direction is referred to as $B_{x,max,800mm}$.

To obtain the leakage flux fields from FEM simulations, the relative coil position and the respective currents for the rated power level and the phase between the currents are needed. This requires an FEM simulation for each position and OP, which is a time-consuming process. When investigating interoperability, many combinations may be of interest, so another more efficient and less time-consuming approach is presented later in this chapter.

There are many more restrictions and regulations that apply to an IPTS, such as SAR levels (induced current in human skin), EMI/EMC (CISPR), H-field at 10 m distance and touch currents. To investigate these aspect, a different scope of simulations is required, as they depend on harmonics, frequency interference and EMC issues. Hence, these aspects are out of scope and this thesis focuses on the $B_{max} = 15 \mu\text{T}$ limit. For more information on the limits that an IPTS must meet, refer to [50] and the referenced standards in this document.

¹The general public reference level from ICNIRP 2010 [113] is $27 \mu\text{T}$, but since the CIED reference level is lower, this is used. See [50] for more information.

4.1.3 Shielding

The coupling factor and leakage flux are affected not only by the relative coil position, but also by the proximity of the coils. To shield the main magnetic field from the car, an aluminum backplate is usually deployed as shield², attached to the bottom of the secondary side.

The secondary side of Fig. 3.8b with an 800×800 mm aluminum shield attached is shown in Fig. 4.4. The underbody of an EV is usually made of steel, and the aluminum plate shields the magnetic field. Eddy current losses in the thin aluminum shield are preferable to losses in the steel underbody of the EV. [50] also requires a steel plate to mimic the EV. The impact of a steel plate is minimal, but increases the simulation time significantly. Again, these issues add up when focusing on interoperability, which necessitates such simplifications or assumptions. Therefore, the steel plate is neglected in the FEM simulations within this thesis because the aluminum plate shields the magnetic field sufficiently.

The aluminum shield is necessary, but it changes the shape of the magnetic field and can lead to an increase in leakage flux, which is why a lot of research has been done on shielding as mentioned above. Besides active shielding solutions, Mohammad et al. showed that a magnetic shield (ferrite) is more effective for polarized coupling topologies and conductive (aluminum) shielding should be used for non-polarized coils [130, 150, 158]. Furthermore, studies have been conducted to determine if shielding on the primary side is sufficient enough to reduce leakage flux and save weight on the secondary side [161].

Another effect of the need for shielding is the area to be simulated. A certain distance between the outer edges of the simulated objects to the boundary is required in order not to influence the magnetic field distribution by the boundary condition of the edges of the simulation domain. The shield thickness is 2 mm and surface boundary condition is used to save simulation time (aluminum shield is not meshed and solved inside). The FEM is performed in steady-state and the material properties are linearized, so core losses are neglected. The simulated domain has a size of $3 \times 3 \times 3$ m and the coils are surrounded by air with $\mu_r = 1$.

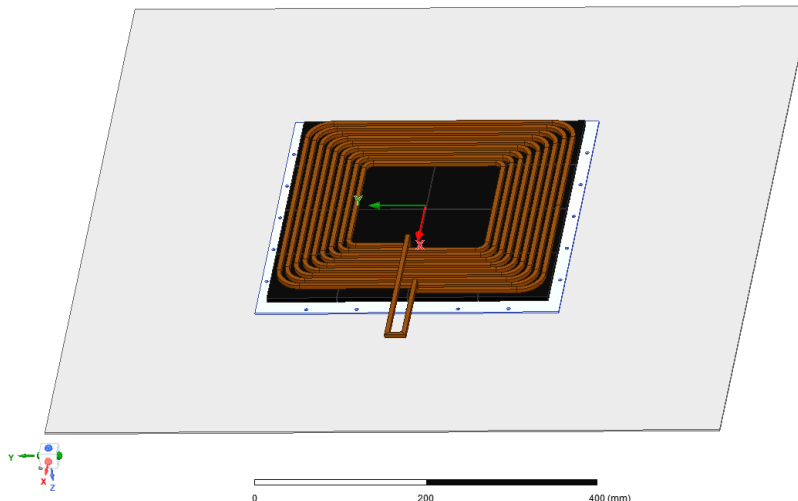


Figure 4.4 – Secondary side aluminum shield in a FEM simulation.

²[50] requires an 800×800 mm shield on the secondary side for reference testing.

4.2 Integration of Magnetic Aspects into the IPM

With the coil design details and interoperability aspects in mind, the integration of these aspects into the IPM can now be performed. Naturally, the metrics to be considered will depend on the application and interoperability requirements, but in any case the most important aspect is the power transfer, which is determined by the coupling. If interoperability is required between many coils or for many positions, a coupling factor range must be provided as a requirement.

As mentioned earlier, considering all the details of the coil design (e.g., shielding, coil size, turns) in interoperability studies (which typically involve many systems or coil combinations) leads to an overly complex analysis. Thus, in this section, only the effects of coupling, coil boundaries (VA_1 and VA_2) and leakage flux field distribution in the IPM are considered, while the other aspects (such as active shielding, redesign of coil geometry) can be used as measures to improve interoperability in a second iteration. It should be noted that this section does not consider these aspects under the conventional coil design aspects (optimizing or designing for an optimal OP/condition), but under interoperability aspects (variation is inevitable and how to deal with it). In order to assess or consider interoperability during design, a different view of these metrics is required.

First, a CCP is introduced, similar to the ICP from Section 3.2.1, then the transfer between the GA and VA interface is discussed, followed by the impact of coupling and its change on the CCPs. Fourth, the coil boundaries that are considered in the method integration are discussed. Finally, an approach is presented for integrating leakage flux information into the IPPs and for introducing a new leakage flux boundary.

4.2.1 Coil Capability Planes

A CCP, as already briefly described and showed in Section 3.4 and Fig. 3.14 can be derived in a similar way to the ICP and will have a shape like the ICP in Fig. 3.5d. The magnetic coils used for IPT are usually limited in maximum voltage and current only by the material (litz-wire). The VA of the coils must be large because they must compensate for the low coupling (see Eq. (4.1)) and there is no phase angle limitation as there was for the ICPs.

In addition, there are no lower bounds for voltage and current, and a minimum active power boundary $P \geq P_{\min}$ is required to create a meaningful CCP to aid in design or evaluation. As a result, each CCP is associated with a specific output power. The minimum active power limit also implies a minimum current to be supplied ($I_{\min} = P_{\text{out},\min}/V_{\max}$). It should be emphasized that the minimum current should be determined with interoperability in mind, as the rated $P_{\text{out},\min}$ does not necessarily need to be provided over the entire coupling range and could be reduced in maximum offset situations. However, the CCP itself must be designed for the output power under consideration.

The CCPs then can be created at each interface and the GA CCPs are shown in Fig. 4.5 in black (no output power boundary, $I_{1,\min} = 5$ A), blue ($P_{\text{out},\min} = 10$ kW), and purple ($P_{\text{out},\min} = 9$ kW) at the GA and VA interfaces on the left and right side, respectively. Additionally, the VA CCPs are shown at the same interfaces in red ($P_{\text{out},\min} = 10$ kW) and magenta ($P_{\text{out},\min} = 9$ kW). This was done for a fixed position and consequently a fixed coupling factor of $k = 0.22$.

To evaluate the magnetic coupling between two coils, the CCP of the VA coil on the GA interface or vice versa is of interest, since it represents the coil capabilities on the other side of the air-gap. Because of the low coupling in IPTSs (due to the high ground clearance), the

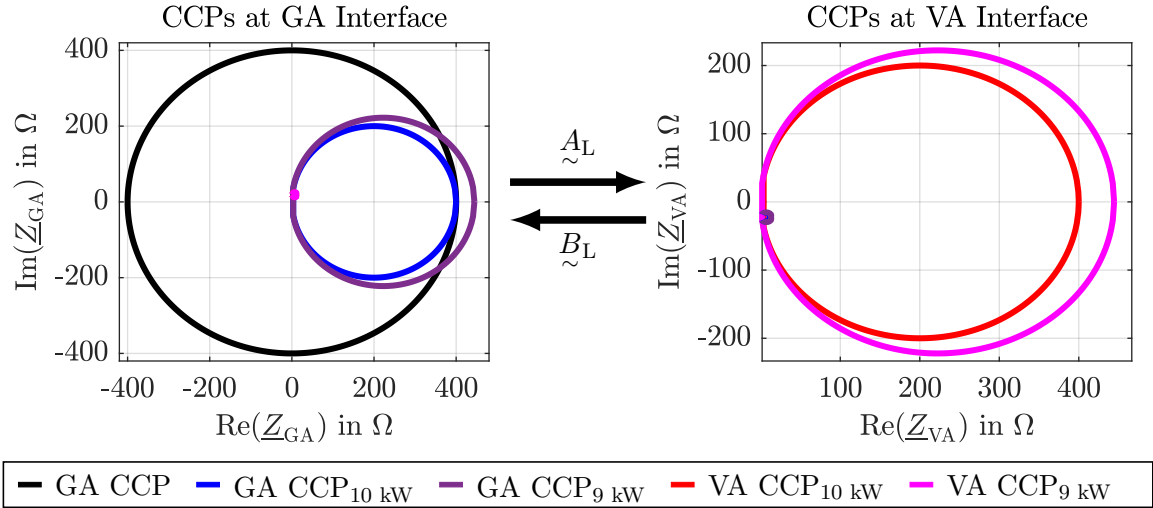


Figure 4.5 – Different CCPs at the GA and VA interface.

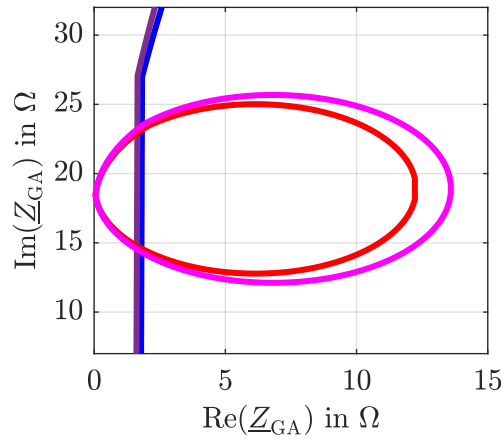


Figure 4.6 – VA CCPs at the GA Interface (zoomed in on Fig. 4.5).

large CCP of the VA coil at the VA interface becomes very small at the GA interface (and vice versa), as can be seen in Fig. 4.5. A closer look at the GA interface of Fig. 4.5 is provided in Fig. 4.6. It can be seen that the CCPs are very sensitive to the transmitted power level.

Besides the sensitivity to the power level, the main aspect that defines a CCP at its opposite interface is the coupling factor k . A closer look at the matrix \tilde{A}_L from (3.10) and Fig. 3.3 shows that it can be split into three parts, each of which is only affected by L_1 , L_2 or M , respectively. The matrices \tilde{A}_{L1} and \tilde{A}_{L2} are upper triangular matrices and represent (like series tuning) a simple shift of the IPP up or down in the complex plane (see Chapter 6), depending on the sign of the impedance (capacitive or inductive). As such, the shrinking effect is mostly related to the mutual inductance M , and since the variations in L_1 and L_2 are usually small (especially at high air-gaps), it is mainly due to the coupling factor k .

To illustrate this, the same VA CCP from Fig. 4.5 ($P_{\text{out,min}} = 10$ kW) is transferred from the VA to the GA interface (using \tilde{B}_L from Eq. (3.11)) for different couplings and the results are shown in Fig. 4.7.

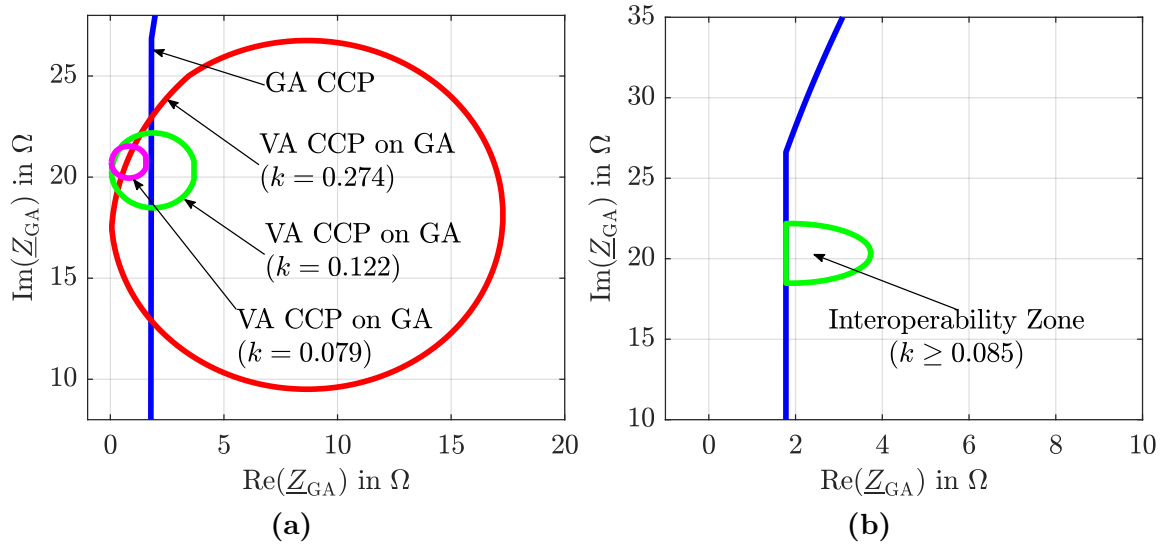


Figure 4.7 – GA CCP (blue) for $P_{\text{out}} = 10$ kW with VA CCPs (red, green and magenta) transferred to the GA interface at different coupling conditions, (a) Detailed view of the VA CCPs for different couplings and (b) the resulting interoperability zone for k_{\min} .

It can be seen that the coupling factor k is directly related to the size of the VA CCP, which shrinks drastically with lower coupling. The coil boundaries were set to $V_{1,\text{max}} = V_{2,\text{max}} = 2$ kV and $I_{1,\text{max}} = I_{2,\text{max}} = 75$ A for all cases, as in the previous example presented in Section 3.4.

If this transfer of the VA CCPs to the GA interface (or vice versa) is repeated for multiple secondaries, or for one secondary at many different positions and air-gaps, an interoperability zone can be derived in which safe operation can be ensured at all positions or all coil combinations (within the coil boundaries). The interoperability zone for Fig. 4.7a is shown in Fig. 4.7b. It can be seen in Fig. 4.7a that the case $k = 0.079$ does not overlap with the GA CCP and therefore this VA cannot operate with the GA under this condition or coupling. As a further result of this process, a minimum coupling factor k_{\min} can be derived for the coils (or coil sets) to be interoperable. For this example, it was determined that the lowest allowed coupling factor to overlap with the GA CCP must be $k_{\min} = 0.085$.

This approach allows the evaluation of different magnetic coils and their coupling by comparing the resulting IPPs without having to consider the electronics. An example of this application was first presented in [P.1].

4.2.2 Boundaries and Limitations of CCPs

The implications of some of the limitations have already been discussed in the previous section. However, this section provides a brief summary of the most important defining aspects of CCPs in terms of interoperability.

Minimum and Maximum Power Boundaries Limiting $S_{\text{in,max}}$ is not as important as it was for the ICP in Section 3.2.1. As mentioned above, the VA of the coils is very high, resulting in large CCPs as shown in Fig. 4.5, e.g. the coils from IPM Example 1 in Section 3.4 were

designed to transfer $P_{\text{out}} = 10 \text{ kW}$, but their maximum rating allowed them to transfer $2000 \cdot 75 = 150 \text{ kVA}$.

The importance of the $P_{\text{out},\text{min}}$ limit has been explained in the section above. It defines the lower coil limits and the size of the CCP as shown in Fig. 4.5 for a power change from 10 kW to 9 kW.

Voltage, Current and Phase Limitations These limitations were discussed in the previous section. The phase angle does not restrict the CCP which is why the full circle can be used. The upper voltage and current limitations are restricted by material ratings. Furthermore, these can be restricted by parasitic effects (maximum coil voltage) and leakage flux limitations (current and phase angles), which will be discussed in detail in the next section.

However, the importance of the upper coil limit on the CCP and therefore the choice of the correct litz-wire must be emphasized here. Fig. 4.8 shows the VA CCP of Fig. 4.7a for different upper secondary coil current limits.

Two things can be drawn from this figure. First, the choice of litz-wire capabilities can help increase the CCP, which is of course limited by cost and weight issues and other effects such as volume, skin and proximity losses, and thermal effects. Second, if this is repeated for more currents, isolines can be introduced into the IPPs. This is shown in the next section.

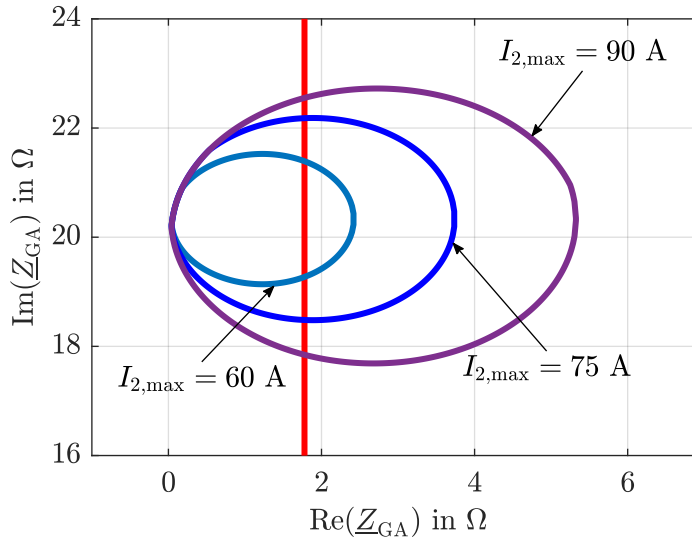


Figure 4.8 – GA (red) and VA CCPs at the GA interface for $P_{\text{out},\text{min}} = 10 \text{ kW}$ for a fixed coupling of $k = 0.1224$ and different secondary coil limitations: $I_{2,\text{max}} = 60 \text{ A}$ (turquoise), $I_{2,\text{max}} = 75 \text{ A}$ (blue) and $I_{2,\text{max}} = 90 \text{ A}$ (purple).

Inductance Limitations As discussed above, the self-inductances are relatively constant and cause the IPP to move up and down. Most of the variation, such as power and current, is due to the change in mutual inductance and hence the coupling factor k .

4.2.3 Magnetic Leakage Flux Density in the IPM

Due to Electromagnetic Field (EMF) exposure and for safety reasons, another requirement of the IPTS for EV charging is that the magnetic leakage flux density must remain below

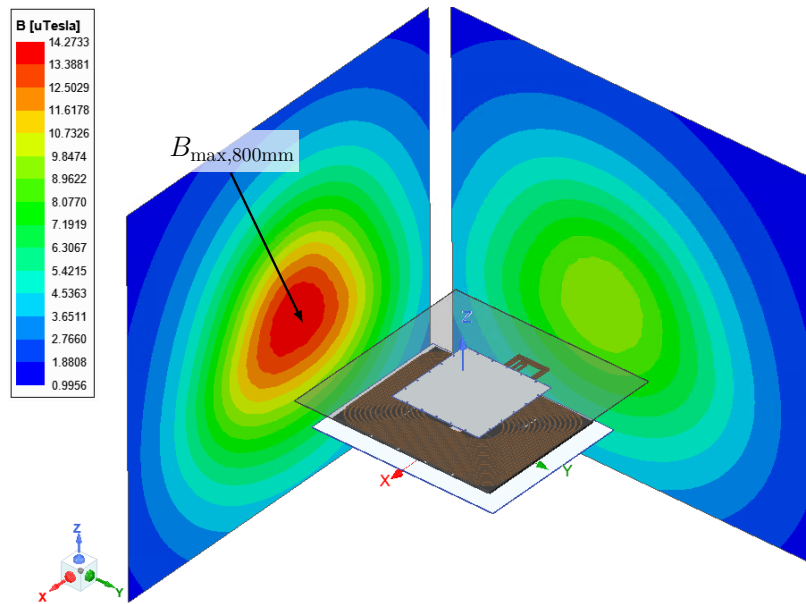


Figure 4.9 – FEM simulation with planes for obtaining the leakage flux values.

the reference value $B_{\max} = 15 \mu\text{T}$ around the vehicle [50, 113]. In order to comply with this, measurements and simulations of the maximum magnetic flux density are performed in the XZ- or YZ-planes at a distance of (800–1000) mm (in x- or y-direction) from the center of the secondary coil, which is where the vehicle body is assumed to end, and thus this is the area of interest for safety [64, 130, 147, 150].

Typically, this is done with an additional FEM simulation step by using the determined coil currents and their phases from the designed OP to validate that the system remains within the guidelines (see [42, 101, P.1, 131, 132, 157, 158]). An example of such an FEM simulation is shown in Fig. 4.9. The leakage flux planes show the magnetic field distribution at the area of interest, in this case at a distance of 800 mm, and the maximum can be extracted from these planes.

In terms of interoperability studies, where many combinations or positions need to be investigated, the time taken by this approach due to the second step is a disadvantage. Furthermore, in early design stages, the system (phase angles, worst case design, nominal design approach) may not be fully defined, which means that the OPs or control strategies are not known, and this also means that the currents are unknown and no early statements about the leakage flux can be made with this approach.

Therefore, in this section, an approach is presented that allows the leakage flux information of the coils to be considered in the IPPs without the need for additional FEM simulation, thus allowing leakage flux assessment at an early design stage.

The idea of this approach is to extract the leakage flux information once for each position and then scale it with the corresponding currents and phases. If ferrite saturation effects are neglected, which is a reasonable assumption for the currents at power levels $P \leq 10 \text{ kW}$, the leakage flux B_{\max} is linearly proportional to i_1 and i_2 . The smallest non-brittle ferrite tile sizes are usually large enough at this power level.

The magnetic flux density \vec{B} at each point in the simulation domain is a three-dimensional vector with the X, Y, and Z components of the magnetic field. For comparison with reference values, the magnitude (root sum squared) is required and can be calculated with Eq. (4.2).

$$B_{\max} = |\vec{B}| = \sqrt{\underline{B}_x \cdot \underline{B}_x^* + \underline{B}_y \cdot \underline{B}_y^* + \underline{B}_z \cdot \underline{B}_z^*}. \quad (4.2)$$

The magnetic flux density vector is a superposition of both coil currents and thus can be divided into the contributions of the primary and secondary currents I_1 and I_2 :

$$\vec{B} = \begin{pmatrix} \underline{B}_x \\ \underline{B}_y \\ \underline{B}_z \end{pmatrix} = \begin{pmatrix} \underline{B}_{x,I1} + \underline{B}_{x,I2} \\ \underline{B}_{y,I1} + \underline{B}_{y,I2} \\ \underline{B}_{z,I1} + \underline{B}_{z,I2} \end{pmatrix}, \quad (4.3)$$

which can be further divided into a fundamental leakage flux contribution per current. For example, the x-component of $\underline{B}_{x,I1}$ can be written as

$$\underline{B}_{x,I1} = \underline{B}_{x1} \cdot \underline{i}_1 = \underline{B}_{x1} \cdot I_1 e^{j\varphi_{I1}} \quad (4.4)$$

with $\underline{B}_{x1} = B_{x1, \text{re}} + j \cdot B_{x1, \text{im}}$ being the contribution of the x-component for $\underline{i}_1 = 1 \angle 0$ A. This can be applied similarly to the other components and the secondary current. As a result, the contributions can be divided into:

$$\vec{B} = \begin{pmatrix} \underline{B}_{x1} \\ \underline{B}_{y1} \\ \underline{B}_{z1} \end{pmatrix} \cdot \underline{i}_1 + \begin{pmatrix} \underline{B}_{x2} \\ \underline{B}_{y2} \\ \underline{B}_{z2} \end{pmatrix} \cdot \underline{i}_2 = \vec{B}_1 \cdot \underline{i}_1 + \vec{B}_2 \cdot \underline{i}_2 \quad (4.5)$$

with \vec{B}_1 being the flux density for $\underline{i}_1 = 1$ A while $\underline{i}_2 = 0$ and \vec{B}_2 vice versa.

Scaling the flux density vector with currents can be achieved if the fundamental contributions are known. These contributions can be extracted as complex values from the FEM simulation, which requires two simulation steps ($(\underline{i}_1, \underline{i}_2) = (1, 0)$ A and $(\underline{i}_1, \underline{i}_2) = (0, 1)$ A), only one more than for the inductance calculation. Despite doubling the time required, this approach allows early assessment of leakage flux.

In summary, the leakage flux contribution of each coil can be determined per current and, through linearization, extrapolated for any current and phase. The contribution of each coil can then be superpositioned to obtain the maximum flux density (B_{\max}). This approach was first published in [P.2].

To illustrate this, the x-, y-, z-components from the IPM Example 1 (Section 3.4) are shown in Fig. 4.10a, Fig. 4.10b and Fig. 4.10c at the BY-plane. In the following, the more critical BY-plane at a distance of 800 mm will be examined, but the principle is similarly applicable to the BX-plane, and its x-, y-, and z-components are shown in Fig. 4.10d, Fig. 4.10e and Fig. 4.10f.

These planes were created for $I_1 = 75$ and $I_2 = 0$ A and the sum of all components, $B_{\max} = |\vec{B}|$, is shown in Fig. 4.10g (BY-plane). It can be seen that the most dominant component is the z-component. This varies for different coil topologies and studies on leakage flux patterns for different topologies can be found in [130, 150, 161].

Aluminum shielding was used here and the study shows the effect of shielding on the field distribution and that scaling is still possible.

To estimate the true leakage flux, the contribution of the secondary cannot be neglected. And the leakage flux plane at the BY-plane for $P_{\text{out}} = 10$ kW at 420 V ($I_1 = 75$ A and

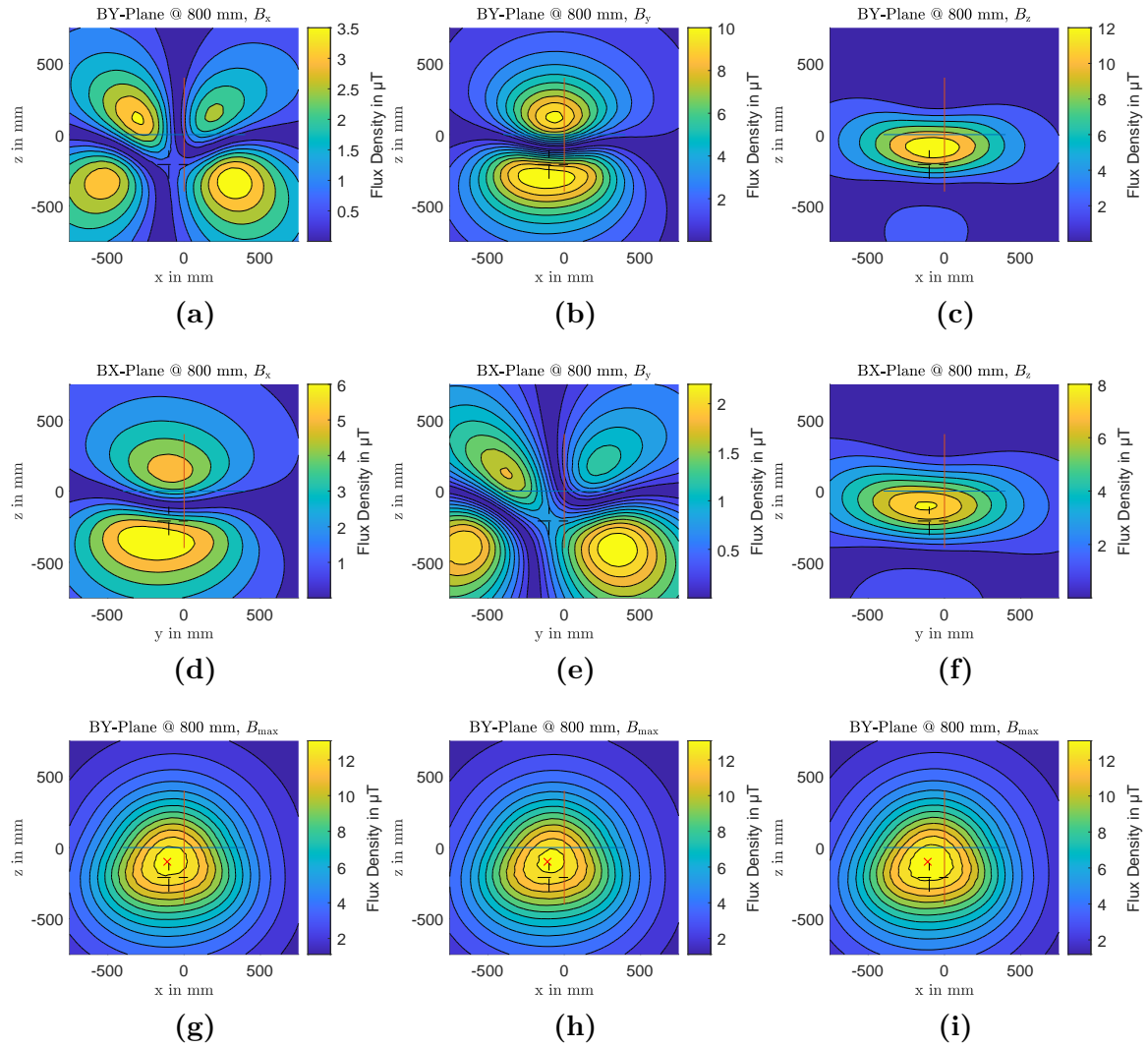


Figure 4.10 – Leakage flux plane analysis of the IPM Example 1. (a)-(c) x-, y-, and z-components and (g) B_{\max} of BY-plane at $I_1 = 75$ A and $I_2 = 0$ A at $(x, y, z) = (0, 75, 210)$ mm, (d)-(f) x-, y-, and z-components of BX-plane for the same operating conditions, (h) B_{\max} of BY-plane at same position with $I_1 = 75$ A, $I_2 = 70$ A and $\varphi_{i2} = 90^\circ$, (i) similar to (h) but with phase adjusted to $\varphi_{i2} = 60^\circ$.

$I_2 = 70$ A) at ideal phase ($\varphi_{i2} = 90^\circ$) is shown in Fig. 4.10h. It can be seen that the contribution to the leakage flux arises mainly from I_1 , as there is almost no difference to the leakage flux distribution with $I_2 = 0$ A. The phases were assumed to be ideal and a change in phase of i_2 (which can occur without active rectification or proper system control) is shown in Fig. 4.10i where the phase was set to $\varphi_{i2} = 60^\circ$.

Furthermore, to emphasize the effect of distance, i.e. car width, Fig. 4.11 shows the BY-planes at 800 mm, 900 mm and 1000 mm distance. This shows the sensitivity of the leakage flux distribution, as the maximum leakage flux decreases significantly with increasing distance.

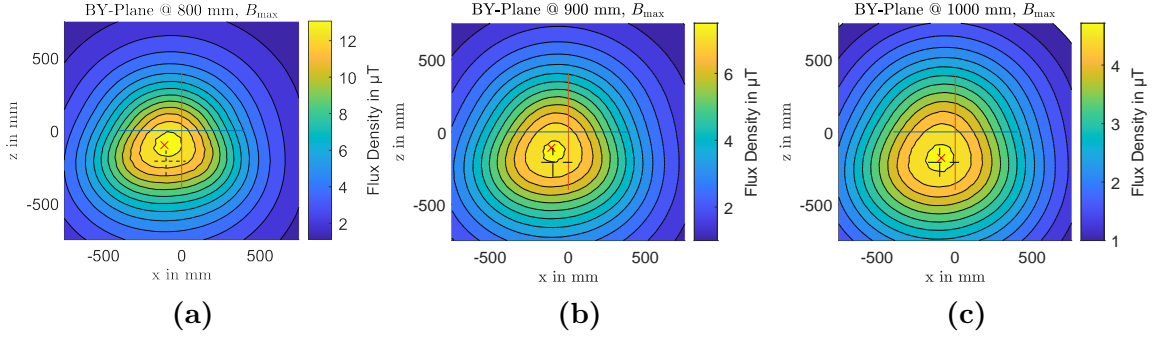


Figure 4.11 – Leakage flux plane analysis of IPM Example 1 (10 kW OP) at different distances (BY-plane), (a) 800 mm, (b) 900 mm and (c) 1000 mm distance of the secondary coil center.

For the implementation of leakage flux planes into the IPM, it is helpful to distinguish between matched (same primary and secondary coil size) and non matched systems. In general, only the maximum of the whole plane is of interest. The flux density depends on both coil currents i_1 and i_2 , but for systems with small secondaries, the primary is the main contributor to the leakage flux [130, 143].

This was also shown in Fig. 4.10 and can be confirmed by observing the magnetic leakage flux of IPM Example 1 (Section 3.4) from the previous section for different coil currents, as shown in Fig. 4.12a. This approach was repeated for a range of primary and secondary currents, with only the maximum flux density in either the BY- or BX-plane being extracted. The gradient on the I_2 axis indicates that the contribution of the secondary current can be neglected and that, in this case, the maximum leakage flux can be simplified to be a function of only i_1 .

The graph from Fig. 4.12a can be used to determine the maximum allowed primary coil current $I_{1,B_{\text{max}}}$ for a given B_{max} limit. This results in a new coil current limit for the IPP at the GA interface, and thus a new $R_{\text{min},I}$, see Eq. (3.27). As a result, a new boundary for the ICP is introduced from Fig. 3.6 and illustrated in Fig. 4.13.

This was done for $B_{\text{max}} = 15 \mu\text{T}$ for the system from Fig. 4.12a. The resulting $I_{1,B_{\text{max}}}$ values for different air-gaps are shown in Fig. 4.12b for nominal (solid red) and offset (dashed red) positions. Fig. 4.12b also shows the primary current required to transmit $P_{\text{out}} = 10 \text{ kW}$ for different air-gaps (series-series tuning assumed for simplicity).

It can be seen that the allowed primary current is very high for small air-gaps, but decreases significantly with offset as well as with increasing air-gap. In some cases, the required primary current (to transfer a certain output power) cannot meet the EMF exposure limits. Usually, there is another limitation on the coil currents caused by the litz-wire capabilities, which depend on the material as well as the turns of the coil and should generally also be considered in such assessments.

For the CCP, this means that the minimum allowable real part (impedance) depends on the coil positioning and thus on the coupling factor k . As a result, for example, this can change the k_{min} from Section 4.2.1, as shown in Fig. 4.12c. This will be discussed in more detail in the next section.

As shown earlier, even small changes in the I_2 constraint have a huge impact on the CCPs (see Fig. 4.8), which is similar to I_1 . It is therefore important to keep this in mind when

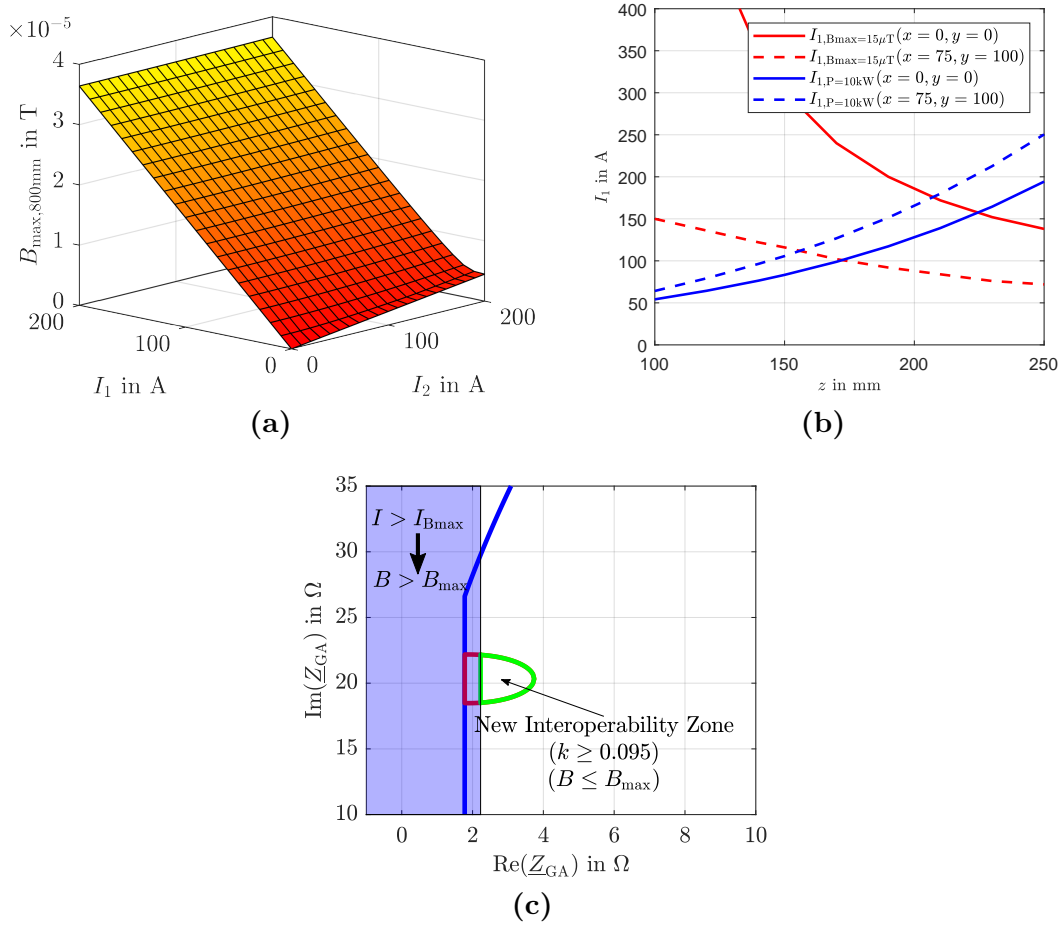


Figure 4.12 – Integration of leakage flux effects into the CCP, (a) $B_{\max,800\text{mm}}$ as a function of i_1 and i_2 , (b) maximum allowed primary coil current for $B < 15 \mu\text{T}$ (red) and required I_1 for $P_{\text{out}} = 10 \text{ kW}$ (blue) and (c) effects of leakage flux consideration on the CCP with a new interoperability zone and new k_{\min} .

designing the magnetics. A metric such as leakage flux per current or leakage flux per power could help to assess this in early magnetic design studies, as was done in [143, 146, P.5]. But the details of the geometric design of the magnetics are beyond the scope of this thesis.

The new interoperability zone now also ensures that the desired leakage flux limits are met. To achieve this, only the relations $B_{\max} = f(i_1)$ and $B_{\max} = f(i_2)$ are required.

It must be emphasized that the proposed method also works for systems with larger secondaries when the leakage flux contribution of i_2 is not negligible. The same procedure can be applied with the difference that $I_{B_{\max}}$ at the GA interface is also a function of i_2 .

Fig. 4.14a shows the leakage flux density similar to Fig. 4.12a, but for identical coils on the primary and secondary (the primary is mirrored to the secondary). This does not resemble a good design, but is only done to show matched system effects. The primary coil from the previous section was used with the same air-gap as in Fig. 4.12a. It can be seen that the influence of I_2 increases significantly. As a consequence, the maximum allowable primary current cannot be described by a single curve as was done in Fig. 4.12b. It now changes with different I_2 values as shown in Fig. 4.14b. Since I_2 is usually known in a fully determined

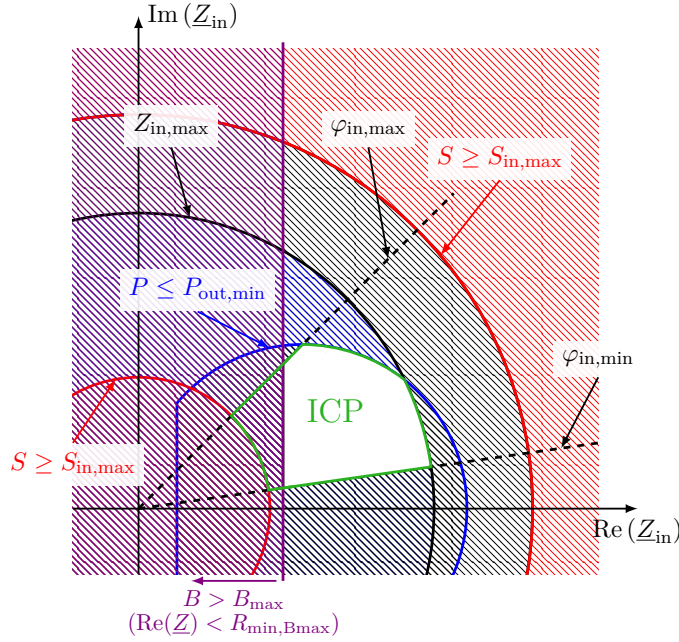


Figure 4.13 – ICP (green) for delivering $P \geq P_{out,min}$ (blue) with a maximum apparent power limitation (red), inverter boundaries (black) and leakage flux considerations (purple).

circuit, this is not a problem. Otherwise, a worst-case assumption for I_2 can also be made. Further information can be found in [P.6], where the methodology was applied to a 50 kW matched system.

Additional complexity is added by the coupling dependence. The leakage flux as a function of both currents is again shown in Fig. 4.14c but for three different coupling conditions. The effect of misalignment is critical as it is not scalable and also changes the gradient in both directions differently. For each coupling condition, the maximum allowable primary current was derived for a range of $I_2 = 0 - 200$ A and is shown Fig. 4.14d. These graphs now show different combinations of I_1 and I_2 , and it can be seen that operation under the k_{min} condition can be challenging (depending on the current limits, which could be even more critical at higher power, see next Chapter 6).

A comprehensive solution for matched systems can be derived using isolines in the IPP. The CCP (similar to an ICP) can be divided into a fine grid and for each point in the IPP the current can be calculated with

$$I = \frac{P_{out}}{\text{Re}(Z_{GA})}. \quad (4.6)$$

This can also be extended to many other parameters and will be discussed in the next chapter. The results for the GA and VA CCPs from Fig. 4.5 with I_1 - and I_2 -heatmaps are shown in Fig. 4.15a and 4.15b.

The current information for each point in the CCP is linked to the impedance, and when the CCP is transferred to another interface, the current information is transferred as well. As a result, the I_2 -heatmap can also be applied to the GA CCP at the GA interface, as illustrated in Fig. 4.15c.

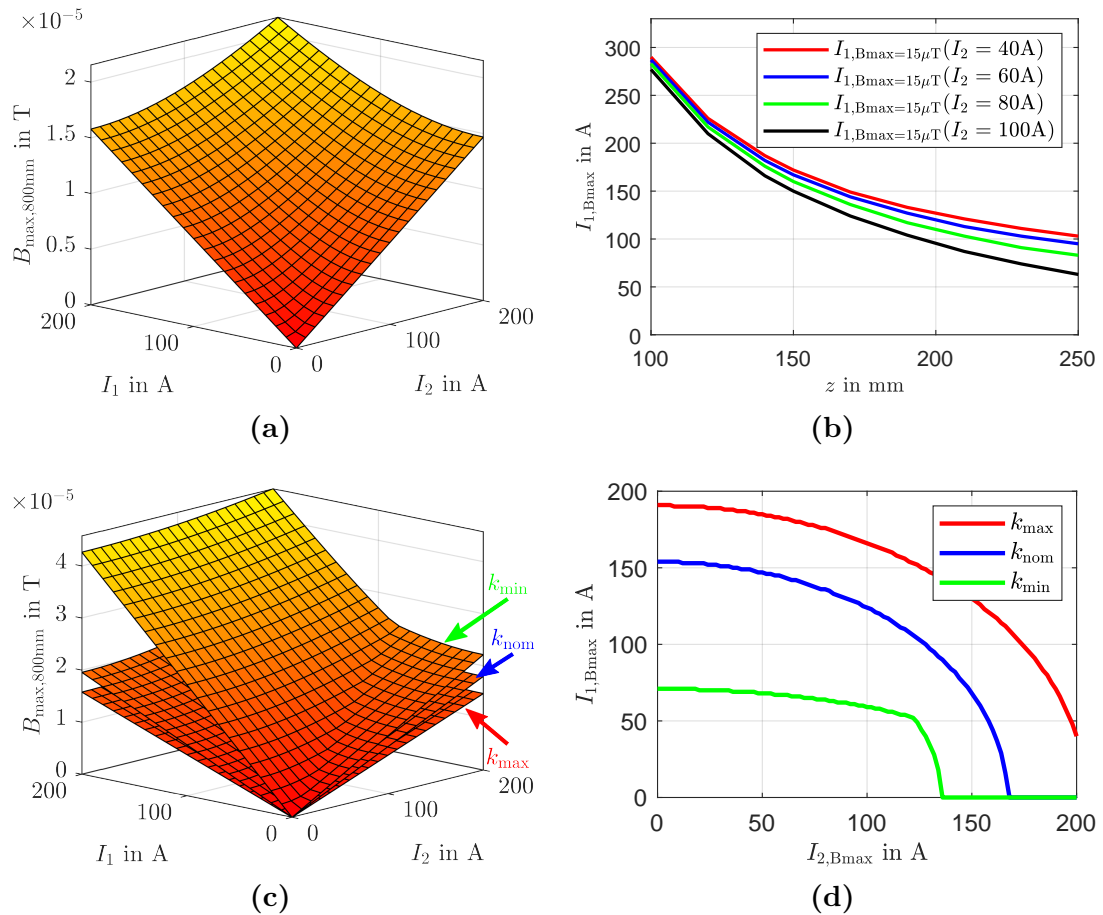


Figure 4.14 – Leakage flux effects for a matched coil system. B_{\max} as a function of I_1 and I_2 for (a) nominal coupling and (c) three coupling conditions (both at 800 mm distance); (b) maximum allowed primary coil current for $B < 15 \mu\text{T}$ for different values of I_2 and (d) the maximum allowed coil current combinations to stay below $15 \mu\text{T}$ for the coupling conditions from (c).

In general, this approach allows to consider different aspects, such as calculating losses etc., which will be described in the next chapter, while the focus of this section remains on the leakage flux.

In addition to evaluating the VA operation (finding low current regions) at the GA interface, this heatmap, together with Fig. 4.15a, allows the leakage flux to be calculated for each OP. With these heatmaps, the coil current combinations for each point within the CCP are known, and this can be used (with the approach described above) to calculate B_{\max} for each point. This has been done for the leakage flux planes at 800 mm distance and is shown in Fig. 4.15d.

Overall, the leakage flux is less than $15 \mu\text{T}$ and therefore not critical. However, as can be seen, the effect of the secondary current is not negligible, in contrast to the unmatched system. The boundary is no longer parallel to the y-axis (new $R_{\min,I}$). The isolines are curved and new hull curves have to be created as new boundaries (instead of R_{\min} boundaries).

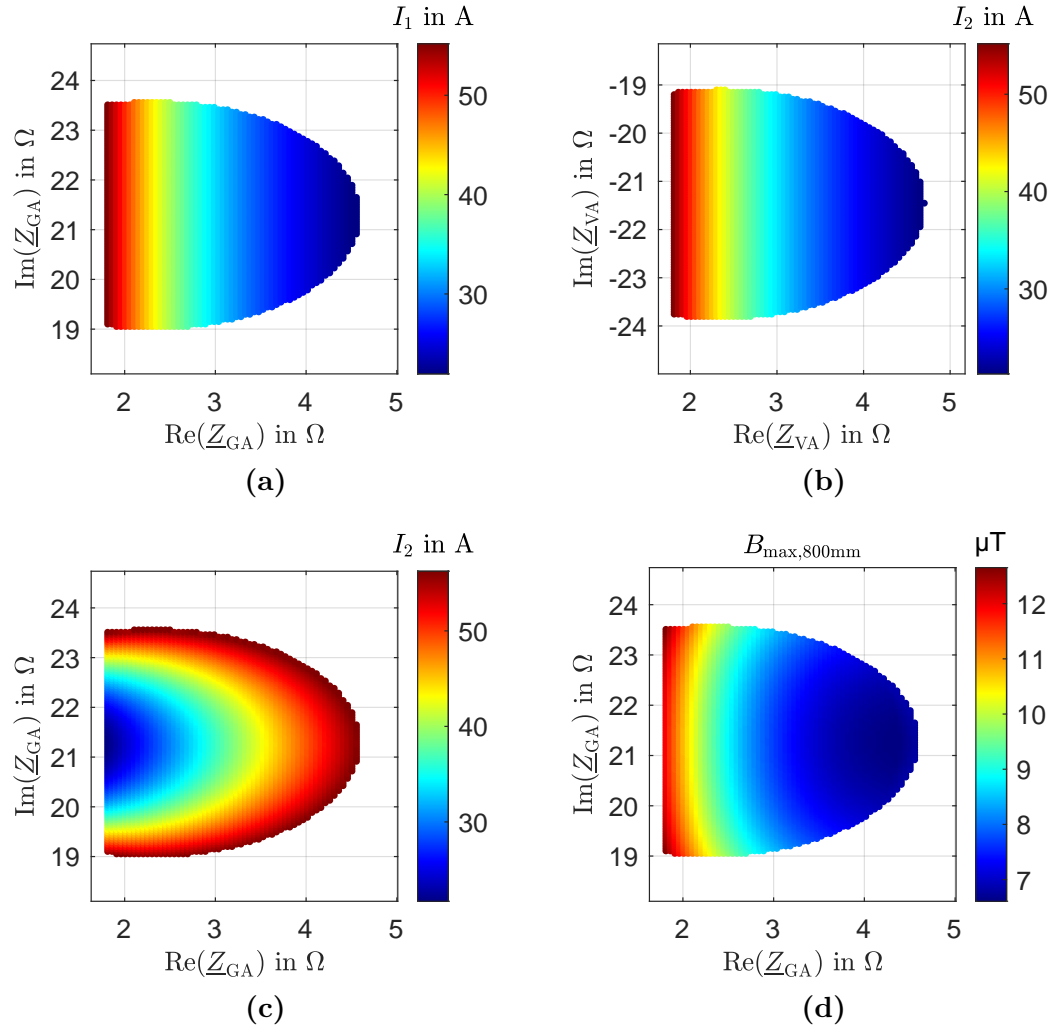


Figure 4.15 – CCP heatmaps of the matched 10 kW system at k_{\min} , GA CCP with (a) I_1 , (c) I_2 and (d) B_{\max} heatmaps; (b) VA CCP with I_2 heatmap.

The phase angle was assumed to be 90 degrees, but in (real) matched systems the control of the secondary and thus the effect on the phase influence is more important, as was the case in Fig. 4.10i. This will be discussed in more detail in Chapter 5.

The presented approach is also applicable to non-matched systems, but since the influence of I_2 can be neglected, the effort is not necessary and it is easier and time-saving to derive a new $R_{\min, I_{\max}}$ and apply it to the CCP.

4.3 IPM Example 2: Inverter Design Space for an Interoperable Primary System

The second example is described by the flowchart in Fig. 4.16 and can be seen as a continuation of Section 3.4. The aim of this example is to derive a design space for the electronics of a primary side in a public charging scenario. This requires interoperability with different secondaries. To avoid further simulations and validations, in this case different secondaries

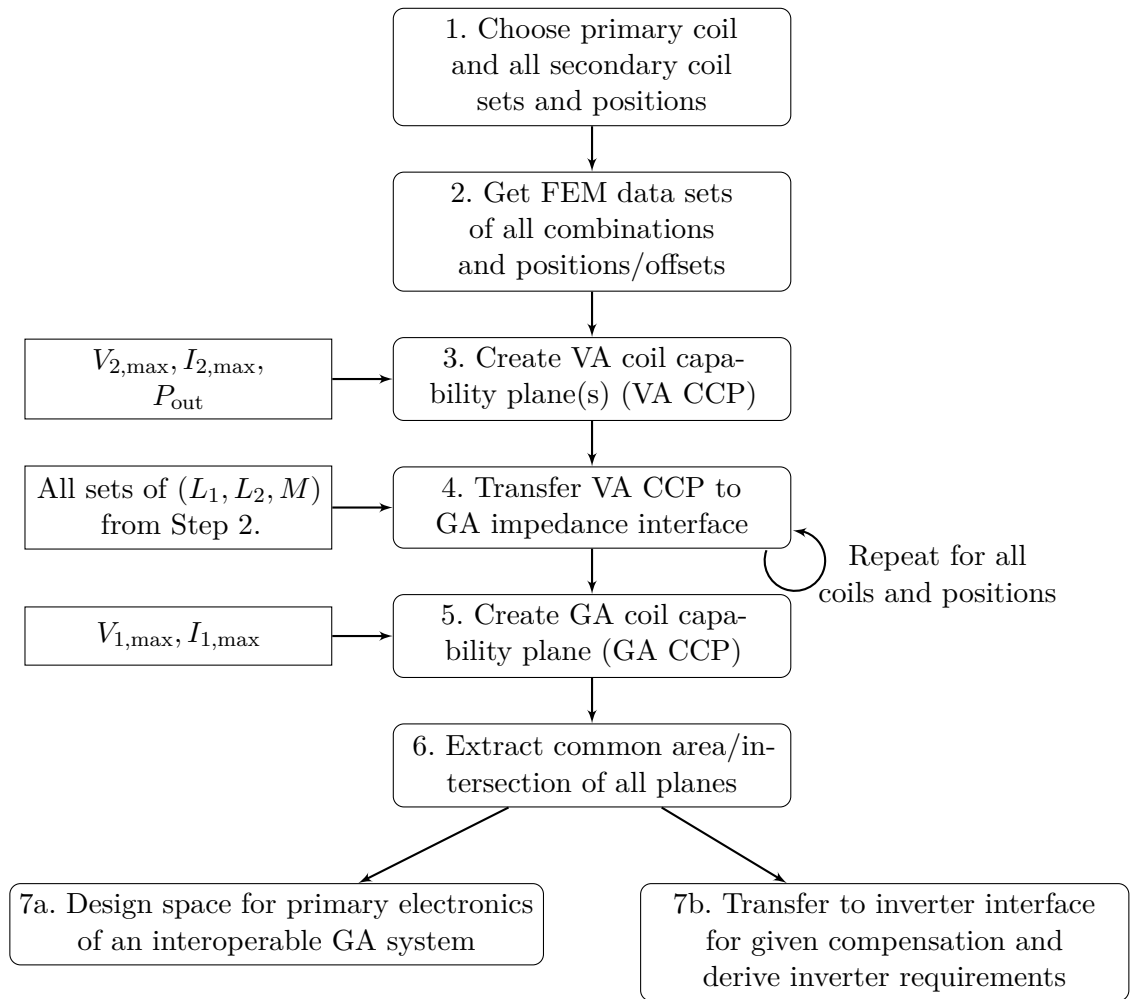


Figure 4.16 – Flowcharts of the methodology for evaluation of the coil couplings and guideline for deriving a design space for interoperable GA electronics.

are simulated by changing the air-gap of the secondary side from 140–210 mm in steps of 10 and 20 mm, which can be interpreted as cars with different ground clearance. Since only the difference in magnetic parameters or couplings is important in this case, it is sufficient to show the effects of the aspects studied in this chapter.

In the first two steps, the number of different secondary coils and the ground clearances that the primary must operate with must be defined, and the corresponding simulation data of the magnetics (or measured data) must be obtained for all positions/offsets and coil sets.

In the next step, the limits of the VA coils are used to derive the VA CCPs of all coils for a given output power level, and the results are transferred to the GA impedance interface in step 4. This must be repeated for all coils (sets of inductors). It is assumed that all secondary coils have the same limits and differ only in their inductances and coupling factors with the primary.

A similar GA CCP can then be derived with the primary coil boundaries. The common area of all transferred VA CCPs and the GA CCP marks the interoperability zone. This is the impedance range in which all the studied secondary sides and their offsets can be operated within the boundaries of both coils.

The interoperability zone can serve as a design space for interoperable primary side electronics because this area ensures operation within the coil boundaries for all air-gaps and offsets. The GA designer must provide the primary-side electronics capable of driving this “golden” area to achieve full interoperability. This includes the assumption that the secondary is also capable of matching this impedance range.

Furthermore, the results can be used to derive inverter requirements if a given compensation topology is used to transfer the interoperability zone to the inverter impedance interface.

As done with the IPM Example 1, this process was also applied to the system from Section 3.4. The results for different operating conditions are presented in Fig. 4.17.

The first figure (Fig. 4.17a) shows the GA CCP on the GA impedance interface with the boundaries of Tab. 3.5 for WPT3 ($P_{\text{out}} = 10$ kW). This CCP is a large IPP because the coil boundaries are not critical and are usually very high. The power level and the terminal voltage limits both affect the circle radius r_1 defined by Eq. (3.30).

The current limit in the primary coil can be seen as the dashed blue line in Fig. 4.17b, which shows a small part of Fig. 4.17a. The minimum real part of the GA impedance is limited by Eq. (3.28).

The VA CCP on the VA impedance interface looks similar because the same coil boundaries are applied. To transfer the VA CCP from the VA to the GA impedance interface (step 3 in Fig. 4.16) the matrix \tilde{A}_L (see (3.10)), which changes for each position, is used. This has been done for the nominal position (0,0,210) mm and is shown as the dark blue area in Fig. 4.17b. The red boundary now marks the area that can be driven by the primary coil but does not meet the boundaries of the secondary side. The dark blue area is the impedance range that lies within the boundary conditions of both coils. The smaller size of the resulting impedance region is due to the low coupling of IPTSs in general.

If this process is performed with the secondary at maximum offset, the impedance zone will deteriorate even further as the coupling decreases. Fig. 4.17c shows the results of repeating step 4 for the positions (0, 100, 210) mm, (75, 0, 210) mm and (75, 100, 210) mm. The color gradient heatmap indicates how many OPs could be driven in these areas (within the boundaries), where dark blue corresponds to the impedance area where only one of the four positions can be driven (nominal position (0, 0, 210) mm) and the golden area marks the impedance zone where all four examined positions can be driven within the coil boundaries. This is the interoperability zone resulting from step 6 (Fig. 4.16).

It is important to note that only the magnetics and coil boundaries are used to derive this interoperability zone. The electronics of both sides are not considered yet/here. The golden area allows the coupling to be evaluated for interoperability at the impedance interfaces. The interoperability requirements can be freely selected and adjusted.

To show the effect of larger coupling, the same study from Fig. 4.17c was repeated with the air-gap between the coils reduced to $z = 140$ mm and the results are shown in Fig. 4.17d. It is noteworthy that the interoperability zone increases with better coupling, which can serve as a design guide for a magnetics designer while also relaxing the design requirements on the electronics.

The effect of choosing a higher secondary coil current limit on the interoperability zone can be seen in Fig. 4.17e. Here, the analysis of Fig. 4.17c has been repeated with a secondary coil current limit set to $I_{2,\text{max}} = 100$ A. It shows that a robust coil design can help to relieve stress on other components, as a higher current limit significantly increases the interoperability zone.

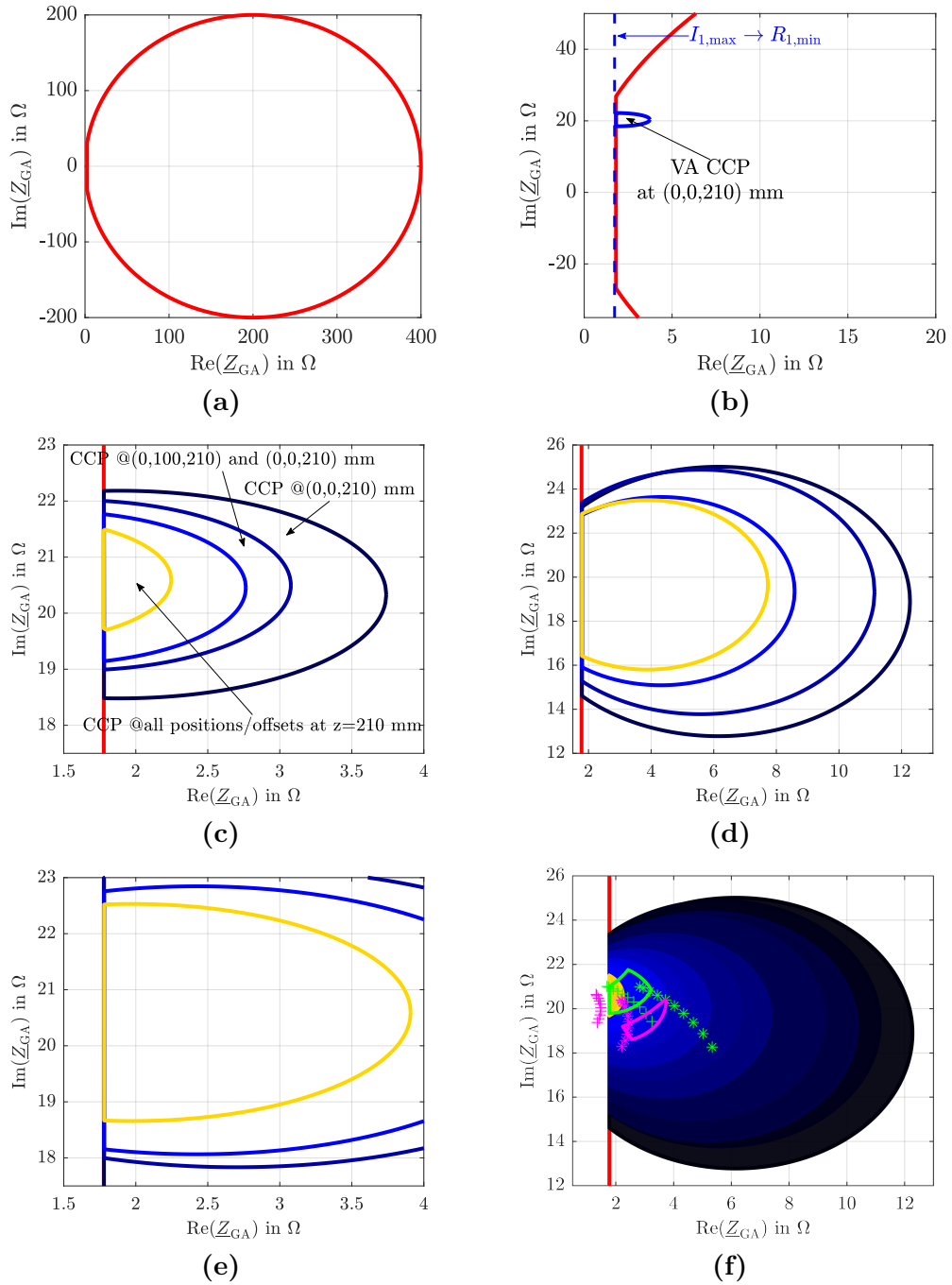


Figure 4.17 – Different WPT3 CCPs, (a) GA CCP at the GA interface. In (b)-(f) the red zone describes the impedance area which lies within the primary coil boundaries but outside the secondary coil boundaries. In (c)-(f) the blue and golden zones represent the impedance areas which lie within both coil boundaries, where the golden zone describes the interoperability zone. The gradient of the blue color represents the amount of operable points from almost all positions in light blue to only one in dark blue.

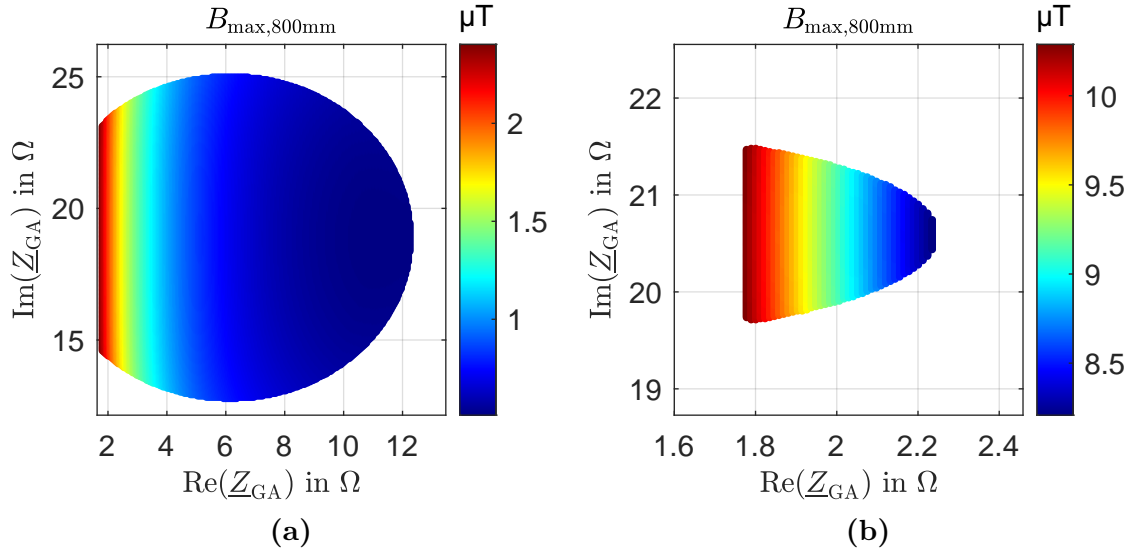


Figure 4.18 – IPM Example 2: CCPs with leakage flux heatmaps under (a) k_{\max} and (b) k_{\min} coupling conditions.

To further explore the relationship between coupling and interoperability zone, the study was repeated a third time, but this time with 20 different positions covering the entire Z2 air-gap class³ with the results shown in Fig. 4.17f. In particular, the inclusion of these additional couplings has a significant effect on the size of the interoperability zone.

As a last step, the leakage flux heatmaps were derived as explained in the previous section and the results for k_{\max} at (0,0,140) mm (Fig. 4.18a) and k_{\min} at (75,100,210) mm (Fig. 4.18b) of Z2 are shown in Fig. 4.18.

Overall, the study shows that it will be very challenging to achieve full interoperability at high power with the SAE J2954 reference system [50] unless there is an active tuning network on both sides that can shift the impedance to the desired area. Another conclusion is that simple, low-cost secondary systems with passive tuning are very restrictive because they cannot provide the same impedance and cannot mitigate against varying battery voltages.

To emphasize this, some OPs with constant output power ($P = 10$ kW) and different battery voltages ($V_{\text{bat}} = 280 - 450$ V) were calculated and transferred to the GA interface, similar to the first example presented (Section 3.4). This was done with the secondary placed at its nominal position (green asterisk marker) and also at its maximum offset (magenta asterisk marker) as shown in Fig. 4.17f. The different battery voltages result in a varying load distribution outside the controllable region, and active elements are required to shift the load into a feasible impedance zone. To show the effect of impedance tuning, these OPs were calculated and transferred back to the GA IPP with different values in the secondary LCC compensation. The results are shown as “+” markers (same colors) in Fig. 4.17f. While the OPs of the nominal position have been moved closer to the interoperability zone, the offset position cannot be driven by the new secondary tuning setup because the required primary current would be too high. This illustrates the complexity of an interoperable IPTS design.

This conclusion was reached after only evaluating the coils. However, the situation becomes more complex when the limits of the inverter are considered. For emphasis, Fig. 4.17f shows

³The total range of coil positions studied was (0, 0, 140) – (75, 100, 210) mm.

the ICP from Section 3.4 for two different primary LCC compensation settings. While one combination adequately covers the interoperability zone (green), the other is misaligned and the system cannot address offset positions (magenta).

In practice, many additional assumptions may be imposed on a real system, making it even more difficult to establish an interoperability zone.

4.4 Summary

This section provided a more in-depth look at the magnetics aspects of interoperability, introducing the CCPs and identifying the parameters that define them, while also providing a sensitivity analysis. The assessment of magnetics for full system interoperability was discussed and ferrite linearization was considered.

The impact of magnetic leakage flux on the system and its compliance with standards was presented, along with a solution to study it using FEM. These aspects were then integrated into the IPM from the previous section, and an example of how to evaluate magnetics with the IPM was given. The coils of the previous system were shown to have no leakage flux issues at the Z2 air-gap class, and the sensitivity of the ICP to tuning was discussed. An interoperability assessment of the coils was also demonstrated, emphasizing the need for early interoperability assessments implied by the small interoperability zone.

Before examining the sensitivity analysis in Chapter 6, the next chapter focuses on the electronics side of the system, providing a comprehensive analysis of the entire IPTS.

It is important to note that this study focused on examining the magnetics and accurately representing them in the IPM. There is potential to extend this to the design of the magnetics; however, the magnetic coupling between the coils is a significant challenge to independent design. Coil normalization could be a solution, as presented in [126], which provides a way to normalize and use the IPPs. The future work section 8.4 will explore this topic further, but magnetic design is out of the scope of this thesis.

5 Impact of Power Conversion Aspects and Losses on Interoperability of IPT Systems

In Chapter 3, several simplifications such as the FHA and idealized switches in the inverter and rectifier were used. As a result, harmonics and losses were neglected. These are reasonable assumptions when a ballpark solution is desired in a first iteration, and allowed to focus on explaining the procedure and introducing the interfaces and the method. Chapter 4 reversed these assumptions for the magnetic parts as it covered the details of the magnetics in the power transfer.

However, the efficiency of IPTSs, particularly in EV charging applications, is still a major concern. Despite the simplifications introduced in FHA, the complexity and losses of the power conversion stages make fundamental analysis insufficient in the long term.

Furthermore, efficiency becomes more important as the power transfer level is increased, as will be done in Chapter 6 and 7. This is also true for leakage flux emissions, since coil currents increase with higher power transfer, but the EMF exposure limit remains the same. It is therefore essential to consider system losses and leakage flux emissions comprehensively.

Therefore, this chapter aims to provide a full system and loss analysis, with a focus on interoperability. These issues are addressed by extending the IPM, introducing losses into the IPPs, and reversing some of the previously made assumptions in order to provide more information about various parameters, such as leakage flux exposure, within the created IPPs. However, the loss calculations in detail are very complex and individual, making it challenging to grasp them entirely. In addition, many dependencies affect these losses, which is why it is impossible to cover all of them in this thesis. Consequently, simplifications are necessary when integrating losses in the IPM, which is done in this chapter by investigating the losses on a system level. System efficiency can then be evaluated within the IPPs, allowing for better design decisions and extending its usefulness for evaluating control approaches. The extended approach including losses is then compared against the simplified approach and experimentally verified with the 10 kW system used in Chapter 3 and 4.

First, the losses in an IPTS are investigated for each component separately, starting with the inverter, followed by the rectifier stage and continuing with the remaining components. The losses are then integrated into the IPM, allowing isolines/heatmaps of different metrics to be introduced into the IPPs. The loss estimation and integration procedure is shown in two different ways, fixing either the input or the output power. The extended method is then applied to a 10 kW system in a comprehensive use-case, and comparisons are made with the simplified analytical approach, a physical circuit simulation, and the experimental results, which serve as a summary of the work in Chapters 3, 4 and 5. The results and an evaluation of how the different simulation methods can account for the losses are then discussed. Finally, a summary is given.

5.1 Modeling of Losses in IPT System Components

Chapter 3 introduced four impedance interfaces along the IPM. An IPTS topology with the impedance interfaces and their simplifications is shown again in Fig. 5.1. For the purpose of loss calculation, the four impedance interfaces must be extended and six power interfaces (P_{in} , P_{inv} , P_{GA} , P_{VA} , P_{rect} and P_{out} ,) are introduced as shown. This is necessary to cover the power conversion effects in the inverter and rectifier.

As mentioned earlier, the exact calculation of all system losses is challenging and may not be possible without the help of simplifications, simulations or physical experiments. However, many approaches for analytical loss estimation can be found in the literature (e.g., [164–172]) that can be applied here.

The assumptions made for the components of each interface and the equations used in this thesis are discussed below, separately for each component.

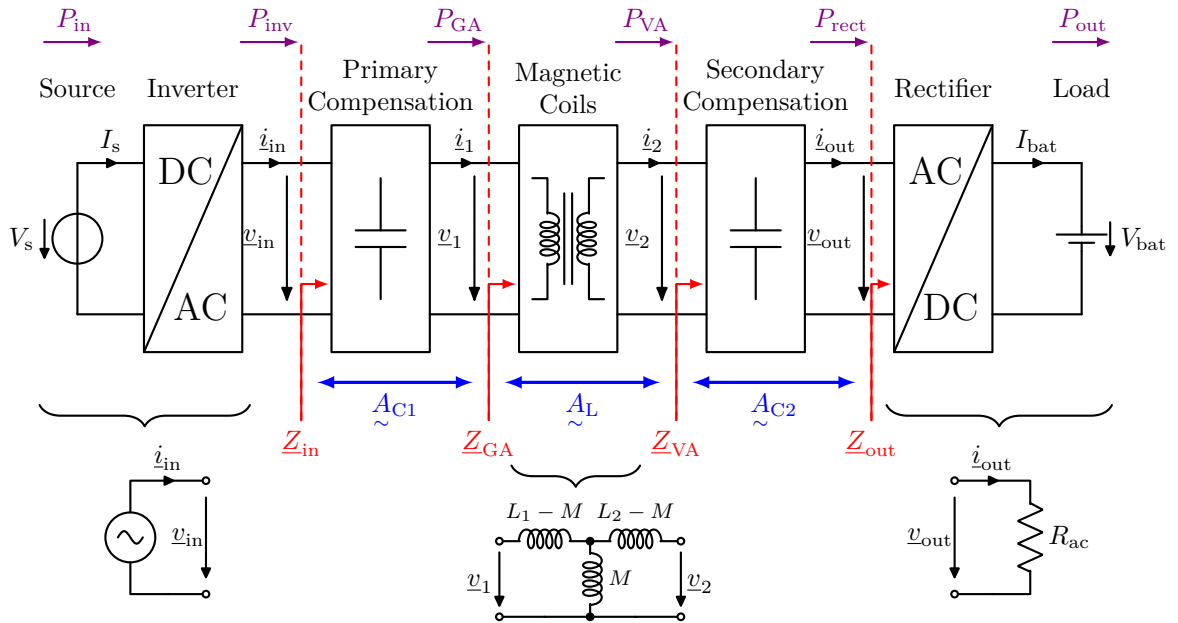


Figure 5.1 – IPTS topology with simplifications, impedance interfaces, transfer matrices and power definitions.

5.1.1 Primary Side Inverter Losses

The operating principle of the inverter and its important parameters have been described in Section 2.2.4. As mentioned, it is desirable to achieve ZVS to reduce losses, as MOSFETs have high turn-on losses and ringing can occur [172]. An important metric for achieving ZVS as well as balancing losses and control current is the conduction angle α . Losses are generally a function of the inverter current i_{in} , which in turn depends on the input voltage V_s . The design of the nominal voltage and current should always consider the losses that will occur because higher voltage means higher stress on the components and higher current leads to more generated heat, both of which increase the losses.

Inverter losses can be divided into switching (MOSFET) and conduction (MOSFET and diode) losses, which depend on conduction angle, characteristics of the switches such as forward voltage, on-state resistance, and dead time, and current.

The equations for the conduction losses of a full-bridge inverter are derived in detail in [165–167]:

$$P_{l,\text{diode}} = \frac{2\sqrt{2}}{\pi} V_f I_{\text{in}} \left[\sin\left(\frac{\alpha}{2} + \delta_d\right) - \sin\left(\frac{\alpha}{2}\right) \right] + \frac{2}{\pi} R_D I_{\text{in}}^2 \left[\delta_d + \frac{1}{2} (\sin(\alpha + 2\delta_d) - \sin \alpha) \right] \quad (5.1)$$

$$P_{l,\text{mos}} = \frac{2}{\pi} R_{\text{DS}} I_{\text{in}}^2 \left[\pi - \delta_d + \frac{1}{2} (\sin \alpha - \sin(\alpha + 2\delta_d)) \right] \quad (5.2)$$

where V_f , R_D , R_{DS} and δ_d are the threshold (or forward) diode voltage, equivalent on-state resistances of diodes and MOSFETs and dead-time, respectively. These values can typically be found in a data sheet. α and I_{in} are the conduction angle and inverter output RMS current.

The main loss contribution of the inverter arises from the switching of the MOSFETs. Depending on the phase angle φ_{in} (between the inverter voltage and current, also called the input impedance angle) and the conduction angle α , a conduction current can occur when a switch is operated, resulting in turn-on and turn-off losses. In this thesis, it is assumed that ZVS operation is achieved and therefore no turn-on losses exist when the condition of Eq. (5.3) is satisfied, according to [165]. Therefore, the next part focuses on turn-off losses, but these equations are similarly valid for turn-on losses when ZVS cannot be achieved.

$$\varphi_{\text{in}} \geq \frac{\pi - \alpha}{2} + \delta_d. \quad (5.3)$$

The turn-off losses can be calculated with Eq. (5.4) and depend on the switching frequency f_s . The turn-off energy $E_{\text{off,sw}}$ of each switch must be determined individually and can be found in the data sheet as a function of the DC source voltage V_s , and the amplitude of the instantaneous current $I_{\text{inst,sw}}$ through the switch at the turn-off moment¹. This current depends on the waveform of the inverter bridge current which in turn depends on the selected tuning topology and the operating and coupling conditions.

$$P_{l,\text{sw}} = f_s \cdot (E_{\text{off,sw1}} + E_{\text{off,sw2}} + E_{\text{off,sw3}} + E_{\text{off,sw4}}) \quad (5.4)$$

Fig. 5.2 shows I_{inst} and I_{in} in an LCC–LCC tuned system. The conduction angle in this case was $\alpha = 180^\circ$, and it can be seen how turn-off losses could be reduced by changing the conduction angle to α_2 , but advanced control methods are beyond the scope of this thesis.

Furthermore, it can be seen, that the harmonics strongly influence the current waveform [173]. As a result, FHA is no longer applicable and a physical circuit simulation model (e.g. PLECS or LTSpice) is required to obtain I_{inst} . Thus, the switching losses are neglected in the IPP when the inverter current is sinusoidal.

Generally, these switching losses could be considered in the IPP. However, a physical simulation for each of the numerous OPs studied within an IPP to obtain the switching losses would be required. Since these losses are small compared to the magnetic losses, as will be shown later in Section 7.3, this approach is too time consuming. A Fourier decomposition can be used to derive the switching losses analytically, but this is beyond the scope of this thesis (see future work, Section 8.4).

¹If no ZVS is achieved, then the turn-on losses can be considered by adding the turn on energy $E_{\text{on,sw}}$ which is a function of the instantaneous turn-on current through the switch.

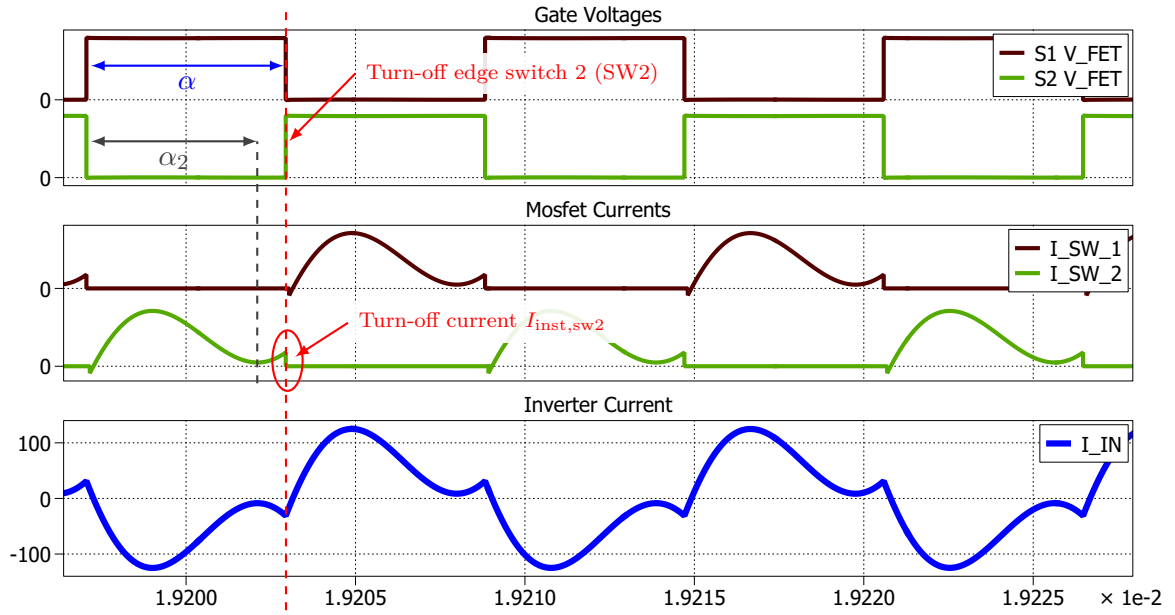


Figure 5.2 – Waveforms of the MOSFET switch gate voltages and currents and the resulting inverter output current (LCC–LCC system).

If the bridge current is sinusoidal (e.g., in a series-series tuned system), then the approximation in Eq. (5.5) can be used to obtain the switching losses [165, 167]. E_{on} and E_{off} are the turn-on and turn-off energy of the MOSFET switch under reference conditions, V_{R} and I_{R} are the reference drain-source voltage and source current, respectively. Q_{RR} and I_{RD} are the reverse recovery charge and the reference current of the diode.

$$P_{\text{l,sw}} = 2\sqrt{2}V_{\text{s}}I_{\text{in}} \cos\left(\frac{\alpha}{2}\right) \cdot f_{\text{s}} \left(\frac{E_{\text{on}} + E_{\text{off}}}{V_{\text{R}}I_{\text{R}}} + \frac{Q_{\text{RR}}}{I_{\text{RD}}} \right) \quad (5.5)$$

In both cases, the total inverter losses can then be calculated as

$$P_{\text{l,inv}} = P_{\text{l,diode}} + P_{\text{l,mos}} + P_{\text{l,sw}}. \quad (5.6)$$

For the purpose of this thesis, the analysis is performed under the assumption that only the conduction angle α of the inverter (see Fig. 5.2) can be varied as a control variable. Due to the system level approach, the dead-time is considered to be zero and any thermal dependencies (e.g., of the resistors in data sheets) are also neglected. Furthermore, all components such as diodes etc. are assumed to be linear.

5.1.2 Rectifier Losses

Rectifier losses are highly dependent on the topology chosen. If an active switching solution is chosen, the calculation of losses is similar to the inverter losses and switching effects must be considered in a similar way.

Within this thesis only a passive diode full-bridge is considered, which has similar conduction losses as the inverter [165]:

$$P_{\text{l,rect}} = \frac{4\sqrt{2}}{\pi} V_{\text{rf}} I_{\text{out}} + 2R_{\text{RD}} I_{\text{out}}^2. \quad (5.7)$$

Here, the rectifier diode forward voltage is V_{rf} and equivalent on-state resistance is R_{RD} which can be obtained from the data sheet of the diodes.

Other effects such as ripple currents and their impact on efficiency are neglected because they are comparatively small. Another assumption is that the rectifier always operates in CCM. If the rectifier goes into Discontinuous Conduction Mode (DCM), then the R_{ac} simplification of the FHA can no longer be made, and the effect of the passive rectifier on the phase angle φ_{12} is unclear, since more harmonics are also introduced into the system [174]. This also depends on the secondary tuning, which makes the DCM complex and is all part of the control strategy decisions. Finally, the effect of the passive rectifier on the phase angle is neglected and an ideal phase angle of $\varphi_{12} = 90^\circ$ is assumed. Chapter 7 will discuss the effects of the rectifier on the phase angle in detail.

5.1.3 Magnetic Losses

Magnetic losses are an important consideration in the design and analysis of IPTSs as they can have a significant impact on the efficiency and performance of an IPTS, but it is difficult to obtain reliable simulation results. Accurately modeling these losses is challenging and requires detailed knowledge of the system components and operating conditions [68]. These losses can be divided into three main components: coil losses, core losses, and eddy current losses.

Coil losses occur in the windings of the coils due to the resistance of the wire and are the major source of magnetic losses. The use of litz-wire helps to minimize the proximity and skin-effect losses that can occur in high-frequency applications. The modeling of litz-wire is very complex, so it is usually simplified and skin and proximity effects can be neglected or estimated with an AC/DC factor.

Core losses occur in the magnetic core of the ferrite due to hysteresis and eddy current losses. Hysteresis losses occur when the magnetic domains in the core are magnetized and demagnetized with each cycle of the alternating magnetic field. Eddy current losses occur when the magnetic field induces circulating currents in the core material, resulting in resistive losses [169].

Accurately calculating core losses is challenging because they depend on several factors, including the material properties of the core, the frequency and amplitude of the magnetic field, and the temperature of the core. The most common method for estimating core losses is to use the Steinmetz equation [138]. However, these methods are only approximations and do not account for local heating or saturation effects.

Eddy current losses occur in conductive materials, such as aluminum shields, when they are exposed to a varying magnetic field. Eddy current losses can be reduced by using non-conductive materials or by minimizing the exposure of conductive materials to the magnetic field.

The most common approach to characterize losses is to use the simplified Equivalent-Series-Resistance (ESR) measured with an LCR-meter [169]. An analytical calculation is difficult due to the magnetic material. FEM simulations can give an estimate that is difficult to agree with under all varying conditions and is therefore not preferred. The ESRs are usually obtained by small signal measurements and these include but underestimate the core losses [169]. This is discussed further in Section 7.3 where a loss breakdown is provided.

To summarize, within this thesis, the magnetic losses are only related to the ESR R_{GA} and R_{VA} of the primary and secondary coils and their respective currents and the magnetic loss can be calculated as

$$P_{l,\text{mag}} = R_{GA} \cdot I_{GA}^2 + R_{VA} \cdot I_{VA}^2. \quad (5.8)$$

5.1.4 Other System Losses

There are other component losses in IPTS, such as parasitic effects, ripple effects, and DC inductor losses, which are usually not considered due to being negligible.

Similar to the magnetic losses, the compensation network losses are related to the ESR R_C of the capacitors and are usually very small or negligible. However, this could change as the ESR depends on the chosen capacitors and tuning networks. In this case, the losses of the primary and secondary compensation networks can be calculated as

$$\begin{aligned} P_{l,\text{comp}} &= P_{l,\text{comp1}} + P_{l,\text{comp2}} \\ &= R_{C1} \cdot I_{\text{in}}^2 + R_{C2} \cdot I_{\text{out}}^2. \end{aligned} \quad (5.9)$$

5.1.5 Efficiency

In Section 2.3, the efficiency was defined as ratio between output and input power (Eq. (2.63)). With the consideration of losses this can be rewritten to

$$\eta = \frac{P_{\text{out}}}{P_{l,\text{inv}} + P_{l,\text{mag}} + P_{l,\text{comp1}} + P_{l,\text{comp2}} + P_{l,\text{rect}} + P_{\text{out}}}. \quad (5.10)$$

5.2 Loss Extension of the IPM

In Chapter 3 the ICPs were derived for the same output power at all interfaces. Only the magnetic losses in the impedances Z_{GA} and Z_{VA} were considered in the ESRs. However, this introduces a slight error because each component must be supplied with more power to cover its own losses. In other words, the source must supply more power to the system to achieve a desired $P_{\text{out}} = P_{\text{out,min}}$. This changes the $P_{\text{out,min}}$ boundary that must be imposed, as shown in Fig. 3.5d, and therefore affects the size of the ICP or IPPs in general. In addition, the need for higher input power also changes the FHA calculations of the circuit, as higher rated currents and voltages result.

To account for this, this section shows an extension to the IPM to correctly integrate the losses while maintaining correct boundary imposition and nominal metric estimation. In particular, the estimation of the coil current, as it is important for the calculation of the leakage flux.

There are two general ways to include losses in the IPPs. One way is to fix P_{in} at the DC interface (see Fig. 5.1) and calculate the losses from the inverter to the output interface while subtracting the losses from P_{in} at each interface to see how much output power P_{out} can be achieved for a given input power. The other way is to set the required P_{out} at the DC output and then add the losses at each interface (from the output to the inverter interface) to see how much input power P_{in} is required under the assumed conditions.

Both approaches aim for different results, and it is important to choose the correct one when performing an efficiency study. They are based on the different power class definitions that exist in SAE J2954 (LD) and J2954/2 (HD) [50, 112].

In the first version, the active LD standard, the power class is defined by the maximum apparent input power in kVA (see Section 2.5.1). Assuming unity power factor, this means $S_{\text{in,max}} = P_{\text{in,max}}$. In this case, it is often interesting to see how much output power can be achieved for a given power class, and to assess whether the efficiency regulations are still met. In terms of IPPs, this means that the same input power should be transferred at the input or DC interface, while the power at the output interface can vary for different OPs, as each point within the IPP produces individual losses.

The HD standard, which is still in the Technical Information Report (TIR) stage at the time of this writing, aims to define power classes by active output power in kW. This means that a designer of an IPTS must ensure that a certain amount of active power $P_{\text{out,min}}$ is transferred to the EV battery. As a result, the same power level at the output interface is of interest, while the input power can vary for certain OPs, as long as the desired output power is achieved.

To account for both cases, the flowcharts for the first (P_{in} is constant) and second (P_{out} is constant) approaches have been derived and are shown in Fig. 5.3 and Fig. 5.4, respectively. For simplicity, the compensation loss calculation steps have been neglected in the first approach, but they can easily be added at the right places between the inverter and the magnetic and rectifier losses.

Since both approaches work in a similar way, only the second approach will be detailed below by examining the IPM Example 1 from Section 3.4.

P_{out} constant: To illustrate the extension of the method, the (lossless) results of IPM Example 1, the ICP with the various component constraints (for k_{min}) are again shown in Fig. 5.5 at all interfaces. In addition, heatmaps of each interface current are shown, as introduced in Chapter 4. These ICPs were all obtained with the assumption that $P_{\text{out}} = 10$ kW must be transferred at each interface. As a result, the same $P_{\text{out,min}} = P_{\text{out}} = 10$ kW limit was imposed on all interfaces.

Using the current heatmaps to calculate losses would introduce an error. Taking losses into account requires that the output power, and thus the $P_{\text{out,min}}$ boundary, be adjusted so that the input power required by each component is increased by the amount of losses because the component must compensate for the losses. To solve this problem, the flowchart from Fig. 5.4 can be used, which will be demonstrated below.

To study and visualize the implementation of the losses, the ICP_{in} (green) from Fig. 5.5 is used as a starting point (step 1 in the flowchart). The implementation of the limits must be done separately at each interface after the power level adjustments, because they also depend on the individual power transfer requirements that each OP now has. Only the initial $P_{\text{out,min}}$ boundary, in this case 10 kW, should be implemented. This step can be skipped (and the black ICP can be used as a starting point instead), since each ICP will be updated with its new $P_{\text{out,min}}$ limit after the loss calculation.

As shown in Chapter 4, the usable zone can be divided into a fine grid and transferred to the output interface. Each point represents an OP that can be addressed by the system within the initial system boundaries. The first step is to associate each OP with the selected output power $P_{\text{out,min}} = P_{\text{out}} = 10$ kW at the output interface.

With $P = \text{Re}(\underline{Z}) \cdot I^2$, the current (I_{out}) required to transmit P_{out} can be derived for each OP within ICP_{out}. Using the rectifier datasheet [175] (see next section for details), I_{out} and Eq. (5.7) the losses of each OP can be calculated. With the IPM, these losses can now be

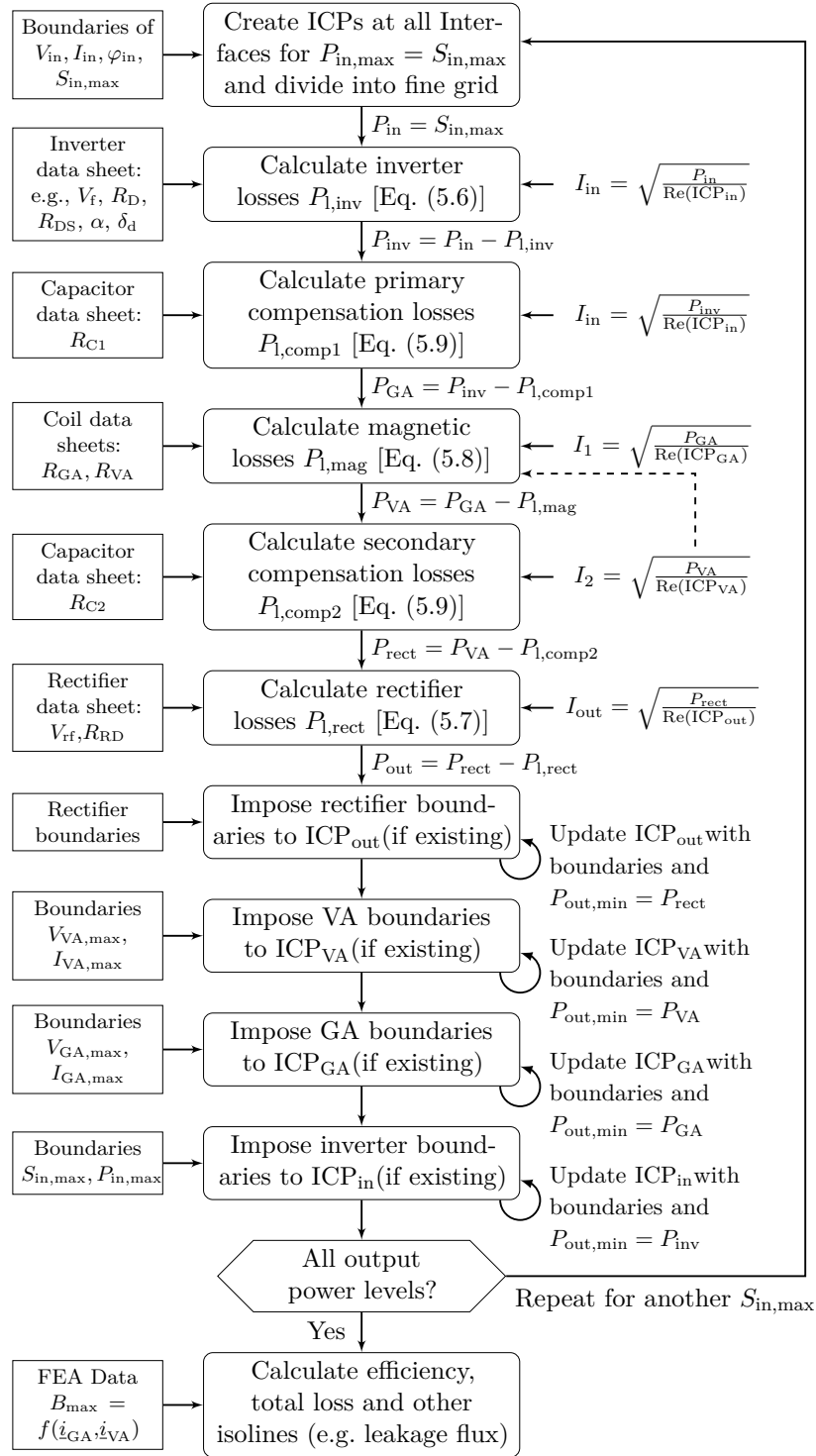


Figure 5.3 – Flowchart for loss implementation with constant P_{in} into the IPM.

studied at any interface. The rectifier losses shown at the output interface and transferred to the inverter interface for the previously discussed ICP are shown in Fig. 5.6.

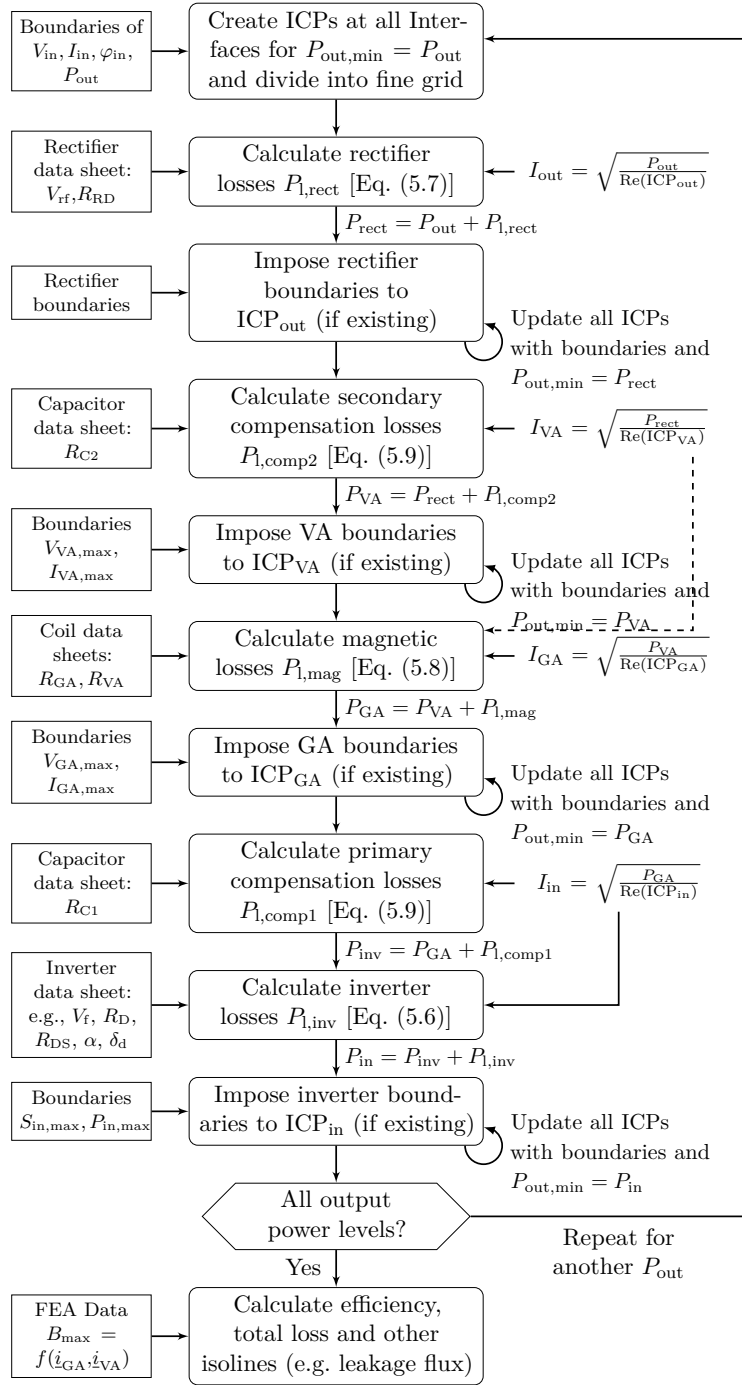


Figure 5.4 – Flowchart for loss implementation with constant P_{out} into the IPM.

Since $P_{1,rect}$ depends only on the output current, the heatmap also indicates where high output currents are expected at the inverter interface within the ICP, which can be useful for design or control considerations.

To transfer 10 kW at the output interface, the system must provide the rectifier losses, so the next step is to change the required power at the output interface to $P_{rect} = P_{out} + P_{1,rect}$.

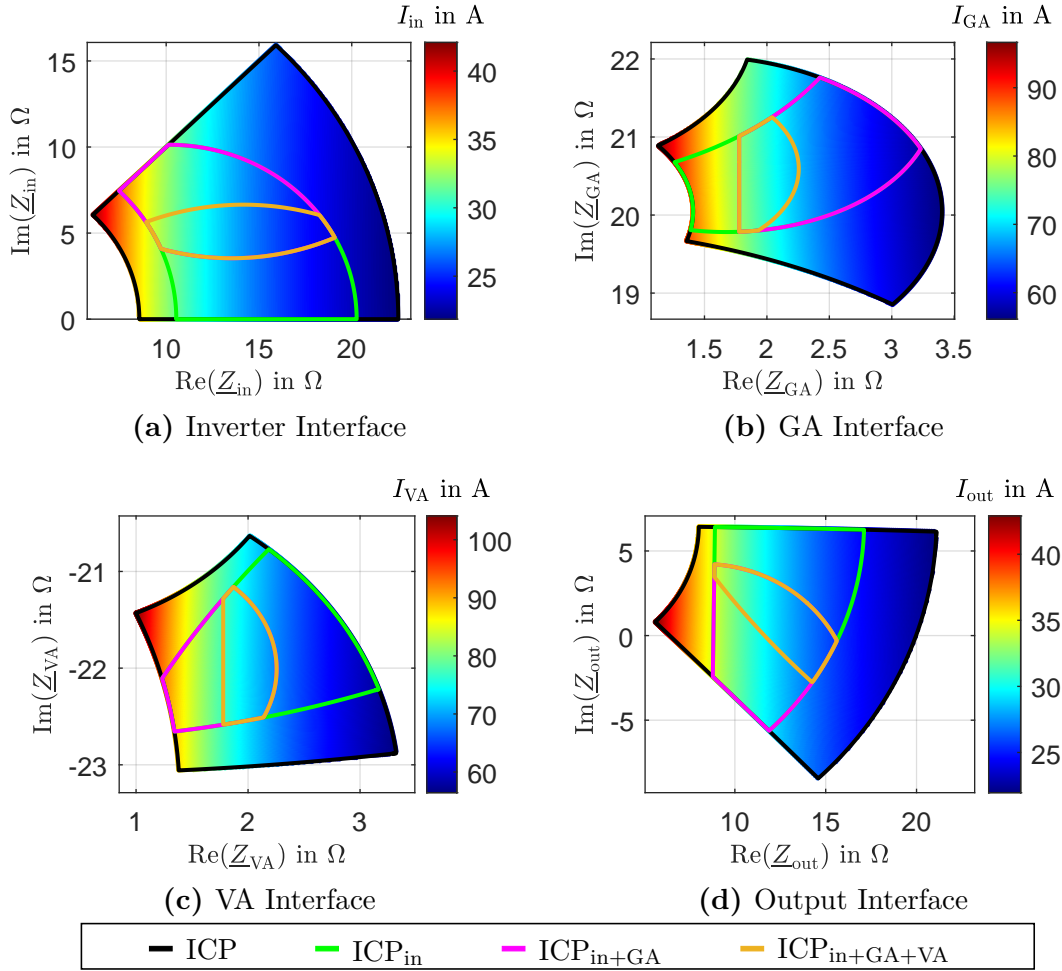


Figure 5.5 – ICPs of IPM Example 1 with the respective interface current as heatmap.

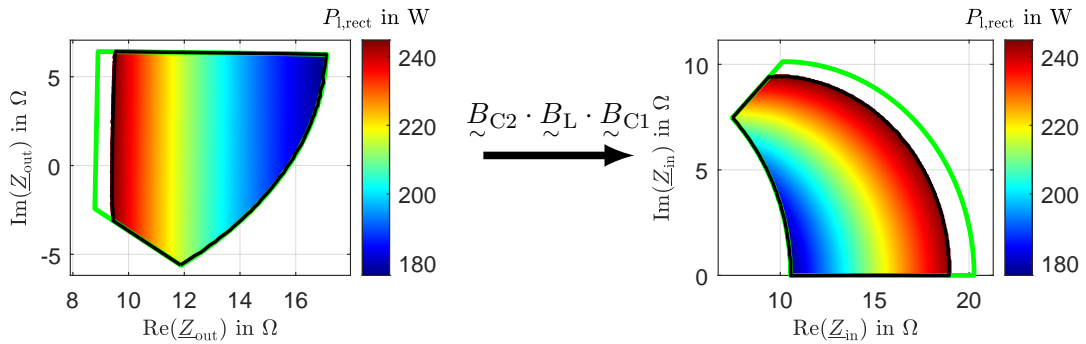


Figure 5.6 – Rectifier losses in the ICP at the rectifier and inverter interface. The ICP without losses is shown in green for comparison.

Due to the different losses of each OP, the required power now varies within the ICP, as can be seen in Fig. 5.7, which shows the same ICP but with P_{rect} as the heatmap.

When imposing the boundaries at the rectifier interface (according to Chapter 3), it is important to update $P_{\text{out,min}}$ to $P_{\text{out,min}} = P_{\text{rect}}$ for each OP, since the change in required

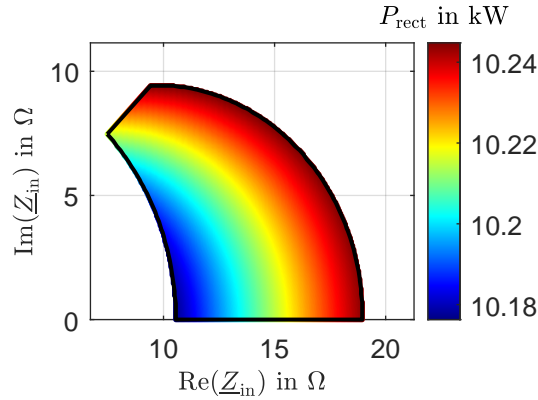


Figure 5.7 – ICP with P_{rect} heatmap at the inverter interface.

output power affects the ICP (higher power means smaller ICP) and the boundary imposing results. The hull curve of the initial lossless ICP_{in} is shown in green in Fig. 5.6 for comparison. It can be seen that increasing the required power has a negative effect on the size of the ICP, which illustrates the need to consider the losses within the IPM.

This process must be repeated at each interface as described in the flowchart, and it is important to use the correct data sheets, limits, and equations to calculate the losses and impose the limits step-by-step.

To provide further insight into the process and demonstrate the ability of the approach to represent the losses of each component separately, Fig. 5.8 and show the magnetic and inverter losses under different considerations.

To illustrate how high the magnetic losses can get within the complete ICP, Fig. 5.8a shows the magnetic losses without considering any limitations. However, to follow the process flowchart, the real usable ICP with all losses and component boundaries considered and the magnetic loss heatmap is shown in Fig. 5.8b with the lossless (golden) hull curve from Fig. 5.5a for comparison.

The next step in the flowchart is the calculation of the inverter losses and the results without switching losses (as this is an LCC–LCC system only conduction losses are considered and Eq. (5.5) does not apply) are shown in Fig. 5.8c. Again, not all boundaries were considered to show the distribution within the (then larger) ICP. To demonstrate the impact of switching losses, the inverter losses including switching losses are shown in Fig. 5.8d over the entire ICP area. Although the calculated switching losses only apply to a series-tuned system, the results can provide a ballpark solution and illustrate the importance of switching losses as they significantly increase the total losses.

However, only the golden area is of interest for system design, and after calculating the inverter losses, the total loss heatmap can be calculated as shown in Fig. 5.9a. To illustrate the effect of changing the desired output power on the ICP, the lossless ICP is used. It can be seen that $P_{\text{out,min}}$ increases due to the loss and results in a smaller ICP. This is very important because some OPs that were previously inside the ICP are now outside the IPP.

The process ends when the inverter’s constraints, such as the grid limits ($S_{\text{in,max}}$), are imposed, and the final step is to update the minimum required output power for the ICP at the inverter interface to $P_{\text{out,min}} = P_{\text{in}}$. P_{in} can also be used to calculate efficiency, since it indicates the required power that must be supplied to the system to obtain the predefined P_{out} .

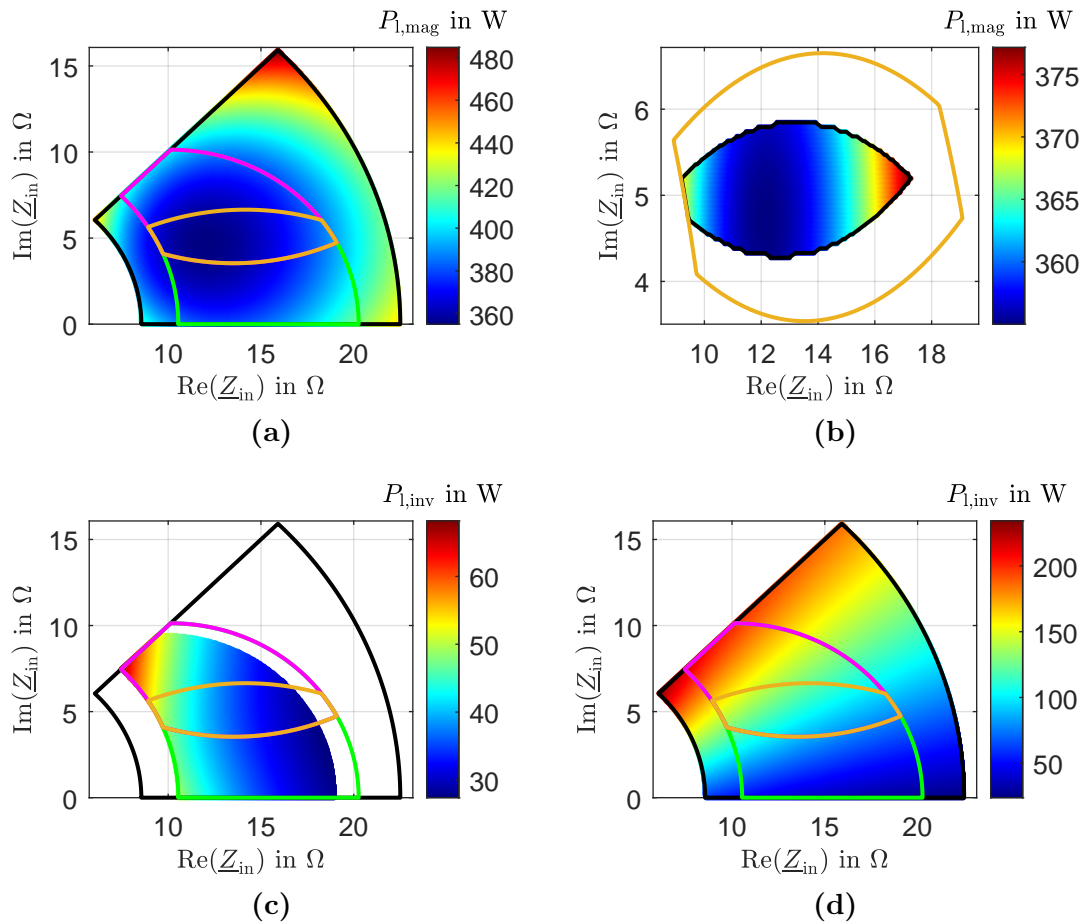


Figure 5.8 – Loss analysis of the IPM Example 1 at k_{\min} with (a)-(b) magnetic loss and (c)-(d) inverter loss heatmaps.

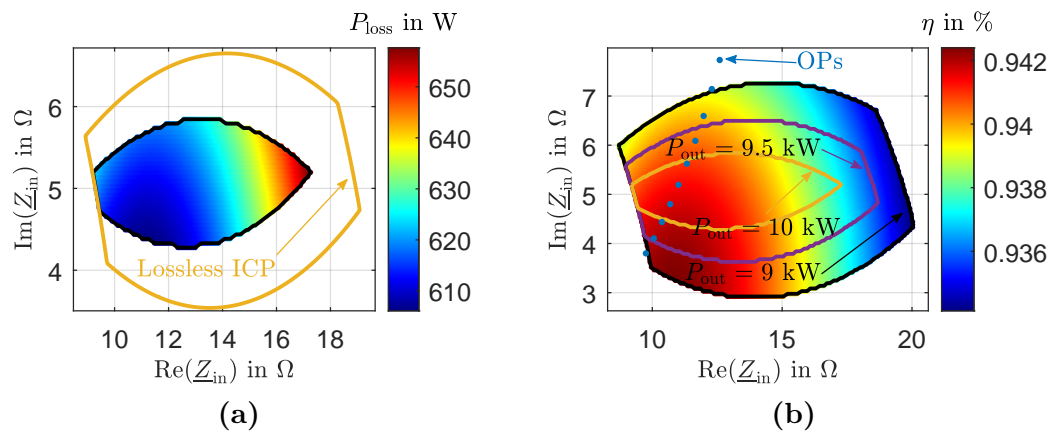


Figure 5.9 – (a) Loss and (b) efficiency analysis of the IPM Example 1 at k_{\min} with isolines for different power levels.

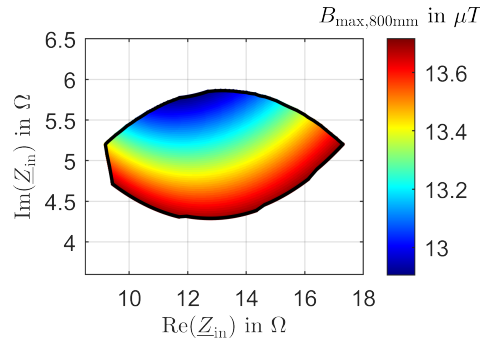


Figure 5.10 – $B_{\max,800\text{mm}}$ leakage flux heatmap of the IPM Example 1 at k_{\min} .

The entire process can be repeated if another P_{out} value is of interest. The efficiency map with the OPs from Chapter 3 (Fig. 3.17) is shown in Fig. 5.9b. Two repetitions with $P_{\text{out}} = 9.5$ kW and $P_{\text{out}} = 9$ kW have been performed and are also highlighted. An evaluation of the system efficiency is now directly possible for all OPs and varying conditions.

Similar to Chapter 4, the leakage flux heatmap within the final ICP are shown in Fig. 5.10, which is also a very valuable evaluation step.

In terms of interoperability, the loss extension is a powerful and useful feature of the methodology, since variations in power and battery voltage need to be covered by an interoperable system, and it is quite difficult to study this with a conventional approach due to the amount and complexity of the generated data sets. The loss-extension IPM provides a fast and convenient solution to analyze and visualize such aspects.

The impact of losses on an IPTS design is discussed in next section, where the method is applied to an extensive use-case using the constant P_{out} approach (see flowchart in Fig. 5.4). Another loss study is presented in Chapter 7 for a 50 kW system.

5.3 IPM Example 3: Public Charging

In this example, the IPM and its loss extension are applied to a system already known from Chapters 3 and 4 and the previous section. The aim is to integrate the knowledge gained from the previous chapters in a comprehensive study relevant to a practical scenario. A scenario for a public charging primary side is created and the goal is to achieve higher interoperability.

First, the system and the use-case are presented, along with the boundaries used. A flowchart of the process for this example is then provided. To evaluate the accuracy of the simulation tools used, experimental measurements were performed and the results are compared with the simulation results. The flowchart is then implemented and the results are discussed in detail. Finally, potential measures to improve interoperability are presented and the estimated losses are discussed.

5.3.1 System, Use-Case and Boundaries

In order to assess whether a primary can be used for public charging, the interoperability of this primary should be investigated. To demonstrate the IPM's ability to investigate this, a scenario was created where a primary needs to operate with four different secondaries, each differing either in their respective air-gap or tuning topology (Case 1–4). This results in four coil combinations with different couplings.

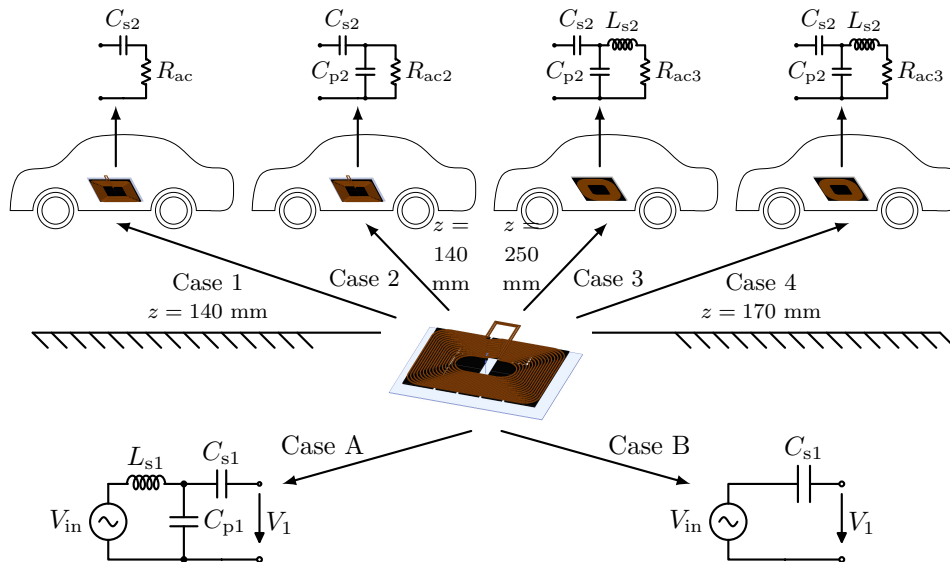


Figure 5.11 – Overview of the use-case scenario. The electronics of Case A or Case B are connected to the primary coil and four different cars are parking over this charging station and should be charged under different parking and battery voltage conditions with $P_{\text{out}} = 10 \text{ kW}$.

The goal of the use-case scenario is to compare two different sets of primary electronics consisting of the same inverter with different tuning, Case A and Case B in Fig. 5.11, and to assess which one is better suited to work with the primary coil (SAE UGA WPT3 [50]) as a public charging station under these requirements.

The secondary coil for Cases 1 and 2 is similar to the already used SAE VA WPT3 Z2 system from Section 3.4 (tuning topology is changed), while Cases 3 and 4 use the SAE VA WPT3 Z3 system from [50], see Tab. 2.11.

As for the secondary electronics, Case 1 is series-tuned with a passive diode rectifier, which can be simplified to R_{ac} with Eq. (2.9). Case 2 uses a partial series tuned system and a passive rectifier which can be simplified to $R_{\text{ac}2}$ with Eq. (2.12). Cases 3 and 4 use the same electronics, both LCC tuned with an impedance compression network (Eq. (2.19)). These two cases use the reference electronics topologies from [50] and differ only in the air-gap of their EVs – Case 3 is at the maximum height of Z3 and Case 4 is at the minimum Z3 height. Cases 1 and 2 have the same air-gap, but differ in the electronics.

In total, four completely different EVs (coil, electronics and coupling conditions) are presented on the primary side, which is not unusual for a public charging scenario. The schematics of the described use-case are shown in Fig. 5.11. Case 2 is similar to the experimentally validated system in Section 5.3.3.

Each case is considered at its air-gap (z -height) and its nominal as well as offset ($x = 75 \text{ mm}$ and $y = 100 \text{ mm}$) position, resulting in 8 different CCPs presented to the GA interface. Battery voltage variations are also considered, as in the previous examples, resulting in different loads and thus different OPs presented to the GA.

The system boundaries set for this example are summarized in Tab. 5.1. The boundaries were estimated and differ from the previous examples in Chapters 3 and 4 because the use-case was specifically created for this example. In addition, the loss parameters in terms of forward voltages and on-state resistances are listed. The datasheets of the (used) switches and diodes

Table 5.1 – IPM Example 3: System Boundaries for the Use-Case Scenario

Grid/Inverter	Coils	Rectifier/Load
$S_{\text{in,max}} = 11.1$ kVA	$V_{1,\text{max}} = V_{2,\text{max}} = 2.5$ kV	$V_{\text{bat}} = (280 - 420)$ V
$V_s = (50 - 500)$ V	$(I_{1,\text{max}}, I_{2,\text{max}}) = (100, 100)$ A	$P_{\text{out}} = 10$ kW
$I_s = (5 - 60)$ A	$(x, y, z)_{\text{min}} = (0, 0, 140)$ mm	$R_{\text{ac}} = 8/\pi^2 \cdot V_{\text{bat}}^2/P_{\text{out}}$
$\varphi_{\text{in}} = (0 - 45)$ deg	$(x, y, z)_{\text{max}} = (75, 100, 250)$ mm	$R_{\text{ac2}} = \pi^2/8 \cdot V_{\text{bat}}^2/P_{\text{out}}$
	$B_{\text{max}} = 15$ μT	$R_{\text{ac3}} = (X_{\text{rect}}^2 + R_{\text{ac}}^2)/R_{\text{ac}}$
$V_f = 0.7$ V	$R_1 = 34.1$ m Ω	$V_{\text{rf}} = 3.7$ V
$R_D = 49$ m Ω	$R_2 = 35.5$ m Ω	$R_{\text{RD}} = 7.8$ m Ω
$R_{\text{DS}} = 25$ m Ω	$R_{\text{C1}} = 10$ m Ω	
$\alpha = 180^\circ$	$R_{\text{C2}} = 10$ m Ω	
$\delta_d = 0$ s		

Table 5.2 – Overview of Tuning Equations for the IPM Example 3

Topology	$C_{s1,s2}$	$C_{p1,p2}$	$L_{s1,s2}$	$X_{1,2}$
Series	$\frac{1}{\omega^2 L_{1,2}}$	–	–	$\omega L_{1,2}$
Partial-Series	$\frac{1}{\omega^2 L_{1,2} - \omega X_{1,2}}$	$\frac{1}{\omega X_{1,2}}$	–	$\omega L_{1,2} - \frac{1}{\omega C_{s1,s2}}$
LCC	$\frac{1}{\omega^2 L_{1,2} - \omega X_{1,2}}$	$\frac{1}{\omega X_{1,2}}$	$\frac{X_{1,2}}{\omega}$	$\omega L_{1,2} - \frac{1}{\omega C_{s1,s2}}$

were taken according to the components used in the experiments of the next section and can be found in [175].

Information on the tuning values is listed in Tab. 5.3, and the equations on how to calculate the values can be found in the fundamentals (see Section 2.2.3) and are summarized again in Tab. 5.2. Perfect or active tuning is beyond the scope of this use-case and is thus not discussed in detail². The approach of this use-case is to present four secondaries to each primary and to analyze the capabilities of the primaries even if the secondaries are detuned, with which a public charging station may nonetheless has to deal with.

With the circuits fully parameterized, the IPPs and OPs can be derived for all cases of the use-case. The details of the procedure are explained in the next section.

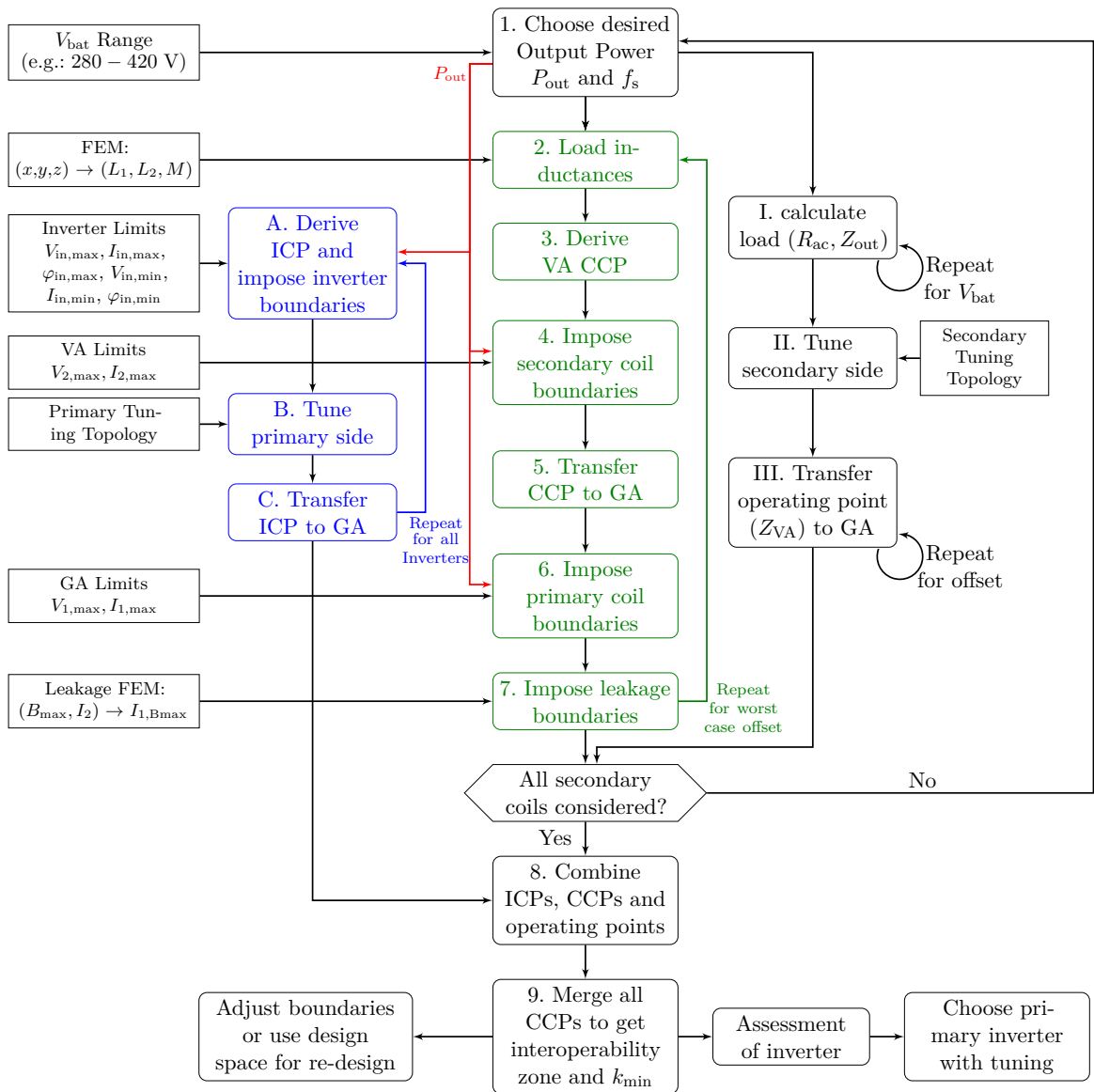
5.3.2 Process Flowchart of the Use-Case

In Fig. 5.12 the flowchart of the target application is shown. The blue colored steps describe the electronic part of the process to derive the ICP, while the green colored steps describe the magnetic part of the process to derive the CCPs. The inverter boundaries and power limits can be implemented with the procedures described in Section 3.2.2 to derive the ICP

²The sensitivity study in Chapter 6 will discuss the impact of active tuning.

Table 5.3 – Overview of Tuning Values for the IPM Example 3

Case	X_1	X_2
S-S	ωL_1	ωL_2
S-PS	ωL_1	5.5
S-LCC1	ωL_1	7
S-LCC2	ωL_1	11
LCC-S	4.5	ωL_2
LCC-PS	4.5	5.5
LCC-LCC1	4.5	7
LCC-LCC2	4.5	11


Figure 5.12 – IPM Example 3: Flowchart of the public charging use-case.

and must be repeated for each inverter under investigation, in this case (twice) for Case A and Case B. With the primary tuning topology, the transfer matrices \tilde{A}_S and \tilde{A}_{LCC} can be determined and each ICP can be transferred to the GA interface.

With the inductances as input, any VA CCP can be derived for the given power level as shown in Section 4.2.1. After imposing the VA limits on the CCP, the IPP can be transferred to the GA interface using the corresponding A_L , where the primary side as well as the leakage flux limits can be imposed as described in Section 4.2.3 (a simplified approach is sufficient since the coils are non-matched). This must be repeated for each offset position and each secondary coil considered.

As a third part of the procedure, the OPs depending on the power level, battery voltage and frequency have to be calculated and transferred back to the GA interface using the transfer matrices defined by each secondary tuning topology and the coil transfer matrices of each coil position and secondary coil.

The investigated ICPs, the considered CCPs and their respective OPs from the use-case conditions can now be combined at the GA interface and directly compared or evaluated.

These steps were intentionally done without considering the losses to allow an initial comparison to highlight the impact of the losses later. The loss extension with constant P_{out} must be performed for each of the eight combinations. The results of the flowchart process and the loss extension are presented and discussed in Section 5.3.5.

5.3.3 Experimental Verification

It is not feasible to set up experiments for all OPs of an IPP and for all system combinations. Therefore, measurements have been performed for a known system (Case 2) to validate the simulations in general (also used in Chapters 3 and 4, thus validating these results as well), so that they can be used to apply the presented method in the next section.

The system used for experimental verification consists of two circular coils similar to the SAE UGA WPT3 and SAE VA WPT3 Z2 systems from [50]. The circuit of the measurement setup is shown in Fig. 5.13.

The switching frequency was set to $f_s = 85$ kHz and the input and output voltages were set to $V_s = 450$ V and $V_{bat} = 420$ V, respectively. The compensation networks consist of an LCC topology on the primary and a partial series compensation on the secondary, and the values are listed in Tab. 5.4. A boost converter was used on the secondary to regulate the output voltage. All measurements were made with a car mimic plate (aluminum shielding, $800 \times 800 \times 1$) mm) on top of the secondary and a picture of the measurement setup in the lab is shown in Fig. 5.14.

Two OPs were set up and the input and output voltages and currents were measured, with the results shown in Tab. 5.5. The difference between the two OPs was in the coil position,

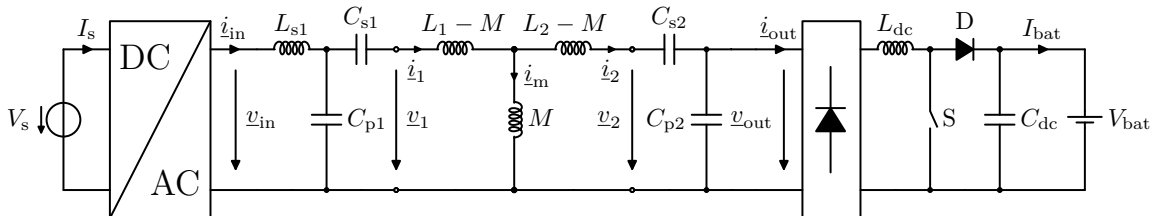
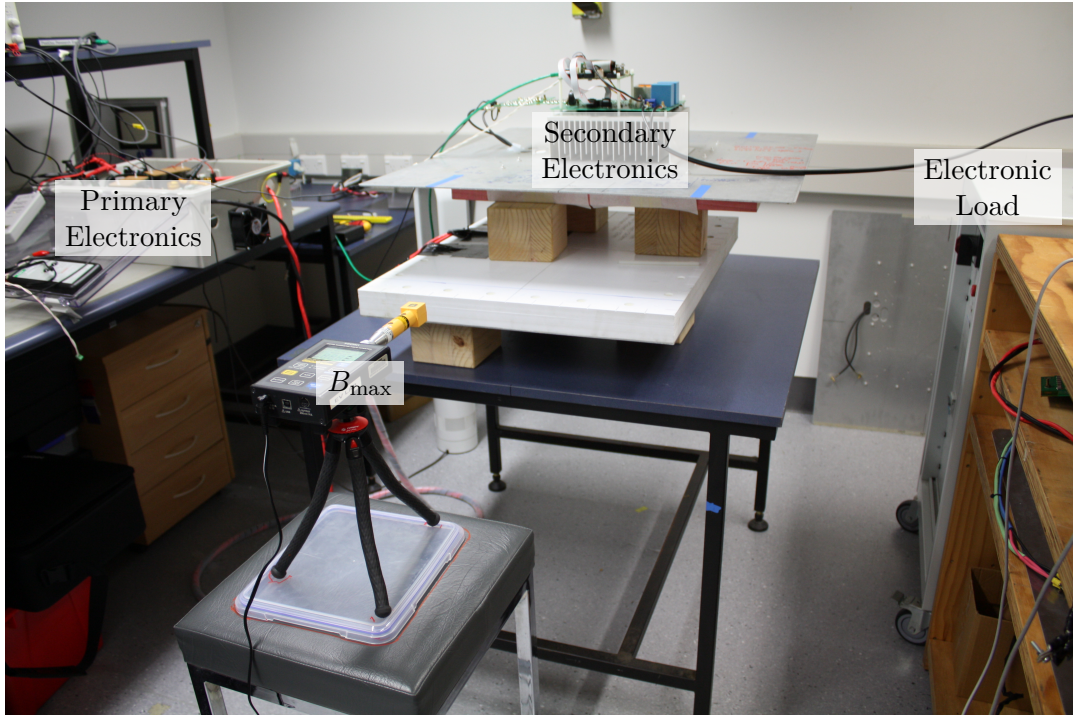


Figure 5.13 – Circuit topology of the measured system.

Table 5.4 – Tuning Values of the Experimental Setup

Parameter	Value	Parameter	Value
L_{s1}	12.3 μH	–	–
C_{s1}	122 nF	C_{s2}	110 nF
C_{p1}	356 nF	C_{p2}	287 nF

**Figure 5.14** – Lab leakage flux measurement setup.

which in the first OP was set at the nominal position, $(x,y,z) = (0,0,210)$ mm, and in the second OP at the offset position, which is $(x,y,z) = (75,100,210)$ mm.

To keep the output voltage constant, the duty cycle of the boost converter was set to $D = 0.23$ in the nominal position and $D = 0$ in the offset position. Fig. 5.15a shows the recorded waveforms of the coil currents and the inverter bridge and Fig. 5.15b shows a screenshot of the measured output values, both for the nominal OP. A loss breakdown and comparison with simulation results will be discussed in the next section.

The leakage flux probes were placed at the same position where $B = B_{\max}$ occurred in the FEM simulation as discussed in Section 4.2.3 and shown in Fig. 4.9. These measurements were performed for two distances, 800 mm and 1000 mm, both in the XZ- and YZ-planes, and the leakage flux measurement results as well as the inductances and coupling factors are listed in Tab. 5.6.

5.3.4 Full System Simulation

To validate the simulation models, the same system and similar OPs were set up in the circuit simulations and the results are also shown in Tab. 5.5. Ansys Maxwell was used for

Table 5.5 – Comparison between Measurements and Circuit Simulations

	I_1 (A)	I_2 (A)	I_s (A)	I_{bat} (A)	P_{in} (kW)	P_{out} (kW)	P_{loss} (kW)	$\eta_{\text{dc-dc}}$ (%)
Nominal Position $\rightarrow (x,y,z) = (0,0,210)$ mm, $V_{\text{in}} = 450$ V, $V_{\text{bat}} = 420$ V, $D = 0.23$								
Meas.	75.5	59.2	25.0	24.6	11.3	10.4	0.9	92.0
Sim.	71.8	66.9	25.7	26.3	11.6	11.1	0.5	95.7
Offset Position $\rightarrow (x,y,z) = (75,100,210)$ mm, $V_{\text{in}} = 450$ V, $V_{\text{bat}} = 420$ V, $D = 0$								
Meas.	77.5	68.3	25.0	24.5	11.3	10.4	0.9	92.0
Sim.	75.6	76.8	25.1	25.5	11.2	10.7	0.5	95.6

Table 5.6 – Comparison between Magnetics Measurements and FEM Simulations

	L_1 (μH)	L_2 (μH)	k	$B_{\text{max},800\text{mm}}$ (μH)	$B_{\text{max},1000\text{mm}}$ (μH)
Nominal Position $\rightarrow (x,y,z) = (0,0,210)$ mm					
Meas.	38.16	43.41	0.116	5.9	2.5
Sim.	38.03	41.03	0.122	6.7 (6.68)	2.6 (2.63)
Offset Position $\rightarrow (x,y,z) = (75,100,210)$ mm					
Meas.	38.78	43.44	0.088	13.6	5.2
Sim.	38.56	40.99	0.089	14.3 (14.17)	5.1 (5.04)

the FEM simulations and the coil models are identical to those used in the IPM Example 1, see Fig. 3.8. PLECS was used for the circuit simulations and the model is shown in Fig. 5.16.

The simulated waveforms are shown in Fig. 5.17 and can be used to compare the simulation results with the measured scopes.

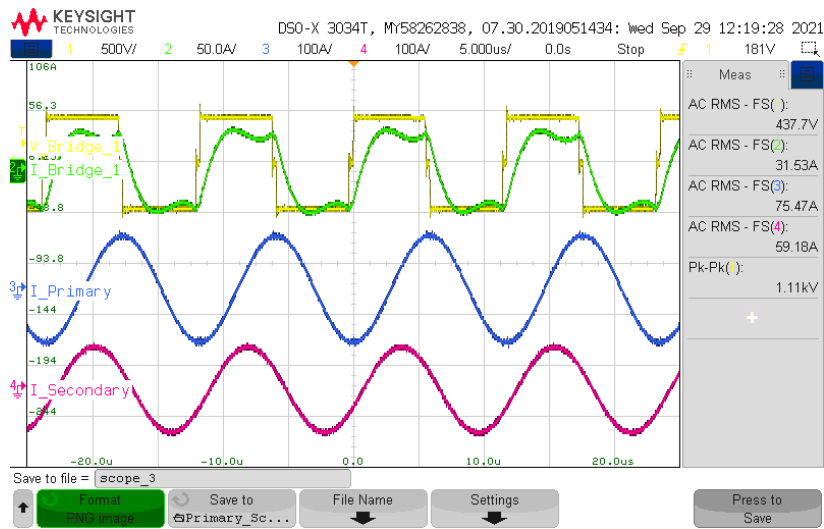
To obtain the maximum leakage flux values at their exact position (which was necessary for comparison with the measurements), the measured currents of both OPs were set in another FEM simulation and the results are listed in Tab. 5.6. The second value shown in brackets was determined using the simplified scaling method described in Section 4.2.3. The values are almost identical, confirming that the simplified approach can be used in this case.

The boost converter can either be modeled (in circuit simulations) or included in the R_{ac} load. The formula is given in Tab. 2.1:

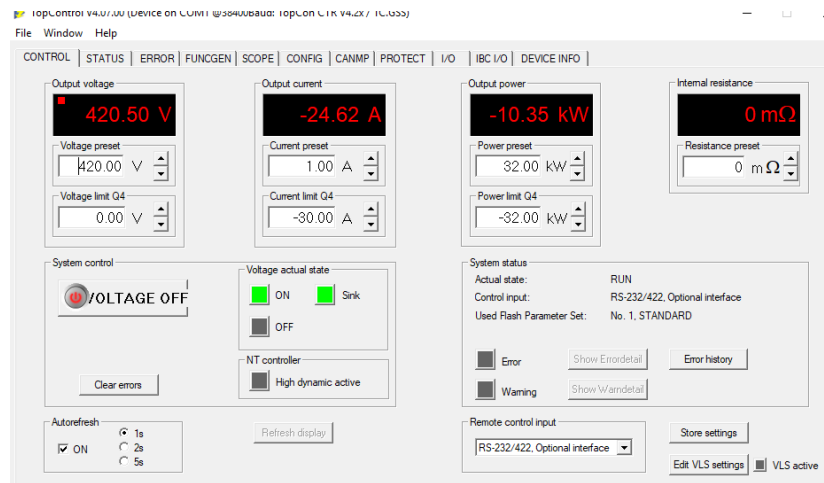
$$R_{\text{ac}} = \frac{\pi^2}{8}(1 - D)^2 R_{\text{bat}}. \quad (5.11)$$

The comparison between measured and simulated values in Tab. 5.5 shows very good agreement with the simulations and with the measurements in general. There are slight deviations in the secondary currents caused by the rectifier. The thermal and ohmic losses of the diodes and MOSFETs were not modeled in PLECS and account for about 3.5 % of the efficiency and also explain the slightly higher current in the simulations.

The losses could not be measured separately for each component, but the equations from Section 5.1 can be used to investigate the loss distribution and the deviation between measurements and simulation, which is done below for the offset position (k_{min}).



(a)



(b)

Figure 5.15 – Scopes of the circuit measurements for the nominal position, (a) waveforms of coil currents and inverter bridge and (b) captured output values.

Tab. 5.5 shows that the total measured losses were $P_{\text{loss}} = P_{\text{in}} - P_{\text{out}} = 11.3 \text{ kW} - 10.4 \text{ kW} = 0.9 \text{ kW}$. The datasheet parameters for the loss calculation of each component are listed in Tab. 5.1. The losses of the inverter (conduction only), the magnetics and the rectifier can then be calculated with Eq. (5.1), (5.2), (5.8) and (5.7):

$$\begin{aligned} P_{\text{inv}} &= 51 \text{ W} \\ P_{\text{mag}} &= 370 \text{ W} \\ P_{\text{rect}} &= 175 \text{ W}. \end{aligned}$$

To account for the switching losses, a closer look at the currents through the MOSFET switches from the PLECS simulation is shown in Fig. 5.18. It can be seen that the instantaneous currents at the turn-off moments are $I_{\text{inst},1} = 18.9 \text{ A}$ and $I_{\text{inst},2} = 25.3 \text{ A}$ for the left and

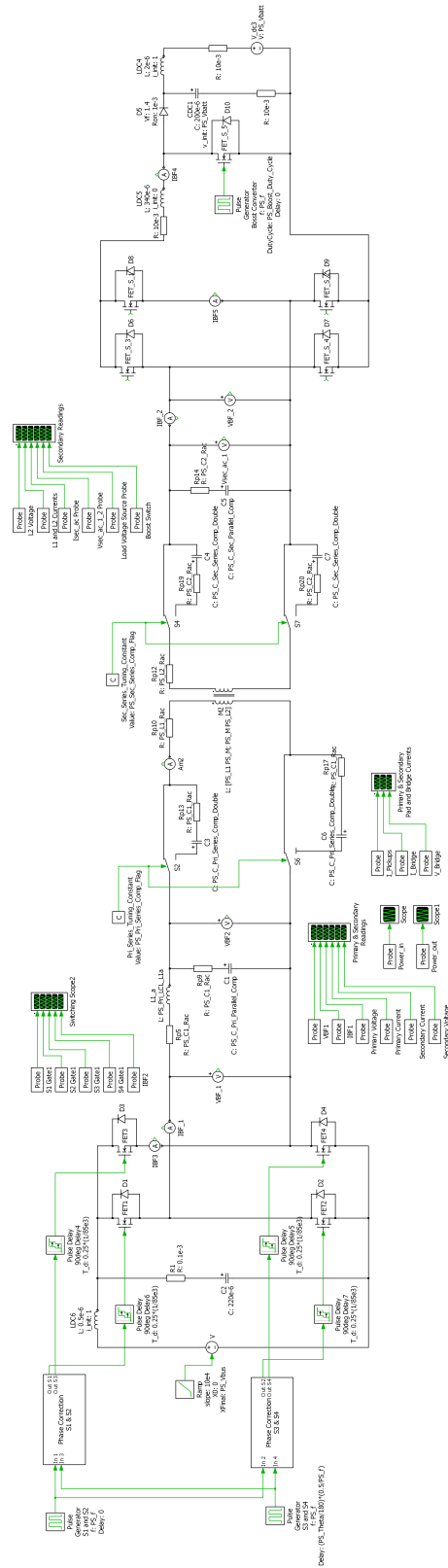


Figure 5.16 – Schematics of the PLECS simulation.

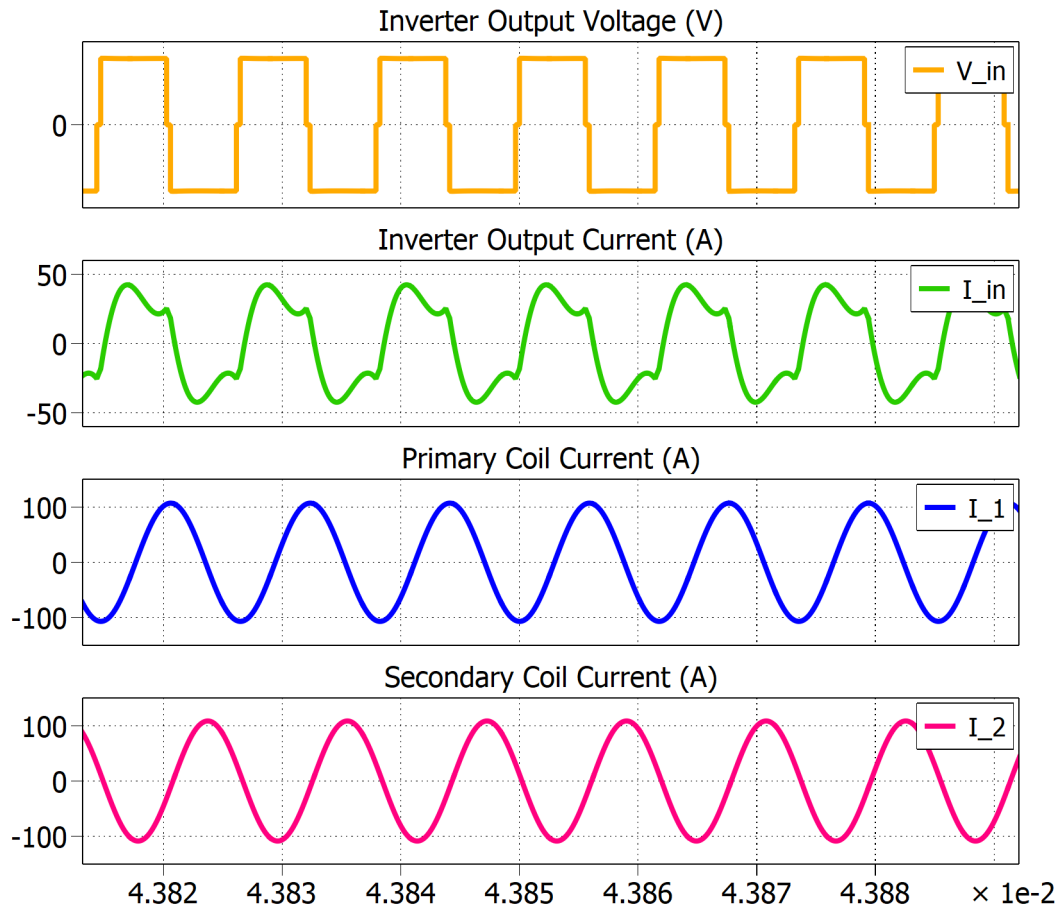


Figure 5.17 – Waveforms of the PLECS simulation.

right legs of the inverter, respectively. The data sheet [175] can be used to obtain the turn-off energy for each switch, and Eq. (5.4) can be used to calculate the switching losses.

$$P_{1,sw} = f_s \cdot (0.2 \text{ J} + 0.2 \text{ J} + 0.2 \text{ J} + 0.2 \text{ J}) = 70 \text{ W}$$

To narrow it down further, the core losses in the ferrite and the eddy current losses in the aluminum shielding for this specific operating condition were derived in a FEM simulation³:

$$\begin{aligned} P_{1,core} &= 24 \text{ W} \\ P_{1,shield} &= 43 \text{ W} \end{aligned}$$

The total calculated losses then add up to $P_{loss} = P_{1,inv} + P_{1,mag} + P_{1,rect} = 121 \text{ W} + 437 \text{ W} + 175 \text{ W} = 733 \text{ W}$, leaving about 170 W for the boost converter and other losses such as compensation capacitors and DC inductors.

Furthermore, the simulated leakage flux values at 800 mm distance are slightly higher than the measured ones. This can be explained by the fact that it is very difficult to place the probe in exactly the same position as in the simulation and to place the coils in exactly the same position, which also explains the slight offset in L_2 . Especially at low leakage flux, it is

³Anslys allows the core loss to be extracted and is able to calculate the surface loss density on the aluminum surface, which can be integrated over the entire surface to obtain the eddy current losses.

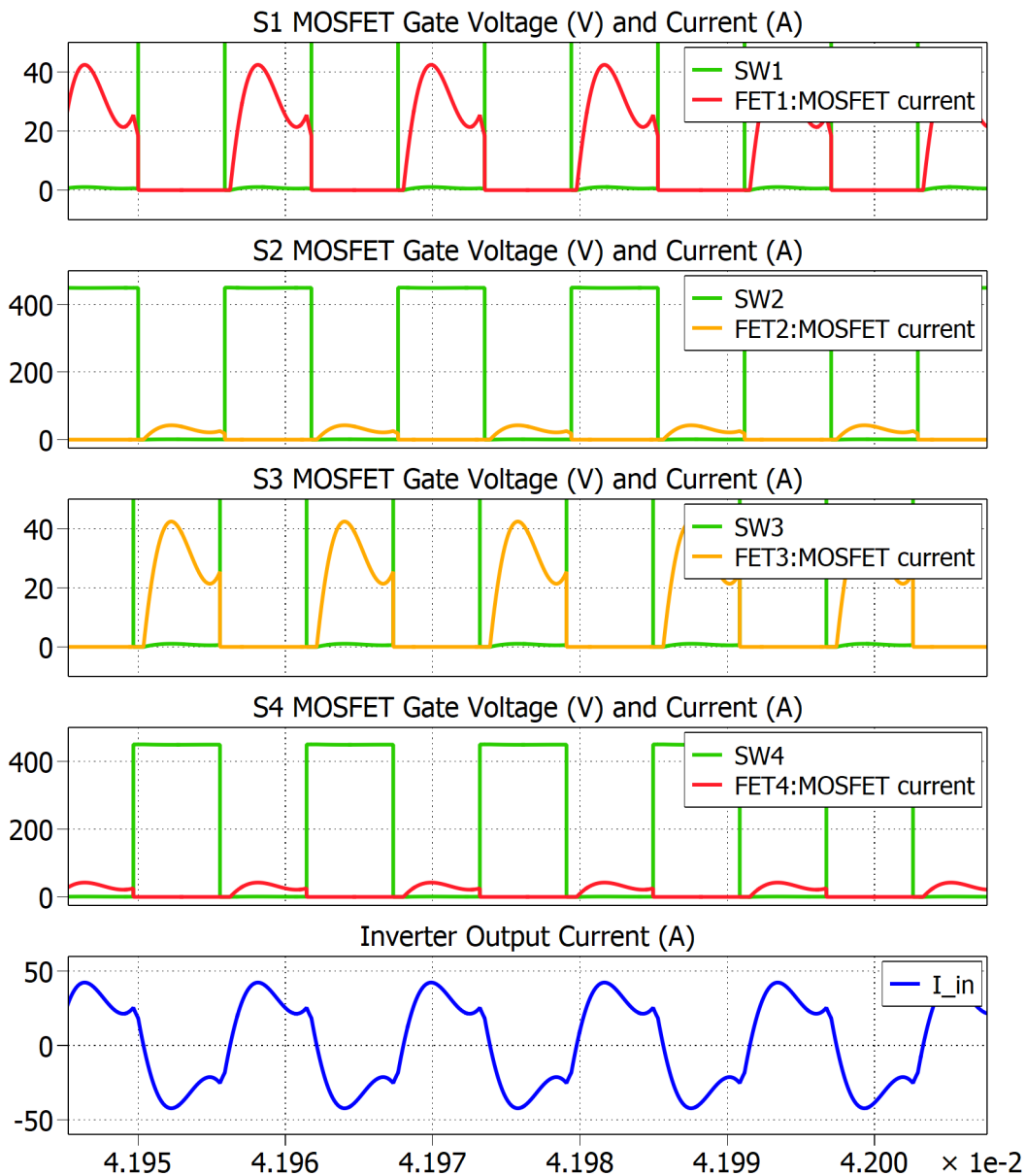


Figure 5.18 – Waveforms of the inverter switches in the PLECS simulation.

difficult to capture the correct leakage flux since there is also a manufacturing margin of the probe.

Overall, the results agree quite well, and with the loss estimation the results are even closer, hence the simulation models and loss equations can be considered validated.

5.3.5 Results and Discussion

Steps 1 to 7 of the flowchart in Fig. 5.12 have been done separately for each secondary coil and the results are shown in Fig. 5.19a–Fig. 5.19d while all results are visualized together in Fig. 5.20 (step 8).

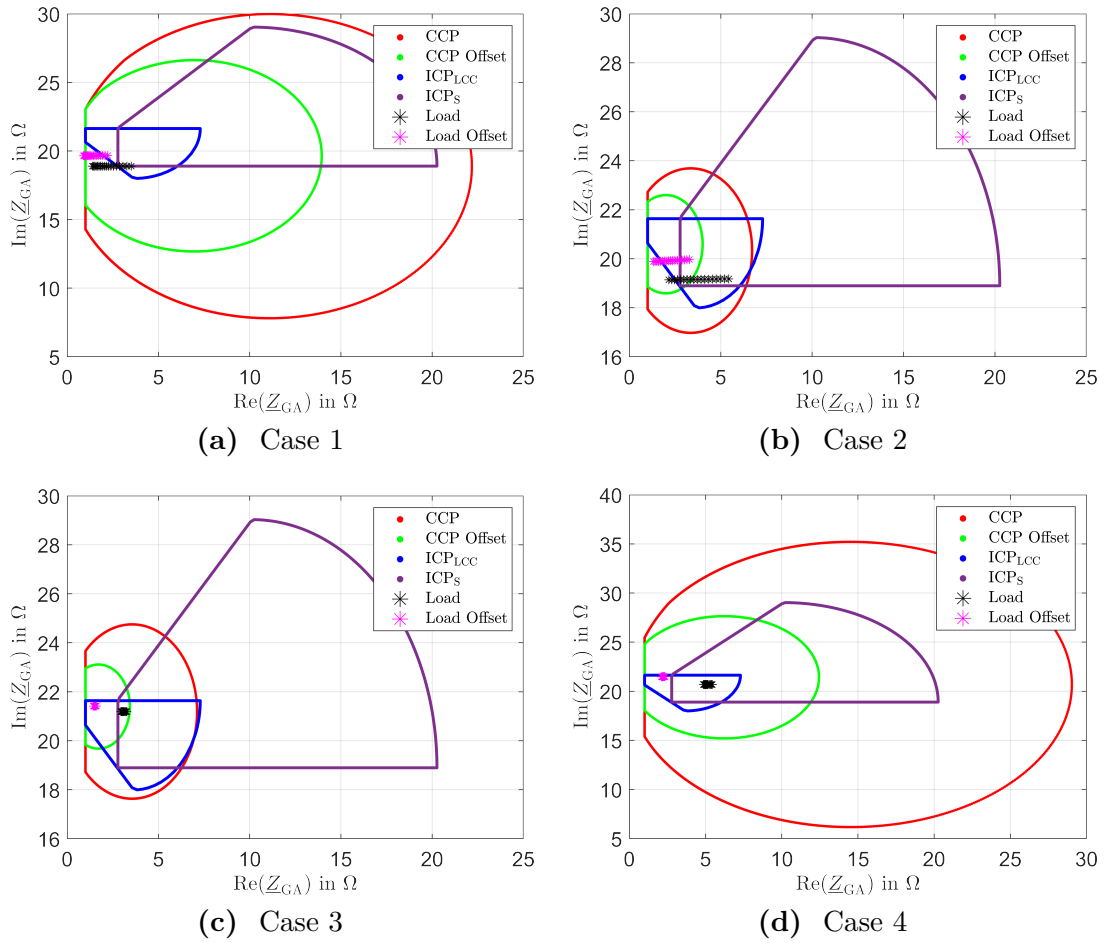


Figure 5.19 – Results of the process flowchart from Fig. 5.12 for (a)-(d) each secondary case.

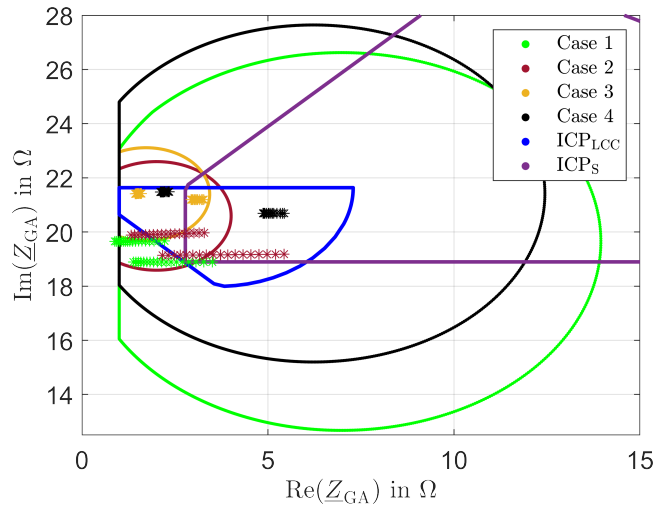


Figure 5.20 – Results of the process flowchart from Fig. 5.12 for all cases at k_{min} .

As shown in Fig. 5.12, these results can now be used to evaluate the ICPs and thus the inverters with their tuning topologies, or the resulting combination of ICPs and CCPs (if any) can be used as a design space for a new set of primary electronics.

In each subfigure of Fig. 5.19, the red and green planes represent the CCP at the nominal and offset positions, respectively. The OPs are also shown for the nominal (black) and offset (magenta) positions. The ICP of Case B, the series tuned ICP_S, is shown in purple and the ICP_{LCC} of Case A is shown in blue.

It can be seen that although Case B provides a much larger ICP, fewer OPs can be driven compared to Case A. Here, the OPs for the offset positions are mostly outside the ICP_S. The reason for this is the current limitation of the inverter. The current flowing through the inverter is similar to the coil current in series tuned systems, and the required primary coil currents exceed the inverter current limit for Case B. Increasing the inverter coil current limitation moves the left boundary of the ICP_S to the left.

Furthermore, it can be seen that the coupling quality is sufficient for all cases, since all nominal (black) OPs lie within their corresponding CCP (red), which is also true for the offset cases (magenta OPs in green CCP), although Case 2 and Case 3 provide very small CCPs.

Another observation is that the secondary LCC tuning OPs (Cases 3 and 4) are very closely grouped at the GA interface. This simplifies the design of the primary-side electronics because there is less area to cover. In addition, closely grouped OPs place less stress on the electronics, result in a more tolerant system, and are therefore preferable. Another design goal should be to create CCPs that have a small buffer to the OPs or vice versa. If most of the OPs are close to the left CCP boundary, as in Cases 1, 2, and 3, the system will always operate close to the coil current limit. This means that the real system may exceed the leakage flux limit, given the assumptions made for this use-case (FHA) and the comparison of measurements and results from Section 5.3.3, which show slightly higher primary currents in the measurements.

The previous results were obtained without loss consideration. The presented loss approach of Section 5.1 was performed for a constant P_{out} and the new ICPs with their efficiency maps are shown in Fig. 5.21 for Case A and in Fig. 5.22 for Case B (with each secondary) at nominal position. The lossless ICPs (blue) are also shown for comparison.

If misalignment is introduced, these figures change again and the efficiency degrades, an example for both Cases A and B at k_{min} is shown in the Appendix A.1.

Since the magnetics do not pose a significant constraint, interoperability in this case can be ensured for both Cases A and B if all OPs lie within their ICPs. To achieve this, the tunings and boundaries of both cases were adjusted and the redesigned ICP_S and ICP_{LCC} (with losses and lossless) are shown in Fig. 5.23 and their new boundaries are listed in Tab. 5.7.

By increasing the allowed current and the phase angle, the ICP_S now reaches almost all OPs. It is not mandatory for a charger to deliver rated power at the rectifier interface under all conditions and positions [50], so the OPs from Case 1 that are still outside the ICP can be reached if the required output power is reduced slightly as the ICP then increases (see Fig. 5.9b). The initial ICP_{LCC} already covered almost all OPs, so in this case only the allowed phase angle and the tuning had to be slightly adjusted to ensure interoperability.

There are many other ways to approach this use-case to improve a case or achieve interoperability. The interoperability zone of all coil combinations could be used as the ultimate design space since it is guaranteed to stay within the magnetic and leakage flux limits. If both primary and secondary electronics are designed to match the CCP, interoperability is assured. The same is true for active tuning designs, which could be designed to move all OPs (secondary tuning) or the ICP (primary tuning) into the CCP.

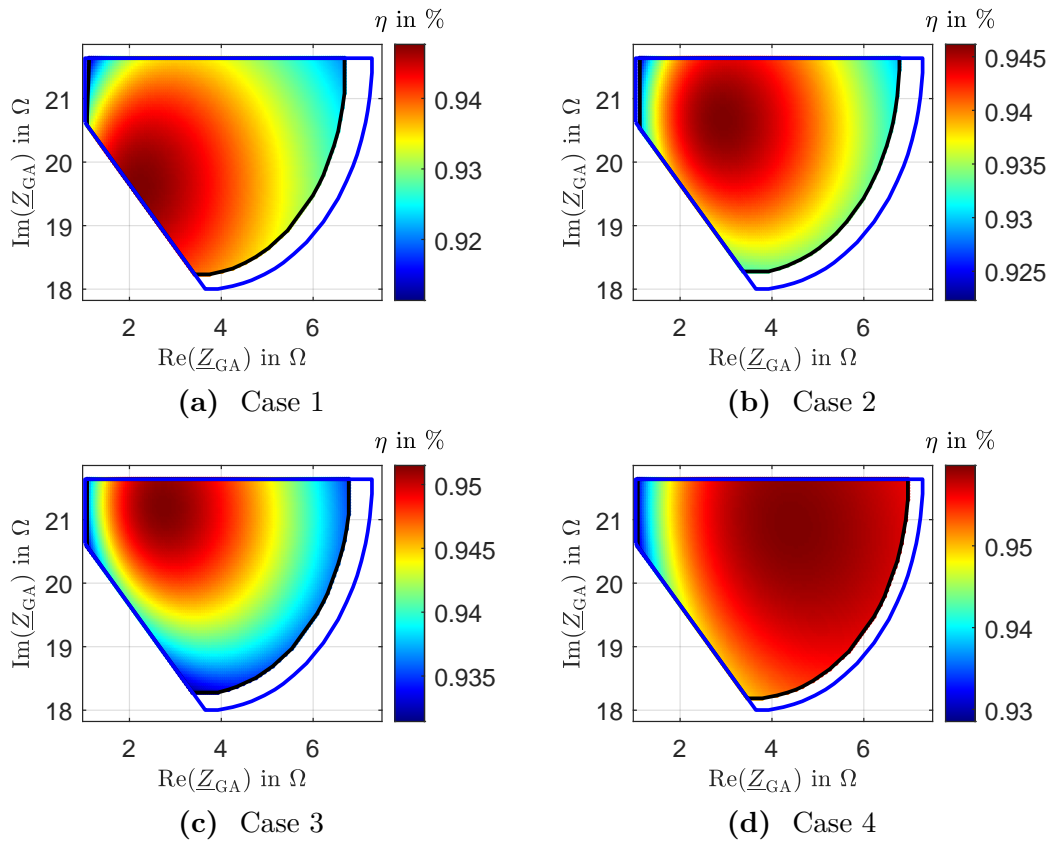


Figure 5.21 – Results of the loss considerations (black hull curve with efficiency heatmap) for Case A on the primary and (a)-(d) each secondary case at the GA interface and k_{nom} . The blue hull curve represents the lossless ICP.

Table 5.7 – New Inverter Boundaries

Inverter	
Case A	Case B
$V_{\text{in}} = (50 - 500) \text{ V}$	$V_{\text{in}} = (50 - 500) \text{ V}$
$I_{\text{in}} = (5 - 66) \text{ A}$	$I_{\text{in}} = (40 - 100) \text{ A}$
$\varphi_{\text{in}} = (0 - 65) \text{ deg}$	$\varphi_{\text{in}} = (0 - 65) \text{ deg}$
$X_{1,\text{new}} = 4.2$	$X_{1,\text{new}} = \omega L_1$

Another approach could be to evaluate the system and derive constraints on its interoperability. For example, the consequences of the evaluation could be to allow only coils with a coupling factor higher than a certain k_{min} , to allow only lower air-gap classes (e.g., only Z1 can be driven), or to reduce the transferred power (e.g., the system is only capable of providing WPT1-2). Some of these limitations lead to the conclusion that the system may not be suitable for public charging, but could be reasonably good for cost-reduced or fleet-based systems.

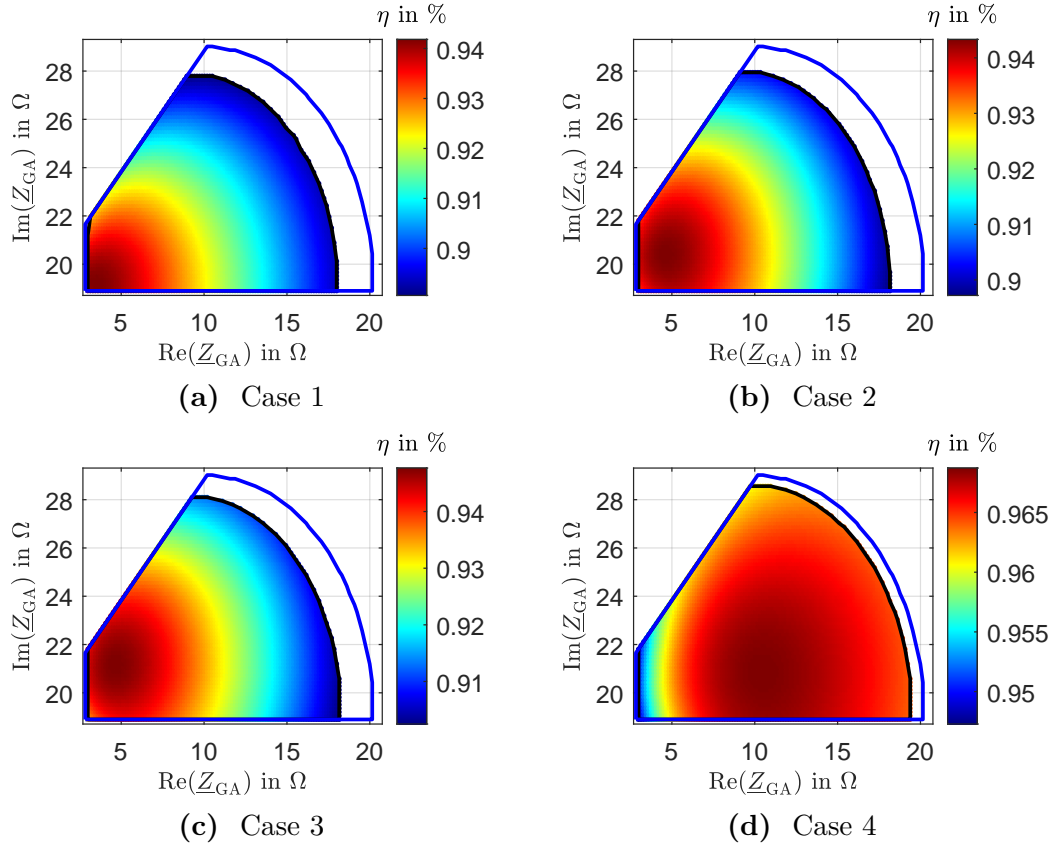


Figure 5.22 – Results of the loss considerations (black hull curve with efficiency heatmap) for Case B on the primary and (a)-(d) each secondary case at the GA interface and k_{nom} . The blue hull curve represents the lossless ICP.

With slight changes in the flowchart from Fig. 5.12, the proposed method can also be used to evaluate coupler geometries for given electronics. An evaluation can be done by comparing the resulting CCP sizes, interoperability zones and $I_{B\text{max}}$ curves of all combined couplers.

The loss extension shows that the redesign still addresses most of the OPs, while some move out of the ICP. It can be seen that the ICPs decrease because the inverter has to cover the losses and that this affects only a few OPs from Case 1 that can no longer be driven by the $\text{ICP}_{S,\text{wLoss}}$ (the series tuned ICP with losses considered). However, the efficiency distribution varies and the leakage flux is within limits for the presented OPs.

It must be emphasized that these results were obtained without considering the inverter (switching) losses and harmonics. These losses are highly dependent on the actual circuit and the OP itself. Therefore, it is quite difficult to derive exact losses for a variety of OPs. A thorough study of losses, harmonics and their impact on ICPs and CCPs is important for good quality results and is part of future work (see Section 8.4).

The compensation topologies in Tab. 5.2 were designed to cover most of the associated ICPs, and in some cases a trade-off had to be made between covering the CCP or the ICP. Perfect or active tuning is beyond the scope of this example and will be covered in the next chapter.

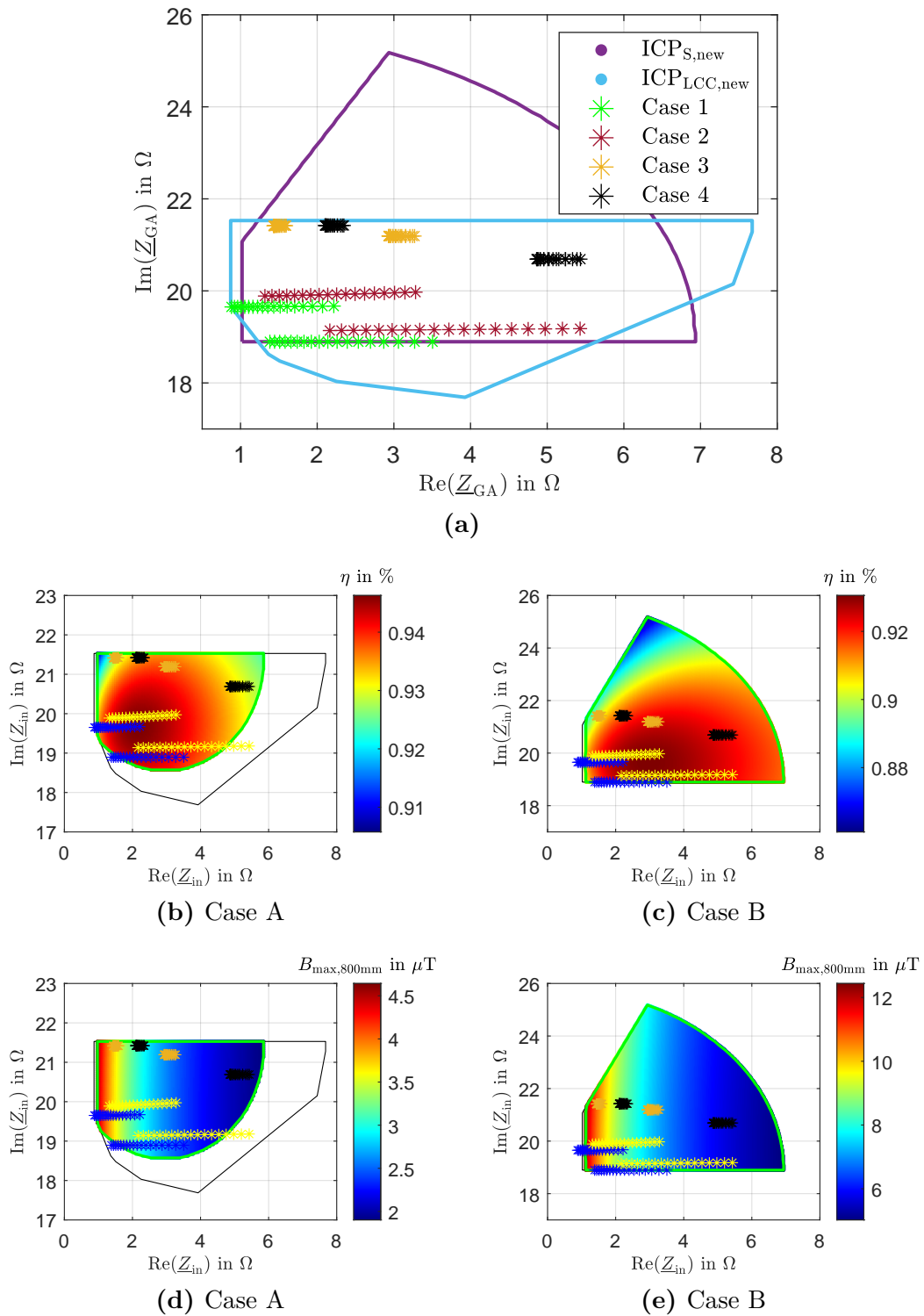


Figure 5.23 – Results of the redesigns of the Case A (light-blue) and Case B (purple) electronics in (a), with (b)-(c) efficiency heatmaps and (d)-(e) leakage flux heatmaps, respectively.

5.4 Summary

In this chapter, the electronics of an IPTS were studied with the aim of improving its reliability. An extension of the IPM to include loss analysis was introduced, and the losses of individual components were studied, with the necessary assumptions for each component discussed. The effects of harmonics and switching losses were still neglected in the interoperability study due to the required calculation effort.

Two different flowcharts for integrating losses into the IPTS were presented, one for keeping output power constant and the other for keeping input power constant. The application of the constant output power flowchart to the IPM Example 1 from Chapter 3 demonstrated that losses have an impact on the size of the ICP, as higher input power is required to cover the losses. The extension now allows a comprehensive study of the IPTS with heatmaps such as leakage flux and efficiency. However, it has also been shown that heatmaps can be derived for almost any circuit parameter.

In addition, a comprehensive use-case, IPM Example 3, was presented to summarize the contents of Chapters 3, 4, and 5. This example focused on a primary charging station design with the requirement to address various secondaries under public charging assumptions. The IPM was first applied without losses to allow comparison of the lossless approach with the loss extension and to evaluate the extension. Although it is challenging to achieve full interoperability under public charging conditions, especially without active tuning or adaptation of the secondaries, the presented redesign demonstrates that interoperability still can be achieved.

This chapter concludes by highlighting that achieving full power transfer under all coupling conditions for a primary without active tuning is challenging and comes at a high cost to the inverter or component stress. However, active tuning can significantly reduce component stress by allowing the IPPs and OPs (and efficiency) to be shifted. The next chapter examines the sensitivity of an IPTS, with a focus on active tuning and how it can help achieve greater interoperability. In general, a better understanding of system sensitivity is necessary to make better design decisions.

6 Tuning Sensitivity Analysis within IPT Systems

In the previous two chapters a comprehensive study of magnetic and power conversion components was conducted. The IPM was expanded to incorporate losses. This method was then applied to a broad use-case aimed at evaluating primary electronics for public charging scenarios, with various secondaries under different conditions, including battery voltage and positional offset.

The results enable the sensitivity of IPTSs to be studied under specific conditions. Designing a compatible primary can be challenging even for seemingly similar secondaries, and this difficulty escalates as the number of secondaries that must be driven increases. Several factors contribute to this complexity and make achieving interoperability a challenging task. Consequently, a deeper understanding of the factors that influence and shape IPPs is essential.

Achieving interoperability requires an understanding of how an IPPs can be designed or moved to minimize stress on the electronics while allowing more OPs to be driven overall.

This is important for two reasons. First, it can be used at the design stage to develop efficient and universally deployable systems. On the other hand, it can facilitate a good understanding of system control to find the optimal setting for different operating conditions.

Sensitive parameters in this regard are the compensation networks on both sides, which are also the last components of the IPTS targeted for deeper analysis in this thesis. This chapter investigates the impact of tuning topologies, the design of their nominal values as well as the variations of these values and how this can be utilized for system design or control in terms of active tuning.

Therefore, a sensitivity analysis is first performed focusing on variations in tuning and how this shapes an IPP as well as how this can be used to move an IPP into an impedance zone or towards a better operating region, for various parameters such as efficiency, leakage flux, loss, and system currents. The primary objective of this study is to achieve interoperability, which means addressing numerous OPs under reasonably efficient conditions, as opposed to conventional design approaches that usually prioritize efficiency for a single condition. Furthermore, as mentioned above, this can be utilized for control, although this is beyond the scope of this thesis, see Section 8.4. In this work, the focus will be on deploying it for system design.

Variations in each tuning component are investigated, followed by an analysis of active tuning and its impact on the system requirements, all under consideration of various heatmaps. The focus of this work is to determine how both tuning networks can improve interoperability.

The knowledge gained from this study is then used to design and assess tuning networks for a set of 50 kW coils intended for EV charging applications. Here the objective is to compare S-S tuning with LCC-LCC tuning. Lastly, a summary is provided.

6.1 Impact of Tuning Changes on IPT Systems

For simplicity, losses are initially disregarded and the primary tuning focuses on the ICP while the secondary will be looked at by the means of moving the OPs. To study this, the IPPs from Chapter 3 will be used, see Fig. 3.13.

The coil component boundaries (GA and VA boundaries) are first neglected (the green ICP with the $P_{\text{out,min}} = 10 \text{ kW}$ boundary from Fig. 3.17 is used). Section 6.1.3 will investigate their impact via heatmaps. For a better understanding, each edge of the ICP will be represented by a different color and the initial ICP (LCC–LCC tuning) with the inverter boundaries from Tab. 3.5 is shown in Fig. 6.1 at all interfaces.

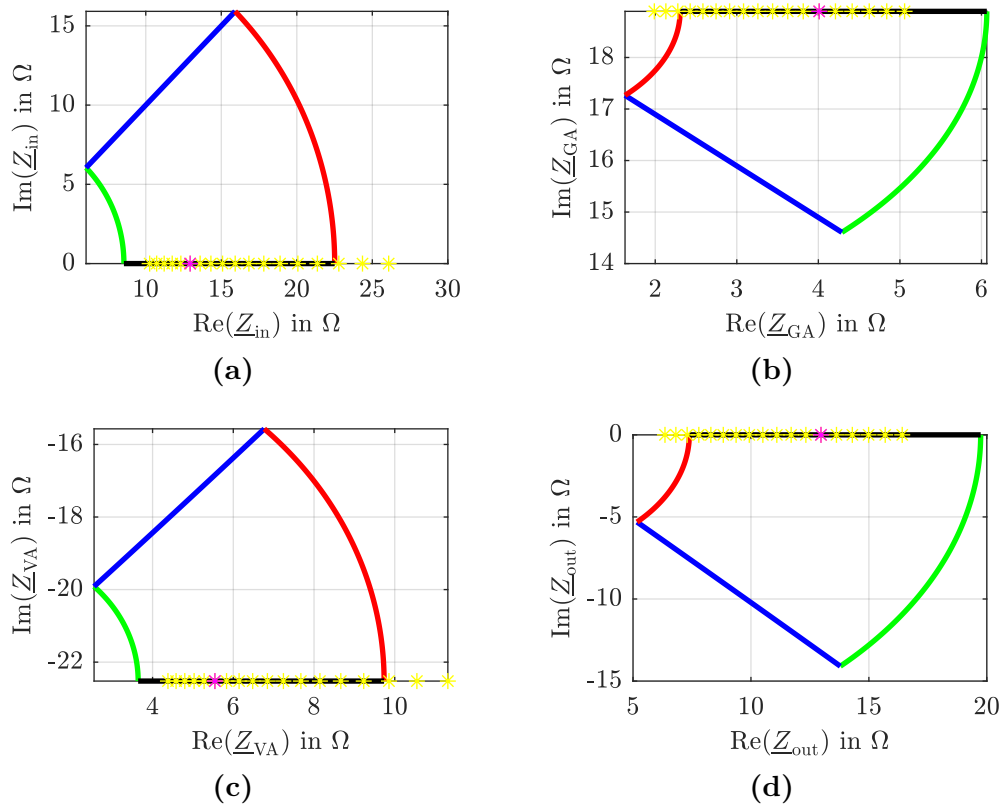


Figure 6.1 – 10 kW ICP_{in} with different colored edges at all four impedance interfaces for ideal resonance LCC–LCC tuning ($X_{\text{GA}} = 7.2 \Omega$, $X_{\text{VA}} = 8.5 \Omega$). The OPs for $V_{\text{bat}} = 280 - 450 \text{ V}$ are shown in yellow with the nominal voltage $V_{\text{bat}} = 400 \text{ V}$ highlighted in magenta.

This system was tuned in a conventional way under ideal resonance conditions, as explained in Section 2.2.3. The position was set to (0,0,140) mm with a resulting coupling factor of $k = 0.22$. With Eq. (4.1) and the assumption of $VA_1 = VA_2$, an initial primary current can be derived to

$$I_1 = \sqrt{\frac{VA_1}{\omega L_1}} = \sqrt{\frac{P_{\text{out}}}{k \cdot \omega L_1}} = 48.1 \text{ A.} \quad (6.1)$$

Without a series capacitor C_{s1} , this results in a required DC voltage (2.39) of

$$V_s = \frac{\pi}{2\sqrt{2} \cdot \omega L_1 \cdot I_1} = 1010 \text{ V.} \quad (6.2)$$

Since this value is very high, a series-tuned capacitor can be used on both the primary and secondary coils to adjust the coil voltages to a more desirable value. If an I_1 of 50 A and an inverter DC input voltage V_s of 400 V is desired, Eq. (2.40) can be used to determine X_{GA} to

$$X_{GA} = \frac{2\sqrt{2} V_s}{\pi I_1} = 7.2 \Omega \quad (6.3)$$

which then can be used with Tab. 2.2 to determine L_{s1} , C_{s1} and C_{p1} .

Generally, there are various ways on how to approach this and here only one “conventional” way is shown. When I_1 is determined, V_{oc} and I_{sc} can be calculated (for a fixed position and battery voltage, here $V_{bat} = 400 \text{ V}$ was set) which then in turn can be used to determine Q_2 and X_2 as described in Section 2.2.3.

The nominal tuning point is highlighted in magenta in Fig. 6.1. It can be seen that the system is in resonance since ideal tuning conditions were assumed for this example. However, the full battery voltage range of $V_{bat} = 280 - 450 \text{ V}$ is shown in yellow and the results show that some OPs cannot be addressed by the ICP.

A conventional approach always requires designer experience and is an iterative approach. The complexity increases drastically with more OPs and secondaries. Designing a primary that can drive all existing secondaries is impossible which is why standardization proposes an IPP approach which both sides can follow to achieve interoperability.

Therefore, the following section will study how typical variations within the tuning parameters affect the ICP, and then how they can be used to design a tuning that focuses on addressing all OPs. This will be done for the primary side, but the results are similarly applicable to the secondary side. It must be noted that the definition of tuning for the secondary side is in the opposite direction to the impedance definitions, as explained in Section 2.2.3.

6.1.1 Variations in L_s , C_s and C_p

In Fig. 6.2, a closer look on the inverter to GA transfer (from Fig. 6.1a to Fig. 6.1b) is shown.

The LCC matrix can be deconstructed, as was done for the T-Transformer of the coils in Fig. 3.3. It can be seen that the series elements represent a shift upwards (C) or downwards (L) in the imaginary axis, as already discussed in Section 4.2.1, where the influence of the mutual inductance on the size of the transferred CCP was shown. The C_{p1} value affects the size of the IPP and also mirrors the edges as is highlighted by the different colors.

The first impedance \underline{Z}_{Ls1} shifts the IPP on the imaginary axis by $-X_{GA}$. However, the transfer due to the parallel \underline{Z}_{Cp1} results in the lower black line being at $+X_{GA}$. The subsequent series \underline{Z}_{Cs1} transfer, moves the ICP up on the imaginary axis, with the black line being at the impedance ωL_1 , when ideally tuned at resonance condition.

The deconstructed LCC transfer was repeated for different tuning values and is shown in Fig. 6.3a and Fig. 6.3b for $X_{GA} = 5 \Omega$ and $X_{GA} = 10 \Omega$, respectively. The ICP always ends up with the initial bottom line being at ωL_1 .

However, changes in X_{GA} (and therefore in \underline{Z}_{Cp1}) change the size of the final ICP as well as the location on the real axis. As a result, a larger X_{GA} results in a larger ICP and shifts

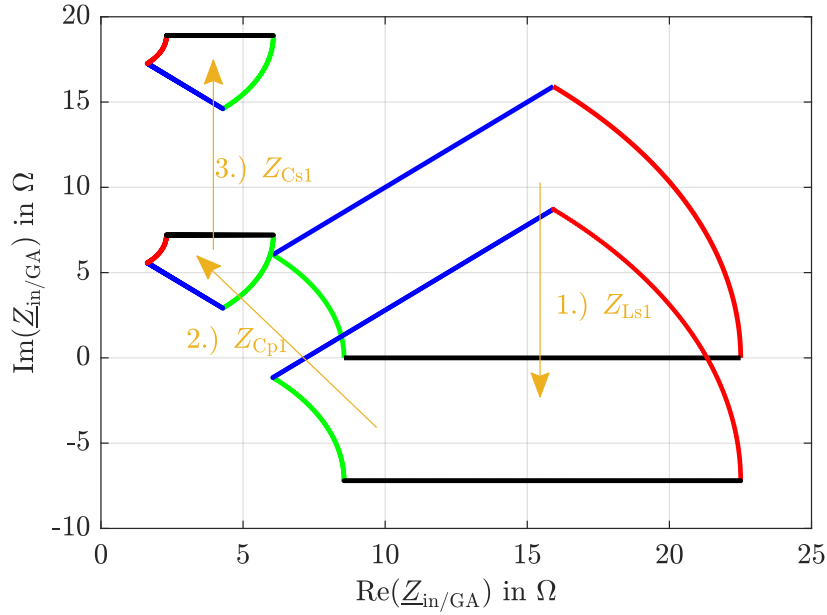


Figure 6.2 – Deconstructed IPP transfer from inverter to GA interface for an ideal LCC tuned primary side ($X_{GA} = 7.2 \Omega$).

the ICP towards the positive real axis (to the right). Fig. 6.3c shows the deconstructed LCC IPP transfer for a range of X_{GA} values ($3.6 - 10.8 \Omega$).

To get a better understanding of the effect of the \underline{Z}_{Cp1} element, Fig. 6.3d shows the LCC tuning transfer for a range of $X_{GA} = 2.16 - 21.6 \Omega$, without the L and C series elements ($\underline{Z}_{Ls1} = \underline{Z}_{Cs1} = 0 \Omega$), thus a plain parallel tuning. Without the series shift first, a rotation is introduced in the ICP, based on the X_{GA} value, where a high value means less rotation and a larger ICP size.

Additional complexity is introduced if one of the three elements is out of resonance or if only one parameter of the LCC network is varied. Thus, variances of \underline{Z}_{Ls1} while keeping \underline{Z}_{Cp1} constant and vice versa are shown in Fig. 6.3e and Fig. 6.3f, respectively. The constant value was set to $X_{GA} = 7.2 \Omega$ and the variation range was set to $\underline{Z}_{Cp1} = 0.5 - 20 \Omega$. The \underline{Z}_{Cs1} series transfer is not shown since it is only an upward shift as discussed earlier.

This effectively shows that variations in tuning have a significant effect on the IPP and its size and position, even if only one parameter is varied, either actively tuned or due to unintentional tolerances. As shown, the variation of all potential tuning parameters is complex. To show the complexity of this, variations of all three separate LCC parameters are shown in Fig. 6.4.

This illustrates the possibilities of active tuning. In principle, a IPP could be moved in many ways. However, it may be impractical or costly to introduce variations in all parameters, especially variations in C_{p1} or C_{s1} . Therefore, a tuning setup that requires minimal variations in LCC tuning values while providing a large ICP is desired. In detail, these ranges have to be individually tailored to the requirements of a primary side. This is shown in an example in Section 6.2.

To fully utilize all tuning variations for perfect system control and design is beyond the scope of this thesis and can be part of future work and is further discussed in Section 8.4. Further complexity is introduced when the secondary also employs active tuning, making

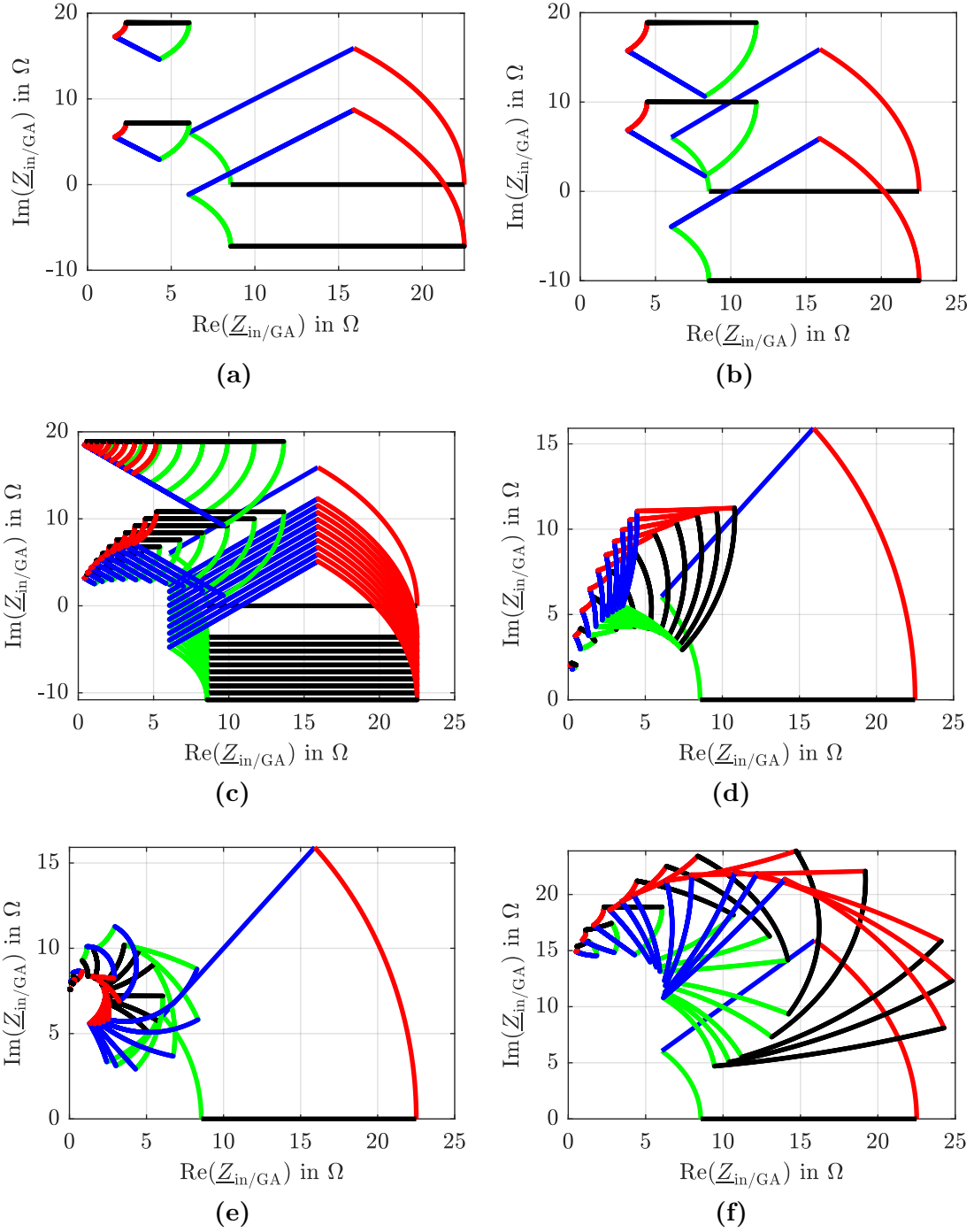


Figure 6.3 – Sensitivity analysis of the IPP transfer from inverter to GA interface for various conditions; (a)-(c) LCC transfer for (a) $X_{\text{GA}} = 5 \Omega$, (b) $X_{\text{GA}} = 10 \Omega$ and (c) $X_{\text{GA}} = 3.6 - 10.8 \Omega$; (d) $\underline{Z}_{\text{Ls1}} = \underline{Z}_{\text{Cs1}} = 0$ and $\underline{Z}_{\text{Cp1}} = 2.16 - 21.6 \Omega$; (e) $\underline{Z}_{\text{Cp1}} = 7.2 \Omega$ (const.) and $\underline{Z}_{\text{Ls1}} = 0.5 - 20 \Omega$ (f) $\underline{Z}_{\text{Ls1}} = 7.2 \Omega$ (const.) and $\underline{Z}_{\text{Cp1}} = 0.5 - 20 \Omega$.

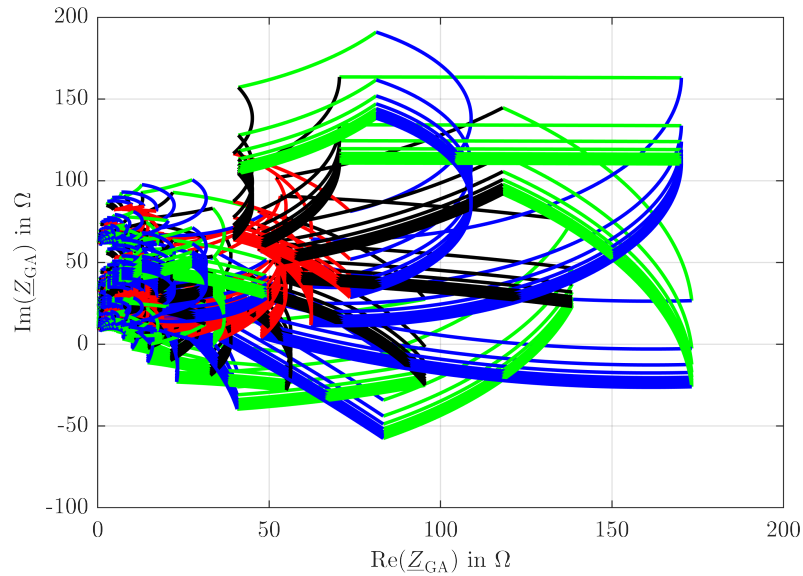


Figure 6.4 – IPP transfer from inverter to GA interface for variations in each LCC parameter and their combinations.

conventional analysis difficult. However, the IPM is well suited for such complexities. To explore this further, the next section looks at the active tuning of the series L_{s1} element in both compensation topologies as it is used in the SAE J2954 reference systems [50].

6.1.2 Active Tuning

As discussed in Section 2.5.1, a public charging station is required to have Class I interoperability. This means that the primary is required to address the full power and air-gap range (Z1–Z3) under certain conditions. From a magnetics point of view, this results in a wide range of coupling factors that the primary has to cover, and this can be difficult as was shown in previous studies within this thesis.

To achieve interoperability, the reference systems in SAE J2954 introduce an additional degree of freedom by deploying active tuning on both sides with variable series L_{s1} and L_{s2} elements as shown in Fig. 6.5. The ranges are defined in [50] as $X_{GA} = 8 - 32 \Omega$ and $X_{VA} = -30 - 0 \Omega$.

To study the impact of these tuning ranges on the interoperability of the full IPTS, first Z2 (red) and Z3 (blue) WPT3 VAs are investigated at their maximum coupling conditions for

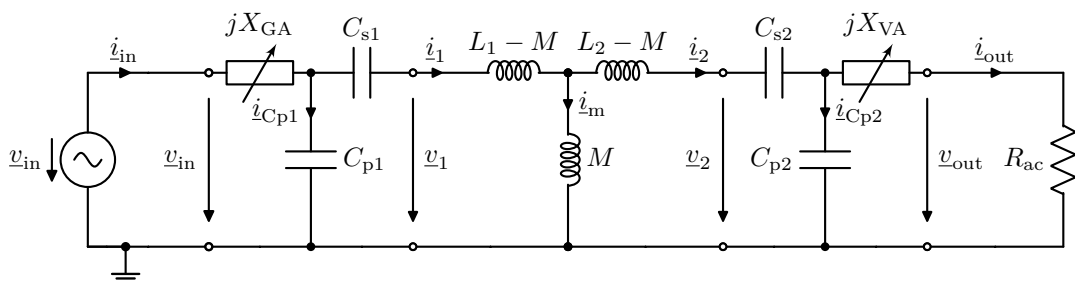


Figure 6.5 – IPTS circuit with LCC–LCC compensation and active tuning.

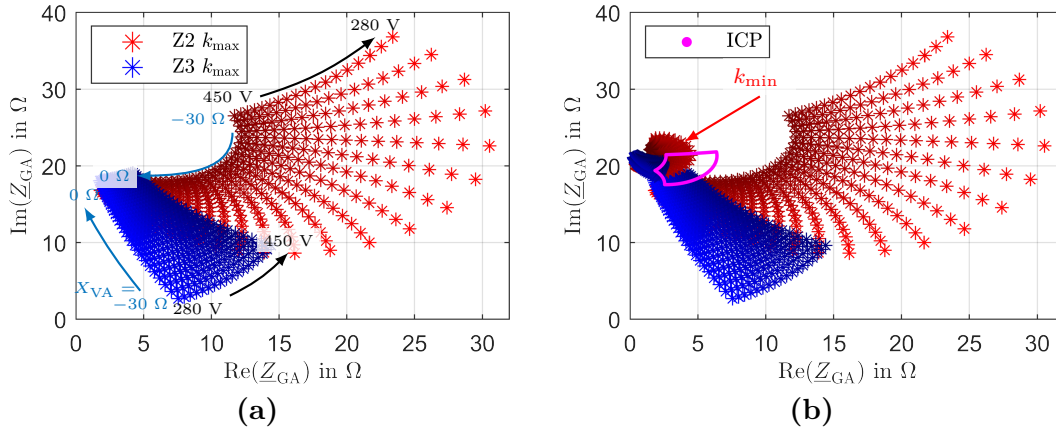


Figure 6.6 – OPs of Z2 (red) and Z3 (blue) VAs with passive rectification for different coupling conditions (each at their k_{min} and k_{max}) over the full battery voltage and active tuning X_{VA} ranges.

the full X_{VA} and variation of the battery voltage range in Fig. 6.6a at the GA interface. The increase in battery voltage is highlighted with a colormap (darker color = higher voltage) and the change in X_{VA} is also shown.

The results allow several conclusions. First, the OP range can be distributed quite differently, depending on the secondary coil as well as the chosen X_{VA} value. Second, it seems challenging to address the entire voltage range. Ideally, however, this can be made easier by tuning each voltage separately. Furthermore, this could be utilized to achieve constant operating conditions, e.g. constant current in the primary coil.

Fig. 6.6b shows the same OPs, but also for the k_{min} coupling conditions of both secondaries (Z2 red and Z3 blue) and an ICP for only one $X_{GA} = 16 \Omega$ condition in magenta. The ICP covers only a fraction of the impedance range and is therefore not able to operate with the coils under all coupling conditions.

As mentioned earlier, variations in primary tuning are possible, and the ICPs for different X_{GA} values are shown in Fig. 6.7a in yellow, and if the entire X_{GA} range of the primary LCC tuning is considered, then the green ICP is the area which can be addressed by the primary electronics. With this ICP and an appropriate setting of the X_{VA} value, almost all OPs can be driven.

However, this ICP does not take into account other system limitations (as discussed in Chapter 3). If a GA coil current limit of $I_1 = 75 \text{ A}$ is imposed, the ICP changes and the final ICP is shown in Fig. 6.7b in orange. This ICP never violates the primary coil current boundary¹. Thus, by considering the primary current limit, an essential part of the ICP can no longer be driven and interoperability is limited.

To emphasize the impact of the secondary rectification topology (as discussed in Chapter 5), the OPs in Fig. 6.7b were derived under the same conditions as previously shown, but with an impedance compression network (see Section 2.2.2) deployed. The distribution of the OPs is now completely different, with less spread, especially for the Z2 system. On the other hand, the k_{min} condition of the Z2 system cannot be addressed at all. Here, Fig. 6.7c shows only the OPs with properly selected X_{VA} values (-2Ω and -8Ω at k_{max} and -23Ω and

¹Other limits could be imposed, but are beyond the scope of this study.

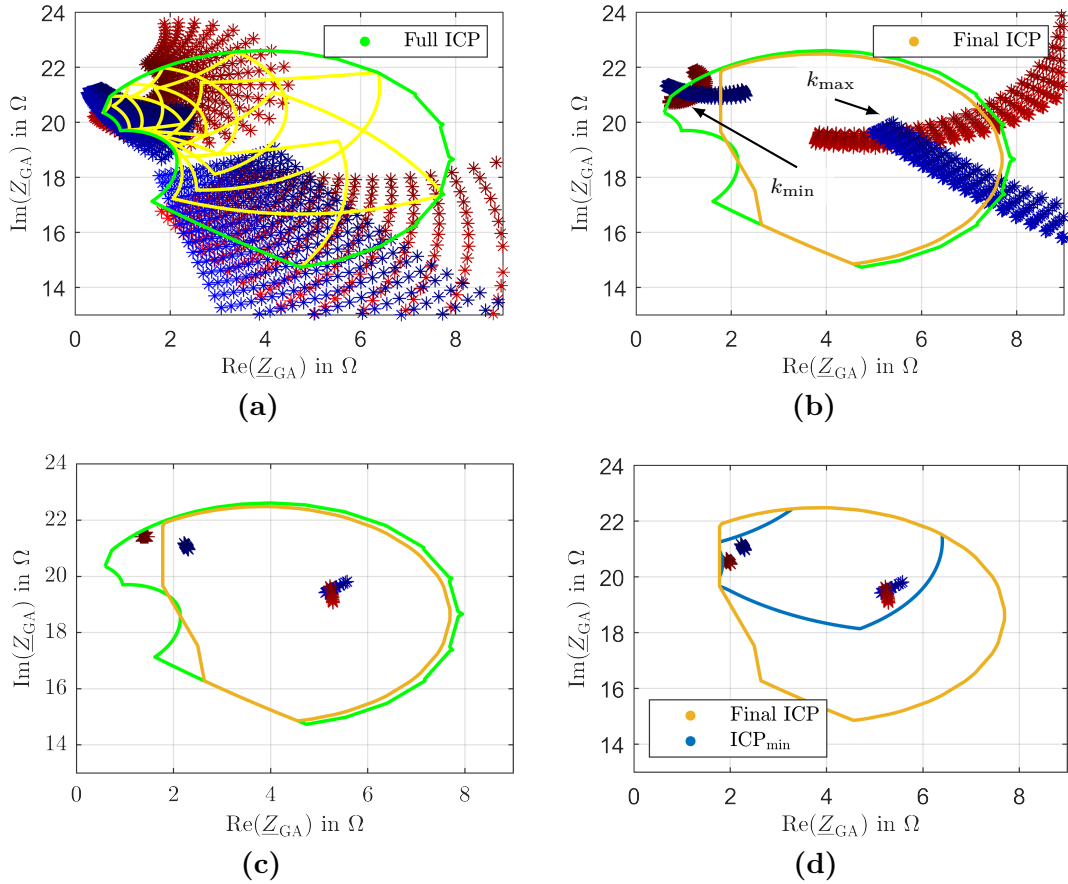


Figure 6.7 – Impact of active tuning on the ICP and the system interoperability; (a) variations of X_{GA} and the resulting ICP (green), (b) new OPs (same conditions but with impedance compression network) and final ICP (orange) after GA current boundary is imposed, (c) selections of X_{VA} values and (d) adjusted X_{VA} values and minimum X_{GA} range (16 – 20 Ω , new ICP in blue) for achieving full interoperability.

–31 Ω at k_{\min} for Z2 and Z3, respectively). The values at maximum coupling were chosen to have the least variance in primary coil current.

To operate the Z2 system at k_{\min} , a slight re-tuning of the C_{s2} capacitor was conducted (iteratively changed from 135 nF to 150 nF) and the results are shown in Fig. 6.7d. With this adjustment the full battery voltage range of both secondaries under all operating conditions can be driven by the IPTS.

The proper control of the secondary OPs is very important, as can be seen. It is needed to stabilize the system, to enable power transfer, or to achieve full interoperability. The choice of rectifier and tuning topology has a significant impact, as discussed in Section 2.2.2. Various other works discussing secondary tuning and active rectification solutions can be found in the literature, e.g. [28, 74, 78, 87, 88, 90, 176–178], and could also be evaluated, but this is beyond the scope of this thesis.

To conclude the study, Fig. 6.7d shows that the ICP does not need the full X_{GA} range for the operational requirements in this study. The range can be reduced to $X_{GA} = 16 - 20 \Omega$

(blue ICP) and still cover all OPs. For example, if this range were covered with variable capacitors, the range would be reduced from 0–780 nF (initial range is 8–32 Ω) to 0–470 nF, allowing a smaller and less expensive tuning board.

This highlights an advantage of the IPM in that it can be utilized and tailored to the desired operating conditions, and once this is done, tuning ranges and design decisions in general can be made while considering many different aspects at once. This can help to make IPTS designs smaller and more efficient because they can be designed precisely to the requirements using this method.

6.1.3 Impact on Efficiency and Heatmaps

The above section has shown how active (or changes in) tuning impacts the ICPs and the OPs, and how this can be used to assess or determine design ranges with the IPM.

However, as shown in Chapter 5, the IPM can be used to extract more information from the IPPs. This usually helps to get a better insight and allows to make better design decisions. Thus, Fig. 6.8 shows the previously discussed ICPs with different heatmaps. For simplicity, losses have been neglected. Nonetheless, the study could easily be extended to include a loss analysis.

When an ICP is moved to a desired area, it is useful to know more about the system conditions within the ICP and an important parameter is the inverter current as it affects ZVS and switching losses. The ICP over the entire X_{GA} range with I_{in} as a heatmap is shown in Fig. 6.8a. If a constant or low inverter current is desired, this map can help shift the OPs in the desired area. However, such a strategy requires active secondary tuning and communication between the primary and secondary, which is beyond the scope of this thesis.

For further analysis, a $X_{GA} = 8 \Omega$ was set and the ICP at the GA interface with I_1 (Fig. 6.8b), I_2 at k_{max} (Fig. 6.8c) and I_2 at k_{min} (Fig. 6.8d) are shown using heatmaps in Fig. 6.8. The GA current is independent of the coupling, but the heatmaps of the VA current vary greatly². As discussed in Chapter 4 and 5, this ultimately impacts the leakage flux distribution and the heatmaps of $B_{max,800mm}$ for k_{max} and k_{min} are shown in Fig. 6.8e and Fig. 6.8f, respectively.

This again demonstrates the dominance of the primary current in the leakage flux distribution. Nevertheless, the total value depends on the I_2 current or coupling condition. This was repeated for the ICP over the full X_{GA} range and is shown in Fig. 6.9, again for both coupling conditions.

As shown, the OPs can be evaluated directly and countermeasures can be initiated if the results are unsatisfactory. Besides the assessment and design of tuning networks, this approach can also be used for efficiency control approaches, as is discussed in Section 8.4.

Much more can be implemented and studied with the methods and approaches provided in this thesis. However, the scope of this thesis is to provide a method that is versatile enough to be used for a wide range of interoperability problems. The user of the method must always adapt the method to the application and the interoperability requirements, otherwise the problem will be too complex and it will be too difficult to find a satisfactory result. This is further discussed in Section 8.4.

With a better understanding of the tuning impact on the IPP provided, the next section deploys this knowledge to a high power use-case. The goal is to decide on a tuning topology for an already designed coil set and the desired inverter boundaries.

²It has to be noted that no boundaries were introduced to the IPP in this study for simplicity.

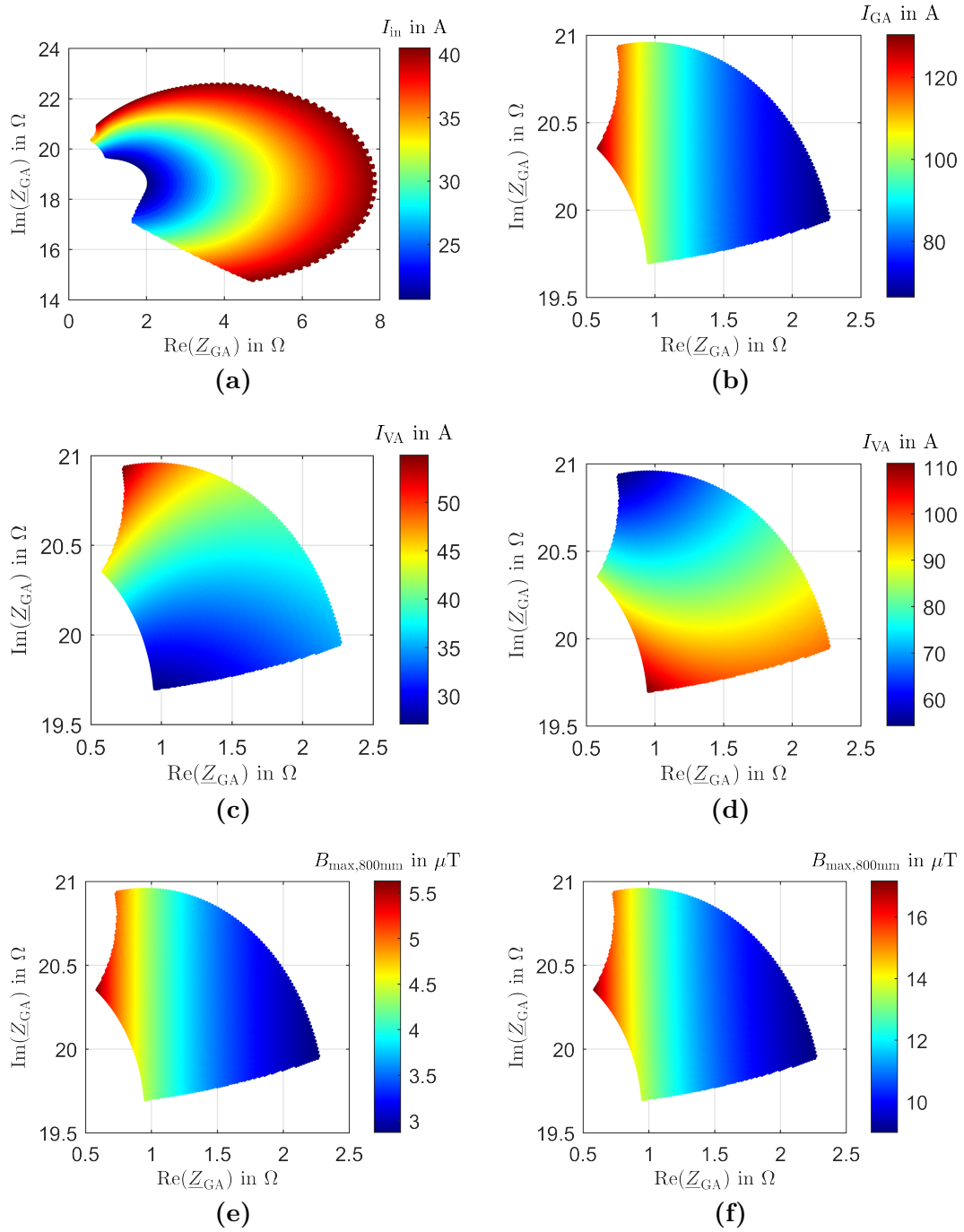


Figure 6.8 – ICP Heatmaps with variations in active tuning; (a) full ICP with I_{in} heatmap, (b)-(f) ICP ($X_{GA} = 8 \Omega$) with (b) I_1 , (c) I_2 at k_{max} , (d) I_2 at k_{min} heatmaps, (e) and (f) respective $B_{max,800mm}$ heatmaps.

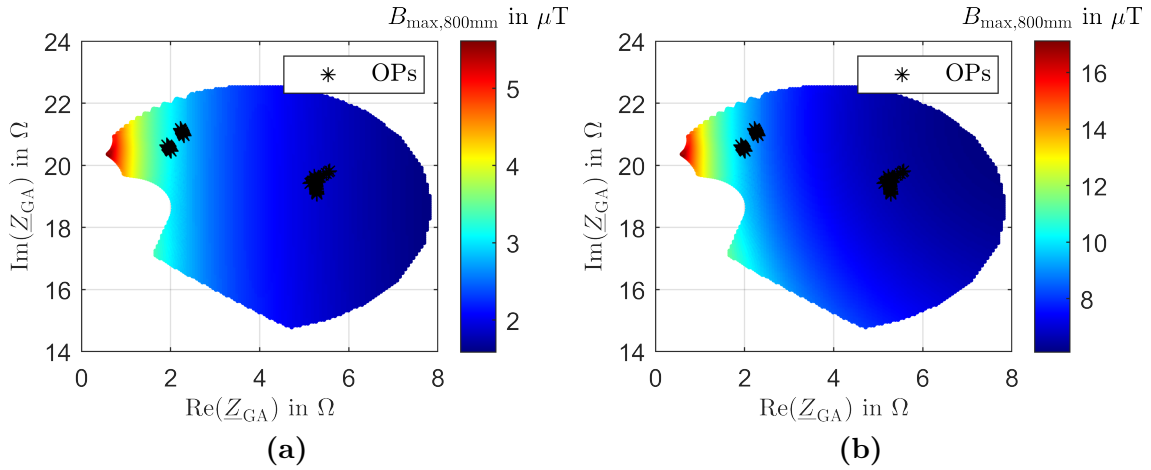


Figure 6.9 – Leakage flux heatmaps of ICP over full active tuning range for (a) k_{\max} and (b) k_{\min} coupling conditions with the OPs from Fig. 6.7d.

6.2 Application of the IPM: Compensation Design for a 50 kW IPT System

In this section, the IPM is used to evaluate two common compensation topologies, series tuning and LCC tuning, for a given 50 kW coil set³. Leakage flux limitation is a key aspect in high power IPTS to enable safe operation and is therefore part of the assessment. Primary and secondary compensations are designed separately with the objective that the resulting IPPs cover the coil capabilities and as many OPs as possible for different coupling and load conditions.

The previous sensitivity analysis of the tuning topologies is used to determine the IPTS behavior with LCC–LCC or series-series (S–S) tuning, and to discuss how to parameterize the tunings to achieve maximum interoperability. The goal is to find two compensation designs for the coils, so this section focuses on the coils and less on the power electronics (although they should be considered in a real design stage).

First, the coils and their limitations (some assumed) are described. Second, the design considerations are presented, using a two-step approach where secondary and primary tuning are first examined separately. A full system analysis with a discussion of the results concludes this chapter.

6.2.1 Coils and Boundaries

The coils for this study are based on results from [P.5] and were designed within a research project (NIIKOHLA, see Section 8.3).

A matched system with circular topology is used (both coils are identical) and the FEM simulation models are shown in Fig. 6.10. The simulations were conducted for an air-gap range of $z = 170 - 210$ mm and the horizontal offset is considered at each air-gap and set to $x = 75$ mm and $y = 100$ mm, according to SAE J2954 [50]. An aluminum shield as a car mimic plate is used on the secondary ($800 \times 800 \times 1$) mm. The inductances and coupling factors for six investigated positions are listed in Tab. 6.1. For simplicity, the study focuses

³Parts of this study were first published in [P.6].

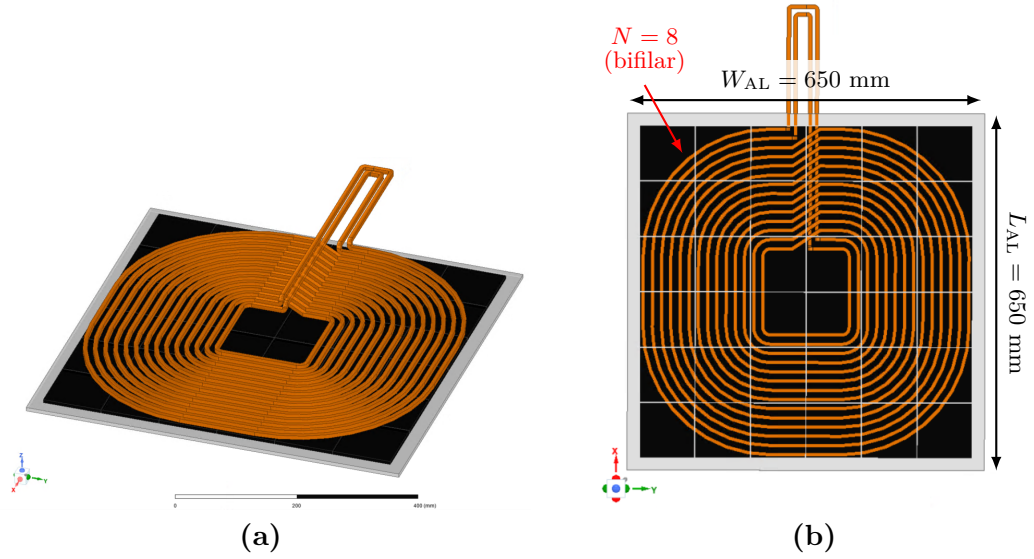


Figure 6.10 – FEM simulation models of the matched primary and secondary coils, (a) 3D view and (b) top view. The car mimic aluminum shield is not depicted. The aluminum is shown in grey, ferrite in black and the litz-wire winding in brown.

Table 6.1 – Inductances and Coupling of the 50 kW Coils for all Positions

Index	(x,y,z) (mm)	L_1 (μH)	L_2 (μH)	k
1	$(0,0,170)(k_{\max})$	35.05	34.99	0.3438
2	$(75,100,170)$	34.86	34.88	0.2465
3	$(0,0,190)(k_{\text{nom}})$	34.71	34.63	0.2922
4	$(75,100,190)$	34.63	34.59	0.2127
5	$(0,0,210)$	34.50	34.40	0.2488
6	$(75,100,210)(k_{\min})$	34.47	34.40	0.1835

on three main positions, each labeled by its coupling (maximum, nominal and minimum) k_{\max} , k_{nom} and k_{\min} .

As previously discussed, IPTS for EV charging must ensure that the leakage flux surrounding the vehicle remains below $B_{\max} = 15 \mu\text{T}$ for safe operation. The maximum leakage flux densities of the XZ- and YZ-planes at 800 mm and 900 mm from the center of the secondary coil as a function of different coil currents are shown in Fig. 6.11a and Fig. 6.11b for different couplings, with the isolines for $B = B_{\max}$ shown in Fig. 6.11c (800 mm) and Fig. 6.11d (900 mm).

It can be seen that in the case of minimum coupling, the primary coil current is limited and the secondary coil current must remain below 180 A to keep the leakage flux within these limits. This affects the IPPs and makes the compensation design challenging, as shown in the next section.

One solution to this is to implement an interoperability restriction and require that this system can only be used for car widths greater than 1700 mm. It is assumed that the leakage flux measurements will be made with a 100 mm diameter flux probe, with the flux captured

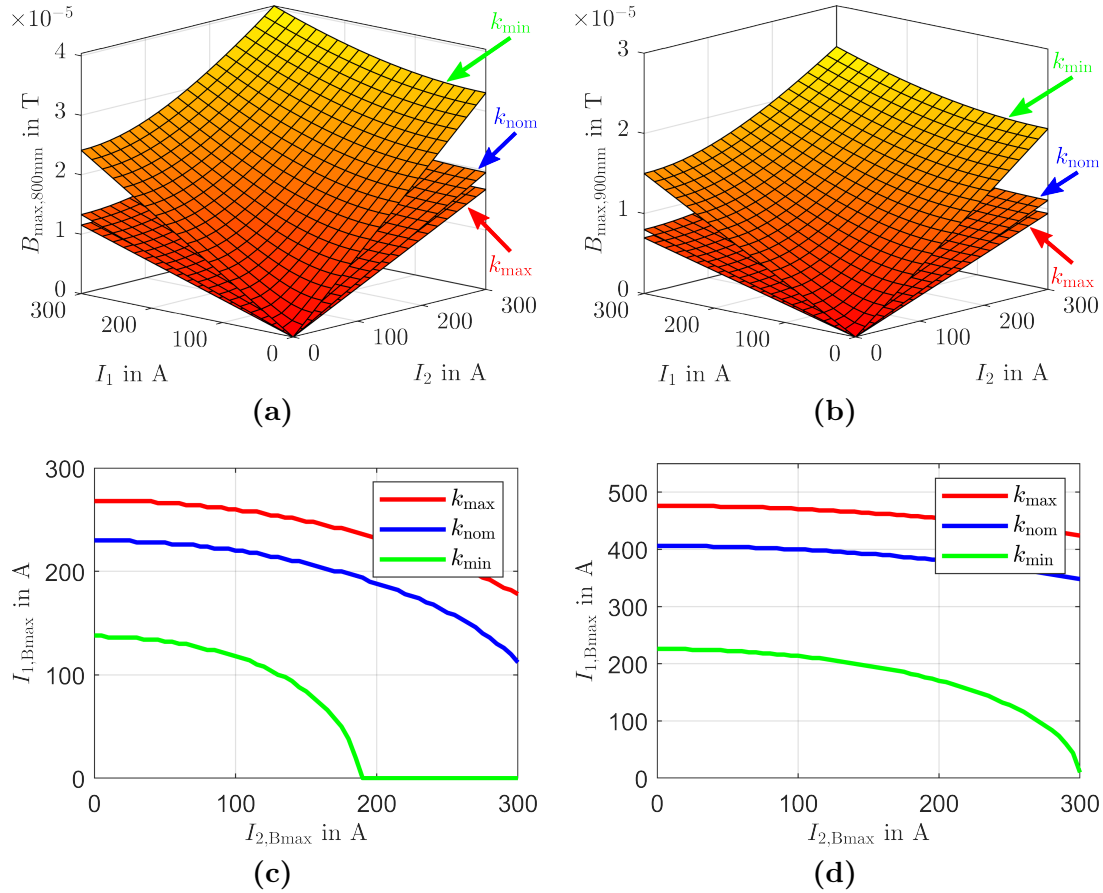


Figure 6.11 – Leakage flux study for changing currents and couplings; (a) $B_{\max,800\text{mm}}$ and (b) $B_{\max,900\text{mm}}$ as a function of (I_1, I_2) for three coupling conditions. The maximum allowed coil current combinations to stay below $15 \mu\text{T}$ for the same coupling conditions at (c) 800 mm and (d) 900 mm distance.

in the center of the probe. This must be taken into account in the simulation and in the placement of the leakage flux planes. As a result, the leakage flux plane at 900 mm from the secondary coil represents a car width of 2×850 mm instead of 2×900 mm. The 900 mm leakage flux results in Fig. 6.11b showing that this greatly simplifies the problem. Since most cars are wider than 1700 mm, this does not represent a real limitation.

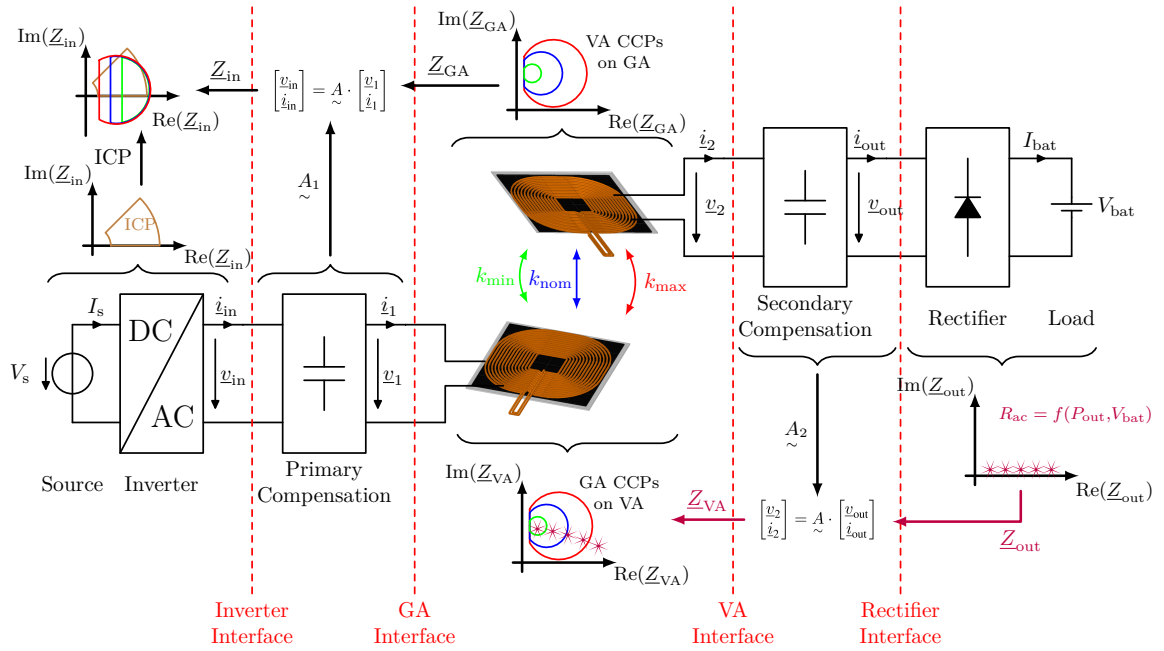
However, the IPM enables different leakage flux planes to be considered without additional effort. Consequently, the leakage flux planes at both distances (800 mm and 900 mm) are included in the following analysis. The results can then be used to determine a minimum car width requirement for the designed system, with the lowest possible width being preferred.

6.2.2 Design Considerations: Series-Series and LCC–LCC Compensation

The system boundaries and load conditions for this compensation design study are summarized in Tab. 6.2. The design and comparison of the two compensation topologies is done in two steps.

Table 6.2 – System Boundaries for the Compensation Design

Grid/Inverter	Coils	Rectifier/Load
$S_{in,max} = 75 \text{ kVA}$	$V_{1,max} = V_{2,max} = 3 \text{ kV}$	$V_{bat} = (280 - 420) \text{ V}$
$V_{in} = (500 - 900) \text{ V}$	$(I_{1,max}, I_{2,max}) = (200, 200) \text{ A}$	$P_{out} = 50 \text{ kW}$
$I_{in} = (20 - 100) \text{ A}$	$(x, y, z)_{min} = (0, 0, 170) \text{ mm}$	$R_{ac} = 8/\pi^2 \cdot V_{bat}^2/P_{out}$
$\varphi_{in} = (0 - 60) \text{ deg}$	$(x, y, z)_{max} = (75, 100, 210) \text{ mm}$	
	$B_{max} = 15 \text{ }\mu\text{H}$	
	$(I_{1,Bmax}, I_{2,Bmax}) = f(k, Q_2)$	


Figure 6.12 – IPTS topology, impedance interfaces (red dashed), impedance transfers and coupling conditions for the compensation design procedure.

The secondary side is designed by evaluating the OPs for each tuning topology and the CCPs for the different coupling conditions at the GA interface, as was done previously. In a second step, the CCPs are evaluated for different primary tuning topologies and design values at the inverter interface. The motive is to study how secondary and primary tuning design can be conducted separately and still achieve interoperability.

The design procedure using the IPP is shown in Fig. 6.12. Variations in battery voltage and coupling (three coil positions, k_{max} , k_{nom} and k_{min} as described in Tab. 6.1) are taken into account in order to achieve a power transfer of 50 kW under different interoperability conditions.

Once the results have been evaluated, the full S–S and LCC–LCC system can be compared, along with any limitations of the two step approach examined.

Table 6.3 – Overview of Tuning Design Values for 50 kW Coils

Case	X_1	X_2	X_1	X_2
	Series-Series Tuning		LCC-LCC Tuning	
k_{\max}	$\omega L_{1,\max}$	$\omega L_{2,\max}$	5.85/10.13	2.54
k_{nom}	$\omega L_{1,\text{nom}}$	$\omega L_{2,\text{nom}}$	5.85/10.13	2.53
k_{\min}	$\omega L_{1,\min}$	$\omega L_{2,\min}$	5.85/10.13	2.55

Secondary Tuning

The compensation networks for the coils are designed separately, starting with the secondary side.

The output impedances are a function of output power and battery voltage, and all OPs are transferred to the VA interface with the secondary compensation transfer matrix \tilde{A}_{C2} . This is done for both series and LCC tuning using the matrices from Tab. 3.1. Each topology is tuned three times (resonance at k_{\max} , k_{nom} or k_{\min}) in order to find the best tuning condition.

In the case of the secondary LCC tuning, X_{VA} was varied for each coupling condition based on the findings of the previous sensitivity analysis in Section 6.1. The design goal was to balance the coil currents and stay below the limits of Fig. 6.11. The values for both tunings are summarized in Tab. 6.3. The compensation parameters can be calculated with X_{VA} and Tab. 2.2.

The OPs for secondary series and LCC tuned systems are shown in purple in Fig. 6.13a and Fig. 6.13c respectively. A closer look at both can be found in Fig. 6.13b and Fig. 6.13d. To distinguish between the different tuning conditions, the OPs are marked with an asterisk (k_{\max}), a circle (k_{nom}) or a plus sign (k_{\min}). This is kept consistent throughout the study.

To see if the coils can drive these impedances, the GA CCPs are transferred to the VA interface, also for the same coupling conditions, and shown in Fig. 6.13 in red (maximum coupling), blue (nominal coupling) and green (minimum coupling). This shows that all OPs (for both tunings) lie within the CCPs, meaning that the coils are capable of driving them under all conditions. However, some OPs of the series tuned system are close to the boundary and if losses are included, as shown in Chapter 5, the CCP can become smaller and some points cannot be driven anymore.

To determine if the OPs can be driven within the given leakage flux limitation, the OPs from Fig. 6.13 are transferred to the GA interface with the matrix \tilde{A}_L . The results are shown in Fig. 6.14. The series tuned OPs are shown in Fig. 6.14a and the LCC tuned in Fig. 6.14b. The transfer was done for the three coupling conditions k_{\max} (red), k_{nom} (blue) and k_{\min} (green) and the OPs are no longer position independent, so they are colored with respect to the coupling condition.

The VA CCPs transferred to the GA interface are also shown, similar to Fig. 6.13.

The series tuned OPs lie all within their respective CCP (coupling condition dependent). However, the overall distribution of the OPs is wider in x- and y-direction than for the LCC tuned OPs. This can lead to stress and complexity in the power electronics as many different conditions have to be set.

To study the leakage flux limitation issue, the simplified approach from Section 4.2.3 is deployed first. The maximum allowed coil currents and thus new $R_{\min, B_{\max}}$ values are derived (again for each coupling condition) using the results from Fig. 6.11 and are shown in Fig. 6.14a

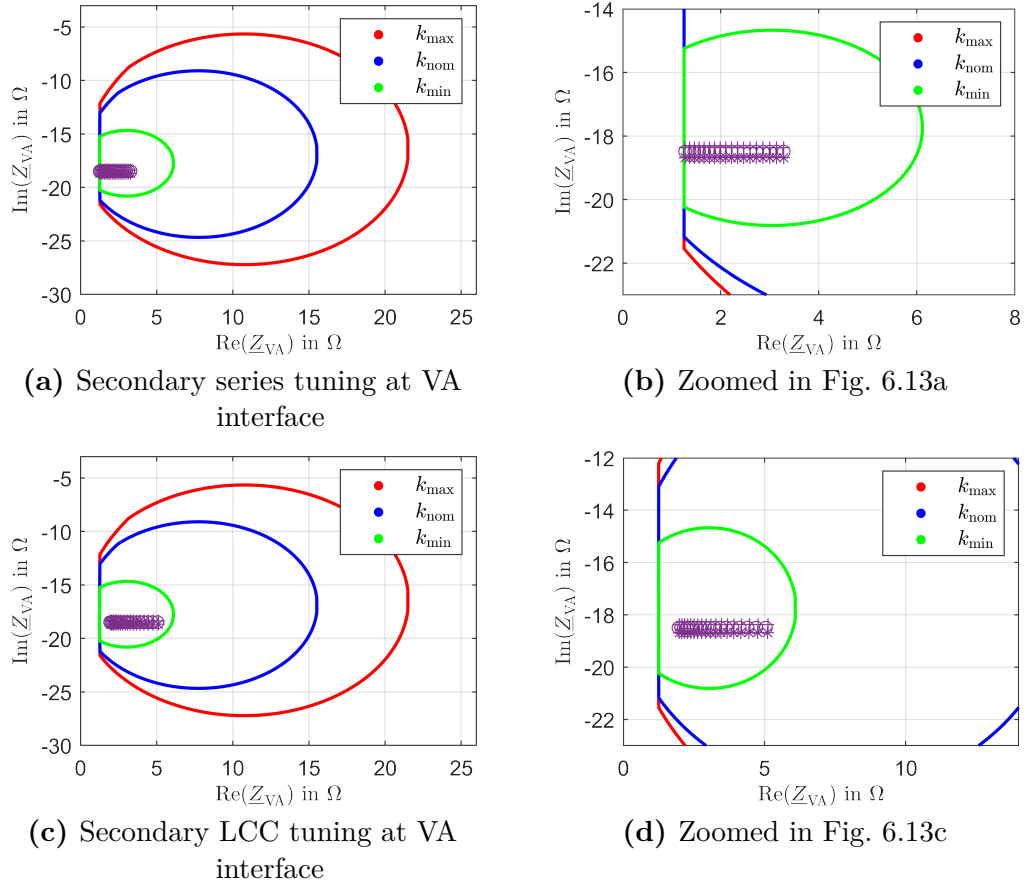


Figure 6.13 – VA interface analysis of the secondary compensation design. The CCPs are shown for maximum (red), nominal (blue) and minimum (green) coupling. Each topology was tuned for resonance at each coupling condition and the OPs are represented in purple with an asterisk (k_{\max}), circle (k_{nom}) or plus (k_{\min}) marker.

and Fig. 6.14b with the leakage flux boundary imposed at 800 mm distance and in Fig. 6.14c and Fig. 6.14d at 900 mm distance. The restricted area is shown as a shaded area where the color matches the coupling condition.

It can be seen that the leakage flux limit is violated only at the minimum coupling condition at 800 mm distance (for both tuning topologies). Due to the different tuning designs, more OPs are affected when using the LCC topology. For the series tuned system, only a few OPs are affected at minimum coupling. At 900 mm, the leakage flux does not interfere with the CCPs and OPs, so it is not a problem if this distance is set as the minimum requirement. It is important to note that this is only an evaluation of the fundamental wave of the leakage flux and neglects harmonics which may change the results.

However, in Chapter 4 it was shown that matched systems cannot neglect the impact of the secondary coil current when it comes to leakage flux. To study this issue for these 50 kW coils, Fig. 6.15 provides a closer look on the CCP at maximum coupling. The CCP is shown with the GA and VA current heatmaps in Fig. 6.15a and Fig. 6.15b, respectively. The calculations are based on the output power requirement of 50 kW, the coupling factor k and Eq. (4.1) and are therefore independent of the tuning and only evaluate the coils. These CCPs can be used

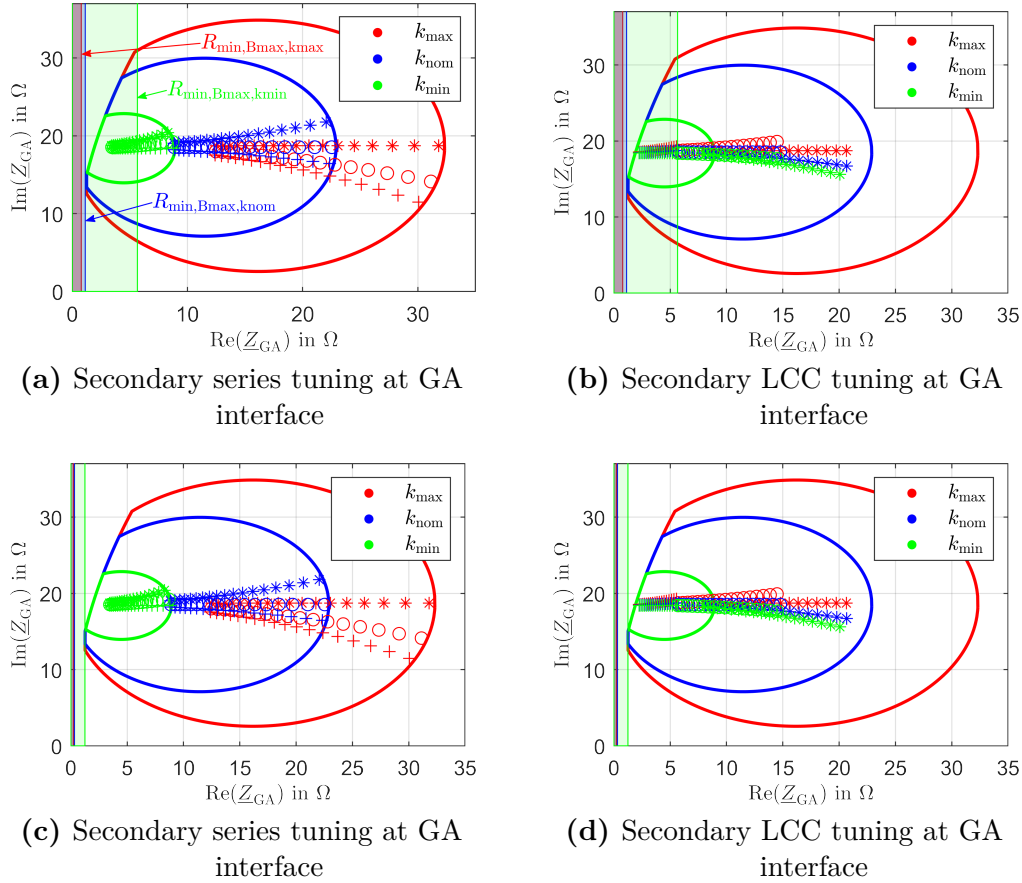


Figure 6.14 – GA interface analysis of the secondary compensation design. The differently tuned OPs (asterisk (k_{\max}), circle (k_{nom}) and '+' (k_{\min}) marker) are presented at the GA interface for the three coupling conditions in red, blue and green; simplified leakage flux boundaries for k_{\max} (red), k_{nom} (blue) and k_{\min} (green) are shown as shaded areas in (a)–(b) 800 mm and (c)–(d) 900 mm distance.

to obtain the leakage flux field distribution as shown in previous studies and B_{\max} at 800 mm and 900 mm distance is shown as a heatmap in Fig. 6.15c and Fig. 6.15d, respectively.

The results confirm that matched systems require a detailed leakage flux study. The maximum values are similar to the simplified approach, but the GA current isolines parallel to the imaginary axis are no longer dominant. The leakage flux heatmap has more of a circular isoline distribution which resembles the impact of the VA current. These results again show how the leakage flux issue is more relaxed at the 900 mm boundary.

Primary Tuning

For the design of the primary compensation, the VA CCPs at the GA interface are transferred to the inverter interface for the same three coupling conditions by using the same matrices (Tab. 3.2) with different values (this time tuned to the primary coil resonance at k_{\max} , k_{nom} or k_{\min}). As such, nine CCPs result in total (three primary tunings combined with three secondary tunings). This allows for the consideration of mistuned cases. The X_{GA} values are listed in Tab. 6.3.

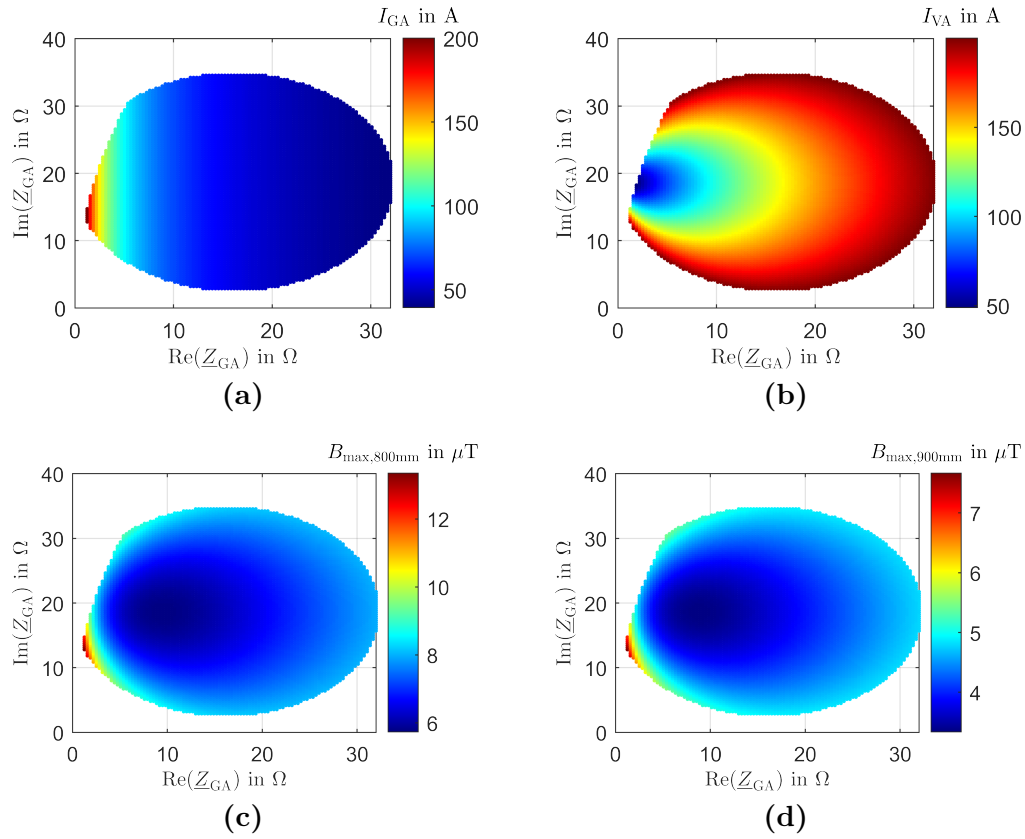


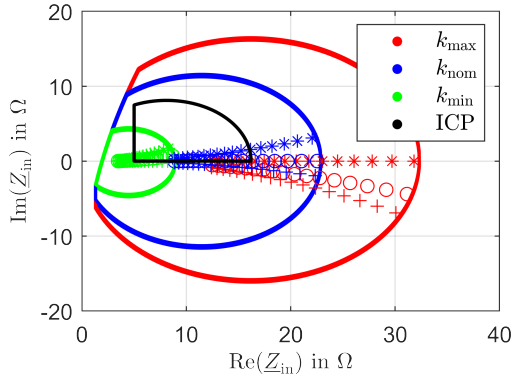
Figure 6.15 – CCP assessment at k_{\max} coupling condition with (a) I_1 , (b) I_2 , (c) $B_{\max,800\text{mm}}$ and (d) $B_{\max,900\text{mm}}$ heatmaps.

The ICP can be derived with the data from Tab. 6.2. The resulting ICPs and CCPs for primary series and LCC tuning are shown in Fig. 6.16. The OPs from the secondary assessment were also included in the results and will be discussed in the next section.

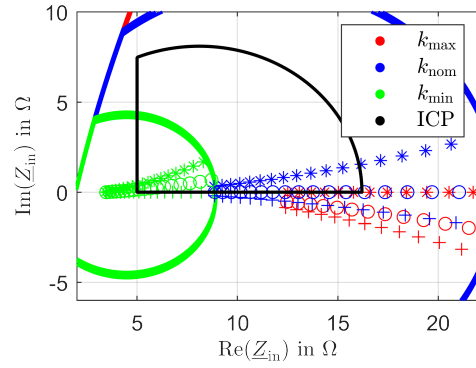
The mapped CCPs for the different primary series tunings are shown in Fig. 6.16a, with a closer look in Fig. 6.16b. The change of the tuning condition is so small that the different CCPs cannot be distinguished. As a result, there are few degrees of freedom when S–S tuning is chosen as the topology, so this topology should be considered from scratch, as its operating mode has a direct impact on the design of all components. To cover more OPs, the inverter boundaries must be adapted or the coupling variation must be restricted (e.g. no k_{\min} allowed), which affects the interoperability capability of the system (class I interoperability is no longer possible).

It can be seen that the given inverter is only capable of driving a small part of the k_{\min} -plane when the system is series tuned. More of the ICP of this coupling condition can be covered with LCC tuning which is shown for two different X_{GA} settings in Fig. 6.16c and Fig. 6.16e, again with close looks provided in Fig. 6.16d and Fig. 6.16f, respectively.

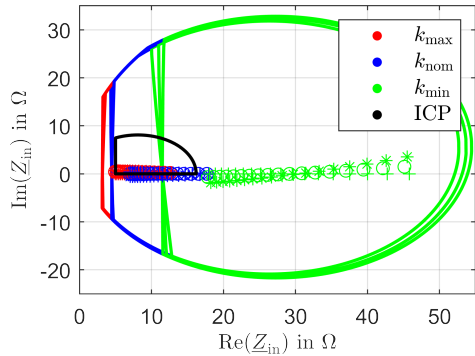
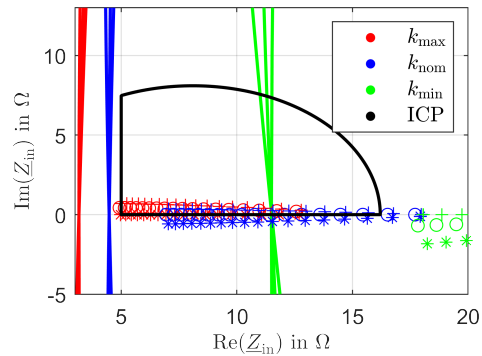
The changes of the resonant conditions (resonance at k_{\max} , k_{nom} or k_{\min}) for the primary tunings has a visible impact when LCC tuning is used. As described in Section 6.1, there is an additional degree of freedom which is why two settings of the LCC tuning are shown.



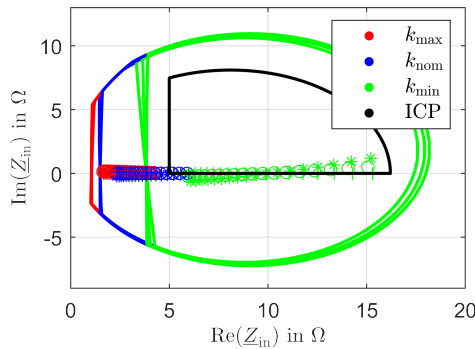
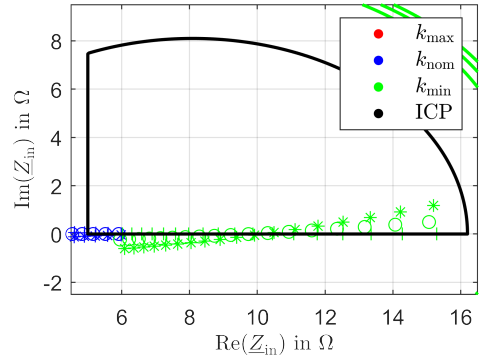
(a) Primary series tuning at inverter interface



(b) Zoomed in Fig. 6.16a


 (c) Primary LCC tuning at inverter interface ($X_{GA} = 10.13 \Omega$)


(d) Zoomed in Fig. 6.16c


 (e) Primary LCC tuning at inverter interface ($X_{GA} = 5.85 \Omega$)


(f) Zoomed in Fig. 6.16e

Figure 6.16 – Inverter interface analysis of the primary compensation design. The differently tuned OPs ('*' (k_{max}), 'o' (k_{nom}) and '+' (k_{min}) marker) are presented at the inverter interface for the three coupling conditions in red, blue and green. The ICP is shown in black.

The first compensation in Fig. 6.16c has an $X_{GA} = 10.13 \Omega$ and targets to address the k_{max} and k_{nom} operating condition. The compensation parameter can be calculated (similar to the secondary side) with Tab. 2.2.

The second setting targets the k_{\min} condition and is shown in Fig. 6.16e ($X_{GA} = 5.85 \Omega$). The size and position of the CCP varies greatly with the chosen X_{GA} . However, in both cases the ICP is greatly covered, but a full assessment needs to consider the resulting OPs at the inverter interface, which will be done in the next section. Furthermore, the sizes of the CCPs with LCC tuning are similar for different coupling conditions which means LCC tuning is more robust against offset tolerances.

For comparison, a third setting is shown in Fig. 6.17, where, similar to the S–S system, k_{nom} was targeted, while still being able to drive some OPs at k_{\min} and k_{\max} . This shows that a balanced solution can also be achieved, while some minor adjustments (here in L_{s1}) would be required to shift more OPs in the ICP, which is beyond the scope of this study. This configuration achieves a similar result to the S–S tuning in terms of driveable OPs. However, the operating conditions for the inverter are inverted at k_{\min} and k_{\max} coupling conditions. As a result, the inverter operates with high inverter current at maximum (and nominal) coupling with the LCC–LCC tuning, while requiring high current at minimum coupling with the S–S tuning.

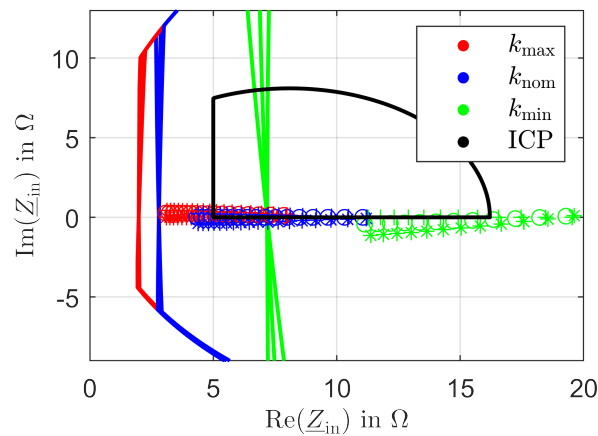


Figure 6.17 – Balanced configuration of the primary LCC tuning at the inverter interface with $X_{GA} = 8 \Omega$.

6.2.3 Evaluation and Results

To evaluate the characteristics of the full IPTS, the secondary and primary series tuning and the LCC tuning on both sides were combined. The ICP assessment can then be repeated with the OPs transferred to the inverter impedance interface and the results are shown in Fig. 6.16.

The results show that the S–S tuning is more sensitive to the different resonance tuning conditions compared to the LCC–LCC tuned system. The OPs are widely distributed over the inverter impedance range, requiring the inverter to address a large range of voltages and currents.

Active tuning (here a change in C_{s1}) can be used to shift the ICP down to address more OPs. However, a shift to the left or right is not possible, as shown in Section 6.1.2.

In addition, the ICP covers many blue OPs in the S–S tuning, and so this system represents a viable solution for mid-range air-gaps around $z = 190$ mm. This could be a practical solution for an Interoperability Class II system if coupling variations can be restricted (and

the system does not have to cover the full air-gap range). A passive S–S tuned system is not well suited for a wide range of couplings.

However, many OPs at different air-gaps and tuning conditions are within the ICP of the LCC–LCC tuned system. Hence, LCC–LCC tuning is preferable for this coil system when different air-gaps are to be covered.

Again, if no active tuning is used, LCC–LCC tuning is not able to address all OPs under the investigated conditions with the used boundary conditions and power electronics. However, an additional degree of freedom can be used to move the OPs and CCPs to a desired position. Overall, LCC–LCC tuning provides greater flexibility and robustness for a wide range of couplings.

When active tuning is used as shown, the entire range can be addressed by varying X_{GA} accordingly⁴.

For a more comprehensive assessment, the different inverter current heatmaps at the GA interface are shown in Fig. 6.18a and Fig. 6.18b for the S–S and LCC–LCC tuned systems, respectively. Since the primary compensation affects the ICP mapping on the GA interface, the required inverter current is different depending on the tuning topology chosen. The OPs for all coupling conditions are also shown, allowing a direct assessment of the system operation and therefore better design decisions.

As the primary series tuning only represents an upward shift in the IPP, I_{in} remains proportional to the real part of Z_{in} . This distribution is completely different for the LCC tuned primary, as can be seen. As a result, the LCC–LCC tuned system requires less inverter current to drive the OPs, which is an important information when designing the primary electronics and selecting components.

Additionally, Fig. 6.18 shows the previously presented leakage flux heatmaps for $B_{max,800mm}$ (Fig. 6.18c) and $B_{max,900mm}$ (Fig. 6.18d) at the GA interface, this time at the k_{min} coupling condition to show the worst case in terms of leakage flux fields.

For direct evaluation, the OPs of the S–S and LCC–LCC tuned systems are shown in green and orange, respectively. This method allows a designer to easily evaluate the leakage flux fields of many OPs, and it can be seen that all OPs violate the limit at k_{min} at 800 mm distance. Since most EVs are wider than 1.5 m, the requirement of a minimum distance of 900 mm is not a real restriction in terms of interoperability class I (if desired), and if used, the leakage flux problem is greatly alleviated.

In both cases, not all OPs can be covered by the ICP. There are various conditions and tolerances that IPTS must deal with, especially if a high degree of interoperability is desired, which makes it difficult to design a system that transfers full power with high efficiency in all OPs. This is a common problem in IPTS design, which is why SAE J2954 [50] requires only 75-85% efficiency while operating at rated power under offset, low coupling conditions or across power classes. Thus, a feasible solution to improve system interoperability is to reduce the required output power for the OPs (at the rectifier interface) outside the ICPs in Fig. 6.16 to make them accessible to the inverter.

As this study shows, the use of IPPs is an effective tool to understand and improve system characteristics or interoperability. The presentation of many OPs, the CCPs and the ICP on the same interface allows a comprehensive evaluation of the entire system, since the transfer of the OPs is affected by each component. Furthermore, the transfer between impedance

⁴Here X_{GA} was set and L_{s1} , C_{s1} , and C_{p1} were adjusted, which may be impractical or costly to change all parameters in a real system. However, Section 6.1 can be used to determine the minimum tuning range as shown.

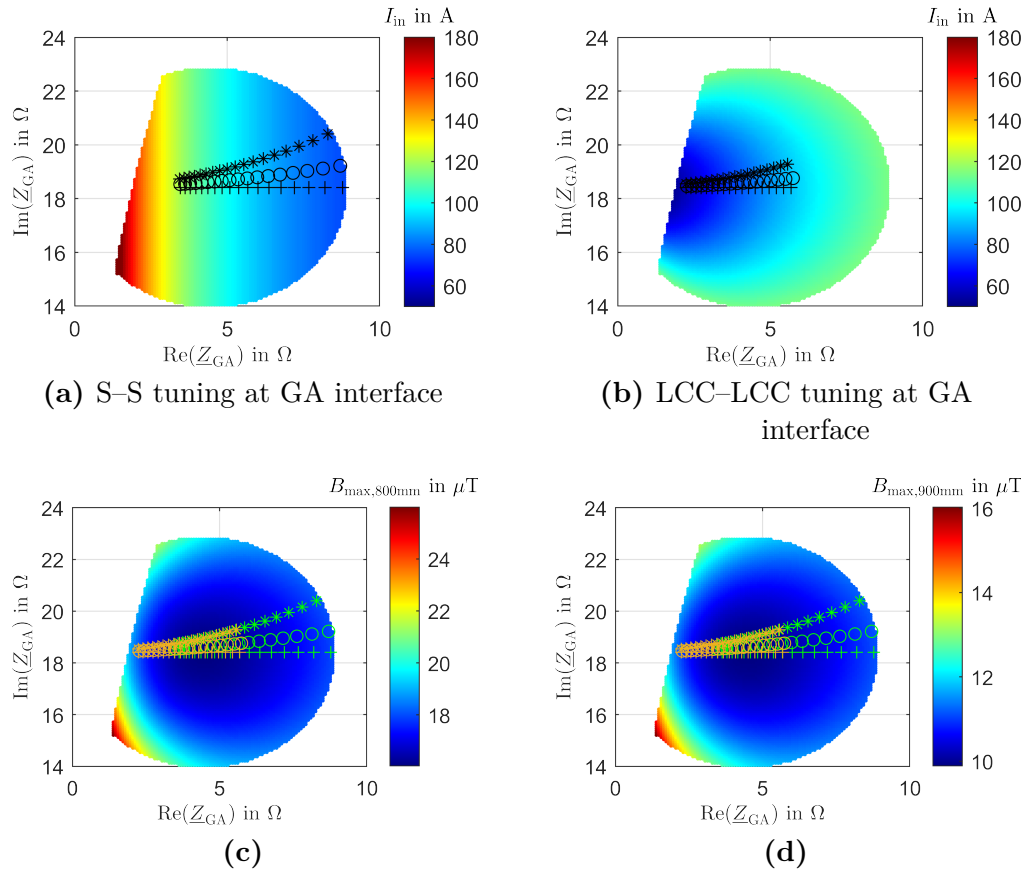


Figure 6.18 – Full system tuning, OP and leakage flux assessment at k_{min} coupling condition. The OPs are shown in black, green (S–S tuning) and orange (LCC–LCC tuning); I_{in} heatmaps for the (a) S–S and (b) LCC–LCC systems, (c) $B_{max,800mm}$ and (d) $B_{max,900mm}$ leakage flux heatmaps (tuning independent).

interfaces can be done step by step, enabling a designer to study the impact of each system component separately.

The results can then be used in various ways, such as re-designing the compensation networks or a re-design of an inverter which covers all OPs. Other possible improvements can be achieved by reducing the required interoperability, e.g. limiting the magnetic coupling factor to greater than 0.1 or allowing only one air-gap class.

6.3 Summary

This chapter provided a look at the sensitivity of tuning networks in IPTSs, and thus investigated the remaining components of an IPTS in detail. The goal was to gain a better understanding of the impact of tuning and its variation on an IPTS, and how this can be utilized for design in such a way that maximum interoperability can be achieved, instead of maximizing efficiency for an OP. Usually, both efficiency and a large operating range are important.

However, to emphasize the possibilities of the IPM in terms of interoperability, the design goal in this chapter has been used to design a system that can drive many OPs under the best possible conditions, which is an important goal (e.g. if Interoperability Class I (see Section 2.5) is desired). Tolerances and different topologies as well as wide coupling ranges are inevitable for such a system, as shown in the IPM Example 2 in Section 4.3.

First, the ICP from the IPM Example 1 (Section 3.4) was deconstructed and the general effects of series and LCC tuning investigated with each boundary highlighted in a different color to provide better insight into the shifts and rotations of the ICP during impedance transfer. For comparison, a conventional design approach was presented, detailing the design limitations over a wide range of battery voltages (or many operating conditions).

Second, variations in the parameters of an LCC tuning network were studied separately. To get a better understanding of how an IPP can be influenced, different LCC X_{GA} tuning conditions were studied.

The above work was used to design active tuning ranges for the primary and secondary tuning networks. Various tunings with different X_{GA} and X_{VA} were assessed with the goal of providing a large total ICP on the primary side and reducing the range of distributed OPs on the secondary side. It was shown that the IPM can be used to design the necessary tuning ranges to achieve interoperability for given conditions, in this case for the primary side to operate with two secondaries at Z2–Z3 air-gap class under aligned and misaligned positions over a varying battery voltage range of 280 – 450 V. The importance of an appropriate power electronics topology was highlighted, as the use of an impedance compression network had a major impact on the results.

Heatmaps can be used to better assess the ICPs and these were used to evaluate and show that the tuning has a large impact on the operating conditions such as leakage flux and inverter current. The IPM allows for a comprehensive system assessment while designing the tuning.

Last, these insights were applied in a sensitivity analysis of a 50 kW system. Two designed coils were used as a base and the goal was to utilize the sensitivity analysis and the IPM to design an interoperability focused compensation network. Three coupling conditions and various battery voltages were considered together with two sets of tunings (S–S and LCC–LCC) while looking at various operating conditions such as inverter current and leakage flux distribution at 800 mm and 900 mm distance.

The results showed that it is difficult to design a S–S system for a wide range of coupling conditions as there is little flexibility in design. If a S–S system is to be designed, it must be considered from scratch, including all appropriate voltages, currents, and winding turns from all known systems, so much more must be properly selected at the outset.

The LCC–LCC system proved to be more flexible and robust against coupling variations, but also struggles to operate under all conditions when no active elements are used in the tuning. The tuning was designed for two conditions to show that it is capable of achieving interoperability when actively tuned.

This study was conducted for a set of coils, and achieving full interoperability (Class I) becomes even more complicated and challenging when different coils are combined, as discussed in the next chapter, where an interoperability assessment of two different 50 kW coil sets is performed.

7 Assessment of Two High-Power 50 kW IPT Systems

In the previous chapters, the IPM was introduced and extended, with different use-cases exploring different components of the IPTS in detail. This chapter aims to apply all the insights gained and to investigate the interoperability of two independently designed IPTSs.

Both systems were designed to deliver high power (50 kW systems) but they were intended for different applications, one for flush mount and the other for surface mount GA operation. Using the IPM, the interoperability between the two systems will be investigated by analyzing aspects such as their ability to transfer full power over the operating and air-gap ranges and compliance with standards. Since there are no reference coils in this power class, it is unclear whether independently designed coils can actually work together, as there are no guidelines for design such as coil sizing, among other factors.

The purpose of this chapter is to assess the degree of interoperability between the two systems, examine limitations, and suggest ways to improve interoperability.

Both IPTSs are introduced in the following section, followed by a discussion of the selected use-case and the applied system boundaries. Before conducting the interoperability assessment, one of the systems is used to validate the IPTS simulation models by comparing them with the simplified analytical approach (derived in Chapter 3), physical circuit simulation, and experimental results. Finally, the results of the interoperability assessment are discussed and evaluated, and a summary is provided.

7.1 50 kW Coil Systems

A set of coils (primary and secondary) was introduced in the previous chapter (see Fig. 6.10). As mentioned, these were designed as part of a research project at the Technical University of Munich (TUM) and will therefore be referred to as the “TUM” coils in this chapter. The other set of coils was designed independently at the same time at the UoA and will be referred to as the “UoA” coils. If the systems are mixed, e.g. UoA at the primary and TUM at the secondary, the system is labeled UoA–TUM, with the primary always listed first.

To make this study possible, it was decided to design each system completely independently and then compare them to mimic real-world conditions where different infrastructure providers design different GA systems, while different VA designers provide different VA systems, and all of these designs must be interoperable with each other, even if the design scope is different¹.

7.1.1 TUM Coils

The coils were discussed in the previous chapter and are shown in Fig. 6.10 (an 800×800×1 mm aluminum shield was used on the secondary). This system was the result of an extensive design study published in [P.5].

¹Under the assumption that Interoperability Class I is desired.

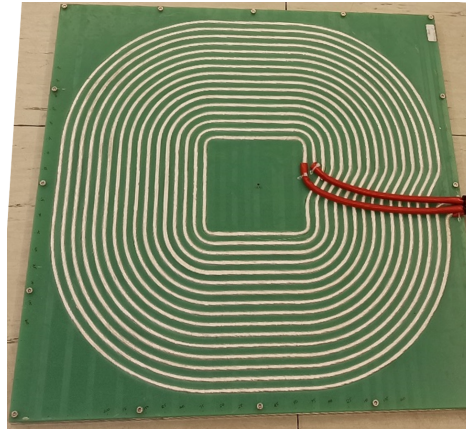


Figure 7.1 – Lab prototype of the TUM coils. Photo Credits: Reiner Nowitzki.

The coils were designed as a surface mount system with a nominal air-gap of 190 mm. For practical reasons it was decided to use a matched system for the laboratory prototype and the coil (used on both sides) is shown in Fig. 7.1.

The boundaries used in the study in Section 6.2 (see Tab. 6.2 and Tab. 6.3) were primarily based on assumed limitations, as this was an early stage study where the rest of the IPTS had not yet been designed. Practical considerations within the research project required that the topology and details of the entire IPTS be designed differently, deviating from the results of the previous chapter. As a result, series-series tuning was used and the (slightly) changed system boundaries and tuning network values are shown in Tab. 7.1 and Tab. 7.2, respectively. The full series-series circuit is similar to Fig. 2.23 and essential coil parameters are summarized in Tab. 7.3. The battery voltage was set to 350 – 450 V. The rectifier utilizes diodes from [179], and SiC-MOSFETs from [180] are used in the inverter.

7.1.2 UoA Coils

The second set of coils is used in this chapter are also circular in shape, rated to transmit 50 kW and were first published in [140, 155]. The FEM models are shown in Fig. 7.2. The coils are a non-matched system and the coil sizes are 720×675 mm and 605×620 mm for the primary and secondary, respectively. The coils were designed as a flush mount system for air-gap class Z2 (140 – 210 mm ground clearance). More details on these coils can be found in [140, 155, 174] and essential coil parameter are compared to the TUM system in Tab. 7.3.

As can be seen, the nominal ground clearance is comparable to that of the TUM system. However, due to the flush mounting of the GA, the resulting magnetic air-gap (coil-to-coil distance) is greater. In addition, there is a difference in the number of turns and size of the coils.

The compensation networks consist of an LCC topology on both sides and the complete circuit topology is similar to Fig. 2.22. The coils each have a lead inductance of $2.04 \mu\text{H}$ (primary) and $0.93 \mu\text{H}$ (secondary) which has to be considered when designing the compensation networks [174], the values of which are given in Tab. 7.2.

The boundaries of the electronics of the UoA system are listed in Tab. 7.1 and the inverter and rectifier deployed the switches in [181] (the rectifier only uses the body diodes).

It has to be noted, that the UoA system was intentionally designed to use an active rectifier or a boost converter on the secondary side. However, in the following study, the system will be

Table 7.1 – System Constraints and Component Limitations of both 50 kW IPTSs

Grid/Inverter	Coils	Rectifier/Load
TUM System		
$S_{\text{in,max}} = 60 \text{ kVA}$	$V_{\text{GA,max}} = V_{\text{VA,max}} = 3 \text{ kV}$	$V_{\text{bat}} = (350 - 450) \text{ V}$
$V_{\text{s}} = (550 - 1000) \text{ V}$	$I_{\text{GA,max}} = I_{\text{VA,max}} = 150 \text{ A}$	$\Delta V_{\text{bat}} = 10 \text{ V}$
$I_{\text{s}} = (30 - 120) \text{ A}$	$(x,y,z)_{\text{min}} = (0,0,170) \text{ mm}$	$P_{\text{out}} = 50 \text{ kW}$
$\varphi_{\text{in,max}} = 60^\circ$	$(x,y,z)_{\text{max}} = (75,100,210) \text{ mm}$	$R_{\text{ac}} = 8/\pi^2 \cdot V_{\text{bat}}^2/P_{\text{out}}$
	$B_{\text{max}} = 15 \text{ }\mu\text{T}$	
$V_{\text{f}} = 5.3 \text{ V}$	$R_{\text{GA}} = 25.2 \text{ m}\Omega$	$V_{\text{rf}} = 1.15 \text{ V}$
$R_{\text{DS}} = 8 \text{ m}\Omega$	$R_{\text{VA}} = 25.2 \text{ m}\Omega$	$R_{\text{RD}} = 0.8 \text{ m}\Omega$
$\alpha = 180^\circ$	$R_{\text{C1}} = 1.5 \text{ m}\Omega$	
$\delta_{\text{d}} = 0 \text{ s}$	$R_{\text{C2}} = 1.5 \text{ m}\Omega$	
UoA System		
$S_{\text{in,max}} = 60 \text{ kVA}$	$V_{\text{GA,max}} = V_{\text{VA,max}} = 2.5 \text{ kV}$	$V_{\text{bat}} = (600 - 800) \text{ V}$
$V_{\text{s}} = (500 - 1000) \text{ V}$	$I_{\text{GA,max}} = I_{\text{VA,max}} = 250 \text{ A}$	$\Delta V_{\text{bat}} = 10 \text{ V}$
$I_{\text{s}} = (30 - 100) \text{ A}$	$(x,y,z)_{\text{min}} = (0,0,170) \text{ mm}$	$P_{\text{out}} = 50 \text{ kW}$
$\varphi_{\text{in,max}} = 60^\circ$	$(x,y,z)_{\text{max}} = (75,100,210) \text{ mm}$	$R_{\text{ac}} = 8/\pi^2 \cdot V_{\text{bat}}^2/P_{\text{out}}$
	$B_{\text{max}} = 15 \text{ }\mu\text{T}$	
$V_{\text{f}} = 1.92 \text{ V}$	$R_{\text{GA}} = 23.1 \text{ m}\Omega$	$V_{\text{rf}} = 1.53 \text{ V}$
$R_{\text{DS}} = 13 \text{ m}\Omega$	$R_{\text{VA}} = 19 \text{ m}\Omega$	$R_{\text{RD}} = 7.8 \text{ m}\Omega$
$\alpha = 180^\circ$	$R_{\text{C1}} = 1.5 \text{ m}\Omega$	
$\delta_{\text{d}} = 0 \text{ s}$	$R_{\text{C2}} = 1.5 \text{ m}\Omega$	

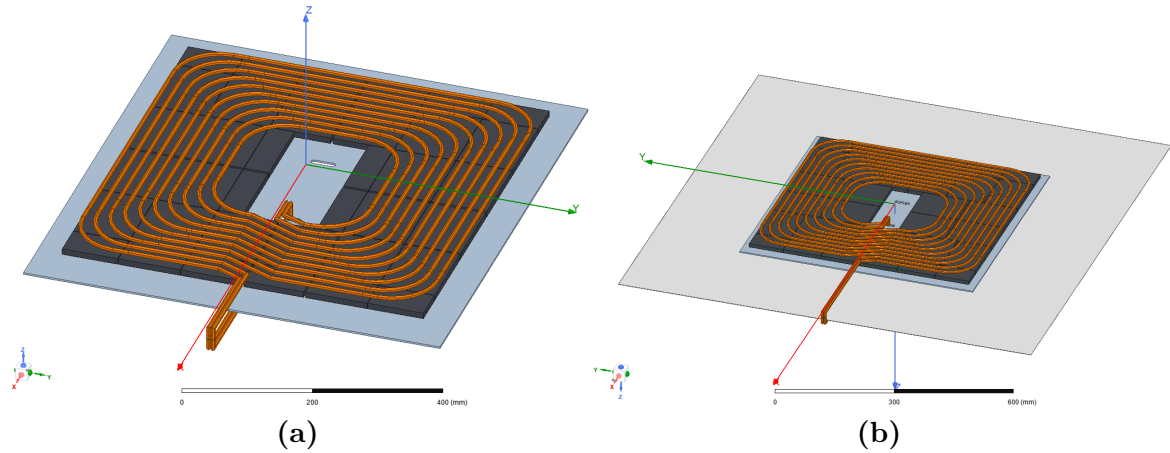
Table 7.2 – Tuning Values of the 50 kW IPTSs

System	Parameter	Value	Parameter	Value
TUM	C_{s1}	100 nF	C_{s2}	100 nF
UoA	L_{s1}	7.5 μH	L_{s2}	7.4 μH
	C_{s1}	263 nF	C_{s2}	304 nF
	C_{p1}	536 nF	C_{p2}	533 nF

evaluated using a passive rectifier for three reasons. One, to allow comparison with the TUM system, two, to represent passive worst-case situations, and three, because the electronics were not yet built at the time the measurements were made (which would make an evaluation

Table 7.3 – Comparison of both 50 kW Coil Parameters

Parameter	TUM System	UoA System
Prim. Coil Size (x,y)	600 × 600 mm	720 × 675 mm
Sec. Coil Size (x,y)	600 × 600 mm	605 × 620 mm
Winding Turns (N_1/N_2)	8/8	5/5
Nom. position	(0,0,190) mm	(0,0,190) mm
Nom. coil-to-coil distance	170 mm	211.9 mm
k_{nom}	0.29	0.19
$k_{\text{min}} - k_{\text{max}}$	0.18 – 0.34	0.13 – 0.22

**Figure 7.2** – FEM simulation models of the UoA coils, (a) primary coil and (b) secondary coil with aluminum shield (1000 × 1000 × 1 mm).

impossible). The topology was chosen to be based on the measured experimental system (see Section 7.3.1), which used passive rectification.

7.2 System Boundaries and Use-Case

Six positions were selected for this study to investigate system performance over the full range of air-gaps and misalignments as well as tolerances in nominal air-gaps. The positions are similar to the previous study² from Tab. 6.1 and the simulated inductances and coupling factors of both systems and their combinations are shown in Tab. 7.4. First index represents the primary side.

The component limits and constraints used in this study are summarized in Tab. 7.1. The leakage flux planes will be investigated at 900 mm distance from the secondary coil center and the study will be conducted at the GA interface.

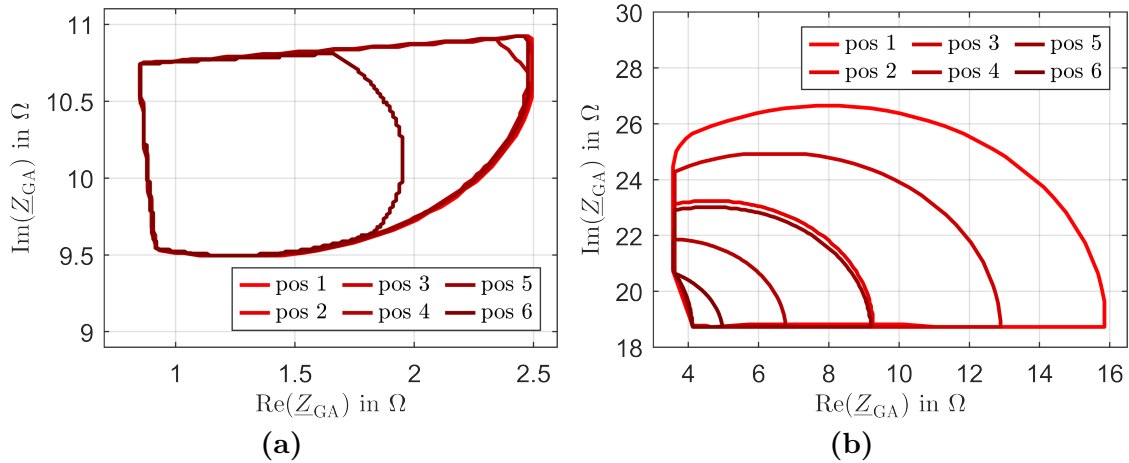
The ICPs for each system determined for this use-case are shown in Fig. 7.3 for all six positions, with Fig. 7.3a showing the UoA-UoA system and Fig. 7.3b showing the TUM-TUM system.

²Due to practical considerations regarding the measurements, the directions of the misalignments were changed to negative. Since the TUM system is symmetrical, the inductances do not change.

Table 7.4 – Simulated Inductances of the 50 kW IPTSs and their Combinations

Position Index	x (mm)	y (mm)	z (mm)	L_1	L_2	k	L_1	L_2	k
				TUM–TUM			UoA–UoA		
1	0	0	170	35.05	34.98	0.34	18.96	17.87	0.22
2	-75	-100	170	34.88	34.86	0.25	19.00	17.82	0.17
3	0	0	190	34.71	34.63	0.29	18.93	17.80	0.19
4	-75	-100	190	34.63	34.58	0.21	18.96	17.78	0.15
5	0	0	210	34.51	34.40	0.25	18.90	17.78	0.16
6	-75	-100	210	34.48	34.40	0.18	18.94	17.75	0.13
				TUM–UoA			UoA–TUM		
1	0	0	170	35.03	18.10	0.32	18.93	34.39	0.24
2	-75	-100	170	34.89	18.00	0.25	18.94	34.30	0.17
3	0	0	190	34.69	17.94	0.27	18.89	34.23	0.20
4	-75	-100	190	34.63	17.88	0.21	18.90	34.12	0.15
5	0	0	210	34.48	17.84	0.23	18.87	34.14	0.18
6	-75	-100	210	34.47	17.80	0.18	18.89	34.12	0.13

A comparison of the efficiency of both systems is given in Fig. 7.4 under nominal and minimum coupling conditions. The blue isoline marks the $B_{\max,900\text{mm}} = 15 \mu\text{T}$ limit. Losses were implemented using the approach outlined in the flowchart of Fig. 5.4, where $P_{\text{out,min}}$ is held constant and losses are added to the required input power P_{in} . It is important to note that the limits of the heatmaps differ between systems, which must be taken into account when evaluating the systems. Aligning the heatmap boundaries will make a comparison between the system much more convenient. However, the information about the efficiency (or other parameters) distribution within the ICP is no longer clearly visible, so the heatmaps are not aligned for the entire study and attention must be paid to the correct values.

**Figure 7.3** – ICPs of the (a) UoA–UoA and (b) TUM–TUM systems for all coupling conditions and system constraints.

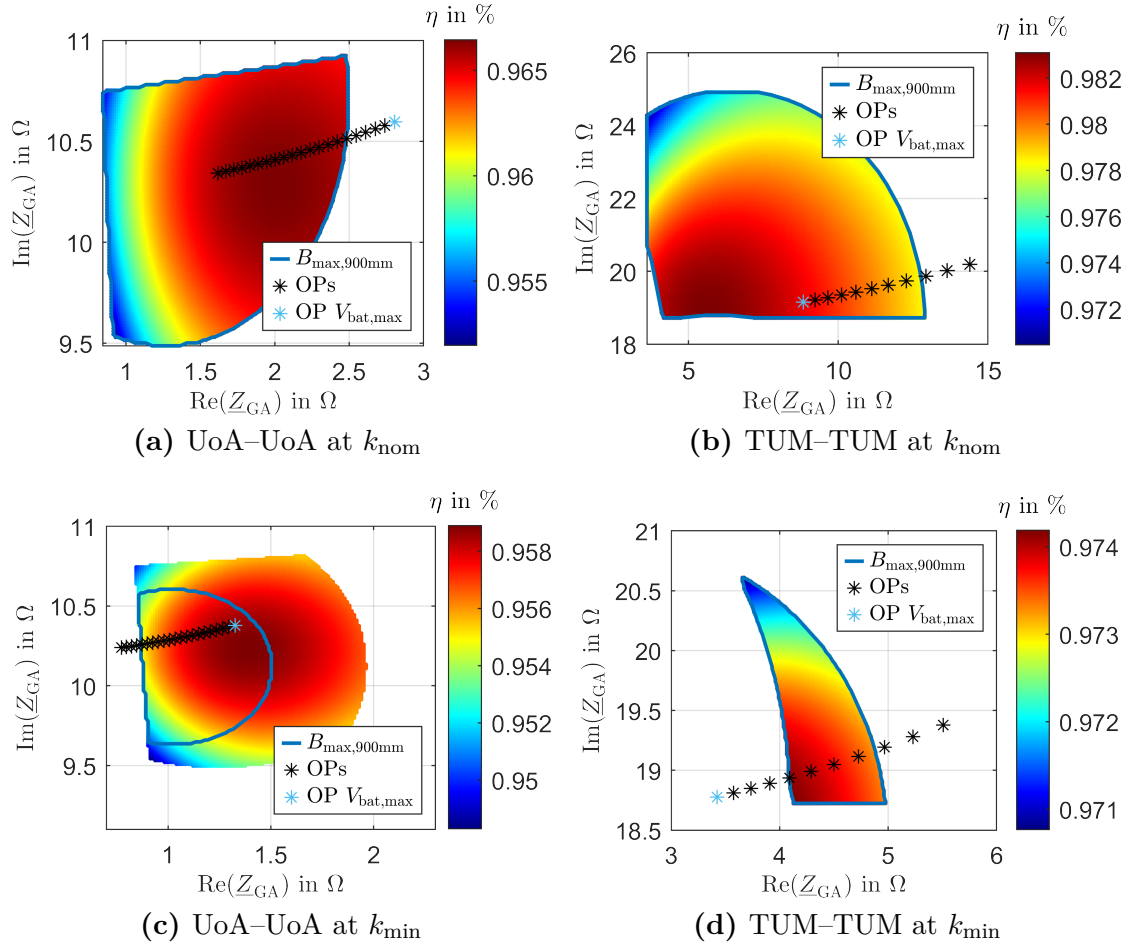


Figure 7.4 – ICP efficiency analysis of both 50 kW systems under different coupling conditions. The OPs (V_{bat} see Tab. 7.1) are shown in black with $V_{\text{bat,max}}$ highlighted in turquoise and the blue isline represents the $B_{\text{max},900\text{mm}} = 15 \mu\text{T}$ constraint.

The final ICPs and OPs with all boundaries (everything within the blue isline from Fig. 7.4) considered are shown in Fig. 7.5 at k_{min} with the $B_{\text{max},900\text{mm}}$ leakage flux heatmap (UoA–UoA in Fig. 7.5a and TUM–TUM in Fig. 7.5b). The effects of reducing the transferred output power are shown in Fig. 7.5c and Fig. 7.5d for the UoA–UoA and TUM–TUM systems, respectively. The black, purple and golden isline represent the areas in which the system can transfer 45 kW, 48 kW and 50 kW, respectively ($P_{\text{out,min}}$). The efficiency heatmaps were calculated at $P_{\text{out,min}} = 45 \text{ kW}$. The heatmaps show minimal changes with power variations, which can be ignored and are thus not displayed.

The results indicate that not all OPs can be addressed in both systems (under the studied restricted operation modes), particularly under minimal coupling conditions. Nevertheless, the LCC–LCC tuning of the UoA–UoA system can address more OPs under all operating conditions, confirming the results of the previous chapter (see Section 6.2.3), where it was shown that a series-tuned system (here the size of the TUM–TUM ICPs in Fig. 7.3) is highly sensitive to changes in coupling.

With decreasing the power transfer, the UoA–UoA system meets the full operation range (see Fig. 7.5c) while the TUM–TUM system cannot operate over the whole battery voltage range.

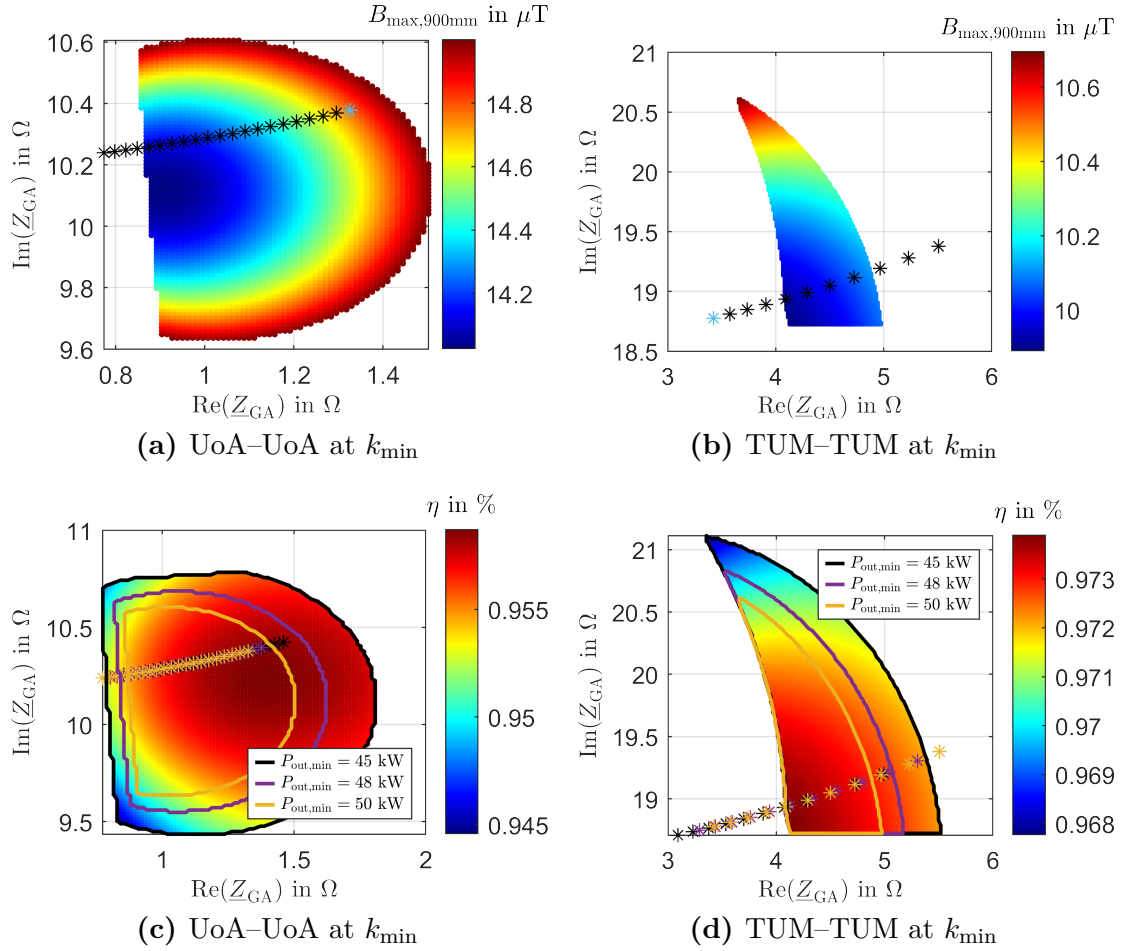


Figure 7.5 – ICP leakage flux heatmaps and output power variation analysis of the two 50 kW systems at minimum coupling. The black, purple, and gold isolines mark the IPPs at which the system can transfer 45 kW, 48 kW, and 50 kW, respectively ($P_{\text{out,min}}$). The corresponding OPs are shown in the same color.

However, this demonstrates that passive systems without the ability to adjust anything (active tuning or rectification or control) will face significant challenges in achieving interoperability, let alone Class I interoperability.

Approaches to improving interoperability were presented in Chapters 3–6, but are not applied here, where the focus lies on interoperability assessment. A full discussion of the results is given in Section 7.4.2.

7.3 Validation of the UoA System

Before proceeding with the interoperability assessment, it is important to first validate the results presented in order to derive assumptions and allow for a meaningful evaluation. This section begins with an examination of the measurement conditions, followed by a comparison of the measured values with various simulated values, and concludes with a discussion of the results.

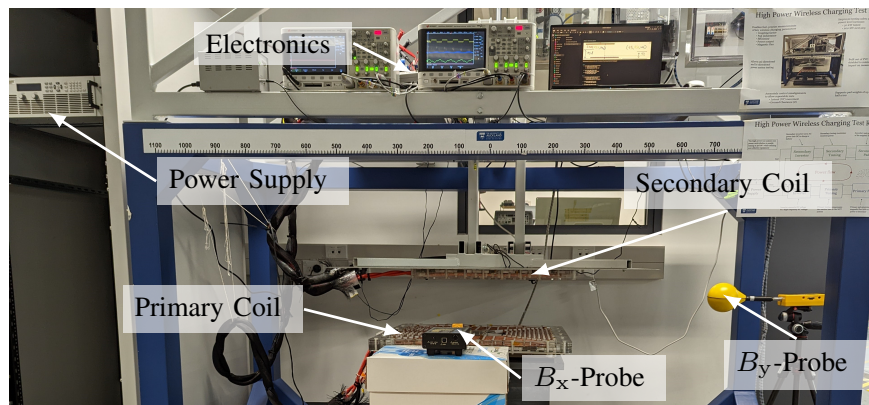
7.3.1 Measurement Setup

In order to validate the presented ICPs and OPs, experiments were conducted with the UoA–UoA system from Section 7.1.2 under the described conditions and boundaries from Tab. 7.1. The laboratory setup is shown in Fig. 7.6.

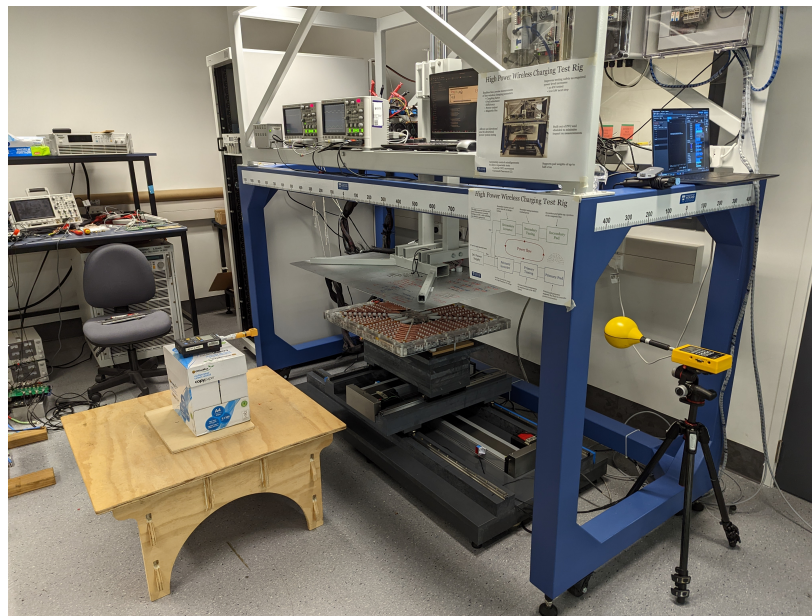
An experimental validation of the FEM model (inductances and coupling) was presented in [140] with less than 5 % deviation and is therefore not shown here.

In order to circulate high power with the equipment available in the lab, the input DC and the output DC were connected. Thus, the experiments were limited to $V_s = V_{bat}$.

Leakage flux probes were placed in the $B_{x,max}$ and $B_{y,max}$ spots from the FEM simulation at k_{min} and at a distance of 950 mm from the center of the secondary coil as shown in Fig. 7.7



(a)



(b)

Figure 7.6 – Experimental setup for full circuit and leakage flux measurements, (a) front view and (b) side view.

($\varphi_{i1-i2} = 90^\circ$ was assumed in this FEM simulation setup). The measured results are shown in Tab. 7.5 and will be discussed in the next section.

Measurements of the full circuit were performed for all six positions. However, this discussion focuses only on positions 1, 3, and 6 (k_{\max} , k_{nom} , and k_{\min}) and the results are shown in Tab. 7.6. The aim of the measurements was to transfer a constant output power of 48 kW, with the bus voltage adjusted accordingly.

7.3.2 Comparison with Simulation Models

FEM models (Leakage Flux) As mentioned in Chapter 4, any values can be obtained from the leakage flux planes and validation is still possible even if the probes are not placed precisely at the maximum leakage flux point. The comparison of measured and simulated leakage flux values and the relative error for all positions are listed in Tab. 7.5.

Due to the linked bus voltages and the passive rectification, the phase angle between the coil currents is no longer ideal ($\neq 90^\circ$, see [174]) and the FEM simulations have been adjusted accordingly in Tab. 7.5. The FEM results show very good agreement with the experiments as the deviations are always less than 9 % (absolute error is less than 0.7 μT).

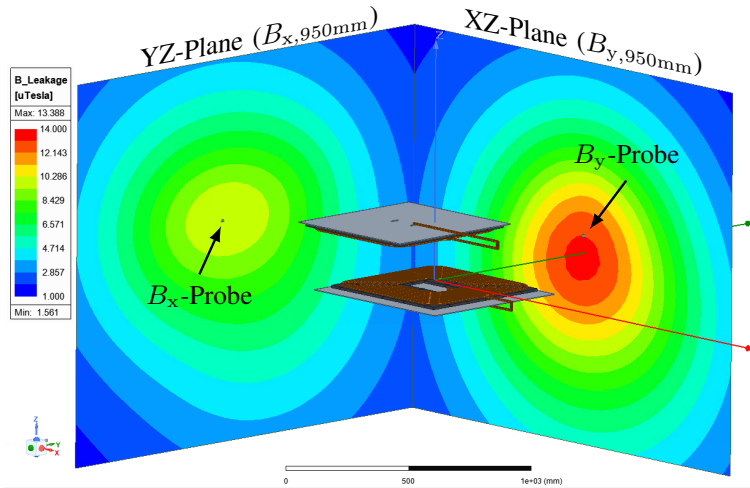


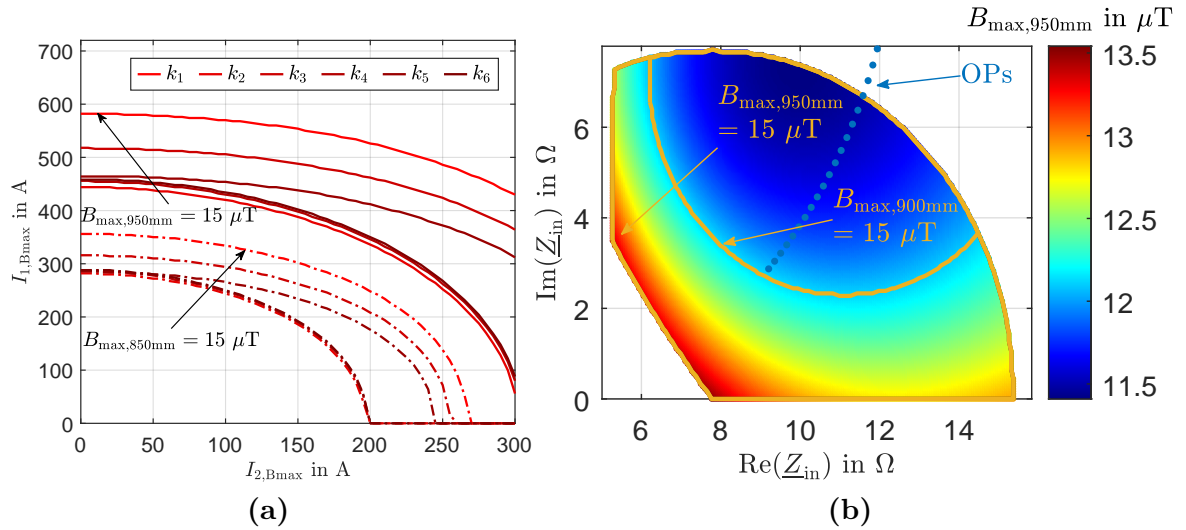
Figure 7.7 – Leakage flux planes and probes in FEM simulation.

Table 7.5 – Leakage Flux Comparison between Measurements and FEM Simulations

Pos.	$B_{x,\text{meas.}}$ (μT)	$B_{x,\text{sim.}}$ (μT)	$B_{y,\text{meas.}}$ (μT)	$B_{y,\text{sim.}}$ (μT)	ΔB_x (%)	ΔB_y (%)
1	5.15	4.76	6.62	6.73	-7.63	1.68
2	7.69	8.35	9.89	9.70	8.60	-1.96
3	6.54	6.06	7.85	7.92	-7.34	0.85
4	8.71	9.24	11.58	11.30	6.08	-2.43
5	8.06	7.48	9.11	9.18	-7.20	0.82
6	9.69	10.18	13.39	13.06	5.05	-2.47

Table 7.6 – Comparison between Measurements, Analytical Calculation (FHA) and Circuit Simulation (PLECS)

Pos.		V_{bus} (V)	I_{in} (A)	I_1 (A)	I_2 (A)	I_{bat} (A)	P_{out} (kW)	P_{loss} (kW)	P_{in} (kW)	$\eta_{\text{dc-dc}}$ (%)
1	Meas.	600	92.75	153.7	156.6	80.60	48.36	2.29	50.65	95.48
	FHA	586	93.82	146.08	154.13	80.67	48.40	0.95	49.35	98.09
	Sim.	600	97.82	153.26	158.90	80.36	48.22	1.63	49.85	96.73
3	Meas.	656	89.25	168.3	171.1	74.10	48.60	2.45	51.05	95.20
	FHA	649	85.23	162.69	168.40	74.08	48.60	1.15	49.75	97.69
	Sim.	656	88.72	167.20	172.72	71.50	46.90	1.82	48.72	96.26
6	Meas.	800	76.40	206.4	205.7	59.90	48.00	3.08	51.08	94.00
	FHA	762	73.00	189.60	205.18	60.12	48.10	1.63	49.73	96.72
	Sim.	800	76.77	202.70	207.30	59.40	47.55	2.35	49.90	95.30

**Figure 7.8** – Leakage flux study of the UoA–UoA ICP for $P_{\text{out,min}} = 50$ kW; (a) maximum allowed currents for $B \leq 15$ μT under all coupling conditions and two leakage flux plane distances, (b) ICP with leakage flux $B_{\text{max},950\text{mm}}$ -heatmap and $B_{\text{max}} = 15$ μT isolines.

The FEM models and leakage flux planes can be used to derive the maximum allowed GA and VA currents to stay below 15 μT and this is shown in Fig. 7.8a for the leakage flux planes at 950 mm and 850 mm (dashed) distance.

As discussed in Section 6.2, the plane distance affects the limit, and although this study is conducted with the assumption of a minimum distance of 900 mm, the UoA–UoA design targeted vehicle widths of ≥ 1800 mm, so the nominal leakage flux plane was set at 950 mm distance for the measurements³.

³An additional 50 mm was added to account for the size of the probe.

The corresponding k_{\min} ICP at the inverter interface with the center of the probe placed at 950 mm distance with heatmaps for B_{\max} is shown in Fig. 7.8b. The phase angle between the coil currents φ_{i1-i2} was assumed to be 90° for this ICP. However, generally the IPM allows the phase angle to be varied for each OP.

The ability to evaluate the leakage flux density within the ICP for different OPs and different conditions is a very helpful feature of the IPM, as it now allows another constraint to be placed on the ICP. To illustrate the effect of different vehicle widths, Fig. 7.8b shows the isoline for $B_{\max} \leq 15 \mu\text{T}$ at 950 mm and 900 mm (represents a smaller car) distance. The heatmap shows that the leakage flux at 950 mm distance is always below $14 \mu\text{T}$, while the ICP is reduced when the same boundary is applied only at 900 mm distance from the secondary coil center (heatmap is not valid for this distance). Depending on the car width, the resulting ICP (one of the golden isolines) is now an impedance range that ensures the ICNIRP limit is never violated.

In addition, different isolines can be obtained and highlighted to provide more information about the leakage flux density at the OPs, which could initiate control schemes to reduce the leakage flux fields.

Full Circuit Simulation The comparison of the experimentally measured values and the analytical calculations is given in Tab. 7.6 for positions 1, 3 and 6.

As mentioned in Section 2.3.1, the FHA neglects harmonics, making it difficult to properly estimate the losses in the switches and diodes, so a physical simulation of the circuit was also performed in PLECS, and the results are also shown in Tab. 7.6 (index Sim.).

It should be noted that this simulation considered the measured inductances, which are slightly different from the simulated inductances in Tab. 7.4 as well as the lead inductances. The simulation model used a similar circuit as shown in Fig. 5.16.

The bus voltages in the experiments were set to achieve a constant output power of 48 kW and were also set in the circuit simulation. The FHA analysis was set up to transfer a similar output power in order to have comparable data sets.

A comparison of the scope screenshots of the measurements with the PLECS simulation outputs is shown in Fig. 7.9. In general, the measurements, analytics and simulations are in reasonably good agreement. However, the losses are underestimated in both simulations.

To interpret the results, a closer look at the deviations between the measured, simulated and calculated power, losses and efficiency is provided in Tab. 7.7 for the three coupling conditions.

Tab. 7.8 also shows the comparison of the switching loss estimate for all positions calculated using the simplified sinusoidal waveform equation (Eq. (5.5), $\alpha = 180^\circ$, $E_{\text{off}} = 0.86 \text{ mJ}$, $V_{\text{R}} = 600 \text{ V}$, $I_{\text{R}} = 120 \text{ V}$, $Q_{\text{RR}} = 2.2 \mu\text{C}$, $I_{\text{RD}} = 173 \text{ A}$, taken from [181]) and the approach using Eq. (5.4) with extracting the instantaneous currents (as described in Section 5.1) with PLECS.

It can be seen that although the power and efficiency are in good agreement, the losses are underestimated by about 24-29 % in PLECS and 47-59 % in the FHA analysis. The FHA analysis only considers the ESR of the coils (without temperature dependency) and does not take into account other losses such as conduction or switching losses, which explains the large deviation from the measured results. The PLECS simulation is closer to the measurements because it includes conduction and switching losses, but still has an offset of about 30 % due to core losses. These are not properly accounted for in the ESR of the coils when they are

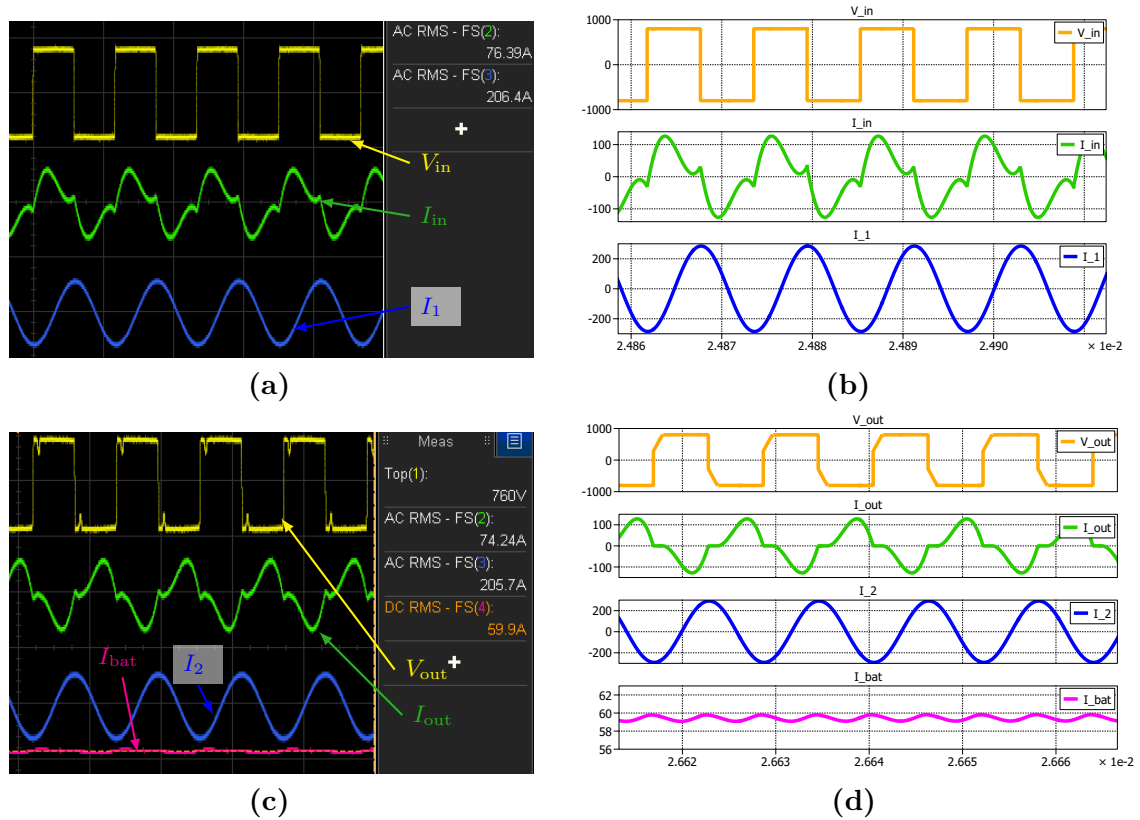


Figure 7.9 – Screenshots of the waveforms and scopes, (a) primary measurements, (b) PLECS primary waveforms, (c) secondary measurements and (d) PLECS secondary waveforms.

Table 7.7 – Offset in Power and Losses between Measurements and Simulations

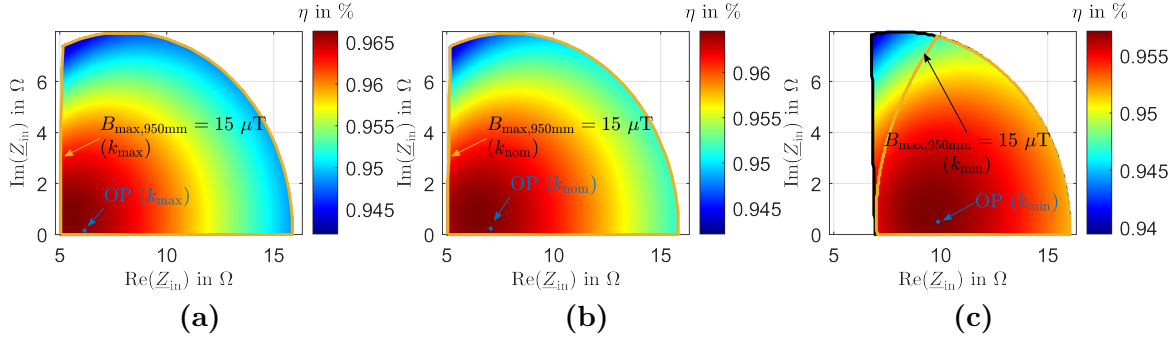
Pos.	ΔP_{out} (%)	ΔP_{loss} (%)	ΔP_{in} (%)	$\Delta \eta_{dc-dc}$ (%)
Measurements vs. Simulations				
	FHA/PLECS	FHA/PLECS	FHA/PLECS	FHA/PLECS
1	0.1 / -0.3	-58.8 / -28.8	-2.57 / -1.58	2.7 / 1.3
3	0 / -3.5	-53.05 / -25.71	-2.55 / -4.56	2.6 / 1.1
6	0.2 / -0.9	-47.1 / -23.8	-2.64 / -2.31	2.9 / 1.4

captured with small signal analysis (as was done in the experiments for this chapter) because they dominate at higher currents (and temperatures) [169].

The overall power and efficiency match well as these losses are not significant in the operations of this system, which is also reflected in the switching loss calculation in Tab. 7.8. Here, ZVS and a conduction angle $\alpha = 180^\circ$ were assumed, resulting in switching losses of less than 140 W. These losses will likely increase under different operating conditions. However, it can also be seen that the simplified approach for a sinusoidal waveform greatly

Table 7.8 – Offset in Switching Loss Calculations for all Positions

Sim./Pos.	1	2	3	4	5	6
$P_{l,sw,FHA}$ (W), Eq. (5.5)	17	23	22	27	26	32
$I_{inst,sw}$ (A)	9.1	17.6	14.2	24	20.4	31.2
$E_{off,sw}$ (mJ)	0.2	0.25	0.25	0.35	0.3	0.4
$P_{l,sw,sim}$ (W), Eq. (5.4)	68	85	85	119	102	136
Err in %	75	72.9	74.1	77.3	74.5	76.5

**Figure 7.10** – Final ICP with experimentally measured values, leakage flux isolines and OPs for different coupling conditions, (a) k_{max} , (b) k_{nom} and (c) k_{min} .

underestimates the switching losses, highlighting the need to investigate in future the impact of harmonics in an LCC-LCC tuned system.

This validation section emphasizes the general importance of loss considerations, which becomes particularly important for high-power IPTSs. The approach presented here for extending the IPM is very well suited for the general consideration of the losses. Future work needs to focus on improving and incorporating a variety of loss contributions, such as core losses (the authors in [169] present a method to better integrate the core losses into ESR measurements) and harmonics as discussed further in Section 8.4.

As a final validation step, the ICPs for all coupling conditions at $P_{out} = 48$ kW, with measured inductances, all system boundaries from Tab. 7.1, the measured OPs (with $V_s = V_{bat}$) with the efficiency heatmap, and $B_{max} = 15$ μ T isolines, are shown in Fig. 7.10.

The results show that leakage flux limitation only affects the ICP at minimum coupling. Furthermore, Fig. 7.10 confirms that the measurements were taken deliberately under well chosen conditions as each OP is located in the highest efficiency region.

7.4 Interoperability Assessment

In the previous sections, both 50 kW systems were presented and studied with the designed VA placed over the corresponding GA, followed by experimental validation of the simulation models used.

The coil sets were found to be fundamentally different in many aspects, such as winding turns, tuning topologies and targeted voltage ranges, as well as their nominal coil-to-coil distance (flush and surface mount GAs) and their coupling ranges.

The primary goal of this section is to evaluate the interoperability of these crossover systems, namely the TUM-UoA and UoA-TUM systems. However, for a complete evaluation, each GA will be examined with both VAs on top. Parts of this study were first published in [P.7].

7.4.1 Combination of Systems

The ICPs for all positions of the crossover systems (similar to Fig. 7.3) are shown in Fig. 7.11.

Comparing the UoA-UoA and TUM-TUM systems, it can be seen that the position of the VA affects the coupling quality (size of the ICP), while the GA dictates the shape of the ICP, similar to the observation made in Section 4.1.1.

To assess the operation of the GAs with both VAs, Fig. 7.12 shows the ICPs of each primary at the GA interface with only the inverter and GA boundaries incorporated (similar to the ICP_{in+GA} of Fig. 3.18) with the OPs of both secondaries over each full battery voltage range. The results are shown for three coupling conditions (k_{min} , k_{nom} and k_{max}) and three power levels ($P_{out,min} = 45, 48$ and 50 kW).

By considering the different power levels, systems can be evaluated for either HD or LD applications, as they differ in the power level definitions (see Section 2.5.1). The $P_{out,min} = 50$ kW results allow performance evaluation under HD WPT5 requirements, since the power class is defined as minimum transferred output power, and the other power levels can be used for LD WPT5 evaluation, since 50 kVA input power will presumably result in about 45 or 48 kW transferred output power at the load, depending on the efficiency. This again shows how universal the method is and how many different applications it can be applied to within a single study. In this study, however, only the LD evaluation is performed for simplicity.

Fig. 7.12 can now be used to evaluate the performance of each GA. It can be seen that the UoA GA performs well under k_{min} coupling, but without an active rectifier or output boost converter (for which it was designed), it is unable to address the full voltage range at higher coupling conditions. The TUM GA, on the other hand, is able to drive many OPs at higher coupling conditions, while it has limited interoperability at k_{min} .

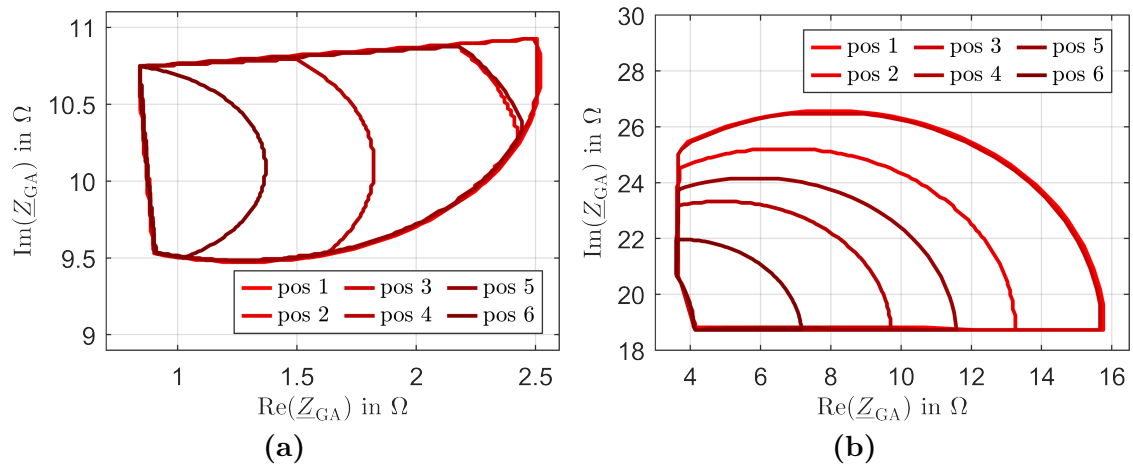


Figure 7.11 – ICPs of the (a) UoA-TUM and (b) TUM-UoA systems for all coupling conditions and system constraints.

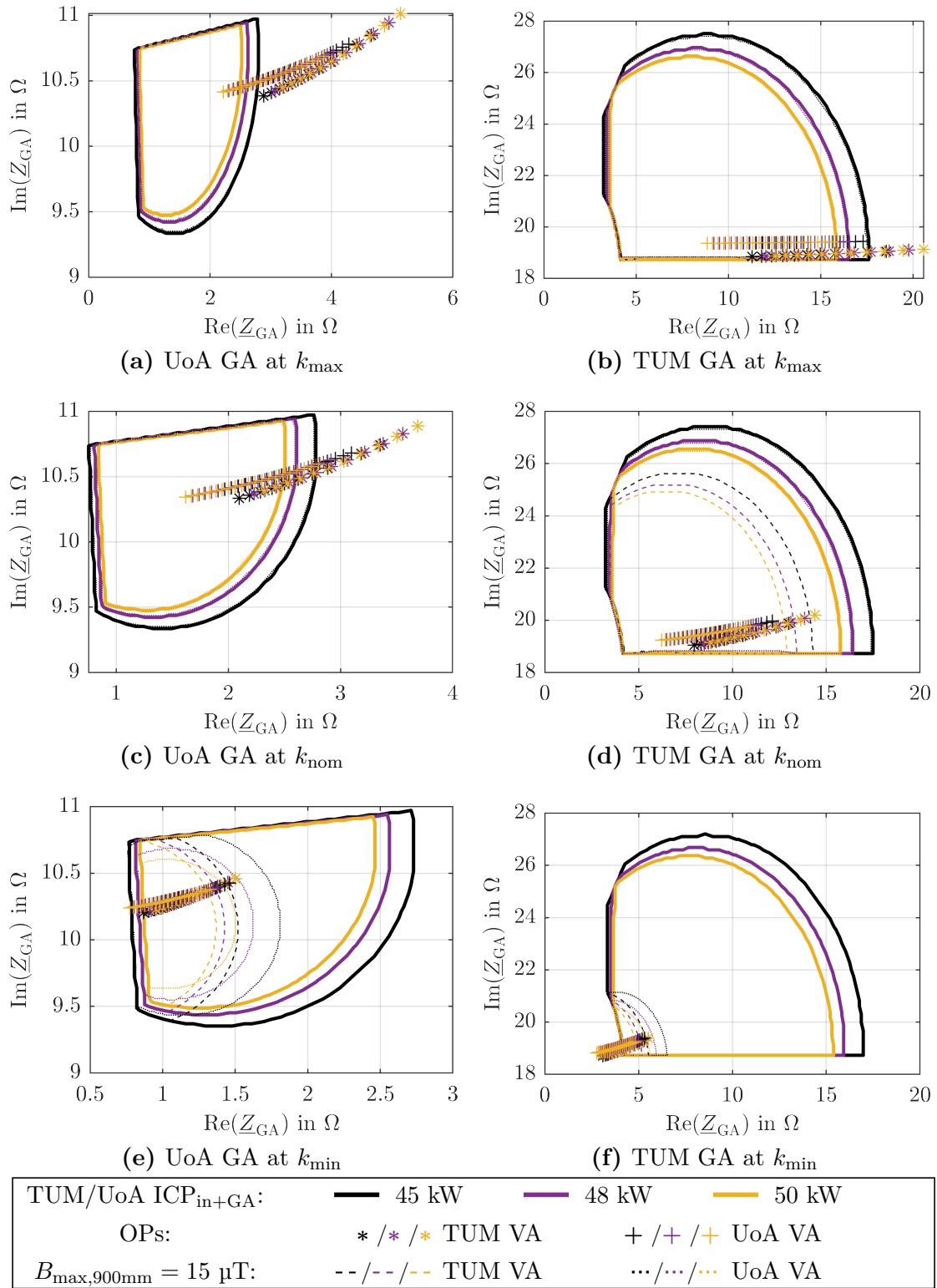


Figure 7.12 – Interoperability Assessment of the UoA and TUM GAs at three different coupling conditions and three power levels.

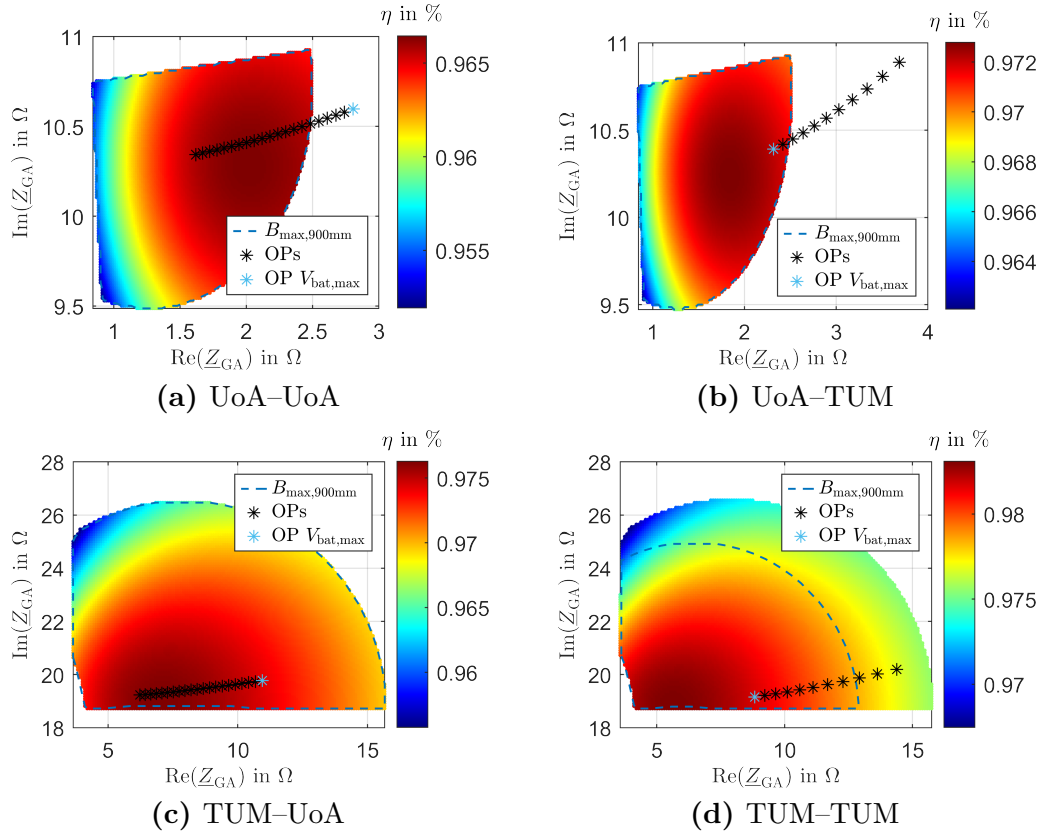


Figure 7.13 – Efficiency analysis of all four systems at k_{nom} .

However, the evaluation of critical points or non-interoperable combinations must always focus on the VAs as well, since the limitation may also come from the secondary side. To demonstrate this and to further investigate the systems, all four system combinations and their OPs will be examined in the following at their nominal coupling position. A similar analysis is shown in the Appendix A.2 for k_{min} and k_{max} .

Fig. 7.13 shows the systems under these considerations with efficiency heatmaps and leakage flux limit isolines. Again, the heatmap axis limits are not aligned and are set individually for each system to allow analysis of the efficiency within the IPPs. The OPs are shown in black, with $V_{\text{bat,max}}$ OP highlighted in turquoise.

The results show that the UoA VA operates close to the highest efficiency regardless of the GA used. Moreover, the TUM GA has good interoperability with both VAs, with some minor leakage flux limitations of the TUM–TUM system at lower voltages (Fig. 7.13d). The UoA–TUM system can only operate at high battery voltages and shows poor interoperability. The reason for this is the combination of the targeted battery voltage of the TUM VA ($V_{\text{bat}} = 350 - 450$ V), the low couplings due to the operation with a surface flush GA, and the coil current limitation of $I_{\text{VA,max}} = 150$ A. When the battery voltage drops, the required currents are too high and the inverter cannot deliver the full power. This will be further discussed in the next section.

In addition, the results show a slightly higher efficiency for the TUM GA due to the higher coupling factor because the system is designed for surface mount. Higher coupling requires lower coil currents (see Eq. (4.1)), which reduces magnetic losses, the main loss contribution

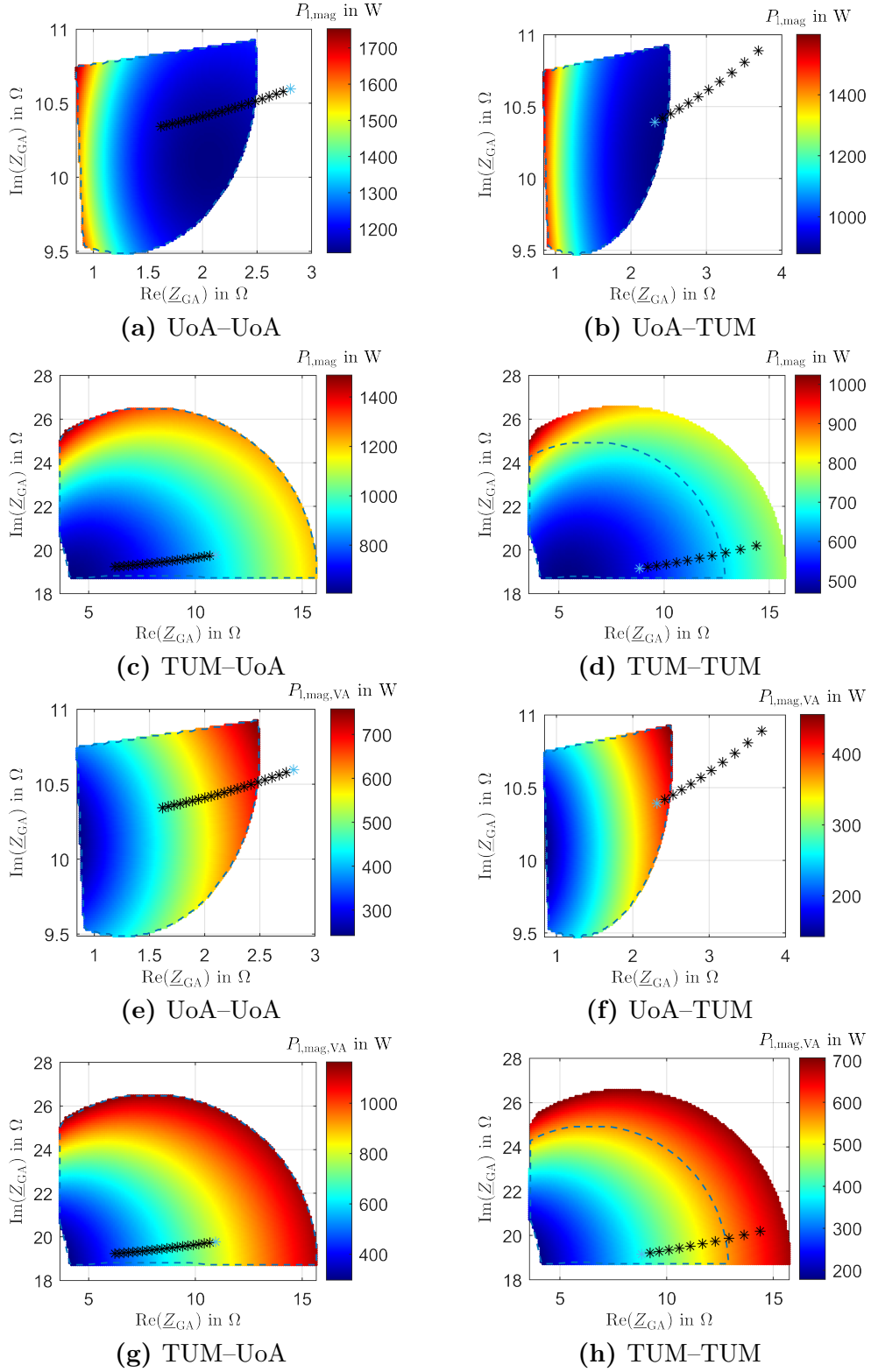


Figure 7.14 – Magnetic loss analysis of all four systems at k_{nom} ; (a)-(d) total coil losses $P_{l,\text{mag}}$ and (e)-(h) only VA coil losses $P_{l,\text{mag,VA}}$.

(see Section 5.1.3). To illustrate this, Fig. 7.14 shows the same systems at k_{nom} with a total magnetic loss heatmap in Fig. 7.14a–Fig. 7.14d.

The distribution of the magnetic losses is similar to the efficiency heatmap, emphasizing the magnetic losses being the main loss contributor in IPTSs. To get an understanding of how much the loss distribution is impacted by the VAs, Fig. 7.14 shows also the VA magnetic losses as heatmap in Fig. 7.14e–Fig. 7.14h.

The results show that the distribution is completely different between the two designed system. This is due to the different tuning topologies in both systems. While the losses with the UoA VA are more evenly distributed between primary and secondary side, the TUM VA is the main contributor of the losses when operating with the TUM GA, see Fig. 7.14h. The heatmaps indicate that the UoA VA is not operating in its most efficient condition which also applies to the TUM VA when operating with the TUM GA. This will be discussed further in the next section.

Besides the magnetic losses, it is important to determine the inverter losses for proper power electronics design and safe switch operation. As presented in Section 5.2 the IPM is able to incorporate the inverter losses to some extent. While it is difficult to consider harmonics and switching losses in LCC tuned systems (see Section 5.1.1) the rectifier conduction losses can be incorporated along with the inverter losses without switching losses (only Eq. (5.1) and Eq. (5.2)) and are shown in Fig. 7.15 for all systems at k_{nom} .

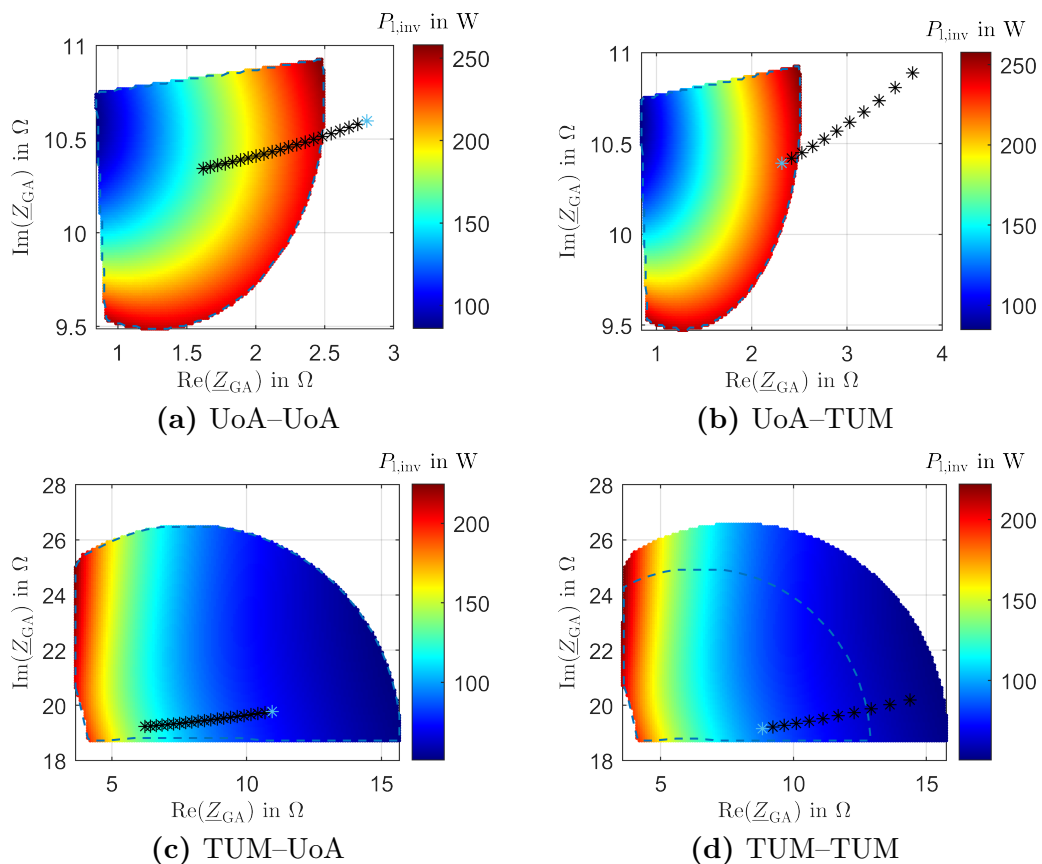


Figure 7.15 – Inverter conduction loss analysis ($P_{\text{inv}} = P_{\text{diode}} + P_{\text{mos}}$) of all four systems at k_{nom} .

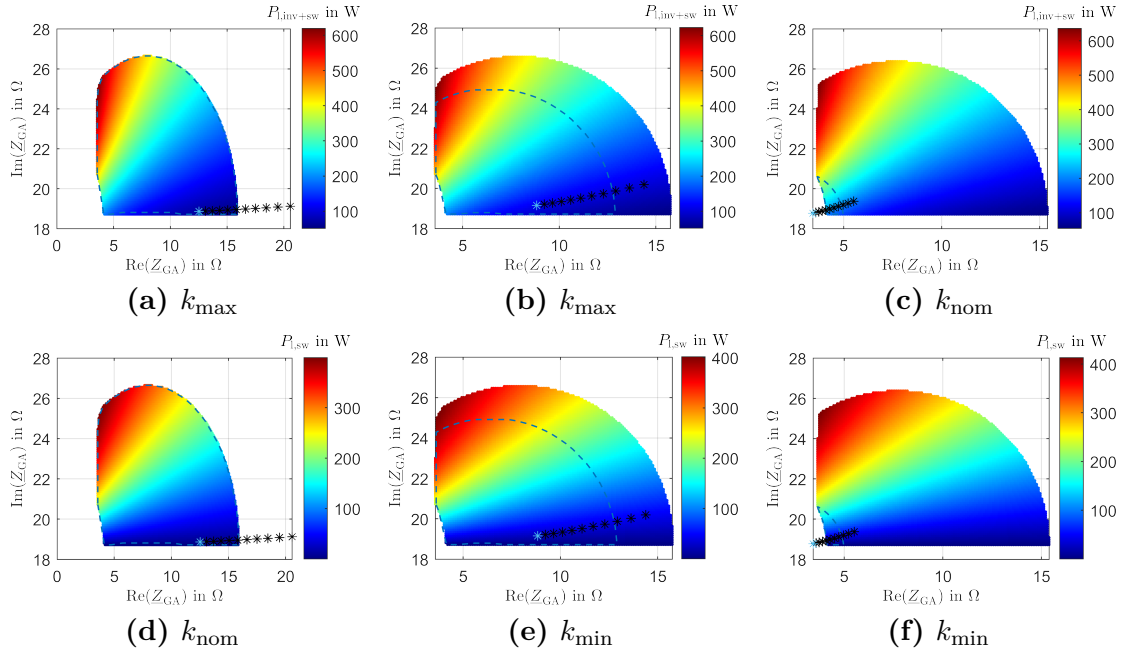


Figure 7.16 – Switching loss analysis of the series-series tuned TUM–TUM system at three coupling conditions with (a)-(c) showing the total inverter losses ($P_{\text{inv}} + P_{\text{1,sw}}$) and (d)-(f) showing only the switching losses $P_{\text{1,sw}}$.

The results show that the losses in the inverter are lower than the magnetic losses. Nevertheless, it can be seen that UoA inverter operates with higher currents because the conduction losses are related to I_{in} . As a result, the UoA design imposes more stress on the inverter components (i.e., switches) which will be discussed in the next section.

However, it has to be emphasized that Fig. 7.15 does not include switching losses, which, if high, reduces its significance. To show the impact of the switching losses on the inverter loss distribution, Fig. 7.16 shows the total inverter losses Eq. (5.6) and the switching losses Eq. (5.5) separately of the TUM–TUM system for three coupling conditions. Since the TUM–TUM system is a series-series tuned system, Eq. (5.5) can be used for the calculation of the switching losses because a sinusoidal waveform can be assumed.

The change in the distribution of the total losses and the change in the heatmap boundaries show that the switching losses are dominant in the inverter, which is why an analysis for an LCC-LCC system provides only limited insight. This will be further discussed in the outlook, see Section 8.4.

Furthermore, it can be seen that the TUM–TUM system operates in good inverter conditions since the OPs are located in low loss areas. If the losses are higher in the ICP, then the phase angle of the input impedance is higher, which results in a higher turn-off current and thus more switching loss, see Eq. (5.5) and (5.3).

7.4.2 Results and Evaluation

This study shows that achieving full interoperability for IPTSs can be very difficult. It is important to point out that the limits of the present study were deliberately set to present many challenges by using systems with different tuning topologies, battery voltage ranges

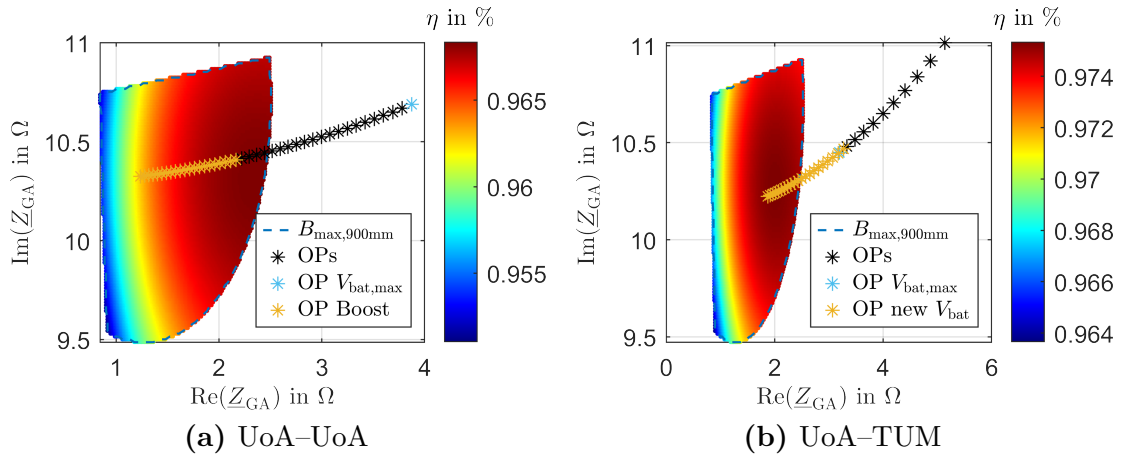


Figure 7.17 – Adjustments for increased interoperability (shown at k_{\max}), (a) boost converter and (b) change of battery voltage range to $V_{\text{bat}} = 600 - 800$ V.

and coil-to-coil distances (large Δk), while only allowing passive rectification on the output side. This represents worst case assumptions and allows the evaluation to identify measures to improve the OPs that are not interoperable or systems in poor condition.

Despite this, the systems generally showed good performance and high interoperability, with a few issues identified that will be addressed in the following.

Fig. 7.12 shows that the UoA GA has good performance at k_{\min} and is not interoperable with systems at k_{\max} under the restricted operating conditions of this use-case, while the TUM GA has good performance at k_{\max} and poor performance at k_{\min} .

As stated earlier, the UoA system was studied with an passive rectifier while initially being designed with an active rectifier or boost converter in mind. This explains the performance of the UoA–UoA system at k_{\max} and k_{nom} where only a few OPs can be addressed (see Fig. 7.12). Fig. 7.17a shows the UoA–UoA system at k_{\max} with an output boost converter (shown in orange) deployed on the secondary side (duty cycle set to $D = 0.4$). For comparison, the old OPs are shown in black.

This shows that the OPs can now be driven. The use of a boost converter comes at the cost of a small loss in efficiency, which is not considered in this figure. However, this is a trade-off that is necessary and feasible for the system to be interoperable. Additionally, the boost converter could be used to move the OPs to a higher efficiency zone (using Fig. 7.13).

The interoperability issues of the UoA–TUM system at high coupling are related to the different voltage range and series tuning used by the TUM VA. Due to the series tuning, the reflected impedance changes and the required primary coil current is low, which means that the required inverter voltage V_{in} is below the lower limit. In an LCC primary tuned system the bridge voltage and coil current are proportional to each other, see Section 2.2.5. In addition to the inverter voltage being out of bounds, the required inverter current is also too high. At k_{\min} , the required primary coil current is higher, resulting in a higher inverter voltage and lower current, which is why the system works well under this condition.

Again, challenges arise from the assumption that the secondary is completely passive, with no active measures to change the load presented. Furthermore, the assumption of transferring 50 kW at 350 – 450 V is unlikely to be used in a real system, given at this power level a battery voltage of 800 V is more likely. As such, the UoA–TUM system at 600 – 800 V

battery voltage is shown in Fig. 7.17b. It can be seen that this increases interoperability to some extent, but an active element such as active tuning or active rectification with a boost converter would still be required to cover the full battery voltage range. A redesign of the primary tuning network would also improve interoperability, but is beyond the scope of this study.

The poor performance of the TUM–TUM system at low coupling is related to the high coil currents required. Due to the series tuning on the primary, the required inverter current is similar to the coil current, which reaches the limit of the primary power electronics. In addition, the low required coil currents at high coupling require a high inverter voltage, which then also exceeds the limit. Again, as shown in previous chapters, the series-tuned system runs into difficulties at large coupling ranges, while the UoA GA shows more stability due to the LCC tuning.

Regarding the loss analysis, the different heatmap limits show that these systems operate at varying currents, resulting in different losses. Even though the analysis and loss calculation is done with some underlying assumptions and simplifications, the drawn results are still valid and can be transferred to real systems.

Furthermore, this study shows that even though the leakage flux is a difficult constraint at these high power classes, many OPs are still within the imposed leakage flux limitations. In particular, the TUM–TUM system does not operate the coils in the best condition as Fig. 7.14 shows. This leads to the leakage flux limit being exceeded at low battery voltages. Again, an active element can be used to solve this problem.

In general, the leakage flux constraint will be difficult to meet at low couplings due to the high coil currents required. However, this study also shows that the IPM presented here is very well suited to investigate this issue in depth by being able to study different aspects within the systems while considering many constraints.

The comparison of surface-mount and flush-mount systems in this chapter shows how difficult it can be for IPTSs to be interoperable under all circumstances. This issue will be even more challenging for real product systems, as this study was conducted in a laboratory environment and designed in a specific way with assumptions that may need to be revised for product systems. This highlights the problem of implementing IPTSs, the need for further guidance from standardization at higher power levels to help guide design, and the need to consider active secondary control while maintaining design freedom and not restricting innovation.

Although achieving full interoperability will be challenging, the study also shows good performance of the TUM-UoA system at nominal and maximum coupling. Furthermore, the UoA GA works well with the TUM VA at minimum coupling, which means that it is possible to achieve interoperability between surface and flush mount systems in general. In addition, Fig. 7.12 also shows that reducing power can alleviate many problems while still allowing for reasonable power transfer. When power is varied and active control measures are taken as suggested, full interoperability can be achieved for different IPTSs with different design goals.

This study has again shown that the IPM developed in this thesis is a powerful and useful tool to address and visualize design and interoperability problems. By using this method, the chance of creating a system with higher interoperability increases or measures to be taken can be accurately identified. Given its ability to help designers easily assess and evaluate numerous interoperability issues and problems.

7.5 Summary

This chapter presented a final study that applied the findings of all the previous chapters. An interoperability study was conducted on two different 50 kW IPTSs, with both coils designed separately for different rated operating conditions and design objectives. As such, this study serves as a comparison between surface mount and flush mount systems.

The first system (TUM) was presented in the previous chapter. The second system (UoA) was described in detail and the experimental verification of the simulation models was presented with measurements performed on the UoA system. Both, the leakage flux and the circuit simulations showed good agreement with measured values.

The boundaries of the study were presented and the IPM was first applied to both systems to provide a initial performance analysis. After validation, the IPM was then used to study both systems as well as the combination of them to allow a full interoperability assessment.

The systems were studied under three coupling conditions and different power levels by investigating the efficiency, magnetic and inverter losses for the full battery voltage ranges under many different constraints such as leakage flux and current limits.

The results were extensively discussed and interoperability issues identified and examined in detail. Conclusions were then drawn about the impact of surface mount and flush mount systems on system interoperability.

8 Summary and Future Work

This chapter summarizes the thesis by providing conclusions and discussing the main contributions of the presented method. In addition, possible future work on this topic is outlined.

8.1 Conclusions and Contributions

The primary goal of this thesis was to investigate the interoperability of IPTSs and to explore how aspects of interoperability can be incorporated into the design phase of IPTSs with a focus on EV battery charging applications. To achieve this goal, a novel approach based on IPPs, referred to as the IPM, was developed. The IPM is an extension of an existing standardization-focused approach that has been methodically and scientifically expanded to incorporate general interoperability considerations while allowing for design freedom. The approach aimed to develop a method that is widely applicable and as variable as possible.

In Chapter 3, the general methodology was established by simplifying the IPTS topology, making necessary assumptions, and then deriving the methodology. Subsequently, the individual components of the IPTS were examined in detail in Chapters 4–6, in particular the associated interoperability issues and critical limitations with respect to magnetics (Chapter 4), power electronics (Chapter 5), and tuning networks (Chapter 6). The IPM was then extended to enable various interoperability aspects to be considered. Each chapter presents tailored use-cases to demonstrate the capabilities of the IPM, focusing primarily on EV battery charging applications and typical interoperability issues. The IPM is sufficiently general such that the techniques used can be applied to other WPT applications, provided that the relevant underlying physics are taken into account.

In Chapter 7, all the findings were summarized and used to study and compare two 50 kW IPTSs to evaluate their interoperability.

The key contributions of this thesis and the advantages of the developed IPM are summarized in the following.

Variable Usage/Versatility of the IPM By utilizing the four impedance interfaces (or six power level interfaces) and introducing capability planes (ICPs and CCPs) based on component limitations, the IPM can be effectively applied to various use-cases and address multiple interoperability issues simultaneously or separately, as demonstrated in this thesis.

The IPM can be tailored to specifically address the design or assessment of individual components or the entire IPTS, while varying other components or imposing constraints on specific components, such as air-gap variations, battery voltage ranges, or output power variations.

This novel approach allows for more practical results while providing a comprehensive understanding of system performance under different operating conditions. In addition, the IPM is not limited to a specific circuit, and components of an IPTS can be exchanged during a study, allowing comparisons with the IPM.

As a result, instead of designing the system for a nominal OP, the IPM allows for broad interoperability as a system design goal.

Integration of Leakage Limitations Chapter 4 presented an approach that enables the consideration of leakage flux at multiple distances of the secondary coil within the IPPs with minimal computational effort and scalability to different coil currents and phase angles. The resulting heatmaps or constraint isolines provide essential information about leakage over the entire operating range, providing valuable insight for multiple OPs. This information is particularly critical during the design phase, as safety requirements demand that the leakage flux remain below certain limits, especially in EV charging applications.

Loss Considerations in the IPM The IPM extension presented in Chapter 5 allows the derivation of information about each parameter as a heatmap over the entire operating range or impedance zone. The distributions, especially the current values, can be used to calculate the loss distribution within the ICP, thus enabling the evaluation of OPs and ICPs. This in turn can be used to design or evaluate components. The extension improves the quality of results by incorporating losses into the information provided, leading to more educated interoperability decisions. Losses were incorporated in two ways, suited to evaluations for either HD and LD applications. Efficiency heatmaps were also used to identify regions where attention should be given to control system design. For example, it may be possible to select better operating states with higher efficiencies or desired system conditions.

Design of Active Tuning Networks Chapter 6 provided a sensitivity analysis that explored the impact of tuning variations on the operation of IPTSs. This analysis demonstrated that the IPM can be utilized to develop compensation tuning network solutions that address variations and tolerances in IPTSs resulting from interoperability requirements (such as full Z1–Z3 coverage for Class I interoperability).

The IPM enables specific interoperability conditions to be examined that could help establish a minimum required active tuning range that results in a more efficient IPTS design to avoid over-design.

Interoperability Assessment of 50 kW Flush and Surface Mount IPTS In Chapter 7, the full IPM, including its extension, was applied to two 50 kW use-cases, providing critical insight into the operation of surface mount systems with flush mount systems and vice versa.

The results demonstrated the capabilities of the IPM, highlighting its suitability for addressing such problems by clearly identifying the limiting factors and enabling suggestions to be made to improve interoperability. As a result, the IPM allows for better design decisions.

8.2 Publications

Some parts of the work in this thesis were published in several conferences and journals. A full list of publications is provided in the bibliography section.

Chapter 3 and 4 contain elements of [P.1] and [P.2]. Chapter 5 and 7 contain elements of [P.2] and [P.7], while Chapter 6 includes parts of [P.5] and [P.6].

8.3 Contributions to Research Projects

Besides the supervision of the student works [S.1–S.34], the research conducted for this thesis partially contributed to two different research projects, which are summarized below.

UnIndCha – Universal Inductive Charging (November 2016 – January 2020) A 3-year government-funded collaborative research project with the participation of the authors' institute was conducted from November 2016 to January 2020. The aim was to investigate and develop a new concept for a universal charging station for wireless public charging of EVs (3.7 kVA–11.1 kVA). The main research focus was on interoperability of WPT systems and coils, efficient inverter topologies, EMC and adaptive (intelligent) compensation technologies. Besides a system with high tolerance and efficiency, a design methodology for interoperable WPT systems was another motivation. Three prototypes were designed and built (circular and DDQ coils). Some key results have been published in [P.1–P.4, P.8–P.10].

NIIKOHLA – New Intelligent, Interoperable Contactless High Power Charging Station (August 2020 – August 2023) As a follow-up to the UnIndCha project, another 3-year government-funded research project was started in October 2020. The main motivation in the NIIKOHLA project is the development of a 50 kW WPT charging station. Major issues to be addressed in this project are (again) interoperability, coil design, development of an efficient PFC and inverter, intelligent compensation, reduction of leakage fields, thermal issues and a design study for interoperable high power WPT systems will also be conducted. The results have been published in [P.5–P.7].

8.4 Suggestions for Future Work

The development and presentation of the IPM in this thesis required several assumptions and simplifications. As a result of this work, additional areas of improvement for the method were identified that could further increase its performance and applicability. These areas of improvement include:

A Relaxation of Some Assumptions The most significant simplification made to the operation of IPTSs is FHA. Although it allows for fast circuit analysis, it limits the analysis to the fundamental and does not consider the impact of harmonics. Future work could explore eliminating the FHA simplification and using a complex Fast-Fourier-Transformation (FFT) to select relevant harmonics to obtain better current waveforms. This would allow the calculation of switching losses for all tuning topologies and also facilitate the use of crest factors as a performance indicator, thus allowing the IPM to perform harmonic evaluation. Some approaches to consider harmonics can be found in [182–185].

In addition, the assumption of CCM could be further investigated, as DCM changes the presented load and introduces errors in the results.

Incorporation of Additional Boundaries While this thesis has addressed several important aspects of IPTS design and interoperability, many other requirements must be met to ensure the safe and effective operation of these systems. Future work could investigate additional requirements, such as FOD and LOP, and consider their associated constraints, such as the maximum surface flux and the H-field at 10 meters (EMC), which can be introduced as additional boundaries within the IPPs.

The work of this thesis could be extended to include other design aspects of concern in future standardization such as bidirectional power transfer and multi-coil systems (e.g., three-phase systems), making the IPM more universally applicable. These extensions could

significantly improve the usability of the IPM and enable its use in a wider range of IPTS applications.

Extensions of the Loss Considerations The incorporation of losses in this thesis was presented with several assumptions. Future work could extend the loss calculations to include neglected losses such as core losses, eddy current shielding losses, and switching losses (harmonics) and the impact of thermal effects. These losses can significantly affect the performance and efficiency of IPTSs, especially in high power applications, and their inclusion in the IPM could provide more accurate and comprehensive information for design and evaluation purposes. Consideration of these neglected losses would require more detailed and complex modeling approaches, such as the FEM and the FFT, which would increase the computational complexity of the IPM, but also improve its accuracy and applicability.

Utilization of the IPM for Control of an IPTS As mentioned earlier, the IPM can be applied to numerous use-cases, and future work could focus on utilizing the IPM for control considerations. For example, the IPM could be extended to actively identify the best operating conditions and provide measures for the ICPs or OPs to operate under these desired conditions. This approach could enable the development of control algorithms that adjust the IPTS operating parameters, optimizing performance in different use-cases and ensuring interoperability with other systems. Such an approach would require a detailed understanding of the IPTS operating conditions and associated performance trade-offs, which the IPM can provide, making it an ideal tool for developing such control strategies.

Expansion of the IPM for Magnetic Design Future work could focus on developing the IPM so that it can be used to design interoperable magnetics. One possible approach could be to normalize the inductances to decouple the coils as much as possible, as presented in [126]. This would allow the IPTS designer to make separate design decisions for each component, providing more flexibility in the design process. This approach could help to derive additional interoperability design guidelines, such as the Δk used in this thesis, to enable the development of more efficient and interoperable IPTSs.

Variation of other Parameters This thesis focused on investigating the impact of parameter variations, such as transferred output power, on the interoperability of IPTSs. Future studies could extend this work by investigating the impact of other parameter variations, such as frequency and duty cycle, to gain a better understanding of their impact on the IPPs and the interoperability of IPTSs.

Use-Case Database Designers of IPTSs for EV battery charging often face recurring issues that can be addressed using the IPM. Future work could identify the most common design issues and challenges faced by designers in this area and use the IPM to develop solutions for these use-cases. This approach could include the development of flowcharts and guidelines to address these issues, making it easier for designers to use the IPM to develop efficient and interoperable solutions.

Deployment for Optimization Future work could focus on investigating the use of the IPM to optimize IPTS performance for specific use-cases, such as wireless EV charging, while ensuring interoperability with other systems.

Future work in all of these areas could potentially increase the applicability and usefulness of the IPM and contribute to the continued advancement of IPTS design and interoperability.

A Appendix

A.1 Extension of the IPM Example 3: Loss Analysis under Misalignment

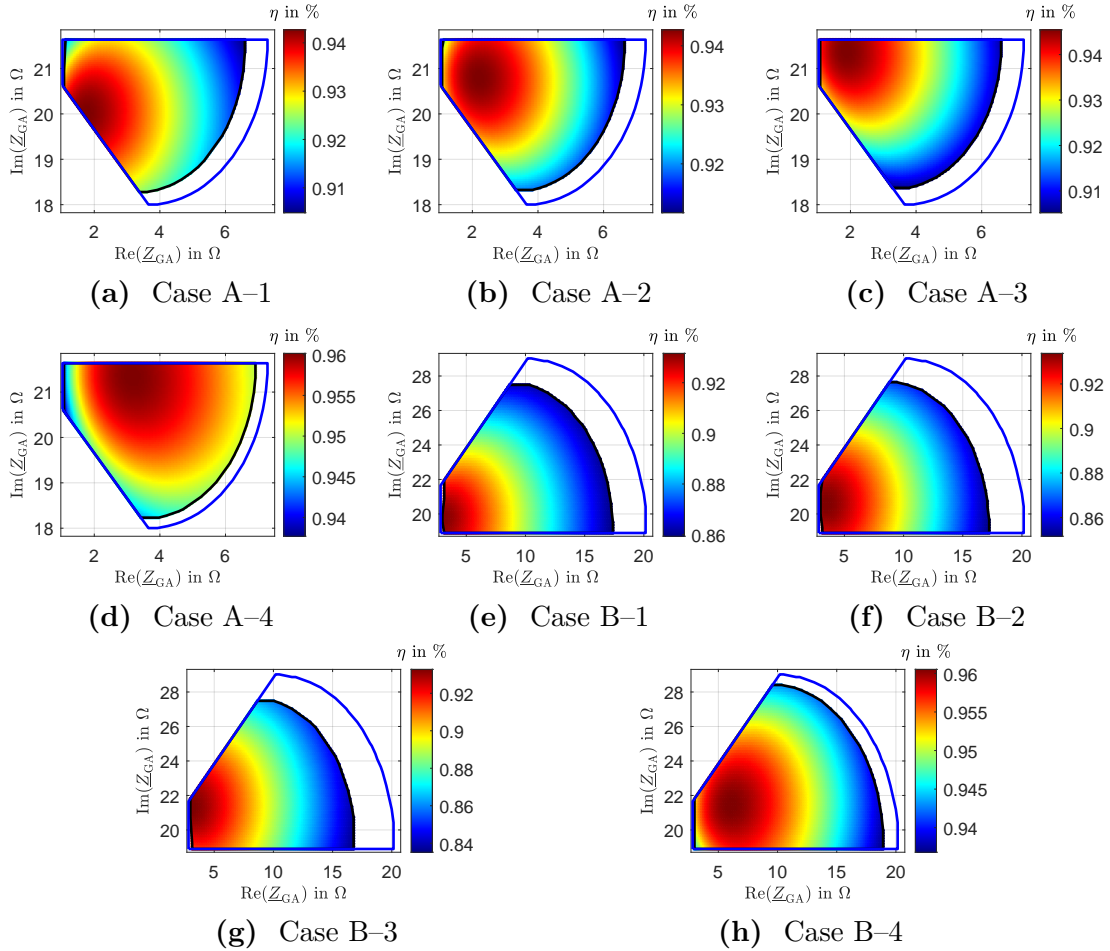


Figure A.1 – Results of the loss considerations (black hull curve with efficiency heatmap) for Case A (a)–(d) and Case B (e)–(h) on the primary and each secondary case at the GA interface and k_{\min} . The blue hull curve represents the lossless ICP.

A.2 Extension of the 50 kW Interoperability Assessment: Results at k_{\min} and k_{\max}

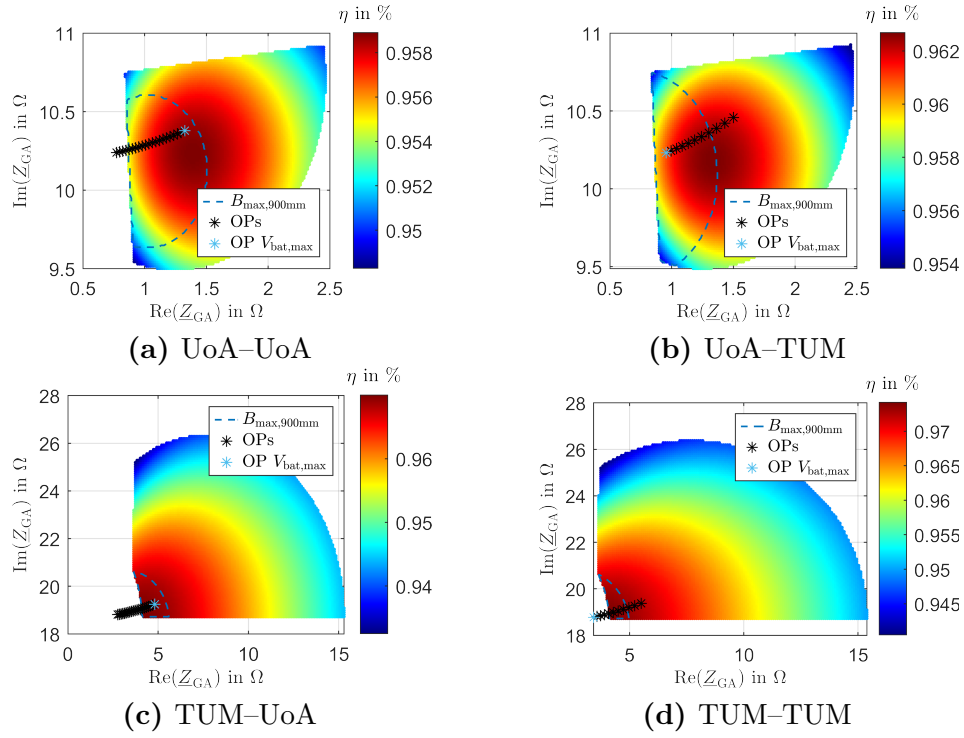


Figure A.2 – Efficiency analysis of all four systems at k_{\min} .

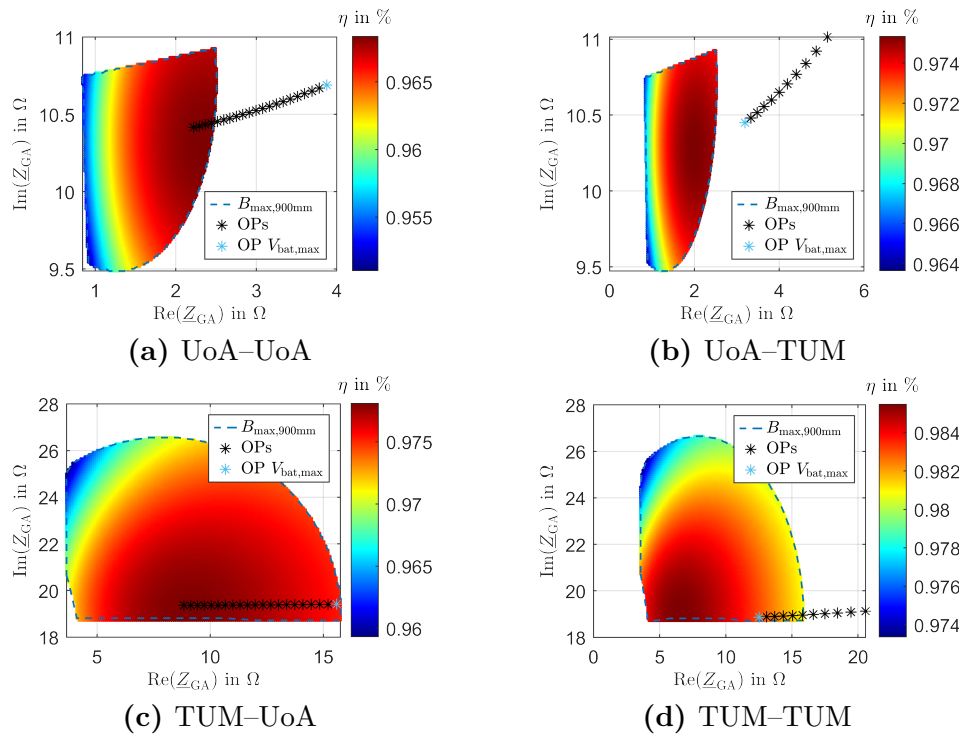


Figure A.3 – Efficiency analysis of all four systems at k_{\max} .

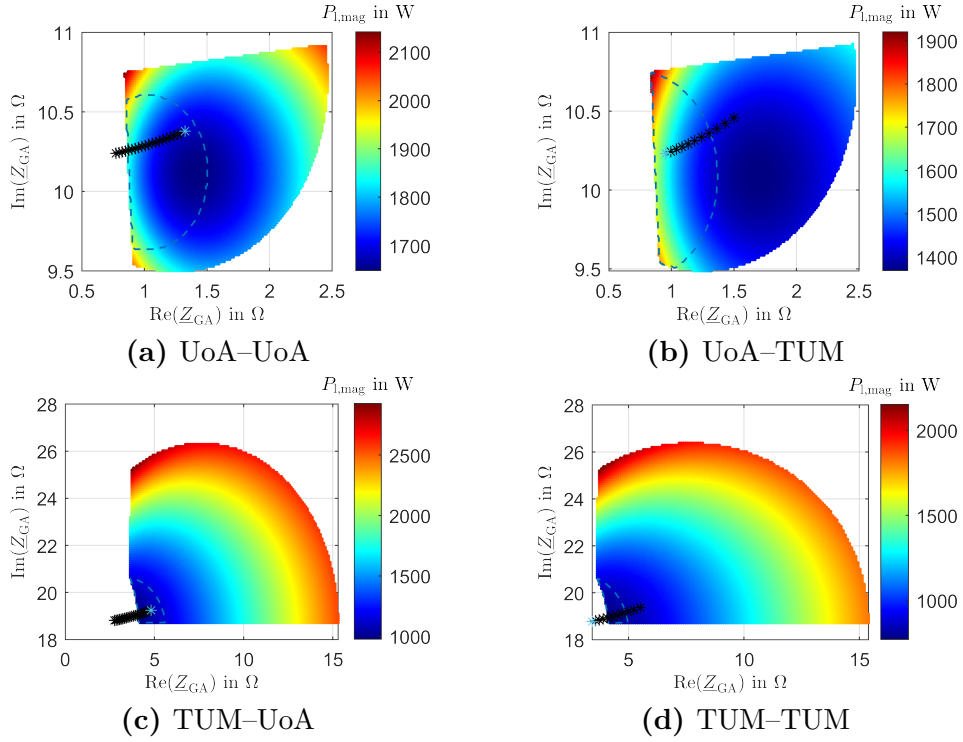


Figure A.4 – Magnetic loss analysis (coil losses $P_{l,\text{mag}}$) of all four systems at k_{\min} .

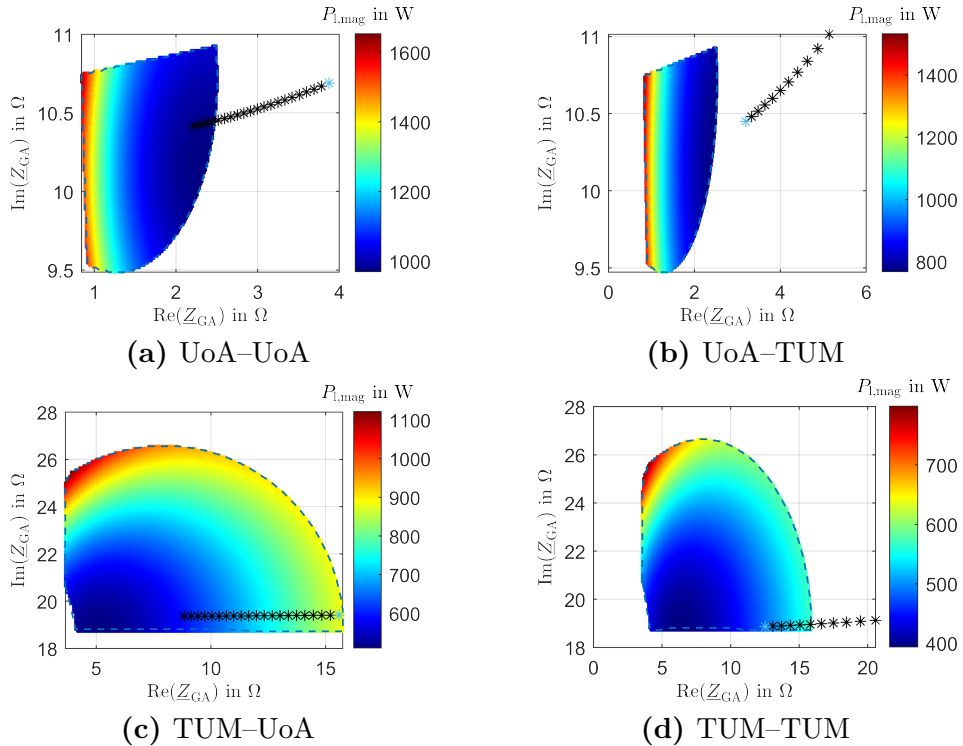


Figure A.5 – Magnetic loss analysis (coil losses $P_{l,\text{mag}}$) of all four systems at k_{\max} .

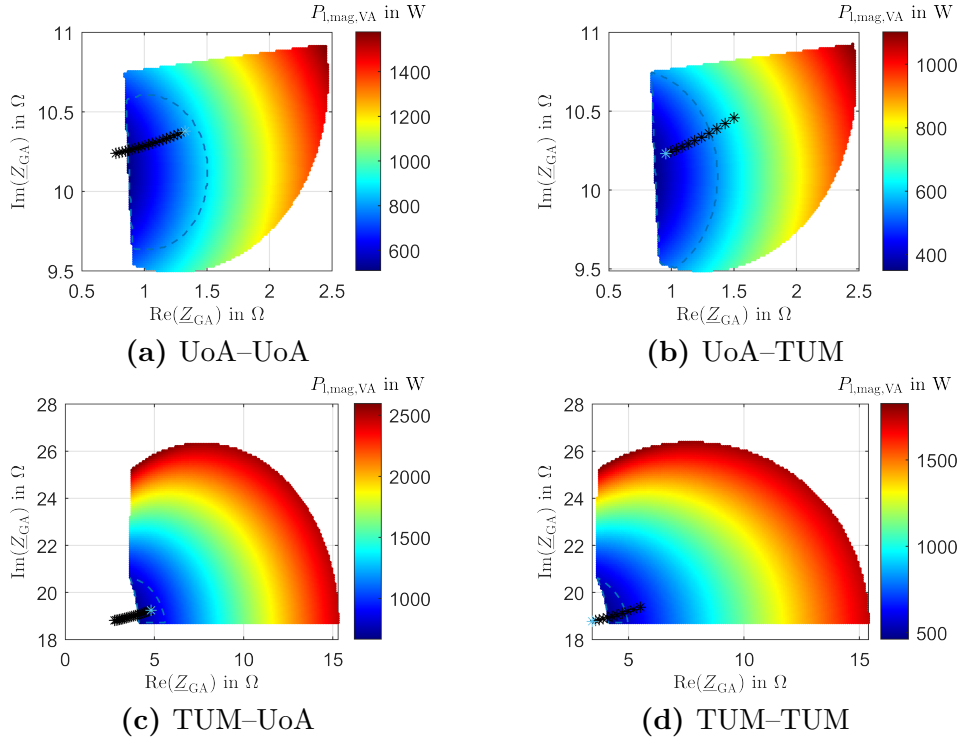


Figure A.6 – VA magnetic loss analysis (only VA coil losses $P_{l,mag,VA}$) of all four systems at k_{min} .

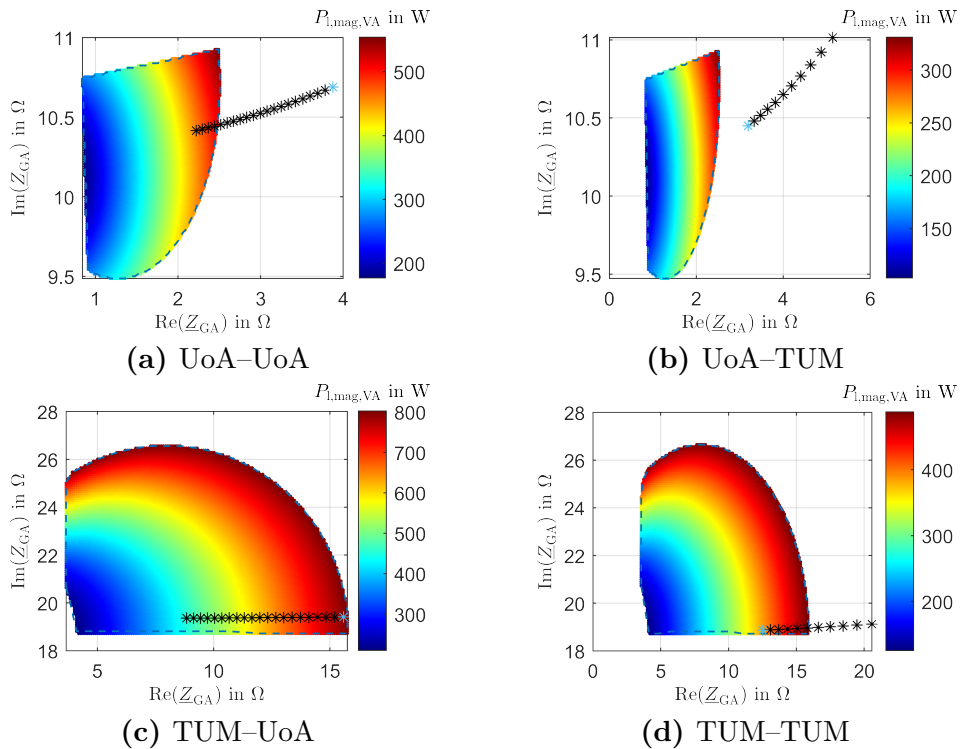


Figure A.7 – VA magnetic loss analysis (only VA coil losses $P_{l,mag,VA}$) of all four systems at k_{max} .

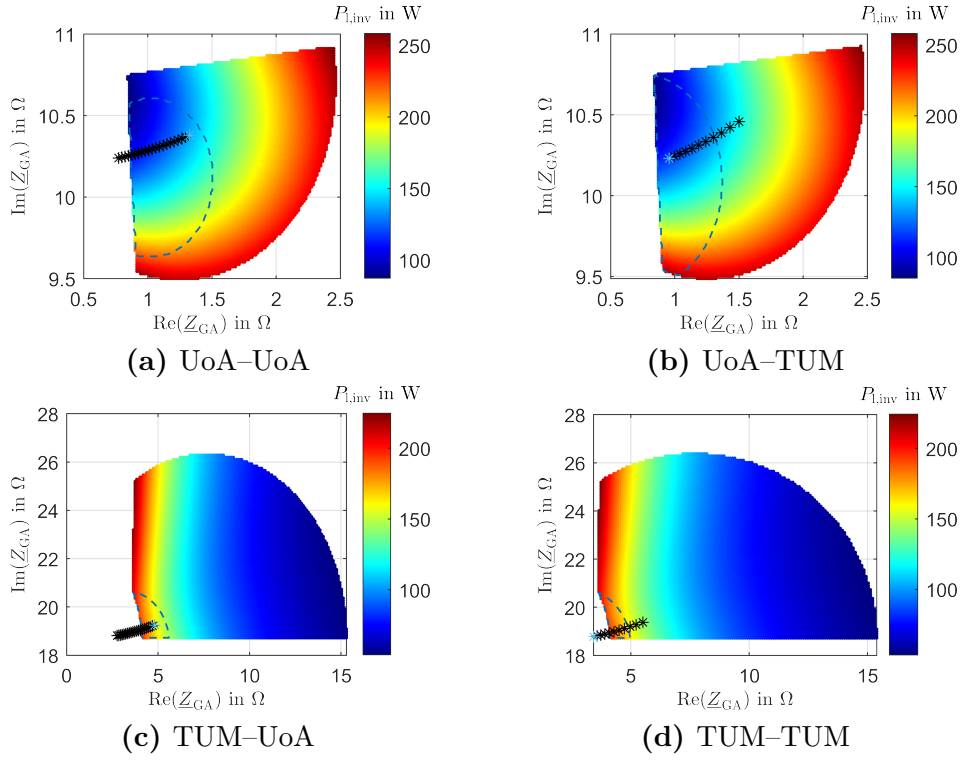


Figure A.8 – Inverter conduction loss analysis ($P_{\text{inv}} = P_{\text{diode}} + P_{\text{mos}}$) of all four systems at k_{\min} .

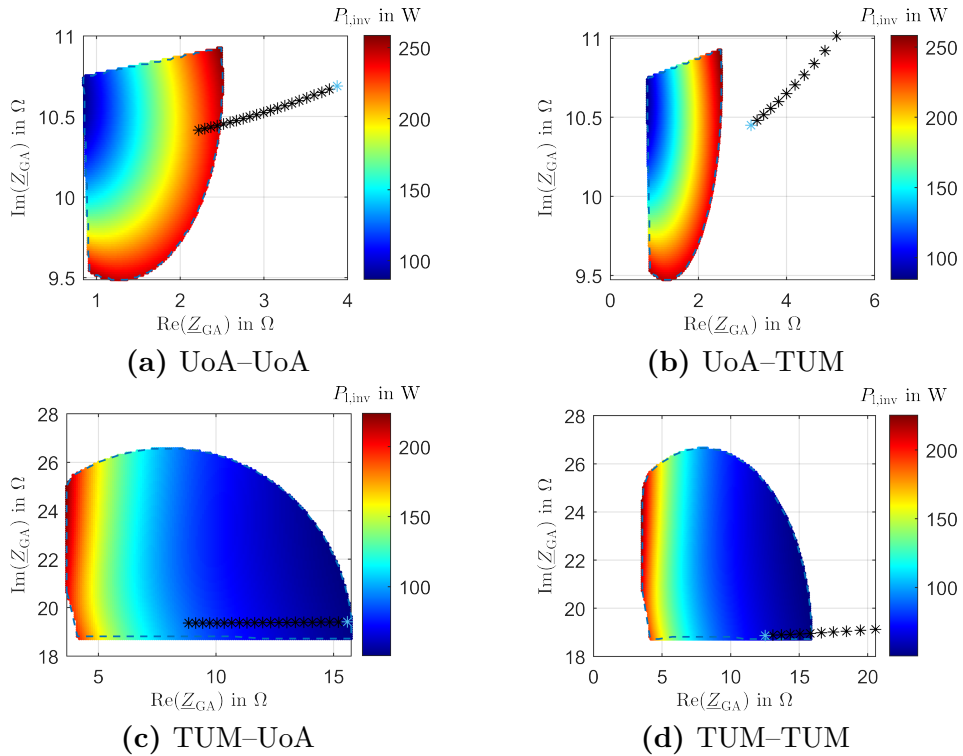


Figure A.9 – Inverter conduction loss analysis ($P_{\text{inv}} = P_{\text{diode}} + P_{\text{mos}}$) of all four systems at k_{\max} .

List of Publications

- [P.1] Kraus, D., Hassler, M., Covic, G., et al.: “Impedance Based Design Method for Interoperable Wireless Power Transfer Systems”. In: *2021 IEEE Energy Conversion Congress*. Vancouver, Canada: IEEE, Oct. 2021, pp. 1580–1587. DOI: 10.1109/ECCE47101.2021.9595472.
- [P.2] Kraus, D., Covic, G. A., Herzog, H.-G., et al.: “Design and Assessment of an Interoperable Wireless Power Transfer System Using an Impedance-Based Method”. In: *IEEE Transactions on Power Electronics*, vol. 38, no. 2 (2023), pp. 2768–2781. ISSN: 0885-8993. DOI: 10.1109/TPEL.2022.3212278.
- [P.3] Kraus, D., Vangapandu, S. V. and Herzog, H.-G.: “Interoperability Analysis of Two Different Coil Systems for Inductive Power Transfer”. In: *2019 21st European Conference on Power Electronics and Applications (EPE '19 ECCE Europe)*. Genoa, Italy: IEEE, Sept. 2019. DOI: 10.23919/EPE.2019.8915228.
- [P.4] Kraus, D. and Herzog, H.-G.: “Magnetic Design of a Q-Coil for a 10 kW DDQ System for Inductive Power Transfer”. In: *2019 IEEE PELS Workshop*. London, UK: IEEE, June 2019, pp. 140–143. DOI: 10.1109/WoW45936.2019.9030643.
- [P.5] Damhuis, C., Kraus, D. and Herzog, H.-G.: “Study on Coil Sizing and Shielding Materials High-Power Wireless Power Transfer Systems for Electric Vehicle Charging”. In: *2022 IEEE Wireless Power Week WPW*. Bordeaux, France, July 2022, pp. 454–459. DOI: 10.1109/WPW54272.2022.9853915.
- [P.6] Kraus, D., Damhuis, C., Covic, G., et al.: “Leakage Field and Compensation Assessment of an Interoperable High Power 50 kW Wireless Power Transfer System Using an Impedance Plane Method”. In: *2022 IEEE Wireless Power Week WPW*. Bordeaux, France: IEEE, 2022, pp. 72–77. DOI: 10.1109/WPW54272.2022.9854000.
- [P.7] Damhuis, C., Kraus, D., Covic, G. A., et al.: “Impedance Plane Based Interoperability Assessment of Two High-Power 50 kW WPT Systems for EV Charging”. In: *2023 IEEE Wireless Power Technology Conference and Expo (WPTCE)*. San Diego, CA, USA: IEEE, June 2023. DOI: 10.1109/WPTCE56855.2023.10216061.
- [P.8] Kraus, D., Heiland, G. and Herzog, H.-G.: “Nonlinear two-step simulation model of a resonant converter for IPT Systems”. In: *2018 IEEE Wireless Power Transfer*. Montreal, Canada: IEEE, June 2018. DOI: 10.1109/WPT.2018.8639365.
- [P.9] Ziegler, C., Heiland, G. and Kraus, D.: “Transfer-Effizienz verbessern”. In: *Elektronik automotive*, no. 12 (2017).
- [P.10] Ziegler, C., Weber, S., Heiland, G., et al.: “Influences of WPT-Coil Losses and Coupling Coefficient on the Resonance Circuits of Wireless Power Transfer Systems”. In: *PCIM Europe 2017*. Nuremberg: VDI, 2017.

List of Supervised Students Work

- [S.1] Schott, M.: “Regelungsentwurf eines resonanten LLC-Konverters für eine induktive Ladestation”. Bachelor’s thesis. Technical University of Munich, May 2017.
- [S.2] Langer, M.: “Nichtlineare Simulation und Interoperabilität resonanter Konverter zur induktiven Energieübertragung”. Master’s thesis. Technical University of Munich, Sept. 2018.
- [S.3] Suwal, R.: “Verluste kontaktloser induktiver Ladestationen”. Master’s thesis. Technical University of Munich, Nov. 2018.
- [S.4] Koderer, S.: “Reglerauslegung und Simulation eines induktiven Ladesystems”. Bachelor’s thesis. Technical University of Munich, Dec. 2018.
- [S.5] Vangapandu, S. V.: “Development of a Tool for the Design and Analysis of Inductive Power Transfer Systems”. Master’s thesis. Technical University of Munich, July 2019.
- [S.6] Kosak, D.: “Universelle Leistungsregelung resonanter Konverter zur induktiven Energieübertragung”. Bachelor’s thesis. Technical University of Munich, Sept. 2019.
- [S.7] Koderer, S.: “Umstrukturierung eines Design Tools zum Entwurf induktiver Ladesysteme”. Research Internship. Technical University of Munich, Oct. 2019.
- [S.8] Schranzhofer, S.: “Dynamische kontaktlose Energieübertragung zur Aufladung von batteriebetriebenen Elektrofahrzeugen”. Advanced Seminar. Technical University of Munich, Nov. 2019.
- [S.9] Maduawan, J.: “Laufzeit- und Qualitätsanalyse eines FE-Modells einer induktiven Ladestation”. Research Internship. Technical University of Munich, Nov. 2019.
- [S.10] Erdi, B.: “Evaluation of the Charging Zones of Three Coil Systems for Inductive Power Transfer”. Bachelor’s thesis. Technical University of Munich, Jan. 2020.
- [S.11] Shahid, M. T.: “Redesign of a 10 kW DDQ System for Inductive Power Transfer”. Master’s thesis. Technical University of Munich, Feb. 2020.
- [S.12] Maduawan, J.: “Untersuchung von Kompensationsmöglichkeiten resonanter Konverter zur induktiven Energieübertragung”. Bachelor’s thesis. Technical University of Munich, Sept. 2017.
- [S.13] Unterweger, S.: “Untersuchung sekundärseitiger Gleichrichtertopologien zur Leistungsflusssteuerung induktiver Ladesysteme”. Advanced Seminar. Technical University of Munich, Feb. 2020.
- [S.14] Zucker, J.: “Tripolare Magnetspulen für induktive Energieübertragungssysteme”. Advanced Seminar. Technical University of Munich, Feb. 2020.
- [S.15] Eichinger, C.: “Coupled Mode Theory zur Analyse induktiver Energieübertragungssysteme”. Advanced Seminar. Technical University of Munich, Feb. 2020.
- [S.16] Zeisberger, J.: “Analyse von Multi-Coil Systemen zur induktiven Energieübertragung”. Advanced Seminar. Technical University of Munich, Mar. 2020.

- [S.17] Zeisberger, J.: "Simulation und Bewertung einer primärseitigen bipolaren Spule zur induktiven Energieübertragung". Research Internship. Technical University of Munich, July 2020.
- [S.18] König, R.: "Erweiterung einer Methode zur Schaltungsanalyse induktiver Ladesysteme". Bachelor's thesis. Technical University of Munich, Feb. 2021.
- [S.19] Zeisberger, J.: "Indirekte Bestimmung der Rotortemperatur anhand eines Flussbeobachters bei permanenterregten Synchronmaschinen". Master's thesis. Technical University of Munich, Apr. 2021.
- [S.20] Heilein, S.: "Impedanzabstimmung induktiver Ladesysteme". Bachelor's thesis. Technical University of Munich, Apr. 2021.
- [S.21] Trigui, A.: "FEM Analysis of Shielding Effects in 50 kW WPT Systems". Research Internship. Technical University of Munich, May 2021.
- [S.22] Senel, E. D.: "Comparison of Different Simulation Softwares for the Design of Inductive Charging Stations for Electric Vehicles". Research Internship. Technical University of Munich, Apr. 2022.
- [S.23] Jaklovsky, M.: "Entwurf und Vergleich dreidimensionaler FE-Spulenmodelle zur kontaktlosen induktiven Energieübertragung". Research Internship. Technical University of Munich, Sept. 2017.
- [S.24] Skordas, K.: "Impedanzraumermittlung von WPT Systemen mittels Schaltungssimulation". Research Internship. Technical University of Munich, May 2022.
- [S.25] Neudecker, M.: "Ferritauslegung bei induktiven Ladestationen für Elektrofahrzeuge mit 50 kW Ladeleistung". Master's thesis. Technical University of Munich, June 2022.
- [S.26] Wagner, T.: "Verluste und Effizienz in Impedanzräumen von WPT Systemen". Advanced Seminar. Technical University of Munich, July 2022.
- [S.27] Li, C.: "Effects of Impedance Matching Networks in Impedance Planes for WPT EV Charging Systems". Research Internship. Technical University of Munich, Aug. 2022.
- [S.28] Jurisic, N.: "Aspects of Modelling the Magnetic Field Distribution of WPT System via Magnetic Dipoles". Master's thesis. Technical University of Munich, Oct. 2022.
- [S.29] Buonavolonta, V.: "Einfluss unterschiedlicher Ferritmaterialien auf das Übertragungsverhalten magnetisch gekoppelter Spulen". Bachelor's thesis. Technical University of Munich, Sept. 2017.
- [S.30] Suwal, R.: "Untersuchung unterschiedlicher Modellierungsmethoden eines LLC-Konverters in Simulink". Research Internship. Technical University of Munich, Nov. 2017.
- [S.31] Ewald, T.: "Erstellung eines Simulationsmodells zur Berechnung von transienten und subtransienten Vorgängen in elektrisch und permanent erregten Synchronmaschinen". Master's thesis. Technical University of Munich, Nov. 2017.
- [S.32] Wendel, S.: "Schaltungsanalyse resonanter Konverter mit unterschiedlichen sekundärseitigen Kompensationsmethoden". Advanced Seminar. Technical University of Munich, Mar. 2018.
- [S.33] Schelling, M.: "Untersuchung der Magnetfeldausbreitung eines induktiven Ladesystems". Advanced Seminar. Technical University of Munich, May 2018.
- [S.34] Kalmbach, O.: "Topologien dreiphasiger induktiver Ladestationen". Advanced Seminar. Technical University of Munich, May 2018.

Bibliography

- [1] Kazmierkowski, M. and Moradewicz, A.: “Unplugged But Connected: Review of Contactless Energy Transfer Systems”. In: *IEEE Industrial Electronics Magazine*, vol. 6, no. 4 (2012), pp. 47–55. ISSN: 1932-4529. DOI: 10.1109/MIE.2012.2220869.
- [2] Suh, I.-S.: *Wireless Charging Technology and The Future of Electric Transportation*. Warrendale, PA: SAE International, 2015. ISBN: 978-0-7680-8177-0. DOI: 10.4271/R-444.
- [3] Shinohara, N.: *Wireless Power Transfer*. Energy Engineering Ser. Stevenage: Institution of Engineering & Technology, 2018. ISBN: 9781785613463.
- [4] Zhang, H., Lu, F. and Mi, C.: “An Electric Roadway System Leveraging Dynamic Capacitive Wireless Charging: Furthering the Continuous Charging of Electric Vehicles”. In: *IEEE Electrification Magazine*, vol. 8, no. 2 (2020), pp. 52–60. ISSN: 2325-5897. DOI: 10.1109/MELE.2020.2985486.
- [5] www.electrive.com: *Chalmers researchers reveal 500 kW induction technology*. URL: <https://www.electrive.com/2023/03/08/chalmers-researchers-reveal-500-kw-induction-technology/> (visited on 3/4/2023).
- [6] www.insideevs.com: *Company Announces 1 MW Wireless Charging For Tesla Semi*. URL: <https://insideevs.com/news/525428/wave-wireless-charger-tesla-semi/> (visited on 3/4/2023).
- [7] Nägele, F. and Sahdrev, S.: *Perspectives on wireless and automated charging for electric vehicles*. URL: <https://www.mckinsey.com/industries/automotive-and-assembly/our-insights/perspectives-on-wireless-and-automated-charging-for-electric-vehicles> (visited on 5/4/2023).
- [8] IEEE-WPT: *WPT History*. 2023. URL: <https://wpt.ieee.org/wpt-history/> (visited on 8/3/2023).
- [9] Rim, C. T. and Mi, C.: *Wireless Power Transfer for Electric Vehicles and Mobile Devices*. Chichester, UK: John Wiley & Sons, Ltd, 2017. ISBN: 9781119329084. DOI: 10.1002/9781119329084.
- [10] Hutin, M. and Leblanc, M. French Patent 209,323. Nov. 1890.
- [11] Hutin, M. and Leblanc, M.: “Transformer System for Electric Railways”. US Patent 527,857. Oct. 1894.
- [12] Tesla, N.: “System of Transmission of Electrical Energy”. US Patent 645,576. March 1900.
- [13] Tesla, N.: “Apparatus for Transmission of Electrical Energy”. US Patent 649,621. May 1900.
- [14] Tesla, N.: “Art of Transmitting Electrical Energy through the Natural Mediums”. US Patent 787,412. April 1905.

- [15] Tesla, N.: “Apparatus for Transmitting Electrical Energy”. US Patent 1,119,732. Dec. 1914.
- [16] Tesla, N.: “System of Electric Lightning”. US Patent 454,622. June 1891.
- [17] Babat, G. I.: “High frequency electric transport system with contactless transmission of energy”. GB657035A. Sept. 1951. URL: <https://patents.google.com/patent/GB657035A/en> (visited on 18/11/2022).
- [18] Otto, D. V.: “Induction Driven Vehicle: Pick-Up Coil Construction”. New Zealand Patent 167422. Sep. 1975.
- [19] Covic, G. A. and Boys, J. T.: “Inductive Power Transfer”. In: *Proceedings of the IEEE*, vol. 101, no. 6 (2013), pp. 1276–1289. ISSN: 0018-9219. DOI: 10.1109/JPROC.2013.2244536.
- [20] Shladover, S. E.: “PATH at 20—History and Major Milestones”. In: *IEEE Transactions on Intelligent Transportation Systems*, vol. 8, no. 4 (2007), pp. 584–592. ISSN: 1524-9050. DOI: 10.1109/TITS.2007.903052.
- [21] Systems Control Technology Inc.: *Roadway Powered Electric Vehicle Project Track Construction and Testing Program Phase 3D*. Research Report. Berkeley: California Path Programm, Institute of Transportation Studies, University of California, 1994.
- [22] Boys, J. T. and Green, A. W.: “Inductive Power Distribution System”. US Patent 5,293,308. 1994.
- [23] Green, A. W. and Boys, J. T.: “10 kHz inductively coupled power transfer - concept and control”. In: *Proceedings of 5th International Conference on Power Electronics and Variable-Speed Drives*. IET, 1994, pp. 694–699. DOI: 10.1049/cp:19941049.
- [24] Covic, G. A. and Boys, J. T.: “Modern Trends in Inductive Power Transfer for Transportation Applications”. In: *IEEE Journal of Emerging and Selected Topics in Power Electronics*, vol. 1, no. 1 (2013), pp. 28–41. ISSN: 2168-6777. DOI: 10.1109/JESTPE.2013.2264473.
- [25] Boys, J. T. and Covic, G. A.: “The Inductive Power Transfer Story at the University of Auckland”. In: *IEEE Circuits and Systems Magazine*, vol. 15, no. 2 (2015), pp. 6–27. ISSN: 1531-636X. DOI: 10.1109/MCAS.2015.2418972.
- [26] Cirimele, V., Diana, M., Freschi, F., et al.: “Inductive Power Transfer for Automotive Applications: State-of-the-Art and Future Trends”. In: *IEEE Transactions on Industry Applications*, vol. 54, no. 5 (2018), pp. 4069–4079. ISSN: 0093-9994. DOI: 10.1109/TIA.2018.2836098.
- [27] Ahmad, A., Alam, M. S. and Chabaan, R.: “A Comprehensive Review of Wireless Charging Technologies for Electric Vehicles”. In: *IEEE Transactions on Transportation Electrification*, vol. 4, no. 1 (2018), pp. 38–63. DOI: 10.1109/TTE.2017.2771619.
- [28] Feng, H., Tavakoli, R., Onar, O. C., et al.: “Advances in High-Power Wireless Charging Systems: Overview and Design Considerations”. In: *IEEE Transactions on Transportation Electrification*, vol. 6, no. 3 (2020), pp. 886–919. DOI: 10.1109/TTE.2020.3012543.
- [29] Li, S. and Mi, C. C.: “Wireless Power Transfer for Electric Vehicle Applications”. In: *IEEE Journal of Emerging and Selected Topics in Power Electronics*, vol. 3, no. 1 (2015), pp. 4–17. ISSN: 2168-6777. DOI: 10.1109/JESTPE.2014.2319453.

-
- [30] Bai, H. K., Costinett, D., Tolbert, L. M., et al.: “Charging Electric Vehicle Batteries: Wired and Wireless Power Transfer: Exploring EV charging technologies”. In: *IEEE Power Electronics Magazine*, vol. 9, no. 2 (2022), pp. 14–29. ISSN: 2329-9207. DOI: 10.1109/MPPEL.2022.3173543.
- [31] Kurs, A., Karalis, A., Moffatt, R., et al.: “Wireless power transfer via strongly coupled magnetic resonances”. In: *Science (New York, N. Y.)*, vol. 317, no. 5834 (2007), pp. 83–86. DOI: 10.1126/science.1143254.
- [32] Hui, S. R.: “Magnetic Resonance for Wireless Power Transfer [A Look Back]”. In: *IEEE Power Electronics Magazine*, vol. 3, no. 1 (2016), pp. 14–31. ISSN: 2329-9207. DOI: 10.1109/MPPEL.2015.2510441.
- [33] Hui, S. Y. R., Zhong, W. and Lee, C. K.: “A Critical Review of Recent Progress in Mid-Range Wireless Power Transfer”. In: *IEEE Transactions on Power Electronics*, vol. 29, no. 9 (2014), pp. 4500–4511. ISSN: 0885-8993. DOI: 10.1109/TPEL.2013.2249670.
- [34] www.enrx.com: *ENRX Homepage*. URL: <https://www.enrx.com/de-DE> (visited on 3/4/2023).
- [35] *WAVE Homepage*. URL: <https://waveipt.com/> (visited on 24/9/2019).
- [36] www.electrive.net: *Momentum Dynamics: Induktives 200-kW-Ladesystem für Busse*. URL: <https://www.electrive.net/2018/04/19/induktives-200-kw-ladesystem-fuer-e-busse-betriebsbereit/> (visited on 3/4/2023).
- [37] www.inductev.com: *InductEV Homepage*. URL: <https://www.inductev.com/> (visited on 3/4/2023).
- [38] *WiTricity Homepage*. URL: <https://witricity.com/> (visited on 17/4/2023).
- [39] Suh, N. P. and Cho, D. H.: *The On-line Electric Vehicle*. Cham: Springer International Publishing, 2017. ISBN: 978-3-319-51182-5. DOI: 10.1007/978-3-319-51183-2.
- [40] *PluglessPower Homepage*. URL: <https://www.pluglesspower.com/gen2-tech-specs/> (visited on 17/4/2023).
- [41] www.insideevs.com: *VW Working On Wireless Charging Breakthrough With ORNL, UT*. URL: <https://insideevs.com/news/544699/vw-wireless-charging-breakthrough-ornl/> (visited on 3/4/2023).
- [42] Zhang, B., Carlson, R. B., Galigekere, V. P., et al.: “Electromagnetic Shielding Design for 200 kW Stationary Wireless Charging of Light-Duty EV”. In: *2020 IEEE Energy Conversion Congress and Exposition (ECCE)*. IEEE, 2020, pp. 5185–5192. ISBN: 978-1-7281-5826-6. DOI: 10.1109/ECCE44975.2020.9235329.
- [43] *FABRIC Project Homepage*. URL: <https://www.fabric-project.eu/> (visited on 24/9/2019).
- [44] Sanz, J. F., Villa, J. L., Sallan, J., et al.: “UNPLUGGED project: Development of a 50 kW inductive electric vehicle battery charge system”. In: *2013 World Electric Vehicle Symposium and Exhibition (EVS27)*. Barcelona, Spain: IEEE, Nov. 2013. ISBN: 978-1-4799-3832-2. DOI: 10.1109/EVS.2013.6914934.
- [45] *STILLE Press release*. URL: https://www.zu.de/lehrstuehle/cfm/assets/pdf/20160930_STILLE_PM_STILLE-erfolgreich-gestartet.pdf (visited on 17/4/2023).

- [46] Baier, K.: *BIPoLplus Berührungsloses, induktives und positionstolerantes Laden (Teilvorhaben Fahrzeugintegration)*. Final Report. Elektromobilität SüdWest Daimler AG, 2017.
- [47] Simon, O., Mahlein, J., Hoppe, A., et al.: *Inductive Norm Test by Exchange in Real Operation (INTEROP)*. Final Report. Leibniz Information Centre for Science and Technology University Library, Hannover, 2017.
- [48] University of Wuppertal: *Taxiladekonzept für Elektrotaxis im öffentlichen Raum*. 2022. URL: <https://ees.uni-wuppertal.de/de/forschung/aktuelle-forschungsprojekte/talako/> (visited on 8/3/2023).
- [49] Tu, H., Feng, H., Srdic, S., et al.: “Extreme Fast Charging of Electric Vehicles: A Technology Overview”. In: *IEEE Transactions on Transportation Electrification*, vol. 5, no. 4 (2019), pp. 861–878. DOI: 10.1109/TTE.2019.2958709.
- [50] Hybrid - EV Committee: SAE J2954: *Wireless Power Transfer for Light-Duty Plug-in/Electric Vehicles and Alignment Methodology*. SAE International, 400 Commonwealth Drive, Warrendale, PA, United States, Oct. 2020. DOI: 10.4271/J2954_202010.
- [51] www.linkedin.com: *LinkedIn Post*. URL: https://www.linkedin.com/posts/joshuaswerdlow_evcharging-electricvehicles-mondayvibes-activity-7000388540819738624-B6Kn/?utm_source=share&utm_medium=member_desktop (visited on 22/11/2022).
- [52] www.engadget.com: *Tesla is offering its proprietary charge connector as a new North American standard*. URL: <https://www.engadget.com/tesla-is-offering-its-proprietary-charge-connector-as-a-new-north-american-standard-193223322.html> (visited on 5/4/2023).
- [53] Lu, J., Zhu, G. and Mi, C. C.: “Foreign Object Detection in Wireless Power Transfer Systems”. In: *IEEE Transactions on Industry Applications*, vol. 58, no. 1 (2022), pp. 1340–1354. ISSN: 0093-9994. DOI: 10.1109/TIA.2021.3057603.
- [54] Kuyvenhoven, N., Dean, C., Melton, J., et al.: “Development of a foreign object detection and analysis method for wireless power systems”. In: *IEEE Symposium on Product Compliance Engineering (PSES), 2011*. San Diego, USA: IEEE, Oct. 2011. ISBN: 978-1-61284-686-6. DOI: 10.1109/PSES.2011.6088250.
- [55] Song, Y., Madawala, U. K., Thrimawithana, D. J., et al.: “Three-phase bi-directional wireless EV charging system with high tolerance to pad misalignment”. In: *IET Power Electronics*, vol. 12, no. 10 (2019), pp. 2697–2705. ISSN: 17554535. DOI: 10.1049/iet-pel.2018.6279.
- [56] Thrimawithana, D. J. and Madawala, U. K.: “A three-phase bi-directional IPT system for contactless charging of electric vehicles”. In: *2011 IEEE International Symposium on Industrial Electronics*. Gdansk, Poland: IEEE, June 2011, pp. 1957–1962. ISBN: 978-1-4244-9310-4. DOI: 10.1109/ISIE.2011.5984458.
- [57] Torchio, R., Cirimele, V., Alotto, P., et al.: “Modelling of road-embedded transmitting coils for wireless power transfer”. In: *Computers & Electrical Engineering*, vol. 88, (2020). ISSN: 00457906. DOI: 10.1016/j.compeleceng.2020.106850.

-
- [58] Chen, Z., Jing, W., Huang, X., et al.: “A Promoted Design for Primary Coil in Roadway-Powered System”. In: *IEEE Transactions on Magnetics*, vol. 51, no. 11 (2015). ISSN: 0018-9464. DOI: 10.1109/TMAG.2015.2440481.
- [59] Chen, W., Lin, F., Covic, G. A., et al.: “Design Considerations of a Bipolar Track for Dynamic Electric Vehicle Charging”. In: *ECCE 2019*. Baltimore, USA: IEEE, Sept. 2019, pp. 1188–1194. ISBN: 978-1-7281-0395-2. DOI: 10.1109/ECCE.2019.8912242.
- [60] Xiang, L., Sun, Y., Ye, Z., et al.: “Combined primary coupler design and control for EV dynamic wireless charging system”. In: *2016 IEEE PELS Workshop on Emerging Technologies: Wireless Power Transfer (WoW)*. Knoxville, USA: IEEE, Oct. 2016, pp. 174–179. ISBN: 978-1-5090-3414-7. DOI: 10.1109/WoW.2016.7772087.
- [61] Liu, F., Ding, Z., Fu, X., et al.: “Parametric Optimization of a Three-Phase MCR WPT System with Cylinder-Shaped Coils Oriented by Soft-Switching Range and Stable Output Power”. In: *IEEE Transactions on Power Electronics*, vol. 35, no. 1 (2019), pp. 1036–1044. ISSN: 0885-8993. DOI: 10.1109/TPEL.2019.2914154.
- [62] Covic, G. A., Boys, J. T., Kissin, M. L. G., et al.: “A Three-Phase Inductive Power Transfer System for Roadway-Powered Vehicles”. In: *IEEE Transactions on Industrial Electronics*, vol. 54, no. 6 (2007), pp. 3370–3378. ISSN: 0278-0046. DOI: 10.1109/TIE.2007.904025.
- [63] Kurpat, T. and Eckstein, L.: “A Three-Phase Inductive Power Transfer Coil with SAE J2954 WPT3 Magnetic Interoperability”. In: *2019 IEEE PELS Workshop on Emerging Technologies: Wireless Power Transfer (WoW)*. London, UK: IEEE, June 2019, pp. 150–155. ISBN: 978-1-5386-7514-4. DOI: 10.1109/WoW45936.2019.9030687.
- [64] Mohammad, M., Pries, J. L., Onar, O. C., et al.: “Shield Design for 50 kW Three-Phase Wireless Charging System”. In: *2020 IEEE Energy Conversion Congress and Exposition (ECCE)*. Detroit, USA: IEEE, Oct. 2020, pp. 842–849. ISBN: 978-1-7281-5826-6. DOI: 10.1109/ECCE44975.2020.9236371.
- [65] Onar, O. C., Su, G.-J., Mohammad, M., et al.: “A 100-kW Wireless Power Transfer System Development Using Polyphase Electromagnetic Couplers”. In: *2022 IEEE Transportation Electrification Conference & Expo (ITEC)*. Anaheim, USA: IEEE, June 2022, pp. 273–278. ISBN: 978-1-6654-0560-7. DOI: 10.1109/ITEC53557.2022.9814053.
- [66] Zeng, R., Onar, O. C., Mohammad, M., et al.: “Modeling and Analysis of a Polyphase Wireless Power Transfer System for EV Charging Applications”. In: *2022 IEEE Applied Power Electronics Conference and Exposition (APEC)*. Houston, USA: IEEE, Mar. 2022, pp. 1885–1890. ISBN: 978-1-6654-0688-8. DOI: 10.1109/APEC43599.2022.9773533.
- [67] Balog, R. S. and Davoudi, A.: “Batteries, Battery Management, and Battery Charging Technology”. In: *Encyclopedia of Sustainability Science and Technology*. Ed. by Robert A. Meyers. New York, NY: Springer New York, 2012, pp. 671–706. ISBN: 978-0-387-89469-0. DOI: 10.1007/978-1-4419-0851-3_822.
- [68] Matthew G. S. Pearce: “Inductive Power Transfer Magnetics for Roads”. Dissertation. New Zealand: The University of Auckland, 2020.
- [69] Steigerwald, R. L.: “A comparison of half-bridge resonant converter topologies”. In: *IEEE Transactions on Power Electronics*, vol. 3, no. 2 (1988), pp. 174–182. ISSN: 0885-8993. DOI: 10.1109/63.4347.

- [70] Beh, H. Z., Neath, M., Boys, J. T., et al.: “An Alternative IPT Pickup Controller for Material Handling Using a Current Doubler”. In: *IEEE Transactions on Power Electronics*, vol. 33, no. 12 (2018), pp. 10135–10147. ISSN: 0885-8993. DOI: 10.1109/TPEL.2018.2801247.
- [71] Pathmanathan, M., Nie, S., Yakop, N., et al.: “Efficiency improvement of a wireless power transfer system using a receiver side voltage doubling rectifier”. In: *2019 21st European Conference on Power Electronics and Applications (EPE '19 ECCE Europe)*. Genoa, Italy: IEEE, Sept. 2019. ISBN: 978-9-0758-1531-3. DOI: 10.23919/EPE.2019.8915022.
- [72] Samanta, S., Rathore, A. K. and Thrimawithana, D. J.: “Bidirectional Current-Fed Half-Bridge (C) (LC)–(LC) Configuration for Inductive Wireless Power Transfer System”. In: *IEEE Transactions on Industry Applications*, vol. 53, no. 4 (2017), pp. 4053–4062. ISSN: 0093-9994. DOI: 10.1109/TIA.2017.2682793.
- [73] Hassler, M., Atasoy, O., Twelker, K., et al.: “A comparison on simulated, analytic, and measured impedance values for an inductive power transfer system”. In: *Wireless Power Transfer* (2020), pp. 1–9. DOI: 10.1017/wpt.2020.6.
- [74] Kamat, M. and Patt, M.: “Active Phase Shifting Method for Different Resonant Converter Configurations in Inductive Power Transfer (IPT) Systems”. In: *2019 21st European Conference on Power Electronics and Applications (EPE '19 ECCE Europe)*. Genoa, Italy: IEEE, Sept. 2019. ISBN: 978-9-0758-1531-3. DOI: 10.23919/EPE.2019.8915179.
- [75] Bosshard, R., Badstubner, U., Kolar, J. W., et al.: “Comparative evaluation of control methods for Inductive Power Transfer”. In: *2012 International Conference on Renewable Energy Research and Applications*. Nagasaki, Japan: IEEE, Nov. 2012. ISBN: 978-1-4673-2330-7. DOI: 10.1109/ICRERA.2012.6477400.
- [76] Lu, S., Lammle, T. and Parspour, N.: “Analysis and Design of a T-Compensation Network with Switch-Controlled Capacitor for Wireless Power Transfer System”. In: *2021 IEEE PELS Workshop on Emerging Technologies: Wireless Power Transfer (WoW)*. San Diego, USA: IEEE, June 2021. ISBN: 978-1-7281-9548-3. DOI: 10.1109/WoW51332.2021.9462860.
- [77] Liu, C., Thrimawithana, D. J., Covic, G. A., et al.: “Active Impedance Control for Inductive Charging of Electric Vehicles”. In: *2020 IEEE PELS Workshop on Emerging Technologies: Wireless Power Transfer (WoW)*. Seoul, South Korea: IEEE, Nov. 2020, pp. 16–20. ISBN: 978-1-7281-3746-9. DOI: 10.1109/WoW47795.2020.9291286.
- [78] Mohammad, M., Onar, O. C., Su, G.-J., et al.: “Bidirectional LCC – LCC -Compensated 20-kW Wireless Power Transfer System for Medium-Duty Vehicle Charging”. In: *IEEE Transactions on Transportation Electrification*, vol. 7, no. 3 (2021), pp. 1205–1218. DOI: 10.1109/TTE.2021.3049138.
- [79] Covic, G. A., Boys, J. T., Tam, A., et al.: “Self tuning pick-ups for inductive power transfer”. In: *IEEE Power Electronics Specialists Conference*. Rhodes, Greece: IEEE, June 2008, pp. 3489–3494. ISBN: 978-1-4244-1667-7. DOI: 10.1109/PESC.2008.4592495.
- [80] Boys, J. T., Covic, G. A. and Green, A. W.: “Stability and control of inductively coupled power transfer systems”. In: *IEE Proceedings - Electric Power Applications*, vol. 147, no. 1 (2000), p. 37. ISSN: 13502352. DOI: 10.1049/ip-epa:20000017.

-
- [81] Huang, C.-Y., Boys, J. T., Covic, G. A., et al.: “Practical considerations for designing IPT system for EV battery charging”. In: *IEEE Vehicle Power and Propulsion Conference, 2009*. Piscataway, NJ: IEEE, 2009, pp. 402–407. ISBN: 978-1-4244-2600-3. DOI: 10.1109/VPPC.2009.5289821.
- [82] Chen, C.-I., Covic, G. A. and Boys, J. T.: “Regulator capacitor selection for series compensated IPT pickups”. In: *2008 34th Annual Conference of IEEE Industrial Electronics*. Orlando, USA: IEEE, Nov. 2008, pp. 932–937. ISBN: 978-1-4244-1767-4. DOI: 10.1109/IECON.2008.4758078.
- [83] Yilmaz, M. and Krein, P. T.: “Review of Battery Charger Topologies, Charging Power Levels, and Infrastructure for Plug-In Electric and Hybrid Vehicles”. In: *IEEE Transactions on Power Electronics*, vol. 28, no. 5 (2013), pp. 2151–2169. ISSN: 0885-8993. DOI: 10.1109/TPEL.2012.2212917.
- [84] Keeling, N.: “A Unity Power Factor IPT Pickup for High Power Applications”. Dissertation. Auckland: The University of Auckland, 2010.
- [85] Zaheer, A.: “A New Magnetic Coupling Pad Topology For Inductively Powered Vehicular Systems”. Dissertation. New Zealand: The University of Auckland, 2014.
- [86] James, J.: “Analysis and Control of IPT Systems with Inherent Secondary VARs”. Dissertation. New Zealand: The University of Auckland, 2015.
- [87] Keeling, N. A., Covic, G. A. and Boys, J. T.: “A Unity-Power-Factor IPT Pickup for High-Power Applications”. In: *IEEE Transactions on Industrial Electronics*, vol. 57, no. 2 (2010), pp. 744–751. ISSN: 0278-0046. DOI: 10.1109/TIE.2009.2027255.
- [88] Zhang, W. and Mi, C. C.: “Compensation Topologies of High-Power Wireless Power Transfer Systems”. In: *IEEE Transactions on Vehicular Technology*, vol. 65, no. 6 (2016), pp. 4768–4778. ISSN: 0018-9545. DOI: 10.1109/TVT.2015.2454292.
- [89] Vu, V.-B., Tran, D.-H. and Choi, W.: “Implementation of the Constant Current and Constant Voltage Charge of Inductive Power Transfer Systems With the Double-Sided LCC Compensation Topology for Electric Vehicle Battery Charge Applications”. In: *IEEE Transactions on Power Electronics*, vol. 33, no. 9 (2018), pp. 7398–7410. ISSN: 0885-8993. DOI: 10.1109/TPEL.2017.2766605.
- [90] Li, S., Li, W., Deng, J., et al.: “A Double-Sided LCC Compensation Network and Its Tuning Method for Wireless Power Transfer”. In: *IEEE Transactions on Vehicular Technology*, vol. 64, no. 6 (2015), pp. 2261–2273. ISSN: 0018-9545. DOI: 10.1109/TVT.2014.2347006.
- [91] Wang, C.-S., Stielau, O. H. and Covic, G. A.: “Design Considerations for a Contactless Electric Vehicle Battery Charger”. In: *IEEE Transactions on Industrial Electronics*, vol. 52, no. 5 (2005), pp. 1308–1314. ISSN: 0278-0046. DOI: 10.1109/TIE.2005.855672.
- [92] Zhang, W., Wong, S.-C., Tse, C. K., et al.: “Analysis and Comparison of Secondary Series- and Parallel-Compensated Inductive Power Transfer Systems Operating for Optimal Efficiency and Load-Independent Voltage-Transfer Ratio”. In: *IEEE Transactions on Power Electronics*, vol. 29, no. 6 (2014), pp. 2979–2990. ISSN: 0885-8993. DOI: 10.1109/TPEL.2013.2273364.

- [93] Wang, C.-S., Covic, G. A. and Stielau, O. H.: “Power Transfer Capability and Bifurcation Phenomena of Loosely Coupled Inductive Power Transfer Systems”. In: *IEEE Transactions on Industrial Electronics*, vol. 51, no. 1 (2004), pp. 148–157. ISSN: 0278-0046. DOI: 10.1109/TIE.2003.822038.
- [94] Aldhafer, S., Yates, D. C. and Mitcheson, P. D.: “Design and Development of a Class EF₂ Inverter and Rectifier for Multimegahertz Wireless Power Transfer Systems”. In: *IEEE Transactions on Power Electronics*, vol. 31, no. 12 (2016), pp. 8138–8150. ISSN: 0885-8993. DOI: 10.1109/TPEL.2016.2521060.
- [95] Kalra, G. R., Thrimawithana, D. J., Riar, B. S., et al.: “A Novel Boost Active Bridge-Based Inductive Power Transfer System”. In: *IEEE Transactions on Industrial Electronics*, vol. 67, no. 2 (2020), pp. 1103–1112. ISSN: 0278-0046. DOI: 10.1109/TIE.2019.2898615.
- [96] Barsari, V. Z., Thrimawithana, D. J. and Covic, G. A.: “Push-pull driven Low-cost Coupler Array for Dynamic IPT systems”. In: *2019 IEEE PELS Workshop on Emerging Technologies: Wireless Power Transfer (WoW)*. London, UK: IEEE, June 2019, pp. 209–213. ISBN: 978-1-5386-7514-4. DOI: 10.1109/WoW45936.2019.9030676.
- [97] Lin, F. Y.: “Research and Development of Magnetic Pad Topologies Involving Inductive Power Transfer”. Dissertation. New Zealand: The University of Auckland, 2017.
- [98] Budhia, M., Covic, G. A. and Boys, J. T.: “Design and Optimization of Circular Magnetic Structures for Lumped Inductive Power Transfer Systems”. In: *IEEE Transactions on Power Electronics*, vol. 26, no. 11 (2011), pp. 3096–3108. ISSN: 0885-8993. DOI: 10.1109/TPEL.2011.2143730.
- [99] Budhia, M., Covic, G. A. and Boys, J. T.: “Design and optimisation of magnetic structures for lumped Inductive Power Transfer systems”. In: *IEEE Energy Conversion Congress and Exposition*. San Jose, USA: IEEE, Sept. 2009, pp. 2081–2088. ISBN: 978-1-4244-2893-9. DOI: 10.1109/ECCE.2009.5316197.
- [100] Budhia, M., Covic, G. A., Boys, J. T., et al.: “Development and evaluation of single sided flux couplers for contactless electric vehicle charging”. In: *IEEE Energy Conversion Congress and Exposition (ECCE)*. Phoenix, USA: IEEE, Sept. 2011, pp. 614–621. ISBN: 978-1-4577-0542-7. DOI: 10.1109/ECCE.2011.6063826.
- [101] Lin, F. Y., Zaheer, A., Budhia, M., et al.: “Reducing leakage flux in IPT systems by modifying pad ferrite structures”. In: *2014 IEEE Energy Conversion Congress and Exposition (ECCE)*. Pittsburgh, USA: IEEE, Sept. 2014, pp. 1770–1777. ISBN: 978-1-4799-5776-7. DOI: 10.1109/ECCE.2014.6953632.
- [102] Gaona, D. E., Jiang, C. and Long, T.: “Highly Efficient 11.1-kW Wireless Power Transfer Utilizing Nanocrystalline Ribbon Cores”. In: *IEEE Transactions on Power Electronics*, vol. 36, no. 9 (2021), pp. 9955–9969. ISSN: 0885-8993. DOI: 10.1109/TPEL.2021.3064902.
- [103] Barth, D., Cortese, G. and Leibfried, T.: “Evaluation of Soft Magnetic Composites for Inductive Wireless Power Transfer”. In: *2019 IEEE PELS Workshop on Emerging Technologies: Wireless Power Transfer (WoW)*. London, UK: IEEE, June 2019. ISBN: 978-1-5386-7514-4. DOI: 10.1109/WoW45936.2019.9030664.

-
- [104] Mayr, T., Niedermeier, F. and Hassler, M.: “Application of composite materials in inductive charging systems for electric vehicles”. In: *Journal of Composite Materials*, vol. 53, no. 16 (2019), pp. 2183–2196. ISSN: 0021-9983. DOI: 10.1177/0021998318824637.
- [105] Albach, M.: *Induktivitäten in der Leistungselektronik*. Wiesbaden: Springer Fachmedien Wiesbaden, 2017. ISBN: 978-3-658-15080-8.
- [106] Budhia, M., Boys, J. T., Covic, G. A., et al.: “Development of a Single-Sided Flux Magnetic Coupler for Electric Vehicle IPT Charging Systems”. In: *IEEE Transactions on Industrial Electronics*, vol. 60, no. 1 (2013), pp. 318–328. ISSN: 0278-0046. DOI: 10.1109/TIE.2011.2179274.
- [107] Hassler, M., Niedermeier, F., Krammer, J., et al.: “A Method for Interoperable Interface Description of Inductive Power Transfer Systems”. In: *2018 IEEE PELS Workshop on Emerging Technologies: Wireless Power Transfer (WoW)*. Montreal, Canada: IEEE, June 2018.
- [108] Deng, J., Li, S., Hu, S., et al.: “Design Methodology of LLC Resonant Converters for Electric Vehicle Battery Chargers”. In: *IEEE Transactions on Vehicular Technology*, vol. 63, no. 4 (2014), pp. 1581–1592. ISSN: 0018-9545. DOI: 10.1109/TVT.2013.2287379.
- [109] Kürschner, D. and Rathge, C.: “Contactless energy transmission systems with improved coil positioning flexibility for high power applications”. In: *IEEE Power Electronics Specialists Conference, 2008*. Rhodes, Greece: IEEE, June 2008, pp. 4326–4332. ISBN: 978-1-4244-1667-7. DOI: 10.1109/PESC.2008.4592639.
- [110] International Electrotechnical Commission: 61980-3: *Electric vehicle wireless power transfer (WPT) systems - Part 3: Specific requirements for the magnetic field wireless power transfer systems*. Nov. 2022.
- [111] Grazian, F., Shi, W., Dong, J., et al.: “Survey on Standards and Regulations for Wireless Charging of Electric Vehicles”. In: *2019 AEIT International Conference of Electrical and Electronic Technologies for Automotive (AEIT AUTOMOTIVE)*. Turin, Italy: IEEE, July 2019. ISBN: 978-8-8872-3743-6. DOI: 10.23919/EETA.2019.8804573.
- [112] Hybrid - EV Committee: SAE J2954/2: *Wireless Power Transfer for Heavy-Duty Electric Vehicles*. SAE International, 400 Commonwealth Drive, Warrendale, PA, United States, Dec. 2022. DOI: 10.4271/J2954/2_202212.
- [113] International Commission on non-ionizing radiation protection: “Guidelines for limiting exposure to time-varying electric and magnetic fields (1 Hz to 100 kHz)”. In: *Health physics*, vol. 99, no. 6 (2010), pp. 818–836. DOI: 10.1097/HP.0b013e3181f06c86.
- [114] International Electrotechnical Commission: CISPR-11: *Industrial, scientific and medical equipment - Radio-frequency disturbance characteristics - Limits and methods of measurement*. June 2015.
- [115] International Electrotechnical Commission: 61980-2: *Electric vehicle wireless power transfer (WPT) systems - Part 2: Specific requirements for communication between electric road vehicle (EV) and infrastructure*. June 2019.
- [116] Barkow, A., Küfen, J., Hudecek, J., et al.: “Positionierungssystem für induktives Laden”. In: *ATZ*, vol. 117, no. 7 (2015), pp. 46–50.

- [117] Hassler, M., Atasoy, O., Kesler, M., et al.: “Impedance Measurement on Inductive Power Transfer Systems”. In: *2019 IEEE PELS Workshop on Emerging Technologies: Wireless Power Transfer (WoW)*. London, UK: IEEE, June 2019, pp. 39–44. ISBN: 978-1-5386-7514-4. DOI: 10.1109/WoW45936.2019.9030639.
- [118] Song, K., Wei, R., Zhang, H., et al.: “Interoperability Evaluation of Wireless EV Charging Systems Using Coil Ampere-Turns”. In: *2019 22nd International Conference on Electrical Machines and Systems (ICEMS)*. Harbin, China: IEEE, Aug. 2019. ISBN: 978-1-7281-3398-0. DOI: 10.1109/ICEMS.2019.8921585.
- [119] Sasatani, T., Narusue, Y. and Kawahara, Y.: “Dynamic Complex Impedance Tuning Method Using a Multiple-Input DC/DC Converter for Wireless Power Transfer”. In: *2018 IEEE Wireless Power Transfer Conference (WPTC)*. Montreal, Canada: IEEE, June 2018. ISBN: 978-1-5386-5159-9. DOI: 10.1109/WPT.2018.8639301.
- [120] Song, K., Yang, G., Wei, R., et al.: “Interoperability Evaluation of Wireless Electric Vehicle Charging Systems Based on Impedance”. In: *2019 IEEE Energy Conversion Congress and Exposition (ECCE)*. Baltimore, USA: IEEE, Sept. 2019, pp. 4580–4583. ISBN: 978-1-7281-0395-2. DOI: 10.1109/ECCE.2019.8912659.
- [121] Yang, G., Song, K., Huang, X., et al.: “Improved Interoperability Evaluation Method for Wireless Charging Systems Based on Interface Impedance”. In: *IEEE Transactions on Power Electronics*, vol. 36, no. 8 (2021), pp. 8588–8592. ISSN: 0885-8993. DOI: 10.1109/TPEL.2021.3053353.
- [122] Yang, G., Song, K., Sun, Y., et al.: “Interoperability Improvement for Rectangular Pad and DD Pad of Wireless Electric Vehicle Charging System Based on Adaptive Position Adjustment”. In: *IEEE Transactions on Industry Applications*, vol. 57, no. 3 (2021), pp. 2613–2624. ISSN: 0093-9994. DOI: 10.1109/TIA.2021.3056639.
- [123] Elshaer, M., Kautz, R., Wang, J., et al.: “Impedance Matching Network Optimization to Maximize Efficiency and Energy Transfer of WPT Systems”. In: *2018 IEEE PELS Workshop on Emerging Technologies: Wireless Power Transfer (Wow)*. Montreal, Canada: IEEE, June 2018. ISBN: 978-1-5386-2465-4. DOI: 10.1109/WoW.2018.8450888.
- [124] Takeda, K., Imura, T., Fujita, T., et al.: “Visualized Evaluation of Feasibility of Power Transmission with Electrical Constraints in Wireless Power Transfer”. In: *2020 IEEE PELS Workshop on Emerging Technologies: Wireless Power Transfer (WoW)*. Seoul, South Korea: IEEE, Nov. 2020, pp. 288–293. ISBN: 978-1-7281-3746-9. DOI: 10.1109/WoW47795.2020.9291302.
- [125] Kurpat, T. and Eckstein, L.: “Analysis of a Three-Phase IPT Secondary Side in Interoperable Single-Phase Operation”. In: *2022 IEEE Energy Conversion Congress and Exposition (ECCE)*. Detroit, USA: IEEE, Oct. 2022. ISBN: 978-1-7281-9387-8. DOI: 10.1109/ECCE50734.2022.9947997.
- [126] Barth, D., Cortese, G., Darrat, A. H., et al.: “Interoperability Rating of Wireless Charging Equipment using a Decoupled Impedance Interface”. In: *2020 IEEE Vehicle Power and Propulsion Conference (VPPC)*. Gijon, Spain: IEEE, Nov. 2020. ISBN: 978-1-7281-8959-8. DOI: 10.1109/VPPC49601.2020.9330964.

-
- [127] Matthaei, G. L., Young, L. and Jones, E. M. T.: *Microwave filters, impedance-matching networks, and coupling structures*. Repr. of the ed. publ. by McGraw-Hill 1964. The Artech House microwave library. Dedham, Mass.: Artech House, 1980. ISBN: 0-89006-099-1.
- [128] Thrimawithana, D. J. and Kim, S.: *Fundamentals of IPT Systems*. Auckland, 2019. URL: <https://wirelesspower.github.io/SeminarsWorkshops/FundamentalsofIPTDJT/presentation.html#10> (visited on 4/2/2023).
- [129] Kürschner, D., Ombach, G., Percebon, L., et al.: “Magnetic Leakage Field Study of a 7 kW Wireless Electric Vehicle Charging System”. In: *World Electric Vehicle Journal*, vol. 8, no. 2 (2016), pp. 501–510. DOI: 10.3390/wevj8020501.
- [130] Mohammad, M., Onar, O. C., Pries, J. L., et al.: “Analysis of Magnetic Field Emissions and Shield Requirements for Interoperating High-Power EV Wireless Charging System”. In: *2021 IEEE Applied Power Electronics Conference and Exposition (APEC)*. Phoenix, USA: IEEE, June 2021, pp. 1586–1592. ISBN: 978-1-7281-8949-9. DOI: 10.1109/APEC42165.2021.9487265.
- [131] Bosshard, R., Iruretagoyena, U. and Kolar, J. W.: “Comprehensive Evaluation of Rectangular and Double-D Coil Geometry for 50 kW/85 kHz IPT System”. In: *IEEE Journal of Emerging and Selected Topics in Power Electronics*, vol. 4, no. 4 (2016), pp. 1406–1415. ISSN: 2168-6777. DOI: 10.1109/JESTPE.2016.2600162.
- [132] Yilmaz, T., Hasan, N., Zane, R., et al.: “Multi-Objective Optimization of Circular Magnetic Couplers for Wireless Power Transfer Applications”. In: *IEEE Transactions on Magnetics*, vol. 53, no. 8 (2017), pp. 1–12. ISSN: 0018-9464. DOI: 10.1109/TMAG.2017.2692218.
- [133] Kürschner, D., Rathge, C. and Jumar, U.: “Design Methodology for High Efficient Inductive Power Transfer Systems With High Coil Positioning Flexibility”. In: *IEEE Transactions on Industrial Electronics*, vol. 60, no. 1 (2013), pp. 372–381. ISSN: 0278-0046. DOI: 10.1109/TIE.2011.2181134.
- [134] Nagendra, G. R., Covic, G. A. and Boys, J. T.: “Determining the Physical Size of Inductive Couplers for IPT EV Systems”. In: *IEEE Journal of Emerging and Selected Topics in Power Electronics*, vol. 2, no. 3 (2014), pp. 571–583. ISSN: 2168-6777. DOI: 10.1109/JESTPE.2014.2302295.
- [135] Chowdhury, M. S. A. and Liang, X.: “Comparative Characteristic Analysis of Circular and Double D Power Pads for Electric Vehicle Wireless Charging Systems”. In: *2019 IEEE Canadian Conference of Electrical and Computer Engineering (CCECE)*. Edmonton, Canada: IEEE, May 2019. ISBN: 978-1-7281-0319-8. DOI: 10.1109/CCECE.2019.8861733.
- [136] Knaisch, K. and Gratzfeld, P.: “Gaussian process surrogate model for the design of circular, planar coils used in inductive power transfer for electric vehicles”. In: *IET Power Electronics*, vol. 9, no. 15 (2016), pp. 2786–2794. ISSN: 17554535. DOI: 10.1049/iet-pel.2016.0392.
- [137] Lin, F. Y., Kim, S., Covic, G. A., et al.: “Effective Coupling Factors for Series and Parallel Tuned Secondaries in IPT Systems Using Bipolar Primary Pads”. In: *IEEE Transactions on Transportation Electrification*, vol. 3, no. 2 (2017), pp. 434–444. DOI: 10.1109/TTE.2017.2648123.

- [138] Bosshard, R., Kolar, J. W., Muhlethaler, J., et al.: “Modeling and η - α -Pareto Optimization of Inductive Power Transfer Coils for Electric Vehicles”. In: *IEEE Journal of Emerging and Selected Topics in Power Electronics*, vol. 3, no. 1 (2015), pp. 50–64. ISSN: 2168-6777. DOI: 10.1109/JESTPE.2014.2311302.
- [139] Bandyopadhyay, S., Venugopal, P., Dong, J., et al.: “Comparison of Magnetic Couplers for IPT-Based EV Charging Using Multi-Objective Optimization”. In: *IEEE Transactions on Vehicular Technology*, vol. 68, no. 6 (2019), pp. 5416–5429. ISSN: 0018-9545. DOI: 10.1109/TVT.2019.2909566.
- [140] Lawton, P. A. J., Lin, F. J. and Covic, G. A.: “Magnetic Design Considerations for High-Power Wireless Charging Systems”. In: *IEEE Transactions on Power Electronics*, vol. 37, no. 8 (2022), pp. 9972–9982. ISSN: 0885-8993. DOI: 10.1109/TPEL.2022.3154365.
- [141] Song, K., Yang, G., Guo, Y., et al.: “Design of DD Coil With High Misalignment Tolerance and Low EMF Emissions for Wireless Electric Vehicle Charging Systems”. In: *IEEE Transactions on Power Electronics*, vol. 35, no. 9 (2020), pp. 9034–9045. ISSN: 0885-8993. DOI: 10.1109/TPEL.2020.2971967.
- [142] Covic, G. A., Kissin, M. L. G., Kacprzak, D., et al.: “A bipolar primary pad topology for EV stationary charging and highway power by inductive coupling”. In: *2011 IEEE Energy Conversion Congress and Exposition (ECCE)*. Phoenix, USA: IEEE, Sept. 2011, pp. 1832–1838. ISBN: 978-1-4577-0542-7. DOI: 10.1109/ECCE.2011.6064008.
- [143] Lin, F. Y., Covic, G. A. and Boys, J. T.: “Leakage Flux Control of Mismatched IPT Systems”. In: *IEEE Transactions on Transportation Electrification*, vol. 3, no. 2 (2017), pp. 474–487. DOI: 10.1109/TTE.2016.2630922.
- [144] Pries, J., Galigekere, V. P. N., Onar, O. C., et al.: “A 50-kW Three-Phase Wireless Power Transfer System Using Bipolar Windings and Series Resonant Networks for Rotating Magnetic Fields”. In: *IEEE Transactions on Power Electronics*, vol. 35, no. 5 (2020), pp. 4500–4517. ISSN: 0885-8993. DOI: 10.1109/TPEL.2019.2942065.
- [145] Pearce, M. G. S., Covic, G. A. and Boys, J. T.: “Robust Ferrite-Less Double D Topology for Roadway IPT Applications”. In: *IEEE Transactions on Power Electronics*, vol. 34, no. 7 (2019), pp. 6062–6075. ISSN: 0885-8993. DOI: 10.1109/TPEL.2018.2883129.
- [146] Zaheer, A., Hao, H., Covic, G. A., et al.: “Investigation of Multiple Decoupled Coil Primary Pad Topologies in Lumped IPT Systems for Interoperable Electric Vehicle Charging”. In: *IEEE Transactions on Power Electronics*, vol. 30, no. 4 (2015), pp. 1937–1955. ISSN: 0885-8993. DOI: 10.1109/TPEL.2014.2329693.
- [147] Lin, F., Covic, G. A. and Kessler, M.: “Design of a SAE Compliant Multi-Coil Ground Assembly”. In: *IEEE Journal of Emerging and Selected Topics in Industrial Electronics*, vol. 1, no. 1 (2020), pp. 14–25. ISSN: 2687-9735. DOI: 10.1109/JESTIE.2020.2999597.
- [148] Gaona, D. E., Ghosh, S. and Long, T.: “Embedded compensation for DDQ/Bipolar-Q IPT Charging Pads”. In: *2019 IEEE Energy Conversion Congress and Exposition (ECCE)*. Baltimore, USA: IEEE, Sept. 2019, pp. 551–556. ISBN: 978-1-7281-0395-2. DOI: 10.1109/ECCE.2019.8913244.

-
- [149] Kim, S., Covic, G. A. and Boys, J. T.: “Tripolar Pad for Inductive Power Transfer Systems for EV Charging”. In: *IEEE Transactions on Power Electronics*, vol. 32, no. 7 (2017), pp. 5045–5057. ISSN: 0885-8993. DOI: 10.1109/TPEL.2016.2606893.
- [150] Mohammad, M., Pries, J. L., Onar, O. C., et al.: “Comparison of Magnetic Field Emission from Unipolar and Bipolar Coil-Based Wireless Charging Systems”. In: *2020 IEEE Transportation Electrification Conference & Expo (ITEC)*. Chicago, USA: IEEE, June 2020, pp. 1201–1207. ISBN: 978-1-7281-4629-4. DOI: 10.1109/ITEC48692.2020.9161726.
- [151] Zhao, F., Jiang, J., Cui, S., et al.: “Research on Bipolar Non-salient Pole Transmitter for High-power EV Dynamic Wireless Power Transfer System”. In: *IEEE Transactions on Power Electronics*, vol. 37, no. 2 (2021), pp. 2404–2412. ISSN: 0885-8993. DOI: 10.1109/TPEL.2021.3105441.
- [152] Dai, Z., Wang, J., Long, M., et al.: “Magnetic shielding structure optimization design for wireless power transmission coil”. In: *AIP Advances*, vol. 7, no. 9 (2017). DOI: 10.1063/1.4990775.
- [153] Mohamed, A. A. S. and Mohammed, O.: “Physics-Based Co-Simulation Platform With Analytical and Experimental Verification for Bidirectional IPT System in EV Applications”. In: *IEEE Transactions on Vehicular Technology*, vol. 67, no. 1 (2018), pp. 275–284. ISSN: 0018-9545. DOI: 10.1109/TVT.2017.2763422.
- [154] Choi, S. Y., Gu, B. W., Lee, S. W., et al.: “Generalized Active EMF Cancel Methods for Wireless Electric Vehicles”. In: *IEEE Transactions on Power Electronics*, vol. 29, no. 11 (2014), pp. 5770–5783. ISSN: 0885-8993. DOI: 10.1109/TPEL.2013.2295094.
- [155] Lawton, P., Lin, F. J. and Covic, G.: “Reducing and Validating Surface Flux Emissions for High-Power Wireless Charging Systems”. In: *2022 Wireless Power Week (WPW)*. Bordeaux, France: IEEE, July 2022, pp. 99–104. ISBN: 978-1-6654-8445-9. DOI: 10.1109/WPW54272.2022.9853991.
- [156] Alsayegh, M., Clemens, M. and Schmuelling, B.: “Misalignment Influence on Resonance Shielding in Wireless Power Transfer for Electric Vehicles”. In: *2019 IEEE PELS Workshop on Emerging Technologies: Wireless Power Transfer (WoW)*. London, UK: IEEE, June 2019, pp. 16–20. ISBN: 978-1-5386-7514-4. DOI: 10.1109/WoW45936.2019.9030670.
- [157] Mohammad, M., Pries, J., Onar, O., et al.: “Comparison of Leakage Magnetic Field from Matched and Mismatched Double-D Coil based Wireless Charging System for Electric Vehicles”. In: *2019 IEEE Energy Conversion Congress and Exposition (ECCE)*. Baltimore, USA: IEEE, Sept. 2019, pp. 5733–5739. ISBN: 978-1-7281-0395-2. DOI: 10.1109/ECCE.2019.8912989.
- [158] Mohammad, M., Pries, J., Onar, O., et al.: “Design of an EMF Suppressing Magnetic Shield for a 100-kW DD-Coil Wireless Charging System for Electric Vehicles”. In: *2019 IEEE Applied Power Electronics Conference and Exposition (APEC)*. Anaheim, USA: IEEE, Mar. 2019, pp. 1521–1527. ISBN: 978-1-5386-8330-9. DOI: 10.1109/APEC.2019.8722084.
- [159] Kim, J., Kim, J., Kong, S., et al.: “Coil Design and Shielding Methods for a Magnetic Resonant Wireless Power Transfer System”. In: *Proceedings of the IEEE*, vol. 101, no. 6 (2013), pp. 1332–1342. ISSN: 0018-9219. DOI: 10.1109/JPROC.2013.2247551.

- [160] Kim, S., Park, H.-H., Kim, J., et al.: “Design and Analysis of a Resonant Reactive Shield for a Wireless Power Electric Vehicle”. In: *IEEE Transactions on Microwave Theory and Techniques*, vol. 62, no. 4 (2014), pp. 1057–1066. ISSN: 0018-9480. DOI: 10.1109/TMTT.2014.2305404.
- [161] Mohammad, M., Onar, O. C., Galigekere, V. P., et al.: “Magnetic Shield Design for the Double-D Coil-Based Wireless Charging System”. In: *IEEE Transactions on Power Electronics*, vol. 37, no. 12 (2022), pp. 15740–15752. ISSN: 0885-8993. DOI: 10.1109/TPEL.2022.3191911.
- [162] Moon, H., Kim, S., Park, H. H., et al.: “Design of a Resonant Reactive Shield With Double Coils and a Phase Shifter for Wireless Charging of Electric Vehicles”. In: *IEEE Transactions on Magnetics*, vol. 51, no. 3 (2015). ISSN: 0018-9464. DOI: 10.1109/TMAG.2014.2360701.
- [163] Bosshard, R. and Kolar, J. W.: “Multi-Objective Optimization of 50 kW/85 kHz IPT System for Public Transport”. In: *IEEE Journal of Emerging and Selected Topics in Power Electronics*, vol. 4, no. 4 (2016), pp. 1370–1382. ISSN: 2168-6777. DOI: 10.1109/JESTPE.2016.2598755.
- [164] Mohammad, M., Onar, O. C., Galigekere, V. P., et al.: “Thermal Design and Optimization of High- Power Wireless Charging System”. In: *2022 IEEE Applied Power Electronics Conference and Exposition (APEC)*. Houston, USA: IEEE, Mar. 2022, pp. 480–485. ISBN: 978-1-6654-0688-8. DOI: 10.1109/APEC43599.2022.9773484.
- [165] Li, Y., Liu, S., Zhu, X., et al.: “Extension of ZVS Region of Series–Series WPT Systems by an Auxiliary Variable Inductor for Improving Efficiency”. In: *IEEE Transactions on Power Electronics*, vol. 36, no. 7 (2021), pp. 7513–7525. ISSN: 0885-8993. DOI: 10.1109/TPEL.2020.3042011.
- [166] Nguyen, B. X., Vilathgamuwa, D. M., Foo, G. H. B., et al.: “An Efficiency Optimization Scheme for Bidirectional Inductive Power Transfer Systems”. In: *IEEE Transactions on Power Electronics*, vol. 30, no. 11 (2015), pp. 6310–6319. ISSN: 0885-8993. DOI: 10.1109/TPEL.2014.2379676.
- [167] Nguyen, T.-D., Li, S., Li, W., et al.: “Feasibility study on bipolar pads for efficient wireless power chargers”. In: *2014 IEEE Applied Power Electronics Conference and Exposition - APEC 2014*. Fort Worth, USA: IEEE, Mar. 2014, pp. 1676–1682. ISBN: 978-1-4799-2325-0. DOI: 10.1109/APEC.2014.6803531.
- [168] Kang, J.-K., Hara, H., Yamamoto, E., et al.: “Analysis and evaluation of bi-directional power switch losses for matrix converter drive”. In: *Conference Record of the 2002 IEEE Industry Applications Conference. 37th IAS Annual Meeting (Cat. No.02CH37344)*. IEEE, 2002, pp. 438–443. ISBN: 0-7803-7420-7. DOI: 10.1109/IAS.2002.1044123.
- [169] Kalra, G. R., Pearce, M. G. S., Kim, S., et al.: “A Power Loss Measurement Technique for Inductive Power Transfer Magnetic Couplers”. In: *IEEE Journal of Emerging and Selected Topics in Industrial Electronics*, vol. 1, no. 2 (2020), pp. 113–122. ISSN: 2687-9735. DOI: 10.1109/JESTIE.2020.3014823.
- [170] Kim, S., Amirpour, M., Dharmakeerthi, T., et al.: “Thermal Evaluation of an Inductive Power Transfer Pad for Charging Electric Vehicles”. In: *IEEE Transactions on Industrial Electronics*, vol. 69, no. 1 (2022), pp. 314–322. ISSN: 0278-0046. DOI: 10.1109/TIE.2021.3055186.

-
- [171] Bühler, G.: *Systemverluste bei der berührungslosen induktiven Energieübertragung*. 1. Aufl. Energietechnik. München: Hut, 2009. ISBN: 978-3-86853-172-5.
- [172] Wintrich, A., Nicolai, U., Tursky, W., et al.: *Application manual power semiconductors*. 2nd revised edition. Ilmenau: ISLE Verlag, 2015. ISBN: 978-3-938843-83-3.
- [173] Kavimandan, U., Galigekere, V. P. N., Ozpineci, B., et al.: “The Impact of Inverter Dead-Time in Single-Phase Wireless Power Transfer Systems”. In: *IEEE Transactions on Power Electronics*, vol. 37, no. 1 (2021), pp. 1074–1089. ISSN: 0885-8993. DOI: 10.1109/TPEL.2021.3092400.
- [174] Lin, F., Lawton, P. and Covic, G. A.: “Discrete Modeling of Passive Rectifiers in LCL Tuned Inductive Power Transfer Receivers”. In: *IEEE Transactions on Power Electronics*, vol. 38, no. 10 (2023), pp. 11751–11762. ISSN: 0885-8993. DOI: 10.1109/TPEL.2023.3272645.
- [175] CREE: *Silicon Carbide Power MOSFET C2M MOSFET Technology, C2M0025120D, datasheet*. 2021. URL: <https://assets.wolfspeed.com/uploads/2020/12/C2M0025120D.pdf> (visited on 11/3/2023).
- [176] Lim, Y., Tang, H., Lim, S., et al.: “An Adaptive Impedance-Matching Network Based on a Novel Capacitor Matrix for Wireless Power Transfer”. In: *IEEE Transactions on Power Electronics*, vol. 29, no. 8 (2014), pp. 4403–4413. ISSN: 0885-8993. DOI: 10.1109/TPEL.2013.2292596.
- [177] Mukherjee, S., Galigekere, V. P. and Onar, O.: “Methods to Synchronize and Control the Secondary Side Active Rectifier in Wireless Power Transfer Systems”. In: *2020 IEEE Transportation Electrification Conference & Expo (ITEC)*. Chicago, USA: IEEE, June 2020, pp. 955–960. ISBN: 978-1-7281-4629-4. DOI: 10.1109/ITEC48692.2020.9161711.
- [178] Desmoort, A., Deblecker, O. and Greve, Z. de: “Active Rectification For the Optimal Command of Bidirectional Resonant Wireless Power Transfer Robust to Severe Circuit Parameters Deviations”. In: *IEEE Transactions on Industry Applications*, vol. 56, no. 2 (2020), pp. 1640–1648. ISSN: 0093-9994. DOI: 10.1109/TIA.2020.2966161.
- [179] IXYS: *Power Semiconductor Modules, High Current Diode Modules, MDD172-08N1, datasheet*. 2019. URL: <https://www.mouser.de/datasheet/2/240/MDD172-08N1-1548104.pdf> (visited on 25/3/2023).
- [180] CREE: *All Silicon Carbide Half-Bridge Module, CAB008A12GM3, datasheet*. 2021. URL: <https://www.mouser.de/datasheet/2/90/CAB008A12GM3-2853770.pdf> (visited on 25/3/2023).
- [181] Wolfspeed: *All Silicon Carbide High Performance, Switching Optimized, Half-Bridge Module, CAS120M12BM2, datasheet*. 2020. URL: <https://assets.wolfspeed.com/uploads/2020/12/cas120m12bm2.pdf> (visited on 25/3/2023).
- [182] Fu, N., Deng, J., Wang, Z., et al.: “A Hybrid Mode Control Strategy for LCC–LCC - Compensated WPT System With Wide ZVS Operation”. In: *IEEE Transactions on Power Electronics*, vol. 37, no. 2 (2022), pp. 2449–2460. ISSN: 0885-8993. DOI: 10.1109/TPEL.2021.3108637.

- [183] Bucher, A.: “Resonante Konverter höherer Ordnung für die kontaktlose induktive Energieübertragung”. Dissertation. Nuremberg: Friedrich-Alexander-University Erlangen-Nuremberg, 2014. URL: <https://opus4.kobv.de/opus4-fau/files/5034/DissertationAlexBucher.pdf>.
- [184] Fang, Y. and Pong, M. H.: “Multiple Harmonics Analysis for Variable Frequency Variable Duty-Cycle Controlled Inductive Power Transfer Systems”. In: *2018 IEEE PELS Workshop on Emerging Technologies: Wireless Power Transfer (Wow)*. Montreal, Canada: IEEE, June 2018, pp. 1–6. ISBN: 978-1-5386-2465-4. DOI: 10.1109/WoW.2018.8450933.
- [185] Fang, Y., Pong, B. M. H. and Hui, R. S. Y.: “An Enhanced Multiple Harmonics Analysis Method for Wireless Power Transfer Systems”. In: *IEEE Transactions on Power Electronics*, vol. 35, no. 2 (2020), pp. 1205–1216. ISSN: 0885-8993. DOI: 10.1109/TPEL.2019.2925050.